Investigation of terrain effects on wind dynamics within the lower atmospheric boundary layer

Dissertation

with the aim of achieving a doctoral degree

at the Faculty of Mathematics, Informatics and Natural Sciences

Department of Earth Sciences

at Universität Hamburg

Submitted by

Sylvio Freitas

from Saint Helier, United Kingdom

Hamburg, 2020

Accepted as Dissertation at the Department of Earth Sciences

Day of oral defense:	15.05.2020
Reviewers:	Prof. Dr. Bernd Leitl
	Prof. Dr. Matthias Hort
	Prof. Dr. Jürgen Böhner
	Dr. Frank Harms
	Dr. Martin Gade
Chair of the Subject Doctoral Committee:	Prof. Dr. Dirk Gajewski
Dean of Faculty of MIN:	Prof. Dr. Heinrich Graener

ABSTRACT

In micrometeorology, it is well established that near-surface winds are strongly affected by orography. Largely oriented to wind energy applications, most efforts to understand microscale atmospheric boundary layer (ABL) flows over orography are centred on quantifying the gains in wind speed over crests of hills or ridges. Less focus has been given to expressing the effects of terrain on flow turbulence. Numerical modelling is presently the main tool used for flow predictions, large-eddy simulation (LES) rapidly becoming the primary approach. Increasing spatial and temporal resolutions of LES imply that smaller features, previously treated as surface roughness, are explicitly resolvable. However, validation datasets of turbulence characteristics for LES studies of flows over orography tend to incompletely reproduce smaller scale features.

The present research addresses the aforementioned topics by providing characterisations of near-surface turbulence of ABL flows over idealised terrain geometries of varying complexity, modelled in a large boundary layer wind tunnel. Four central research questions are proposed and explored with the data resulting from the experiments. Moreover, the extensive high-resolution measurements of flows over several models of idealised three-dimensional (3D) ridges and valleys aim to provide validation datasets for numerical models. Validation data requirements from potential users for the experiments are ascertained through the realisation of two workshops for numerical modellers. Effects of ridge slopes and valley widths on the turbulence characteristics of a moderately rough classed ABL flow (modelled above flat terrain of homogeneous roughness) are evaluated through individual parameter variation. This is performed systematically for the valley widths. The bulk of data analyses consist of mean turbulence parameters. However, transient turbulence features of the flows above valleys are also explored.

Results highlight the impact of local terrain structures on near-ground turbulence. Expectedly, flow separation originates at the crests of all ridges. The resulting flow recirculation zones are slope-dependent, as are increases in turbulence observed throughout the study domains. Systematic modifications of the valley widths generate relevant effects, in particular downstream from the first ridges of the valleys. Data also provides insight relative to the sensitivity of turbulence parameters to orography and their suitability for flow characterisations. Furthermore, the impact of the reference coordinate system of the measurements above orography is assessable with the present data.

Keywords: atmospheric boundary layer flow, complex terrain, environmental wind tunnel, idealised flow, numerical model validation, parameter variation, turbulence characterisation.

KURZFASSUNG

In der Mikrometeorologie ist allgemein bekannt, dass oberflächennahe Winde stark von orographischen Strukturen beeinflusst werden. Aktuell konzentrieren sich im Bereich der Windenergiegewinnung Bemühungen zum Verständnis mikroskaliger atmosphärischer Grenzschichtströmungen (ABL) über strukturiertem Geländekonzentrieren sich auf die Quantifizierung der Windgeschwindigkeitsgewinne über Hügelkuppen oder Graten. Bisher weniger untersucht wurden die Auswirkungen des Geländes auf die Strömungsturbulenzen. Die numerische Modellierung ist derzeit das wichtigste Werkzeug für entsprechende Strömungsprognosen, wobei die Large-Eddy-Simulation (LES) sich zunehmend als favorisierte Methode etabliert. Steigende räumliche und zeitliche Auflösungen von LES bedeuten, dass kleinere Merkmale, die bisher als Oberflächenrauhigkeit behandelt wurden, explizit auflösbar sind. Existierende Validierungsdatensätze zur Überprüfung der Turbulenzeigenschaften für LES-Studien von Strömungen über Orographie bilden die kleinskaligen Turbulenzeigenschaft nur unzureichend ab.

Die vorliegende Arbeit befasst sich mit den oben genannten Themen, indem sie Charakterisierungen der oberflächennahen Turbulenz von ABL-Strömungen über idealisierten Geländeformen unterschiedlicher Komplexität liefert. Die Grundlage bilden systematische Modellmessungen in einem großen Grenzschichtwindkanal. Vier zentrale Forschungsfragen werden entwickelt und mit den aus den Experimenten resultierenden Daten untersucht. Darüber hinaus zielen die umfangreichen hochauflösenden Messungen von Strömungen über mehrere Modelle idealisierter dreidimensionaler Bergrücken und Täler darauf ab, Validierungsdatensätze für numerische Modelle bereitzustellen. Die Anforderungen von potenziellen Anwendern an anwendungsspezifische Validierungsdaten wurden im Rahmen zweier Workshops für numerische Modellierer ermittelt und diskutiert. Die Auswirkungen von Hangneigung und Talbreiten auf die Turbulenzeigenschaften einer mäßig rau klassifizierten ABL-Strömung (modelliert über flachem Gelände mit homogener Rauheit) werden durch individuelle Parametervariationen bewertet; für die Talbreiten wird dies systematisch durchgeführt. Der Schwerpunkt der Datenanalysen liegt auf gemittelten Turbulenzparametern, es werden aber auch transiente Turbulenzmerkmale der Strömungen über Tälern untersucht.

Die Ergebnisse dokumentieren die qualitativen und quantitativen Auswirkungen der Geländeform auf die bodennahe Turbulenz. Erwartungsgemäß wird an den untersuchten Hügeln Strömungsablösung beobachtet. Die resultierenden Rezirkulationsgebiete sind neigungsabhängig, ebenso wie die beobachtete Zunahme der bodennahen Windturbulenz. Systematische

Veränderungen der Talbreiten erzeugen relevante Effekte, insbesondere in Lee des ersten Grates der Täler. Die ermittelten Daten geben auch Aufschluss über die Sensitivität der Turbulenzparameter bezüglich der Orographie sowie deren Eignung für Strömungscharakterisierungen. Darüber hinaus ist die Auswirkung des verwendeten Referenzkoordinatensystems auf die Analyseergebnisse mit den vorliegenden Daten abschätzbar.

Schlüsselwörter: atmosphärische Grenzschichtströmung, komplexes Gelände, Grenzschichtwindkanal, idealisierte Strömung, numerische Modellvalidierung, Parametervariation, Turbulenzbeschreibung.

ACKNOWLEDGEMENTS

As I finalise this enriching chapter of my life, there are many people to whom I'm indebted. Indeed, too many to fit here. Thus, I single out the following people for my gratitude in significantly aiding this accomplishment.

My supervisors Bernd Leitl and Frank Harms, who granted me the opportunity to take on this challenge. Their technical and scientific guidance provided a strong platform that culminated in this thesis. I am deeply thankful for their contributions, without which this work could not have been possible. My gratitude not only contemplates the professional environment but also extends to the very enjoyable occasions outside of work, even those that may or may not have resulted in somebody sustaining a foot injury.

My colleagues of the EWTL working group Benjamin Schliffke and Felix Erdmann, for their help with data processing scripts. Additional thanks are given to the former for his cordiality. Eva Berbekar, Meike Hellweg, and Phillip Palk are esteemed for helping with my early integration and for their friendliness. Further appreciation is addressed to the latter two for being splendid office colleagues.

My student helpers Ge Cheng, Jessica W., and Imke S. for their help with several less desirable chores, including support provided with the scripting for the transient flow data analyses.

Members of the CEN faculty Jan Stofledt, given the unenviable task of building all of my terrain models, and Sabine Ehrenreich, for her valuable help with the organisation of the workshops and the never-ending bureaucracies, warrant my gratitude. Further appreciation is addressed to Heinke Schlünzen and Rainer Senke for their kindness and interesting conversations.

On a more personal note, Melanie for her calmness, patience, perseverance, and tolerance. Without these and her permanent support, this work could not have been possible. Looking forward to all future endeavours together. My parents for all they have done for me. No achievement of mine could have been accomplished without their unconditional love and care. I will always be grateful to them.

My friends Carlos, for the long-term loan of his laptop when mine deceased, and Nuno, for storing all my junk left behind in Aveiro, when moving to Hamburg, for almost two years. Nadine, Lea, and Julian for enjoyable and relaxing times during my time here.

CONTENTS

LIST OF ABBREVIATIONS

ABL	Atmospheric boundary layer
a.s.l.	Above sea-level
ASL	Atmospheric surface layer
B1	Foot of windward (uphill) slope of ridges
B2	Foot of leeside (downhill) slope of ridges
CFD	Computational fluid dynamics
CNC	Computer numerical control
CO_2	Carbon dioxide
Cr	Crest of single ridges
Cr1	Crest of first ridge of valleys
Cr2	Crest of second ridge of valleys
DDW	Extended downwind subdomain of single ridges
DNS	Direct numerical simulation
DW	Downwind subdomain
EWTL	Environmental wind tunnel laboratory (University of Hamburg)
Fig.	Figure
FS	Full scale
LDV	Laser Doppler velocimetry
LES	Large eddy simulation
LW	Leeside slope subdomain of single ridges
MS	Model scale
MV	Mid-valley
NEWA	New European Wind Atlas
NSE	Navier-Stokes equation
PDF	Probability density function
RANS	Reynolds-averaged Navier-Stokes
RMS	Root mean square
SGS	Sub-grid scale (LES)
SSW	South-southwest
UpW	Upwind subdomain of single ridges
URANS	Unsteady Reynolds-averaged Navier-Stokes
UV	Horizontal plane
UW	Vertical plane
V & V	Verification and validation
1D	One-dimensional
2D	Two-dimensional
3D	Three-dimensional

LIST OF SYMBOLS

Geometric parameters

$\boldsymbol{A}$	**Valley width**
$\boldsymbol{H}$	**Ridge height/valley depth**
$\boldsymbol{L}$	**Horizontal (longitudinal) length of ridge**
$\boldsymbol{L_R}$	**Horizontal length of ridge slope**
$\boldsymbol{L/H}$	**Aspect ratio of ridge geometry**
$\boldsymbol{\gamma}$	**Inclination of windward (uphill) slope of ridge**
$\boldsymbol{\theta}$	**Inclination of leeside (downhill) slope of ridge**

Dimensions and coordinates

$\boldsymbol{X}$	**Longitudinal position in absolute coordinates**
$\boldsymbol{x/H}$	**Dimensionless length above flat terrain in relative coordinates (non-dimensionalised by ridge height)**
$\boldsymbol{x/L_R}$	**Dimensionless length above orography in relative coordinates (non-dimensionalised by slope length of ridge)**
$\boldsymbol{Y}$	**Lateral position in absolute coordinates**
$\boldsymbol{Z}$	**Vertical position (height) above sea level in absolute coordinates**
$\boldsymbol{Z_{AT}}$	**Vertical position (height) above local terrain (terrain-following) in absolute coordinates**
$\boldsymbol{z/H}$	**Dimensionless height above sea level in relative coordinates (non-dimensionalised by ridge height)**
$\boldsymbol{z_{AT}/H}$	**Dimensionless height above local terrain (terrain-following) in relative coordinates (non-dimensionalised by ridge height)**

Flow parameters

$\boldsymbol{d_0}$	**Zero-plane displacement**
$\boldsymbol{f}$	**Frequency of velocity fluctuations**
$\boldsymbol{f\ (u > \sigma_U)}$	**Frequency of transient longitudinal velocity fluctuations**
$\boldsymbol{f\ (v > \sigma_U)}$	**Frequency of transient lateral velocity fluctuations**
$\boldsymbol{f\ (w > \sigma_U)}$	**Frequency of transient vertical velocity fluctuations**
$\boldsymbol{f_{red}}$	**Reduced frequency of spectral distributions of turbulence**
$\boldsymbol{G_{T,\tau}}$	**Gust factor of duration τ over sampling period T**
$\boldsymbol{I_U}$	**Longitudinal turbulence intensity**
$\boldsymbol{I_V}$	**Lateral turbulence intensity**
$\boldsymbol{I_W}$	**Vertical turbulence intensity**

L_U^X/H	**Dimensionless integral length scale of longitudinal turbulence in the longitudinal flow direction**
M/U_0	**Dimensionless velocity magnitude**
Re	**Reynolds number**
Re_*	**Roughness Reynolds number**
S_{UU}	**Spectral density distribution of longitudinal turbulence**
S_{VV}	**Spectral density distribution of lateral turbulence**
S_{WW}	**Spectral density distribution of vertical turbulence**
TKE	**Turbulent kinetic energy**
U_0	**Reference longitudinal velocity**
U/U_0	**Dimensionless longitudinal component of velocity**
V/U_0	**Dimensionless lateral component of velocity**
W/U_0	**Dimensionless vertical component of velocity**
X_{RZ}	Length of recirculation zones downwind from single ridges
u'/U_0^2	**Dimensionless transient fluctuations of longitudinal velocity**
v'/U_0^2	**Dimensionless transient fluctuations of lateral velocity**
w'/U_0^2	**Dimensionless transient fluctuations of vertical velocity**
$u'v'/U_0^2$	**Dimensionless horizontal component of turbulent velocity fluxes**
$u'w'/U_0^2$	**Dimensionless vertical component of turbulent velocity fluxes**
u_*	**Longitudinal friction velocity**
z_0	**Aerodynamic surface roughness length**
α	**Power law exponent of velocity profile**
δ	**Depth of atmospheric boundary layer**
ν	**Kinematic viscosity**
ρ	**Density**
σ_U/U_0	**Dimensionless longitudinal velocity fluctuation (standard deviation)**
σ_V/U_0	**Dimensionless lateral velocity fluctuation (standard deviation)**
σ_W/U_0	**Dimensionless vertical velocity fluctuation (standard deviation)**
$\sigma_U : \sigma_V$	**Ratio between longitudinal and lateral velocity fluctuations**
$\sigma_U : \sigma_W$	**Ratio between longitudinal and vertical velocity fluctuations**

1 INTRODUCTION

In atmospheric sciences, complex terrain is the term used to classify irregular orography that exerts effects on local meteorology. In the lower Atmospheric Boundary Layer (ABL), wind dynamics are strongly affected by complex terrain. This is translated by increases of spatial and temporal variability of the flow interactions with the orography that arise from the loss of flow equilibrium conditions at the near-surface due to terrain heterogeneities. Complex terrain winds are relevant to a variety of applications that include for example wind energy, air quality, and wind-loads on engineering structures. Effects of orography on near-surface winds are particularly important for microscale flow domains, characterised by short-lived flow phenomena that occur over small length ($< 10\ km$) and time ($< 1\ hour$) scales. Single terrain features (hills or ridges) constitute the majority of microscale flow investigations related to orography in the Literature. However, ABL flows over complex terrain are also relevant for mesoscale flows, as exemplified by regions of structured terrain such as mountain ranges.

As detailed in Chapter 4, the first studies of terrain winds, dating back to the late 1930s, consisted of flow evaluations over lee-waves and mountains through analytical theory and phenomenological observations in wind tunnels (Meroney, 1990). However, it was the linear theory of flow over gentle-sloped two-dimensional hills (proposed by Jackson & Hunt, 1975) that constituted the first major contribution to the field of flows over complex terrain and instigated a boom of subsequent related publications. The advent of wind energy harvesting, in the context of renewable energies for long-term sustainability, was the second major contributor to the field of investigations of winds over orography. Significant increases of wind velocity above complex terrain can lead to gains in energy production, which reduces the dependence on fossil fuels and the consequent emissions related to their combustion. Since the inception of the wind energy industry, the bulk of investigations of flows over orography has been oriented to expressing energy potential. This consists of quantifying the speed-up (velocity increases) of microscale flows above crests of hills and ridges. Less relevant for wind energy production, fewer efforts have been given to understanding how orography affects the turbulence characteristics of the flows, despite the fact that wind turbulence and gustiness govern structural safety considerations for wind farm installations.

Numerical modelling is the primary tool used for micro- and mesoscale flow predictions over complex terrain. Sub-mesoscale and microscale flows are driven by turbulence and consequent numerical modelling efforts must account for its effects. Depending on the applied grid resolution, terrain structures are partially resolved explicitly in mesoscale study domains, whereas smaller details are parameterised as surface roughness. Earlier predictions used the aforementioned linear theory to quantify speed-ups. These were found to break down for hill and ridge geometries with steep slopes, for which flow separation occurs. Computational advances make it possible to develop and apply higher resolution models, these presently enabling simulations of flows over three-dimensional (3D) complex terrain domains at increasing grid resolutions.

Time-dependent Large Eddy Simulation (LES) models of environmental flows are becoming the most widespread approach for numerical evaluations of flows over orography, succeeding the Reynolds-Averaged Navier-Stokes (RANS) methods that rely on time-averaged quantities. Results of the corresponding simulations of terrain-resolving flows are dependent on the applied turbulence setups, particularly at the near-surface. Whilst equivalent terrain-induced flow characteristics are generally observed between numerical results and experimental datasets at the upper altitudes of the ABL, limited agreement at the nearest heights to the surfaces is frequently reported (discussed in Chapter 4). Further constraints to developments in LES modelling of complex terrain flows originate from the lack of dedicated validation datasets from experimental research. Validation datasets for numerical complex terrain models originate from on-site measurements made in field campaigns or through physical ABL modelling (normally) carried out in environmental wind tunnels.

The most reliable sources of datasets of flows over complex terrain are assumed to be field experiments, which are measurements of real atmospheric flows, thus exempt from modelling-related assumptions. However, field campaigns require assumptions to be made with regard to the corresponding boundary conditions and the representativeness of the selected sites. High costs of related equipment and logistics can limit field campaigns to short periods. Demands for sites that simultaneously fulfil the requisites of well-defined inflow characteristics and maximal representativeness of the landforms are extremely rare in nature. Furthermore, site-specific measurement data cannot be generalised or transferred to other orographic structures without additional assumptions that tend to reduce the accuracy of the results. Field campaigns have the additional drawback of frequently varying meteorological conditions or large periods of calms (without wind).

Physical modelling of ABL flows has the main benefit of enabling wide control over shear-driven flow dynamics. This modelling approach dictates that the scaled wind tunnel flows are assumed to replicate those of the full-scale if certain similarity criteria are fulfilled. The majority of wind tunnel investigations of ABL flows over complex terrain consists of speed-up quantifications over idealised two-dimensional (2D) terrain geometries. Not oriented to LES model validation, measurements are restricted to coarse spatial and temporal resolutions that are deemed sufficient for time-averaged turbulence quantifications. Moreover, it is frequent that resulting flow characteristics and experimental setups are insufficiently documented to enable a comprehensive numerical reproduction of the experiments. The major drawback to LES validation with wind tunnel data corresponds to the resolvability of the small scale features of turbulence of a downscaled flow, both dependent on experimental and measurement setups of the campaigns. These effects are minimised with large enough scales of the modelled flow and the employment of appropriate measurement techniques.

Despite improvements made to experimental measurement techniques, there is an evident lack of quality LES validation datasets of flow turbulence over complex terrain. The growth rate of computational capabilities for LES modelling clearly overpowers the rate of developments made for validation experiments. This is exacerbated by the majority of experiments for validation of numerical models being designed to suit the requirements of RANS models. Furthermore, no clear experimental guidelines for LES validation data exist for flows over orography. This increases the gap between (spatial and temporal) resolutions of LES capabilities and available experimental validation data.

1.1 Scope and challenges of this work

The present dissertation is part of a larger research effort that aims to contribute to an improved understanding of the variability of flow dynamics due to complex terrain. More specifically, the research is centred on evaluating terrain-induced effects on near-surface flow turbulence through physical modelling of atmospheric flows at the Environmental Wind Tunnel Laboratory (EWTL) of the University of Hamburg. The research work presented here is supplemented by the contributions from Erdmann (2017) and Diezel (2019), which focus on sub-problems of flows over orography. To formalise, the proposed outcomes of the research are twofold:

- To address four central research questions related to the turbulence of wind interactions with orography.
- To provide reference turbulence datasets for validation of numerical models of complex terrain winds.

The first outcome is the scientific motivation of the present investigation, founded on the need to understand how orography affects near-surface turbulence of ABL flows. Within this field, there are many open questions related to the impact of small and moderate size terrain structures on near-surface wind and turbulence conditions. To thoroughly address each of these demands, increasing specificity of experimental designs are required. However, these result in increasingly incompatible setups with regard to those designed to answer other questions. There is no single experimental setup capable of providing data that comprehensively answers all potential research questions regarding flows over orography. Thus, finding an appropriate balance between experimental designs and data requirements for each of the proposed research questions is a major challenge of this study. Current research is primarily centred on the following four research questions, which are addressed partially or exhaustively using a single inflow and measurement setup:

1. What influence does complex terrain have on the near-surface wind turbulence and how far upstream and downstream from the orography are changes in the turbulence visible or significant?
2. How does the turbulence structure of the inflow affect the heterogeneity of turbulence above orography and how sensitive are the related turbulence properties with respect to the properties of the inflow ABL?
3. Which between orography and aerodynamic surface roughness exerts the largest influence on the properties of the near-surface wind turbulence?
4. Can characteristic single orographic structures (such as hills, ridges, or valleys) be categorised according to specific properties of near-ground wind turbulence?

The first question is essentially focused on quantifying the influence of individual geometric parameters of ridges and valleys on the near-surface turbulence structure. This is not limited to regions of the flow above the landforms and includes upwind and downwind regions from their location. The majority of comparable studies in the Literature are focused on regions upwind from the crests of hills or ridges (Chapter 4). Less efforts are given to characterising flow fields downwind from the crests, contemplated with the present investigation. Similar considerations can be made for the second research question, which aims to assess the sensitivity of turbulence parameters upwind from orography. In particular, effects of the inflow turbulence characteristics on the overall turbulence structure above the orography are scarcely addressed in the Literature. The third topic of research focuses on verifying if effects of surface roughness on near-ground turbulence are comparable to those produced by orography. In the context of mesoscale flow analyses above complex terrain, this is particularly relevant for the smaller terrain features that cannot be resolved explicitly and parameterised as surface roughness. Finally, the fourth research question aims to ascertain whether single landforms can be grouped according to the effects produced on near-surface turbulence. This consists of verifying the occurrence of turbulence phenomena that are exclusive to specific types of orography.

The second outcome of the present investigation aims to address the lack of validation data for numerical modelling of ABL flows over orography by providing several systematic datasets of wind fields related to terrain geometries of varying complexities. In addition to the raw measurement data, this requires data quality assurance verifications and thoroughly documented experimental setups. The main challenge of this task consists of designing experiments that suit the needs of LES model validation, which demands large spatial and temporal resolutions of the measurement data. A better understanding of the specific validation data requirements for LES modelling of orographic winds is gained through a Workshop for numerical modellers with a background in ABL flows over complex terrain. This event is organised with the aim of providing a foundation for the extensive experimental work of the present investigation and maximising its impact.

1.2 Experimental approach

Experiments of this investigation are focused on microscale flows over idealised (generic) 3D orography. Near-surface turbulence characterisations are performed over idealised ridges and valleys over two experimental campaigns performed in the same wind tunnel (Chapter 5). Idealised terrain features provide maximal data transferability to other landforms of the same type and simplified individual parameter variation without requirements for maintaining given shapes. Further benefits include the less constrained choice of geometric scaling and variable flow scaling within a limited extent (under the fulfilment of flow similarity criteria). Both experimental campaigns share the same ABL setup over flat terrain of homogeneous surface characteristics, at a geometric model scale of about $1{:}\,1000$, generating an inflow profile consistent with an ABL flow over a moderately rough surface. This also provides reference data with which terrain effects on the turbulence can be ascertained through comparison between orography and flat terrain datasets.

For the first campaign, effects of the slopes of single ridges on turbulence is assessed for three possible inclinations of windward (uphill) and leeside (downhill) slopes. Three single ridge geometries, which share the same heights and surface roughness conditions, are studied. The second campaign is centred on symmetric valleys built from combined setups of equivalent ridge geometries, which results in three generic valley geometries. The influence of the valley widths is evaluated through systematic increases of constant amplitude for each of the three valley geometries, resulting in a total of thirteen valley models.

Qualitative flow visualisations and flow measurements, between a fixed inflow location and the landform positions, are performed for every terrain geometry. Similarity criteria of the scaled flow is fulfilled at all locations where checks are performed (including above orography) and a fully turbulent flow is ascertained for a wide range of inflow velocities. The temporal representativeness of the measured (time-averaged) flow statistics is also verified and the statistical reproducibility of the measurement chain quantified. The latter is expressed through data uncertainties that originate from dedicated repetitive measurements for three height ranges above the local surfaces. For the valley campaign, changes made to the measurement setup provide higher temporal resolution of the measurements and transient (time-dependent) analyses of the flows above orography are explored.

The measurement strategy of the present investigation is oriented to providing the fullest possible flow field information at high enough resolutions, mandatory for adequate LES validation datasets. Due to the large volumes of resulting data, measurement positions are grouped into flow regions, each ridge consisting of four subdomains and valleys divided into three. Consequently, turbulence analyses are made for a limited number of locations within each subdomain. Quality-assured raw measurement data series from all positions are available to the numerical modelling community.

1.3 Thesis structure

The present thesis is organised into ten chapters. An initial understanding of the concepts related to ABL flows over orography are obtained from Chapters 2 to 4. This is followed by analyses of experimental requirements and characterisations of the ABL and the flows above orography, made in Chapters 5 to 8. General discussions and conclusions are reserved for Chapters 9 to 10. Chapters are outlined as follows:

Chapter 2 – Provides a summarised introduction to generalized theory of turbulent flows and presents the near-surface properties of ABL flows. The main purpose of this chapter is to briefly familiarise the reader with essential notions underlying the flow analyses made later.

Chapter 3 – Introduces concepts of physical ABL flow modelling and related evaluation techniques. This includes an introduction to the WOTAN wind tunnel of the EWTL, used for the present experiments, and the measurement/visualization methods used.

Chapter 4 – Reviews former investigations made in the field of ABL flows over complex terrain, with particular emphasis on turbulence analyses. This aims to provide an understanding of the state of the art of modelling and field measurements related to flows over complex terrain.

Chapter 5 – Presents the methodology used for the present experiments and discusses the motivations driving the selection made for the experimental setups. Modelled ABL setups and terrain geometries are defined. Considerations related to the aptitude of the measurement setups for high-resolution turbulence measurements are also discussed.

Chapter 6 – Characterises the modelled inflow ABL common to single ridge and valley flows. The data, obtained above a flat surface with homogeneous roughness, acts as flat terrain reference with which effects of the orography on the flow are later evaluated.

Chapter 7 – Presents and analyses the results of the near-surface mean flows over single ridges. Aimed at providing a wider understanding of the turbulence fields above orography, separate analyses are made for the aforementioned four flow subdomains of each ridge geometry. Effects of the ridge slope inclinations on the turbulence are also investigated.

Chapter 8 – Evaluates the flows over four distinct longitudinal positions of the valleys, with particular emphasis given to the effects of the valley types and the systematic modifications of the widths on the flow dynamics. The suitability of the present measurement setup for transient (time-dependent) flow characterisations is also explored.

Chapter 9 – Discusses the experimental findings with respect to the four research questions defined earlier. Relevant topics related to the measurement setups and flow parameter sensitivity to orography are also addressed.

Chapter 10 – Critically reviews the main findings of the present investigation and discusses potential improvements and additional steps for future investigations.

Appendices A-F supplement the aforementioned work and are referred to when relevant.

Unless specified otherwise, all results of the flow analyses in Chapters 6 to 8 are dimensionless. Results of the flows over orography, presented in Chapters 7 and 8, follow a model-specific colour assignment scheme that is defined in Chapter 5. Each ridge geometry is assigned a name and colour, with results systematically presented in compliance (Chapter 7). The results for the valley flows (Chapter 8) use the same colours as the ridges from which they originate. Similarly, measurement locations are also given names for ease of interpretation. This is most relevant for the results of the ridge campaign.

2 ATMOSPHERIC BOUNDARY LAYER THEORY

This chapter aims to briefly introduce theoretical concepts underlying atmospheric boundary layer (ABL) flows, with particular emphasis on those most relevant for the work performed within the scope of the present thesis. To begin with, the governing equations of fluid flow are briefly presented. This is extended to a condensed summary of classical turbulence theory. For more details regarding the general theory of fluid flows, the reader is referred to the works of Pope (2000) and Triton (1988). Finally, a summarized view of the structure of the lower atmosphere and how general fluid flow theory applies to ABL flows is given, with particular emphasis on microscale aspects of near-surface flows. This corresponds to only a small part of the vaster atmospheric flow theory. For further insight into ABL concepts, the reader is redirected to the specialised Literature, such as the works of Stull (1988), Stull (2000), or Foken (2008).

2.1 Equations of motion

Physical laws that describe fluids in motion arise from fundamental laws of mechanics and thermodynamics. The majority of studies involving fluid flow apply the same set of governing equations for which flow velocities are the dependent variables (functions of space and time). Conservation of mass (continuity) and Newton's laws of motion**,** dependent on physical properties of the fluid, are used to characterise fluids in motion and are briefly summarised below.

The continuity equation represents the mass conservation of a fluid in motion and is given in vectorial form by Equation (1), for which its velocity and pressure are functions of position.

$$\frac{\partial \rho}{\partial t} + \nabla \cdot (\rho u) = 0 \tag{1}$$

For the particular case of a fluid of constant density, which is the condition for fluid incompressibility, the continuity equation is reduced to Equation (2) and valid for (quasi-) stationary conditions.

$$\nabla \cdot u = 0 \tag{2}$$

Newton's second law of motion represents the conservation of momentum of the fluid in motion, for which the change in momentum of a given particle of fluid is equal to the forces acting upon it. The rate of change of momentum, dependent on the rate of change of the particle velocity, is given in vectorial form by Equation (3).

$$\rho \frac{Du}{Dt} = \rho \frac{\partial u}{\partial t} + \rho u \cdot \nabla u \tag{3}$$

2.1.1 The Navier-Stokes equation

In its simplest form, the Navier-Stokes equation (NSE) expresses the dynamic characteristics of Newton's second law of motion for a fluid of constant density and is given by Equation (4). The term F corresponds to the body force term and represents the contribution of the forces that act upon the volume of a fluid, more specifically the contribution of gravitational and Coriolis forces.

$$\rho \frac{Du}{Dt} = -\nabla p + \mu \nabla^2 u + F \tag{4}$$

The NSE can be rewritten in non-linear, partial differential form in terms of the velocity vector (u), as presented in Equation (5).

$$\frac{\partial u}{\partial t} + u \cdot \nabla u = -\frac{1}{\rho} \nabla p + \nu \nabla^2 u + \frac{1}{\rho} F \tag{5}$$

It is frequently necessary to express the NSE with regard to a coordinate system, rather than in vectorial forms. This results in a set of coupled differential equations that describe conservation of momentum in each of the flow directions, with time and spatial coordinates constituting the independent variables. The 3D NSE of Equation (6) use Cartesian coordinates. Analogous approaches can also be taken for the continuity equation, Eq. (1). Common coordinate systems also include cylindrical and spherical polar coordinate forms.

$$\begin{gathered}
\rho \left[\frac{\partial u}{\partial t} + u \frac{\partial u}{\partial x} + v \frac{\partial u}{dy} + w \frac{\partial u}{\partial z}\right] = -\frac{\partial p}{\partial x} + \mu \left[\frac{\partial^2 u}{\partial x^2} + \frac{\partial^2 u}{\partial y^2} + \frac{\partial^2 u}{\partial z^2}\right] + F_x \\
\rho \left[\frac{\partial v}{\partial t} + u \frac{\partial v}{\partial x} + v \frac{\partial v}{dy} + w \frac{\partial v}{\partial z}\right] = -\frac{\partial p}{\partial y} + \mu \left[\frac{\partial^2 v}{\partial x^2} + \frac{\partial^2 v}{\partial y^2} + \frac{\partial^2 v}{\partial z^2}\right] + F_y \\
\rho \left[\frac{\partial w}{\partial t} + u \frac{\partial w}{\partial x} + v \frac{\partial w}{dy} + w \frac{\partial w}{\partial z}\right] = -\frac{\partial p}{\partial z} + \mu \left[\frac{\partial^2 w}{\partial x^2} + \frac{\partial^2 w}{\partial y^2} + \frac{\partial^2 w}{\partial z^2}\right] + F_z
\end{gathered} \tag{6}$$

2.1.2 Boundary conditions

The differential equations that govern fluid motion require the specification of boundary conditions of the velocity fields of the fluid. The most common boundary is the rigid impermeable wall, such as the surface of the Earth for ABL flows. Fluid particles cannot permeate through this boundary and the normal component of the velocity of the fluid at the wall is zero (for stationary walls), as expressed in vectorial form by Equation (7), where $\hat{n}$ is the unit vector normal to the surface.

$$u \cdot \hat{n} = 0 \qquad (7)$$

The no-slip condition ensures that there is no relative tangential velocity between the rigid wall and the fluid in its immediate vicinity, which is fundamentally dependent on the action of viscosity, and is given by Equation (8).

$$u \times \hat{n} = 0 \qquad (8)$$

Forces exerted by the fluid on a rigid wall are the same as those applied on other parcels of fluid and the corresponding stresses must be continuous, otherwise fluid particles would have infinite acceleration near the wall. At the wall, the fluid exerts tangential forces (per unit area) on the rigid boundary in the form of viscous stresses. Far enough from the wall, the boundary condition is assumed to be at infinity and the fluid motion is equivalent to flow without obstacles, corresponding to free-stream conditions for ABL flows.

2.2 Turbulence

There are no clear and universal definitions of turbulence. It is generally accepted that turbulence is a four-dimensional flow phenomenon (space and time) that consists of irregular, quasi-random and multiscale variations in flow (magnitude and direction) over a wide range of temporal scales, enhancing mixing (diffusion) and decaying (dissipation) over time. It is characterised by the occurrence of multiscale 3D superimposed eddies that arise due to flow instabilities, generated through mechanical or thermal means, with increasing instabilities reducing the predictability of flows. These eddies consume energy from larger to smaller scales of motion, thus creating the turbulence energy cascade. The dominant size of the turbulent eddies defines the scale of turbulence, large-scale eddies lead to energy-intensive stirring of the flow and break these eddies into smaller ones via non-linear interactions and stretching. This drives the energy cascade from larger to smaller scales, until eddies are dissipated by viscosity at the smallest scales (turbulence microscale). The group of scales at which no energy is added to the eddies (forcing) and no dissipation takes place is known as the inertial subrange. Within the inertial subrange, the energy cascade is dominated by inertial motion. The formation of coherent structures is frequent at the larger scales of turbulence. Coherent structures are large-scale organised motions in turbulent shear flows, corresponding to connected fluid masses that present phase-correlated vorticities over the spatial extent of the structure (Hussain, 1986). Under this rationale, turbulence consists of random motions superimposed on coherent structures (Hussain, 1983).

In modern fluid flow theory the Reynolds number (Re), essentially a non-dimensional velocity, acts as control parameter to determine the flow turbulence regime and is given by Equation (9), which relates the inertial forces to the viscous forces. u and L_C represent the characteristic velocity and characteristic length scale (of the energy-containing eddies), respectively, while ν corresponds to the kinematic viscosity of the fluid. Above a critical value of Re, the transition from the layered laminar flow regime is complete and the flow is fully turbulent. According to Snyder (1981), $Re \geq 1 \times 10^4$ for ABL flows via the specification of u and L_C.

$$Re = \frac{u \times L_C}{\nu} \tag{9}$$

For turbulent flow regimes, the solutions of the NSE become growingly sensitive to the initial flow conditions and small initial uncertainties can be amplified, thus increasing the unpredictability of the velocity field. Indeed, important features of the larger turbulent motions can develop from very small perturbations of boundary conditions, following the Chaos Theory initially proposed by Lorenz (1963). This frequently occurs with atmospheric motions, where very fine details observed at a given period can result in major meteorological patterns at a later time. The occurrence of dominant random flow features (flow irregularities) associated to atmospheric turbulence is such that it corresponds to one of the main constraints to the accuracy of long-term weather prediction.

For turbulent flows, velocity and pressure are never constant with time and, for a given instant, can be split into mean and fluctuating parts, representing the Reynolds decomposition. The mean part corresponds to the ensemble average of the flow field and defined as the average value of the flow parameter that is obtained from a large number of predictions. Ensemble averaging is typically performed over time, with the requirement that averages be made over long enough periods of separate measurements performed at the same positions and converging toward the same results, constituting ergodic signals. Statistical information regarding the fluctuating part of flow velocities is frequently given by the intensity of the fluctuations, which corresponds to the standard deviation (σ_i) of each directional component (i) of the fluctuations. Accordingly, the instantaneous velocity of a turbulent fluid in each spatial direction is defined by Equation (10), where $\bar{u}$, $\bar{v}$ and $\bar{w}$ represent the mean (time-averaged) values in each flow direction (longitudinal, lateral and vertical, respectively) while u', v' and w' represent the fluctuating counterparts over time.

$$u, v, w = \bar{u}, \bar{v}, \bar{w} + u', v', w' \tag{10}$$

Mean values are defined from Equation (11), where T corresponds to the averaging interval.

$$\bar{u}, \bar{v}, \bar{w} = \frac{1}{T}\int_{t_0}^{t_0+T} (u, v, w)\delta t \tag{11}$$

While the mean of the fluctuating parts is zero, their variance ($\sqrt{\sigma_i}$) is not. Consequently, σ_i (or root mean square) is also a non-null quantity. Under this rationale, the directional components of the fluctuations are given by Equation (12).

$$\sigma_{u,v,w} = \sqrt{\frac{1}{T}\int_{t_0}^{t_0+T} \{(u-\bar{u})^2, (v-\bar{v})^2, (w-\bar{w})^2\}\,\delta t} = \sqrt{\frac{1}{T}\int_{t_0}^{t_0+T} (u', v', w')^2 \delta t} \tag{12}$$

The substitution of the instantaneous quantities by the time-averaged sum of their mean and fluctuating parts in the equation of conservation of momentum results in the Reynolds-averaged Navier-Stokes (RANS) equations. A turbulence term, known as the Reynolds stress and equivalent to six new unknown variables, is added to the basic NSE. The Reynolds stress corresponds to the influence of turbulent stresses on the mean fluid motions, frequently represented through a symmetric tensor in which the diagonal elements contain normal stresses and the remaining elements are shear stresses.

The addition of the turbulence term to the equations governing Reynolds stresses and turbulent fluxes leads to a higher number of unknown variables of the NSE than the number of equations. Derivations of additional equations (higher order statistical moments), to determine these unknowns, result in the appearance of more unknown variables. This successively increases the number of required correlations between variables, creating an endless loop of increasing unknowns for each derivation of equations. This describes the turbulence closure problem: a complete description of flow turbulence cannot be achieved through the analytical resolution of a finite set of equations, i.e., the set is not closed. In order to close (parameterise) the non-linear terms resulting from the Reynolds decomposition, a finite number of equations are used for the major variables and the remaining unknown variables are approximated (fixed parameters). These are designated as closure approximations and classified according to the highest order of retained equations. When retaining the equation for the mean variables and approximating the second moments, the approximation corresponds to first-order closure. There is a wide variety of available turbulence closure models, the higher order closures are more universal and considered more accurate but require greater expense or workload in achieving solutions.

Turbulence is highly complex and typically requires simplifications in order to provide proximate expressions. Three major assumptions are frequently made to simplify the quantification of turbulence:

- Stationarity – statistical equilibrium between large-scale energy input and small-scale dissipation.
- Homogeneity – spatially constant flow quantities and circular eddies.
- Isotropy – same variance regardless of direction ($\sigma_U = \sigma_V = \sigma_W$), negligible buoyancy and shear.

Kolmogorov (1941) applied these, together with the assumption of constant energy transfer from large to small scales within the inertial subrange, to describe the spectral behaviour of turbulence. Accordingly, the energy flux is constant and the energy density only depends on the dissipation rate and wavenumber in the inertial subrange. Eddies are frequently embedded within each other, meaning that the majority of the multiple scales of motion can only be identified in spectral space. This consists of obtaining the time scales of the turbulent motion (for example, through Fourier analysis) in which the energy spectrum characterises the contribution of different frequencies to the turbulent energy of the flow. Turbulence is characterised best by spectral properties, which are representations of energy or variance as a function of the scale of motion.

In terms of quantifications, one of the most frequently used quantities for studying flow turbulence is the turbulent kinetic energy (TKE). TKE is a non-conserved flow parameter, given by Equation (13), which relates the directional components of the standard deviations of the fluctuating parts of the instantaneous velocities.

$$TKE = \frac{1}{2}\sqrt{(u')^2 + (v')^2 + (w')^2} \tag{13}$$

TKE is persistently dissipated into internal energy (heat) through molecular viscosity, occurring at the smallest scales. The same energy field can be produced by different forms of velocity fluctuations, thus TKE alone is insufficient to statistically describe flow turbulence. The probability distribution function (PDF), which indicates the probability of a fluctuating velocity being between u' and $u' + \partial u'$, provides more information. PDFs of turbulent quantities typically present a Gaussian shape, allowing them to be minimally characterised through the standard deviations (Morales et al., 2012). These can also be correlated through analyses at different measurement points (or times), these defined as joint PDFs. Alternatively, the superposition of all eddy motion scales can be quantified with the energy spectrum that indicates how much TKE is associated to each of the scales of fully turbulent flows.

The spectral distribution of TKE can be obtained through Equation (14), which approximates the dimensional spectra of turbulence to the dimensionless reduced frequency (f_{red}) at a given height (z). The dimensional spectra is dependent on the spectral density distribution of the one-dimensional velocity component j (S_j), which is normalised with the standard deviation of its fluctuations (σ_j), and the corresponding dimensional frequency (f). Letters A to E represent approximation constants (VDI, 2000).

$$\frac{f \times S_j(f, z)}{\sigma_j^2} = \frac{A \times f_{red}}{(E + B \times f_{red}^C)^D} \tag{14}$$

The reduced frequency is given by (15), which relates the dimensional frequency of the fluctuations (f) to the local mean velocity (U) at the corresponding height (z).

$$f_{red} = \frac{f \times z}{U(z)} \tag{15}$$

Turbulence intensity (I_i), often applied for ABL flow turbulence quantifications, is a dissipative (non-conserved) quantity that relates the directional standard deviations to the local mean velocities at the same heights above the surface. Given by Equation (16), turbulence intensity is a one-point statistic of second order, thus contains limited information (Morales et al., 2012).

$$I_{U,V,W} = \frac{\sigma_{U,V,W}}{\overline{U}, \overline{V}, \overline{W}} \tag{16}$$

Taylor (1938) hypothesized that when turbulence intensities are relatively small with regard to the respective mean velocities, the spatial pattern of the flow convects uniformly passed a fixed observation point in space. This is known as Taylor's hypothesis of frozen turbulence, frequently applied to enable the determination of statistics (fluctuations and spectra) of turbulent flows with a prevailing flow component (Moin, 2009). Turbulence statistics obtained at a single position can be spatially and temporally related under this approximation and flow reconstruction (at other locations) simplified when full spatial-temporal data is unavailable (Moin, 2009). It has been claimed that Taylor's hypothesis breaks down for high shear flows, where its applicability is limited to small frequency ranges (Del Alamo & Jimenez, 2009). This stems from different convection velocities (local mean or eddy propagation velocities) associated to different wavenumbers, the occurrence of temporal fluctuations of convection velocities, and flow patterns that are commonly observed under high shear conditions (Lumley, 1965). While some authors identify shear-induced anisotropy as a cause for the breakdown, it is more influential on the structure of the frozen regions and unrelated to the applicability of the hypothesis (Lumley, 1965). Regions within range of the fixed observation point are isotropic when velocity differences across the frozen regions are relatively smaller than those of the eddies (Lumley, 1965). Previous analyses of relevant experimental data have demonstrated the applicability of Taylor's hypothesis to ABL flows, particularly for homogeneous surface conditions of relatively low roughness (Mizuno & Panofsky, 1975).

2.3 The lower atmosphere

The ABL is the lowest part of the troposphere, through which exchanges of momentum, heat and moisture between the surface and the atmosphere take place. Flow within the ABL is almost always turbulent and strongly driven by the effects caused by interactions with the underlying surfaces. The depth of the ABL is dependent on the conditions of atmospheric stability, which vary due to imbalances in surface temperatures through diurnal/nocturnal cycles, thus being variable in space and time and ranging from hundreds of metres to several kilometres. At higher altitudes, the ABL is influenced by the Coriolis force (effects of planetary rotation) and thermal stratification, the latter affecting turbulence through buoyant forces. Accordingly, the ABL can be classified as a turbulent boundary layer in a rotating, heavy stratified fluid (Monin, 1970). At the top of the ABL is a stable layer known as the capping inversion, where underlying turbulent motions are suppressed and unable to affect the free atmosphere above, which is unmodified by turbulence. In terms of its structure, the ABL is most commonly divided into two major layers:

- Inner layer – called the atmospheric surface layer (ASL) that corresponds to the lowest 10% of the ABL.
- Outer layer – constitutes the bulk of the ABL, typically referred to as the Ekman layer, where turbulence intensities decrease and Coriolis forces become more influential with increasing altitude, forming what is known as the Ekman spiral.

Vertical profiles of the averaged ABL flow velocity ($\bar{u}$) are universally described by Equation (17) and function of local (z) and reference (z_{ref}) heights above the surface, the reference velocity (U_0), the zero plane displacement (d_0), and the profile exponent (α) of the flow (VDI, 2000). d_0 is mostly relevant when individual roughness elements affect the velocity profiles. In the case of the low, homogeneous surface roughness of the modelled ABL flows of the present investigation, d_0 is negligible (Chapter 6).

$$\frac{\bar{u}(z)}{U_0} = \left(\frac{z - d_0}{z_{\text{ref}} - d_0}\right)^{\alpha} \tag{17}$$

According to observable flow regimes, the ASL can be divided into three sublayers that are presented here from lowest to highest altitudes:

- Viscous (or laminar) sublayer – corresponds to a very thin layer ($\leq 1\ mm$) closest to the surface, where the flow is laminar and viscous dissipation exerts friction on the flow.
- Roughness sublayer – where the flow is influenced by individual roughness elements (generating flow inhomogeneities) and wind profiles deviate from a logarithmic shape, corresponding to heights ranging from two to five times the roughness element height (Raupach et al., 1991).
- Inertial sublayer – the remaining ASL, in which Reynolds stresses are assumed to be nearly constant with height and the vertical velocity profile is logarithmic. Within the scope of the present investigation, only flows contained within this sublayer are analysed.

In the neutrally stable ASL, characterised by moderate to strong winds and negligible thermal effects (buoyancy), characteristic velocity profiles follow a perfectly logarithmic trend that increases with height from the surface. This is described, in dimensionless form, by the law of the wall for rough surfaces, Equation (18), which is dependent on the friction velocity (u_*) and the surface roughness length (z_0) at the respective height above the surface (z). The law of the wall is valid for flat terrain with uniform roughness, corresponding to an equilibrium between surface friction and momentum flux and the resulting velocity profiles deemed horizontally homogeneous (VDI, 2000). The remaining term of Eq. (18) corresponds to the von Kármán constant (κ), which is ≈ 0.4.

$$\frac{\bar{u}(z)}{u_*} = \frac{1}{\kappa} \times ln\left(\frac{z - d_0}{z_0}\right) \tag{18}$$

Flow conditions within the ASL are strongly influenced by the surfaces below. For flows over surfaces, a momentum roughness height that quantifies the loss of flow momentum due to the surface roughness, is typically specified (Chappell and Heritage, 2007). This is frequently expressed as the (equivalent) sand-grain roughness, following the first modifications made to the law of the wall for smooth surfaces being used for rough pipe flows (Blocken et al., 2007). For atmospheric flows, the roughness height is related to z_0, which corresponds to the height above the ground surface at which the mean flow velocity approximates zero. Estimates for this parameter can be experimentally obtained from wind velocity profiles, which are susceptible to measurement errors and the specification of a zero-reference level. For numerical applications z_0 can also be related to the equivalent ABL sand-grain roughness (k_s), which is typically larger than z_0 (Blocken et al., 2007).

2.3.1 Turbulence in the ASL

Neglecting buoyancy effects, ASL flows are driven by surface drag (friction), which enhances non-stationarity, inhomogeneity, and anisotropy. Thus, flow within the ASL is strongly influenced by shear-induced turbulence. Stresses caused by fully turbulent motions are orders of magnitude greater than those caused by molecular viscosity, resulting in the use of turbulent stresses (Reynolds stresses or momentum flux) and drag (rather than the friction) for characterisations of near-surface flows. Vertical turbulent fluxes ($u'w'$) are near-constant with height in the ASL, leading to the frequently-used "constant flux layer" or "constant shear layer" designations. $u'w'$ is related to u_* through Equation (19).

$$u_* = \sqrt{u'w'} \tag{19}$$

Eddie sizes range from less than $1\ mm$ at ground level to over $100\ m$ at the upper heights of the ASL, frequently presenting non-circular geometries when stratification and (mean) flow shear are taken into account. Dominant turbulent eddy sizes, in each flow direction, can be quantified through the analyses of the integral length scales of turbulence. For the prevailing wind direction (x), the integral length scales (L_u^x) of the longitudinal velocity component (u) can be obtained from Equation (20), which relates the auto-correlation coefficient (R_i) between consecutive discrete time steps (Δt) and is valid when Taylor's hypothesis is applicable (Erdmann, 2017; Fischer, 2011).

$$L_u^x = u\frac{\Delta t}{2}\sum_{n=0}^{N-2}[R_i(n) + R_i(n+1)] \tag{20}$$

As well as the classic turbulence parameters discussed up to here, turbulence intermittency and gustiness have more recently been applied to characterise ASL turbulence. Intermittency occurs at several scales and intensities. Gaussian distributions of velocity fluctuations are commonly assumed, however turbulence is highly intermittent and often exhibits non-Gaussian statistics. In this context, intermittency is referred to as the exceptionally high probability of extreme events in comparison to a Gaussian distribution (Morales et al., 2012). In such events, PDFs develop long tails that become stronger with increasing levels of turbulence (Johnson & Meneveau, 2017). It is important to distinguish between small-scale intermittency of velocity gradients organized by individual eddies and global intermittency associated with patchiness of turbulence on scales larger than the main eddies (Mahrt, 1989). Global intermittency arises from non-continuous flow organization into scales larger than the main coherent eddies and is not considered for the present thesis (limited size of study domains). Small-scale (microscale) intermittency is continuous and may result from overall modulation of turbulence by the main eddies in the flow or in connection with sharp edges of the main eddies, dissipation of TKE confined primarily to small sub-regions of individual eddies (Mahrt, 1989). No universal criteria to define turbulence intermittency exists, with fluctuations characterised over different temporal scales.

Near-surface gusts are defined as sudden, short-lived increases in wind velocity that are generated by turbulence in the flow. Gusts are normally characterised by magnitude, duration and frequency of occurrence (Gualtieri & Zappitelli, 2015). Gustiness is a direct function of turbulence intensity and is inverse to the gust duration (Frandsen et al., 2007; Gualtieri & Zappitelli, 2015). Under the assumption of stationary and normally distributed flow, the largest expected gust (U_{max}) over a moving average period (τ), equal to the gust duration (t), which is contained within a longer averaging period (T), is given by Equation (21).

$$U_{max,\tau} = \overline{U_T} + k_{P\ T,\tau} \times \sigma_U \tag{21}$$

$\overline{U_T}$ is the mean wind speed over T, σ_U its standard deviation and $k_{P\ T,\tau}$ is the largest gust of the normalised wind speed, also known as the gustiness parameter, peak factor, or gust factor (Bardal & Soetran, 2016). The latter is calculated from Equation (22).

$$k_{P\ T,\tau} = \frac{U_{max,\tau} - \overline{U_T}}{\sigma_U} \tag{22}$$

The gust factor is frequently expressed in a non-normalised form as an empirical parameter ($G_{T,\tau}$) defined by Equation (23), related to its non-normalised form through the turbulence intensity, I_U (Bardal & Soetran, 2016).

$$G_{T,\tau} = \frac{U_{max,\tau}}{\overline{U_T}} = \left(k_{P\ T,\tau} \times I_U\right) + 1 \tag{23}$$

Conversion between wind speeds obtained through different averaging periods is only applicable if the highest average wind speed (the gust) over the shorter averaging period (τ) is contained within the sampling period (T) of lower mean wind velocity (WMO, 2008). Averaging periods vary with the specific application and its relevant spatial scales, but the fixed long-term average (T), usually ranges between 10 and 60 minutes whereas the moving average (τ) between 1 and 10 seconds. Typically, a 3 second gust duration (t) is applied in gust factor calculations (Bardal & Soetran, 2016; WMO, 2008).

3 ATMOSPHERIC BOUNDARY LAYER FLOW MODELLING

Atmospheric boundary layer (ABL) flow modelling consists of replicating real-world flows through analytical, physical or numerical models that simulate the required flow conditions. The work in this thesis is focused on physical modelling of ABL flows in an environmental wind tunnel, thus requires a deeper understanding of related topics. Flow similarity, the fundamental condition for scaled ABL flows, is initially discussed. This is followed by an introduction to the WOTAN wind tunnel, where the experiments take place. Flow visualisation and velocity measurement techniques used for the experiments are also presented here. Unless specified otherwise, the information contained within these subchapters originates from the publications of Meroney (1990), Snyder (1981), or VDI (2000).

As outlined in Chapter 1, one of the objectives of the present research is to provide experimental validation datasets for numerical models. Therefore, a previous understanding of the main features of numerical ABL modelling is warranted. These are briefly introduced in Appendix A and intended as a very summarised introduction to numerical modelling. For further insight, the reader is referred to the publications of Patankar (1980), Versteeg & Malalasekera (1995), or COST732 (2007).

3.1 Physical modelling of ABL flows

3.1.1 Flow similarity

Creating scaled ABL flows in an environmental wind tunnel requires the fulfilment of flow similarity criteria. The concept of similarity is based on the requirement that two systems, the prototype system (full-scale) and its downscaled model counterpart, display correspondence in time and space between fluid particle motions when scaled by characteristic values that are typically provided through prescribed boundary conditions. In general, complete atmospheric flow similarity requires the achievement of geometric (equal ratios of all dimensions in model and prototype), kinematic (equal ratios of the velocities of homologous particles and similar paths of moving particles in model and prototype), dynamic (equal homologous forces in model and prototype), and thermal (equal temperature or density stratification in model and prototype) similarities. These are achieved through the specification of boundary conditions and a set of dimensionless coefficients that, when matched, assure flow similarity between flows.

Prescribed boundary conditions can be classified into two major groups: surface and flow boundary conditions. Surface boundary conditions include matching topography, surface roughness distributions, surface temperature distributions, and geometries of non-topographic obstacles (buildings, fences, etc.) between prototype and model. Flow boundary conditions can be further classified into two sub-groups: approach flow boundary conditions (similarity of velocity, humidity, temperature, and turbulent energy distributions) and model section flow boundary conditions (similarity of flow trajectories and null longitudinal static pressure gradients, for example).

For transient, turbulent atmospheric flows the most relevant dimensionless parameters are the Rossby (Ro), Reynolds (Re), Euler (Eu), Froude (Fr), Richardson (Ri), Peclet (Pe), Prandtl (Pr), Schmidt (Sc), and Eckert (Ec) numbers. Exact (or complete) similarity requires the equality of all these numbers between prototype and model. Ro is strongly influenced by the characteristic length scale of the flow field and is a measure of relative magnitudes of advective (or local) accelerations that result from divergences in the flow field and the effect of the Coriolis acceleration. Laboratory boundary layers are suitable for modelling atmospheric flows if time and length scales are small enough to neglect the effects of Coriolis accelerations; meaning that inertial effects are, at least, an order of magnitude greater than the Coriolis effects. Eu associates relative magnitudes of pressure fluctuations and inertial accelerations and is typically close to unity, thus automatically simulated. Fr, Ri, Pe, Pr, Sc and Ec are associated to thermal (buoyancy, stratification, etc.) effects of the flow or properties of the operating fluid, which are less influential than shear in the ASL and not required for the experimental work of the current thesis.

In a broad sense, it is impossible to concurrently match all aforementioned dimensionless parameters and boundary conditions to achieve complete flow similarity between model and prototype. Therefore, partial or approximate similarity must be applied and achievable model scale parameters matched to the prototype. This implies that the physical modeller is required to design an experiment based on the parameters and scales of fluid motion of greater significance for the specific experimental goals.

Reynolds number independence

Re is the most critical dimensionless parameter governing flow similarity of modelled neutrally-stratified ABL flows. For scaled flows that employ the same operating fluid and approximate (if not equal) pressure and temperature conditions to the prototype, Re solely depends on the characteristic length (L_C) and the flow velocity (U_0). With the exception of pressurised or cryogenic gas tunnels, equal Re between prototype and model cannot be attained for typical model scales. As perceived from Equation (9), L_C is always smaller for the model than it is for the prototype, differences increasing with decreasing model scales. For the case of the indicative model scale of $1:1000$, Re is three orders of magnitude smaller than the full-scale. This flow similarity limitation is overcome under the hypothesis of Re independence, first proposed by Townsend (1956). The hypothesis states that 'geometrically similar flows are similar at sufficiently high Re'. This implies that most mean-value functions are only dependent on space and time variables and not on Re, if sufficiently large. In this context, the structure of the flow turbulence is similar over a wide range of Re once a critical value is surpassed. Under these conditions, model-scale turbulence structures are deemed sufficiently similar to full-scale conditions and the fully turbulent modelled flow is considered Re independent. Exceptions of Re independence are:

- Very small scale turbulence associated to viscous energy dissipation.
- Flow fields closest to a solid boundary where viscosity has a greater effect.

Most flow phenomena in the ABL are driven by the larger scale turbulence and virtually all natural surfaces are aerodynamically rough. Thus, the model-scale flow structure is similar if the scaled surface roughness is large enough to prevent the formation of laminar sublayers, meaning the flow at the measurement locations is independent of molecular viscosity, thus fully turbulent ($Re > 10^4 - 10^6$).

3.2 The WOTAN wind tunnel and applied techniques

3.2.1 WOTAN wind tunnel facility

Experiments of the present investigation are performed in the WOTAN environmental wind tunnel facility at the Environmental Wind Tunnel Laboratory (EWTL) of the University of Hamburg, a closed test section/open return boundary layer wind tunnel of total length $25\ m$ and a test section that is $18\ m$ long with a width of $4\ m$. WOTAN has an adjustable ceiling with maximum amplitude of variation of $0.5\ m$, thus the height can be adjusted between 2.75 and $3.25\ m$ to minimise longitudinal pressure differences in obtaining flow similarity to suit specific ABL characteristics and reduce undesirable flow blockage of the modelled flows. Schematic top and lateral views of the WOTAN wind tunnel are presented in Figure 3-1.

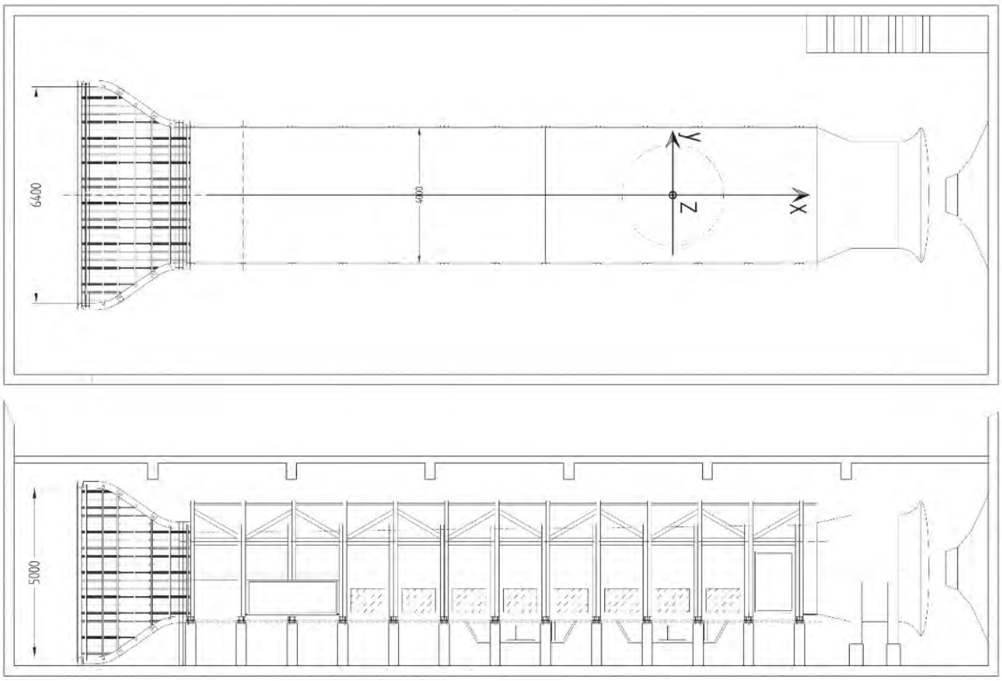

Figure 3-1. Schematic top and side views of the WOTAN wind tunnel facility (Harms, 2010).

Flow is driven by a motor-powered axial fan that has a diameter of approximately $3.2\ m$ (with variable blade orientations to modify flow rates), located near the outlet, which sucks air into the inlet. Undesired swirls in the generated flow are minimised through the use of small-diameter extended hexagonal honeycomb tubes located at the inlet. These also serve the purpose of providing homogeneous inflows and minimising streamwise velocity fluctuations by breaking up large eddies, thus straightening the flow entering the test section. Located between the inlet and the test section is the wind tunnel contraction (also known as the convergent) which increases the inflow velocity while reducing turbulence intensities and non-uniformities in the mean velocity profile. For the modelling of changes in inflow wind directions the test section is equipped with two turntables of diameter $3.5\ m$. For probe positioning, WOTAN is equipped with a traverse system that enables high repeatability with an accuracy of $\approx 0.1\ mm$.

3.2.2 Flow visualisation

Time-dependent fluid motions are highly complex to describe solely through governing theoretical equations or single-point experimental measurements. This makes a full understanding of the development of flow patterns that succeed one another virtually impossible, particularly for highly turbulent flows where non-linear and non-periodic phenomena (associated to turbulence) can occur. Qualitative observations of flows can be obtained through different visualisation techniques that provide physical modellers with an improved perception of the total flow structure. This enables the observation of flow trajectories, coherent structures, and flow separation, among others. While not providing qualified quantitative data, visual techniques have the advantage of providing valuable qualitative information, especially useful to identify measurement positions of fundamental interest.

For the present thesis, flow interactions with the terrain models are observed using a laser light sheet and smoke visualisation technique. The laser light sheet is oriented to generate a vertical observation plane, which illuminates the flow-following particles supplied by a fog machine and diffused into the wind tunnel using a low-energy jet of compressed air, at a far enough distance to not affect the flow in the region of interest. Observations are complemented by a high-resolution camera that enables the recording of videos of particle trajectories, with the temporal scale of approximately $1{:}\,1000$ (flow observed a thousand times quicker than full-scale for Re independent flow), as well as frame captures of instantaneous flow fields and streaklines, the latter through long-exposure photography.

3.2.3 Velocity measurement techniques

Prandtl tube

The Prandtl tube is a differential pressure sensor from which the longitudinal velocity at a single-point of an airflow can be derived. The technique was invented by Henri Pitot in 1732 (non-differential form) and made operational in 1858, following refinements performed by Henry Darcy (Brown, 2003). The design was optimised with regard to probe shape and the location of the static pressure ports by Prandtl and later set as German standard. It measures the total or stagnation pressure (p_{tot}) through its main intake which is oriented parallel to the incoming flow. Simultaneously, the static pressure (p_{sta}) is measured through lateral openings oriented perpendicularly to the main flow. Through Bernoulli's formula, Equation (24), the dynamic pressure (p_{dyn}) can be related to the flow velocity (U), for a known air density (ρ).

$$p_{dyn} = p_{tot} - p_{sta} = \frac{1}{2}\rho U^2 \rightarrow U = \sqrt{2\left(\frac{p_{dyn}}{\rho}\right)} \tag{24}$$

Limitations of the Prandtl tube are related to its performances: it has low sensitivity, unsuitable for very low velocities ($< 0.1\ m/s$), and is influenced by its orientation with regard to the flow, thus must be correctly aligned with the mean velocity vector of the flow (Blackmore, 1987).

In the experimental measurements of the present thesis, a Prandtl tube is employed for reference velocity (U_0) measurements and is permanently located at the beginning of the test section of the wind tunnel at a model-scale intake height of $1.87\ m$. The Prandtl tube is connected to an analog pressure transducer, inputs being posteriorly altered to digital signals using a DAQ converter. In order to enable coincident reference velocity measurements with those measured in the model section, the digital signals contain a trigger mechanism initiated by the Laser-Doppler Velocimetry (LDV) system used for turbulence-resolving flow measurements within the model section. Thus, the flow parameters measured above the model section are made dimensionless with U_0.

The Prandtl tube is located at the inlet, where the modelled ABL flow is undeveloped, thus U_0 is not equal to the developed ABL flow above the model section. In a properly modelled Re independent ABL flow, the measured U_0 forms a fixed ratio with any mean velocity measured within the model section known as the reference velocity scaling factor (SF). Velocity scaling consists of the calculation of SF between the velocity at the intake location (U_P) and the developed ABL flow location (U_0), as in Equation (25).

$$\mathrm{SF} = \frac{U_0}{U_P} \tag{25}$$

For the present experimental setups, a scaling factor of 0.87 is obtained at $Z = 125\ m$ (full-scale) above the surface at $X = -500\ m$ upstream from the start of the model section ($X = 0$). For fully turbulent (Re independent) flow velocity ranges, the scaling factor remains unchanged with variations of U_0, thus has no effect on the shapes of the dimensionless profile shapes.

Laser-Doppler velocimetry (LDV)

LDV is an optical flow velocity measurement technique first employed by Yeh & Cummins (1964) to observe low velocity flows of colloidal suspensions of polystyrene spheres in water. Essentially, this method measures the time required for a particle following the flow path to travel a known distance. The technique is based on the measurement of the Doppler effect or frequency shift (observed change in frequency of a wave from a viewer moving relative to its source) of laser light scattered by small, neutrally buoyant particles that transit through an elliptical measurement volume, produced by crossing laser beams (Buchhave et al., 1979). When a moving particle contained in a seeded flow interacts with the laser light, it provokes a frequency shift of scattered light by an amount that is linearly proportional to the particle velocity (Ruck, 1991; Vetrano & Riethmuller, 2010). Due to the stable linearity of its optical electromagnetic waves, LDV measurements are unaffected by temperature or pressure (Ristic, 2007).

LDV is a non-intrusive, single-point technique that provides very high spatial and temporal resolutions, with a well-defined directional response. The technique is advantageous when compared with alternative single-point measurement techniques such as hot-wire anemometry, which can perform measurements at similar resolutions but is more invasive, requires frequent calibrations (magnitude and orientation), and cannot explicitly resolve flow directions; or Prandtl tubes. Additionally, the LDV technique is advantageous for applications including recirculating flows, such as those associated to turbulent wakes (Nobach, 1999). The technique also has some limitations, the most significant being biased velocity measurements occurring close to highly reflective surfaces due to undesired light backscatter. This can be minimised by applying materials with low reflective properties, as performed in the current experimental work. More details of the LDV measurement approach are provided in Appendix A.

In order to perform measurements with maximal positional repeatability, the LDV probe is affixed to the traverse system of WOTAN. High temporal and spatial-resolution velocity measurements are performed with a commercial two-component (2D) LDV system supplied by *Dantec Dynamics*. Two pairs of laser beams are generated: one with wavelength of $514\,nm$ (green colour), measuring the longitudinal velocity component of the flow (U) and one of wavelength $488\,nm$ (blue colour) to alternately measure lateral (V) and vertical (W) components. The generated measurement volume is an ellipsoid of $0.08 \times 0.08 \times 1.65\,mm^3$. Due to the highly turbulent nature of flows over orography, time-averaging of statistical moments is performed using transit-time weighting. According to George (1988), transit-time weighting is necessary for turbulence intensities $> 10\%$ (further detailed in Appendix A).

Seeding of the flow provides the light scattering medium for LDV measurements and requires an appropriate concentration of particles to ensure a larger reliability of the measured data. Particles of sizes smaller than the microscale of turbulence are desired (Ristic, 2007). As concluded by Gillmeier (2014), seeding has a crucial role in the accuracy of the measurements, particularly at smaller geometric scales, and should be sufficiently homogeneous to provide reliable data. There is no possibility of controlling the particles entering the measurement volume, seeded particles may not be equidistant, resulting in biased velocity measurements. Wake flow measurements are also problematic due to insufficient seeding in such regions of the flows that result in low acquisition rates. To minimise these issues, the wind tunnel and the fog machine are operated for long enough periods to boost particle concentrations and seeding homogeneity prior to each measurement.

4 ATMOSPHERIC FLOWS OVER COMPLEX TERRAIN

The current chapter aims to document the state of the art of ABL flow investigations over complex terrain, with particular emphasis on turbulence. In a historical context, the study of fluid dynamics over orography dates back to as early as the late 1930s with investigations performed in wind tunnels (Meroney, 1990). Due to the requirement of a greater understanding of flows over terrain for a wide variety of applications, subsequent decades were marked by an increase in interest in flow interactions with orography. Key developments in theoretical, experimental, and numerical investigations are briefly presented and discussed here. The reader is referred to Wood (2000) for a detailed chronological perspective of studies of flows over complex terrain.

4.1 Analytical theory

According to Wood (2000), the first theoretical studies regarding complex terrain flows date back to the 1930s and are related to phenomenological observations of flows over 2D lee waves. However, it was in the 40s that the topic gained impetus following the advent of theoretical linear solutions for stratified airflow. Lee waves were studied extensively in the earlier works to avoid non-linear effects of steep slopes. Following a decline in subsequent decades, investigations into flow over hills began to gain prominence in the 1970s. However, these were focused on stratification effects and upper level ABL winds (Jackson & Hunt, 1975).

Using the theory of perturbed turbulent shear layers developed during the 1960s, Jackson & Hunt (1975) formulated the most relevant analytical theory to date. Their linear analytical theory predicts mean turbulent flow velocities over 2D (infinite width) gentle-sloped, isolated hills with constant surface roughness under conditions of neutral stability. This allows for asymptotic matching of the flow characteristics and the equations of motion (Chapter 2) can be linearized. Accordingly, the flow is separated into two regions:

- Inner region – thin local equilibrium layer directly affected by the surface, where local velocity perturbations occur due to the existence of pressure gradients and turbulent eddies adjust to equilibrium with their surroundings prior to advection over the hill.
- Outer region – where flow distortions advect eddies over the hill and velocity tends to equal the undisturbed profiles with increases in height.

Mason & Sykes (1979) provided a third dimension to the linear theory, with later observations over real terrain sites demonstrating good agreement in regions spanning from upwind of the terrain to the hill crests, even for moderate slopes. Sykes (1980) performed an asymptotic analysis of the flow over a 2D hill, finding that the surface boundary condition proposed by linear theory is incompatible at the near-surface, requiring an additional very thin surface layer to be consistently described. Furthermore, turbulence in the outer region of flow was found to be governed by rapid distortion, later supported by the data from the wind tunnel investigation conducted by Britter et al. (1981). Hunt et al. (1988) proposed the division of the inner region of the linear theory into a thin zero-velocity inner (viscous) sublayer, of depth equivalent to the roughness element height, and a shear stress sublayer that extends to the height of the original inner region (where mean flow is affected by shear stress).

4.2 Field campaigns

Field measurements are considered the most reliable source of flow data, without any modelling requirements or assumptions. Several field measurement campaigns have taken place in regions of complex topographies, early studies being focused on flow pattern observations. With the increase of analytical theories for flows over orography and the advent of computational tools that require validation data, demands for higher quality field data have increased. Several field studies have been reported in the Literature, those subsequently resulting in extensive modelling investigations briefly discussed below.

The first major field campaign designed to provide reference datasets for high-resolution numerical modelling took place at Askervein Hill, an isolated hill of height $\approx 100\ m$, located on the island of South Uist (Scottish Outer Hebrides) during the 1980s (Taylor & Teunissen, 1983; Taylor & Teunissen, 1987; Walmsley & Taylor, 1995). The main objective was to measure the spatial variations in the near-surface mean wind fields around the hill (with over 50 measurement towers) and to provide comparisons with the background flow quantities measured in a region of relative flat terrain to the south-southwest of the hill (Taylor & Teunissen, 1987). While providing high quality data regarding near-surface mean wind speeds, turbulence parameters lacked temporal resolution due to low sampling rates (Walmsley & Taylor, 1995).

Perhaps the most important field campaign to date corresponds to Bolund Hill, an isolated $130\ m$ long peninsula of just $12\ m$ altitude located in Roskilde (Denmark). With the exception of a narrow isthmus connecting it to the mainland, Bolund is surrounded by sea (Bechmann et al., 2009). The site provides near-uniform surface conditions ($z_0 \approx 0.02\ m$) together with strong vertical momentum due to a near-vertical windward slope and a well-defined inflow profile (Bechmann et al., 2009; Berg et al , 2011). The field campaign took place between December 2007 and February 2008 and involved 35 instruments (2 LIDARs) placed on 10 measurement masts that formed two transects parallel to the best defined inflow directions (Bechmann et al., 2009). A maximum fourfold increase in turbulence intensity relative to the inflow was observed at the crest, the exaggerated levels of turbulence being attributed to the steepness of the windward slope and varying recirculation characteristics (Berg et al., 2011). According to Scopus (2017), the Bolund experiment yielded the largest amount of modelling initiatives associated to flows over orography, with a total of thirty-two related publications (eleven more than Askervein).

The New European Wind Atlas (NEWA) is focused on updating a previous European Wind Atlas, which dates back to the late 1980s and established a basis for wind energy resource assessment using datasets measured throughout fixed sites, such as weather stations or airports (Mann et al., 2017; Troen & Lundtang Petersen, 1989). NEWA is mainly oriented to providing high-resolution data for numerical model validation of flows over orography through measurements performed during field campaigns, which have been carried out at seven sites around Europe. Each of the terrain locations has particular characteristics of interest, such as heterogeneous roughness (Osterild, Northern Denmark), forested surfaces (Hornamossen, Southern Sweden and Kassel, Central Germany) or large complex terrain areas for mesoscale flows (Alaiz, Northern Spain).

The largest field campaign took place at Perdigão (Portugal) in 2017, a valley built of $\approx 4\ km$ long ridges that are separated by $1.5\ km$ and heights between 500 and $550\ m$ (above sea level). This followed a previous study performed at the same site in 2015 where measurements were taken to evaluate how a wind turbine (on the crest of one of the ridges) modifies the incoming flow (Vasiljevic et al., 2017). With the aim of quantifying wind resource potential, the 2017 field campaign included 30 LIDARs and over 50 measurement masts equipped with sonic anemometers located at heights between 10 and $100\ m$ (above the local surface) to provide flow and turbulence data (Mann et al., 2017). Several publications related to the measurement campaign address specific characteristics of the inner valley flows, such as Letson et al. (2019), Menke et al. (2018), and Menke et al. (2019), for example. Menke et al. (2018) investigate whether the propagation of the wake produced by the aforementioned wind turbine follows the orography. They observe that wake propagation is dependent on the orography and the atmospheric stability, in particular the vertical motions. The wake propagates horizontally for neutral stability, lofted for unstable conditions, and follow the (downhill) orography during stable stratification. Letson et al. (2019) evaluate several gust parameters above crests and inner valley positions. Analyses parameters include the peak and gust factors, expressed by Eq. (22) and Eq. (23), respectively (Chapter 2). Gust factors at $Z = 60\ m$ (above local terrain) are observed to be, on average, 27% larger above the inner valley relative to those of the crest. Furthermore, an observed near-invariance of the gust factors with height above terrain is smaller than height-related variations over flat, homogeneous surfaces. Menke et al. (2019) characterise the recirculation (reversal of main flow direction) zones above the leeside slopes of each of the ridges for opposing inflow directions. They report that recirculation mainly takes place for unstable or neutral atmospheric stabilities and extends to the average length of $X \approx 700\ m$ (about half the distance between ridge crests) and reaches an average depth of $Z \approx 160\ m$ above the valley floor.

4.3 Physical modelling

The first attempts at complex terrain flow modelling were performed in aeronautical wind tunnels, early investigations dating back to the late 1930s. With the aim of evaluating airfield safety, the wind field above the Rock of Gibraltar was modelled in a wind tunnel at a scale of $1{:}\,5000$ (Meroney, 1990). Results were in close agreement with the actual flows measured later, namely in terms of wind directions and vertical currents (Meroney, 1990). Mountain-wave clouds above the peak of Mount Fuji (Japan) were observed (for fifteen years) and physically modelled at a model-scale of $1{:}\,50000$. The wind tunnel investigation acted as a complement to assess how air currents around the mountain could be photographed through modelled streamline analysis (Meroney, 1990; Volter, 2015). The majority of wind tunnel investigations are associated to wind energy, these predominantly focused in quantifying speed-up. Speed-up corresponds to wind acceleration above hill or ridge crests, which increases the available wind power potential. Earlier studies focus on quantifying speed-ups at small model scales using terraced or contoured terrain geometries. Results exhibited the largest differences to the corresponding field data at near-surface heights (Meroney, 1990).

Physical modelling initiatives encompass two main groups of study domains: idealised terrain and comparisons with data from field campaigns. Early wind tunnel studies model real terrain study domains, which are site-specific and frequently require greater levels of model detail to simulate flow phenomena observed at full-scale. These investigations are limited to the availability of field data and frequently require the inclusion of the neighbouring terrain conditions, resulting in large study regions at smaller geometric scales. This leads to declining adequacy of the measurement devices for the scaled flows. Flows over orography require the reproduction of larger depths of the ABL in order to fully contain the elevated terrain features throughout the extension of the limited size of the modelling facility (Bowen, 2003). In addition to size constraints, the majority of wind tunnels exclusively simulate neutrally stable ABL flows that frequently lack correspondence with field observations.

Teunissen et al. (1987) conduct the most relevant of several wind tunnel studies based on the Askervein measurements using 3D models. They model the flow in three different wind tunnels in Toronto (Canada), Christchurch (New Zealand) and Oxford (England) at three different model-scales ($1{:}\,1200$, $1{:}\,2500$, and $1{:}\,800$, respectively) and surface roughness conditions. Authors report agreement of the mean flow results with the full-scale data and a satisfactory degree of consistency between different facilities and model scales. In contrast, longitudinal velocity fluctuations display significant differences between wind tunnels, especially at the leeside of the hill. The smooth surface model displays the best agreement with field data above the hilltop and windward slope. However, the extension of the flow separation region is smaller and the speed-up exaggerated. Rougher surfaces provide the best agreement on the leeside of the hill.

The Bolund campaign has also led to several wind tunnel studies reported in the Literature, the investigations of Conan et al. (2016), Petersen (2013) and Yeow et al. (2015) being examples. Yeow et al. (2015) use the largest model scale of these studies ($1{:}\,115$), the geometry consisting of a smooth surface. No turbulence generation is used for ABL development. Flow measurements are performed at two heights and compared with the data from the blind tests (Bechmann et al., 2011). Turbulent energy and integral length scales are found to be under-predicted relative to the field data downstream from the hilltop. These differences are credited to a mismatch of the inflow profiles, most significantly the profiles of TKE. For their combined physical and numerical Bolund flow modelling initiative, Conan et al. (2016) apply a terraced model, with altitude contours, of scale $1{:}\,500$. The largest differences of TKE to those of the field data are also observed in the region downwind from the hilltop. This is credited to the effects of the terraced iso-contour surfaces, also found to influence the length of the recirculation zone generated at the hilltop. Less focused on exclusively replicating the flow from the field campaign, Petersen (2013) investigates the effects of the geometric resolution on the flow above Bolund, using two models with distinct levels of detail at the scale of $1{:}\,250$ in WOTAN (Chapter 3). From the mismatch between results obtained above corresponding positions of very coarse and fine surface models, a strong dependence on the level of detail of the modelled geometry is concluded.

Other studies involving flows over orography have been performed in WOTAN in recent years, namely those conducted by Gillmeier (2014) and Erdmann (2017), the latter associated to the present research initiative. Gillmeier (2014) models the sub-mesoscale flow over the Alaiz mountain complex (Northern Spain) at a scale of $1{:}\,3650$, the full-scale study domain with an extension of just over $27 \times 14\ km^2$. No vortex-generating spires or roughness elements are employed in the inflow section due to the extremely small model scale. This results in an ABL depth of approximately $300\ m$, with oversized integral length scales. Despite the small scale, geometric blockage of the model is slightly above the 5% threshold proposed by VDI (2000). Erdmann (2017) investigates mean flows above a region of north-western Hainich National Park in western Thuringia (central Germany). The study domain comprises of a main ridge, flanked by small meandering valleys, and significantly smaller than Alaiz ($9 \times 3.5\ km^2$), enabling a model scale of $1{:}\,1750$. A more realistic depth of the inflow ABL ($\approx 1000\ m$ full-scale) is achieved through the use of a metal barrier for vortex generation ($z = 14\ cm$, model scale) and rows of small metal chains as roughness elements, oriented perpendicular to the flow, throughout the inflow section. To provide insight into the effects of the sub-grid details on the flow data, the domain is replicated by two models: detailed ($\approx 7.5\ m^2$ grid resolution) and coarse ($\approx 1.15\ km^2$) models. Similar results between grid resolutions are obtained above the crest of the ridge but differences are observed above the valley positions. Issues with the small model scale are also reported, most significantly the lack of Re independence of the flow at the near-surface above the leeside slope of the ridge and the low temporal resolution of the measured turbulence data.

Issues with scaled flow matching of real flows over complex terrain are avoided with flow investigations over idealised study domains. These are typically focused on single terrain features (mainly hills and ridges) and concerned with quantifications of corresponding speed-up effects. Most of the idealised complex terrain flow studies have been carried out over 2D terrain features of infinite width, meaning that the terrain geometry spans the full width of the modelling facility (wall to wall). The majority of these studies provide no indication of blockage effects posed by the infinite width of the terrain geometries. Furthermore, lateral symmetry of the resulting flow interactions with the 2D orography is scarcely documented.

Takahashi et al. (2002) provide analyses of the mean velocity fluctuations over four locations (including the leeside slope) above a symmetric 2D ridge with $\approx 20°$ slopes. A reported geometric blockage of 11% posed by the model in the wind tunnel affects the resulting observations. Ayotte & Hughes (2004) investigate the effects of slope inclination and surface roughness on speed-up and flow separation above idealised 2D sinusoidal hills of different heights. Two sets of hills with rough and smooth surfaces and four different slopes were investigated. Their results indicate that the speed-up is significantly lower than that predicted by linear theories and that mean and turbulent components of the flow exhibit different behaviours on the leeside of the hills. They conclude that increased temporal and spatial scales of turbulence above this region are more influenced by hill length than by the proximity to the surface, as observed on the windward slopes. A similar study to evaluate the effect of roughness on the flow over a 2D hill is conducted by Cao

& Tamura (2007). The aim of the investigation is to evaluate the speed-up above the crests and measurements are carried out in the separation region to locate the respective reattachment positions. The rougher surface leads to longer flow separation regions, as indicated by the spectra requiring longer to regain the same characteristics as upstream from the hill. A different approach is taken by Loureiro et al. (2008) for their investigation of the effects of a 2D rough hill on the flow in a water channel. The study is focused on exhaustively quantifying mean velocities and turbulent quantities on the leeside of the hill. It is observed that the extent of the flow separation region is longer for larger Re and that turbulence exhibits similar characteristics to those of a mixing layer.

Physical modelling of flows over 2D idealised geometries has limitations with regard to the resulting flow characteristics. The infinite width of the modelled terrain features implies that the presence of the side-walls of the modelling facility creates unrealistic lateral flow phenomena. Additionally, portions of the fluid with insufficient kinetic energy to overcome the terrain features may become entrapped upstream from the terrain models or may be unrealistically advected over the terrain, resulting in larger speed-ups and different downstream effects than would be expected if the flow could pass around the sides of the model (Meroney, 1990; Snyder, 1985). In this context, studies involving 3D terrain features are more advantageous.

There are significantly less studies related to flows above 3D idealised orography than those of 2D geometries. Most are focused on quantifying the mean velocities and turbulence intensities of flows above 3D hills. Hansen & Cermak (1975) perform measurements in the wake of a hemispherical hill and observe flow separation occurring at the hilltop, a common outcome of the 2D hill investigations, but also around the sides of the hill. Horizontal flow separation is observed to affect the flow along the centreline, the resulting wake longitudinally extending to over thirty times the hill height. Arya & Gadiyaram (1986) use two conical hills of the same height and surface roughness, but different slopes ($18°$ and $27°$), with the purpose of investigating the far-wake flow structure. They observe reduced mean velocities and increased turbulence in the wake region of the hills. Additionally, turbulence is found to be independent of the inclination of the slopes. Snyder & Britter (1987) evaluate flow and concentration fields above 3D hill and 2D ridge geometries, observing that the orography strongly distorts the shapes of plumes above the crests. Gong & Ibbetson (1989) study mean flow and turbulence features above a 2D ridge and a 3D hill, both with maximum slope of $15°$. While reporting good agreement with linear theory for the speed-up, strong differences are observed for the mean turbulent stresses. Differences between 2D and 3D orography are most evident from the amplitudes of the turbulent disturbances posed by each, with the 2D ridge generating larger stresses. Focused on quantifying speed-up under systematically varying inflow directions (between $0°$ and $90°$), Lubitz & White (2007) also employ 2D and 3D geometries of hills of constant height and shape, results providing evidence of the influence of the inflow wind direction on the observed speed-ups above the crests.

4.4 Numerical modelling

Due to constant computational improvements, numerical modelling has become the quickest and most cost-effective tool for ABL flow modelling. This is highlighted by the number of publications focused on numerical modelling of flows over complex terrain, published between 2007 and 2017. A total of 310 publications involving the keywords “complex terrain” and “numerical model” originate from this period, versus the 81 obtained using the keywords “complex terrain” and “wind tunnel” or “physical modelling” (Scopus, 2017). Of the publications focused on numerical modelling, 59 correspond to LES approaches and 55 use RANS. While RANS has been the main approach applied for numerical studies, as concluded by Bechmann et al. (2011), LES is becoming more prominent for microscale simulations. Indeed, of the 51 numerical models used for the blind comparison of results from microscale models for the Bolund experiment, 33 used RANS methods (one and two equations), 11 used linearized models and only 6 used LES. This highlights the significant progress made using LES methods between 2011 and 2017.

Several other studies associated to the Bolund field campaign have also been reported in recent years. Following the trend of the blind tests, most of these numerical investigations apply RANS methods (Peralta et al., 2014; Prospathopoulos et al., 2012). However, several studies apply LES to simulate the Bolund experiment (Chaudhari et al., 2016; Conan et al., 2016; Diebold et al., 2013). Good agreement between LES and field data is commonly reported, albeit significant disagreements are reported at the near-surface and for quantifications of TKE. Diebold et al. (2013) apply the same LES model to simulate a wind tunnel experiment based on Bolund and to directly simulate the field experiment. Deviations between results are most significant above the leeside slope, these attributed to the large differences of wind directions between field and numerical data. Similarly, the aforementioned study performed by Conan et al. (2016) uses an LES model for comparisons to wind tunnel and field data. Similar deviations from the field and wind tunnel data are found at the near-surface.

Earlier studies based on the Askervein measurements are reported to show good agreement with the mean velocities on the windward slope of the hill and above the crest (Walmsley & Taylor, 1995). Significant mismatches to the field data are found downwind from the crest and at the near-surface (Abdi & Bitsuamlak, 2014; Castro et al., 2003; Kim & Patel, 2000; Lopes et al., 2007).

In a two-phase investigation, Castro et al. (2003) and Lopes et al. (2007) simulate the Askervein flow using unsteady RANS and LES, respectively. Both numerical approaches yield similar results, the LES model providing better agreement with the field data relative to TKE predictions.

Motivated by the lack of high resolution field campaign data, a larger amount of publications corresponds to numerical investigations centred on idealised single terrain features previously modelled in wind tunnels (Brown et al., 2001; Griffiths & Middleton, 2010; Ishihara et al. 1999; Ferreira et al., 1995; Tamura et al., 2007). Earlier attempts are focused on quantifying speed-ups above the crests of 2D hills (Brown et al., 2001; Deaves, 1980; Ferreira et al., 1995). Ferreira et al. (1995) simulate the flows over 2D sinusoidal hills with four different aspect ratios (ratio of height to half-length) using a RANS method. Results indicate a strong dependence of the downstream recirculation regions on the shape of the hills. Similarly, Griffiths & Middleton (2010) perform RANS and RAMS (regional atmospheric modelling system) simulations over sinusoidal hills, of varying aspect ratios, to evaluate the accuracy of very high spatial grid resolutions ($1\ m$) with regional scale models. Comparisons yield large differences between numerical models and the wind tunnel data, authors attributing differences to the employed wall functions. Iizuka & Kondo (2004) apply LES over a steep hill, using four SGS models, with the purpose of ascertaining which provides the most accurate predictions compared to data from a previous wind tunnel study.

Idealised 3D terrain features have also been the target of numerical modelling investigations (Abdi & Bitsuamlak, 2014; Liu et al., 2016; Tamura et al., 2007). Tamura et al. (2007) investigate the effect of surface roughness on flow above a 3D sinusoidal hill using smooth and rough surfaces for their LES investigation associated to the wind tunnel experiment discussed earlier (Cao & Tamura, 2004). The rough surface aims to replicate the effect of a forested hill on the flow, authors applying a vegetation surface model (feedback forcing) to represent fluctuations inside the forest. Good agreement with the experimental data is reported for mean velocities and turbulence intensities. Furthermore, the rough (forested) hill produces a larger recirculation zone than the smooth surfaced hill. Abdi & Bitsuamlak (2014) compare the performances of RANS and LES for several idealised 2D and 3D hills. With the exception of the leeside regions of the hills, RANS and LES models exhibit good agreement. Similar tendencies are observed from the comparison between different closure methods used for the RANS simulations.

4.5 Concluding remarks

Strongly motivated by wind energy applications, the majority of microscale studies of ABL flows over orography have been dedicated to quantifying mean flow characteristics. Quantifications of speed-up over hills and ridges have been the main focus of these studies. Earlier attempts of microscale flow predictions over terrain features are motivated by the linear theory proposed by Jackson & Hunt (1975). Improvements to the linear theory, applicable when no flow separation takes place, have enabled its application for mean flow predictions in the context of wind harvesting. However, data measured from several field campaigns has demonstrated that the theory has limited applicability in providing accurate predictions where large perturbations are frequent. In particular, the field campaigns performed at Askervein and Bolund hills provide significant insights into the large frequency of non-linearities due to flow interactions with orography, even over relatively simple geometries. However, the extremely high costs associated to such initiatives render the realisation of field campaigns very scarce. This is related to the large amount of simultaneous measurement positions required for an adequate understanding of the flow field, as well as logistical and technical difficulties in finding adequate sites and installing measurement devices. The fact that a new road was built to the site where the Perdigão field campaign (associated to NEWA) took place, exemplifies such issues. Furthermore, the lack of controllable flow conditions may result in long periods of relatively uneventful flows. Specific flow-influencing surface or geometric details that are unique to the site also implies that the data lacks transferability to other terrain features of the same type, thus is locally representative.

ABL flow modelling provides a more available and cost-effective alternative to field campaigns in understanding flows over complex terrain. Earlier modelling studies involve physical ABL modelling in wind tunnels, these focused on sub-mesoscale terrain regions at extremely small scales. The earliest attempts using single terrain features (microscale) consist of idealised 2D structures, predominantly sinusoidal shaped hills. These studies continue to constitute the majority of wind tunnel investigations of complex terrain winds. These are mostly emphasised on predicting speed-ups and provide limited information on the turbulence fields. Investigations related to turbulence use time-averaged quantities and predominantly characterise turbulence intensity and vertical fluxes. Most investigations have been centred on measurements made above the windward slopes and crests of the hills. Less efforts have been made to characterise the flow fields above the leeside slopes and downwind regions, particularly the former. Many of these investigations avoid hills with steep slopes to inhibit the occurrence of flow separation (less than $\approx 18°$ downhill slope inclination according to Kaimal & Finnigan, 1994). In the context of validation data for numerical complex terrain flow models, many of these investigations provide limited turbulence data and frequently the experimental setups are inappropriately documented. However, physical modelling can perform an important role in providing high quality systematic data for model validation as supplement for the scarcity of data from field campaigns.

Improvements in measurement techniques and modelling procedures mean that wind tunnel (or water channel) experiments can supply high resolution turbulence data for numerical models, encompassing the relevant scales of turbulence structures of the flow.

Numerical modelling is the primary tool in predicting ABL flows over complex terrain. In line with the linear theory, earlier attempts simulate flows above gentle-sloped hills. Advances in computational capabilities have enabled the incorporation of RANS methods to terrain flows, the higher resolutions of turbulence modelling resulting in closer agreement with experimental data. However, LES is rapidly overtaking RANS as the primary numerical modelling tool for terrain studies, as highlighted by the surge of related publications observed over the last decade. Providing information on the transient flow fields, LES has the potential to provide greater accuracy of flow predictions over complex terrain. In the presence of orography, variations are abrupt and short-lasting in both spatial and temporal scales. In this context, time-dependent flow analyses can provide more information on the turbulence structures of the flow. However, LES simulations of complex terrain flows performed so far are yet to provide significant improvements over the predictions obtained using RANS. This is highlighted by the lack of agreement observed for near-surface flow predictions downstream from the crests of modelled hills and ridges. Taking into account the relative novelty of LES modelling of terrain flows relative to RANS approaches, this is expected. However, it is also attributable to the absence of appropriate validation datasets, specifically intended for transient flow validation. The rapid improvement of computational capabilities, together with the slower developments in terms of readily available data from field campaigns, has created a void of datasets that characterise sub-grid scale flow characteristics.

5 METHODOLOGY

Selections made for the experimental campaigns are discussed here. First, concepts related to model validation are introduced and potential data requirements for LES validation of flows over orography are explored. This includes a brief summary of a Workshop organised to ascertain validation data requirements from numerical modellers of ABL flows over complex terrain. This is followed by a discussion regarding the experimental requirements that provide the broadest data with which to address the research questions outlined in Chapter 1. Finally, the experimental setups used for both campaigns are presented and topics related to turbulence measurements debated.

5.1 Model validation

The terminology regarding model validation is non-consensual and has different meanings for different authors or applications, as evidenced by the use of terms such as verification, adequacy, credibility, or sensitivity to describe similar procedures (Cobelli et al., 1984; Hamilton, 1991). Within the medical community, Cobelli et al. (1984) define validation as 'the assessment of the extent to which a model is well founded and fulfils the purpose for which it is formulated', thus a valid model is not a true universal representation but adequate for a well-defined and limited set of objectives. In a statistical context, Hamilton (1991) describes model validation as a three-task procedure involving verification, sensitivity analysis and evaluation. Verification determines whether the model is a faithful representation of what is intended in the mathematical model and underlying theory. Sensitivity determines the extent to which model behaviour is affected by changes in parameters and evaluation compares the model output to real world measurements.

For the fluid modelling community, the American Institute for Aeronautics and Astronautics (AIAA) defines validation as 'the process of determining to which degree a model is an accurate representation of the real world from the perspective of the intended use of the model' and is one part of the twofold verification and validation (V & V) approach, which is widely accepted by the modelling community (Ex. Gosseau et al., 2013; Hasselman et al., 2002; Oberkampf & Trucano, 2002). According to the AIAA, verification is defined as 'the process of determining that a model implementation accurately represents the conceptual description of the model and its solution, which is a dual process consisting of code and solution verification (Gosseau et al., 2013). The verification process is more associated to building confidence and credibility of developed or validated models, less so with the experimental data that is a means of validation during model development within the definition of V & V (Kempf, 2008; Oberkampf & Trucano, 2002). In simple terms, validation deals with model physics using the real world as the standard, while verification deals with model mathematics using a conceptual model as the norm (Oberkampf & Trucano, 2002). This thesis aims to provide adequate experimental data for model validation so only the validation part of V & V procedures is addressed.

5.1.1 LES validation

The aim of the validation of numerical models is to characterise and minimise uncertainties and errors in the computational model, as well as in the experimental data. The latter may arise from large uncertainties or biases of the corresponding measurements. This leads to higher confidence in the quantitative predictability of the model. Models that are valid in RANS may not be for LES and particular attention must be given whenever validation methods are adapted to LES. According to Kempf (2008), one of the major limitations to the current applicability and reliability of the LES method is a lack of validation approach centred on LES requirements, i.e., experiments specially designed to provide data for LES models. LES results are normally compared to two experimental statistical moments, mean and variance, which are less sensitive to small variations of the smallest scales.

LES is well-developed for flows involving simple geometries and small-scale isotropic turbulence assumptions, where the quantities governing the flow are driven by large-scale motions that are resolved with LES and assumed to follow the energy cascade to the smaller modelled scales of turbulence. Based on the underlying theoretical assumption that the peaks of the spectral energy between turbulence production (at the larger scales) and dissipation (smaller scales) occur at very distinct wavenumbers (thus independent), LES models the smaller scales of turbulence as statistically isotropic and universal (Jimenez, 2003; Pope, 2004). However, in fully-turbulent complex flows, such as near-wall regions of bounded flows, turbulence is frequently anisotropic and cannot be accurately modelled. Flow-influencing processes may occur at the smaller (modelled) scales of such flows, thus constraining the accuracy of near-surface LES calculations.

As discussed in Chapter 4, the success rate of numerical predictions of near-surface ABL flows over complex terrain continues to be limited, with discrepancies between numerical predictions and experimental observations tending to increase with decreasing heights from the surface. This is partially due to the technical issues with LES methods, but can also be credited to a lack of qualified validation data for LES of ABL flows over orography.

5.1.2 Requirements for validation data of flows over orography

An important step of the research work is a workshop for numerical modellers focused on ABL flows over complex terrain. The main purpose of the event was to extensively discuss and elaborate the experiments of the present investigation with potential users of the data. Thirteen outside participants, including two field experimentalists, frequented the event that took place in February 2017. With the exception of two participants (backgrounds in air quality), all scientists were associated to the wind energy sector. This follows the trend regarding the predominance of wind energy applications in the Literature relevant to microscale flows over orography. The main outcome of the workshop were two main requirements proposed by the modellers: flow separation and enhanced grid resolution. Surprisingly, no requirements were specified for turbulence parameters of interest or resolutions of the experimental data.

As observed in Chapter 4, the majority of studies concerning single terrain features correspond to gentle windward slopes that inhibit the strong non-linearities that characterise flow separation. Thus, validation data from flows involving separation due to orography are beneficial to the numerical modelling community. The requirement for improved grid resolutions arises from the demand to obtain greater accuracy of numerical predictions of flow fields above terrain. A larger amount of experimental measurement points is advantageous in providing numerical modellers with more data validation points. This is also useful for detecting experimental biases in the data, which may occur at some measurement points due to the complexity of the flows but not at alternative locations of the flow field where terrain effects are less influential. As requirement for validation data, the numerical modellers agreed on horizontal and vertical grid resolutions equivalent to the diameter of wind turbine blades. According to the technical specifications provided by AWEO (2018), diameters of industrial wind turbines vary between approximately 70 and $130\ m$.

5.2 Research objectives

The current research aims to provide a deeper understanding of how complex terrain geometries affect local shear-induced flow turbulence. These are achieved by addressing the research questions through physical modelling. To this end, a unique model scale is less adequate to provide complete answers for all proposed topics. Modelling at a larger model scale (microscale study domains) is the optimal approach to understand the influence of individual terrain features on the flow and the distances from the features where flow is affected by the terrain, thus addressing the first research question (Chapter 1). This is also advantageous in investigating if terrain types are classifiable according to the effects produced on the flow (Question 4) and evaluating how influential surface heterogeneities are compared to orography (Question 2). Modelling at smaller scales (sub-mesoscale study domains) is most suited to ascertaining the effects of transitions between terrain types. Based on this rationale, the main focus of the present experimental work is on single terrain features at the largest feasible model scales. This selection is supplemented by the data from the earlier study performed by Erdmann (2017), the sub-mesoscale study providing some insight into the second and third research topics of Chapter 1.

Previous complex terrain studies performed in WOTAN, namely those conducted by Gillmeier (2014), Petersen (2013), and Erdmann (2017), highlight the requirement for the maximum possible model scale in order to achieve meaningful turbulence measurements at high spatial and temporal resolutions. The choice of geometric model scale is influenced by the available facility size and the capacity of producing an ABL flow at the same geometric scale. Taking the above considerations into account and the requirement for maximised grid resolutions for the validation data, the desired model scale for the present investigation is about $1{:}\,1000$.

Another relevant decision concerns the modelling of idealised or real 3D terrain features. Real features have the benefit of providing reference data with which the modelling procedure can be compared and evaluated. In nature, no single terrain feature is exactly the same as another. The more detailed or site-specific are the terrain selections, the less universal or transferrable the resulting data. Idealised models represent a simplified counterpart of a more complex system, in which properties expected to be less influential or unique to a specific real landform can be neglected from the modelling process. These provide more benefits than models based on real terrain in addressing the proposed research questions. Idealised features provide the advantage of simplified geometric and flow scaling procedures, without the constraints of having to replicate real-world conditions. The lack of site-specific geometric details results in maximal data transferability between different domains of the same terrain feature and maximised extensions up- and downstream from the landforms. This is particularly useful in gaining an understanding into which geometric parameters exert larger influence on the terrain flows or establishing the limits of influence of the terrain on flow dynamics. Furthermore, idealised features enable systematic parameter variations without re-scaling requirements or the need to maintain a certain shape (or aspect ratio). In the context of LES model validation, idealised single features are beneficial in terms of constituting simple geometries and enabling small domains, two relevant requirements for validation data (Kempf, 2008).

The majority of past idealised terrain studies consist of flow modelling above single 2D hills of infinite width in wind tunnels, thus constraining lateral flows whilst unrealistically amplifying longitudinal and vertical flow components. More scarce in the Literature, 3D terrain features provide more precise flow predictions through the minimisation of effects from the wind tunnel side walls. Therefore, the evaluation of the effects caused by idealised 3D ridges is warranted for the present investigation. Also rare in the relevant Literature are studies involving 3D idealised valleys, particularly with a view to providing validation data. Under this rationale, the experimental study can be extended to 3D valleys built from the combination of the 3D ridges used in the present investigation. This has the dual benefit of filling a data void for a relatively unexplored terrain type and addressing the possibility of classifying terrain features based on turbulence characteristics of the associated flows. Without any correspondence found in the Literature, assessments of the effects of systematic variation of individual geometric parameters can also be made with the present selection.

5.3 Experimental setups

Experimental work is divided into two modelling campaigns: the first focused on idealised 3D ridges and the second on 3D valleys. Included in the first of the experimental campaigns is modelling an appropriate inflow ABL and flat terrain measurements, the latter to provide reference data with which to ascertain terrain effects on the flows.

5.3.1 Inflow setup

Turbulence generation is required for fully-developed and turbulent ABL characteristics above the model section. Spires (vortex generators) serve the purpose of providing large turbulence structures and are placed at the start of the inflow section. Small roughness elements are responsible for generating near-surface small turbulence features and typically placed throughout the remainder of the inflow section. The main requirement is that the vertical profiles of the generated flow and turbulence match between the inflow and the model sections. Between turbulence generators and wind tunnel ceiling adjustments, twenty-six different setups are tested, as listed in Table C1 (in Appendix C).

The final approach flow setup consists of thirty-one isosceles-shaped spires for the creation of larger scale structures. Each spire is $\approx 28\ cm$ high (model scale) and $\approx 7\ cm$ wide, distributed equidistantly ($\Delta y \approx 6\ cm$). A longitudinal fetch of $\approx 10\ m$ built up of rows of brass chains of alternating diameters (4 and $6\ mm$) positioned equidistantly ($\Delta x \approx 25\ cm$), is used to enhance smaller structures of turbulence. A perspective of this setup is displayed in Figure 5-1.

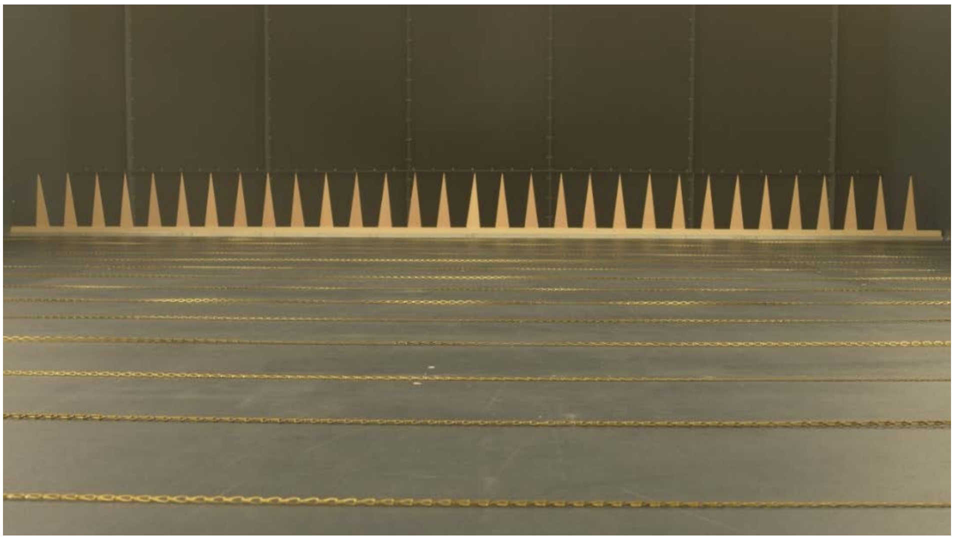

Figure 5-1. Upstream view of the setup of spires and chains used for the modelled ABL flow in WOTAN.

5.3.2 Flat terrain

The model section comprises of fifteen model plates: five central plates with dimensions of $1.5.\,x\ 2\ m^2$ (model scale) and ten side plates of $1.5.\,x\ 0.6\ m^2$, as schematized in Figure 5-2. The origin of the horizontal axis system ($X = Y = 0$) is located at the start of the model section. This is purposefully selected to minimise positional changes that may arise from interchanging model plates for different terrain models downwind from this position. To avoid undesirable and unrealistic friction effects from the wind tunnel side walls, smooth-surfaced empty corridors with widths of $0.4\ m$ are left between the wind tunnel walls and lateral edges of the model surfaces. These are shaded in red in Fig. 5-2. Thus, the effective transversal or span-wise dimension of the model section has an extension of $\approx 3.2\ m$. This approach also has the advantage of allowing the modeller easy access to the model plates for more efficient model changes.

Each model surface is built on wooden base plates of $16\ mm$ thickness, these also used for the inflow section surfaces (surface beneath the chains in Fig. 5-1). Flat terrain and ridge geometries are constructed using *Styrodur* (minimum thickness of $10\ mm$), milled to the desired forms using CNC routines. The milling procedure is performed separately in crosswise directions, models sharing a surface made of 3D pyramids of height $1.2\ mm$. This provides constant roughness for the inflow and inhibits the generation of internal BL characteristics. Reflective backscatter of LDV laser light is minimised with black paint used to coat the surfaces after milling. The additional layer of *Styrodur* creates a $10\ mm$ high step at the transition between approach flow and model sections ($X = 0$), which can induce unrealistic turbulence on the flow above the model section. This is minimised with a gentle-sloped ramp that smoothens the different heights between inflow and terrain zero-height.

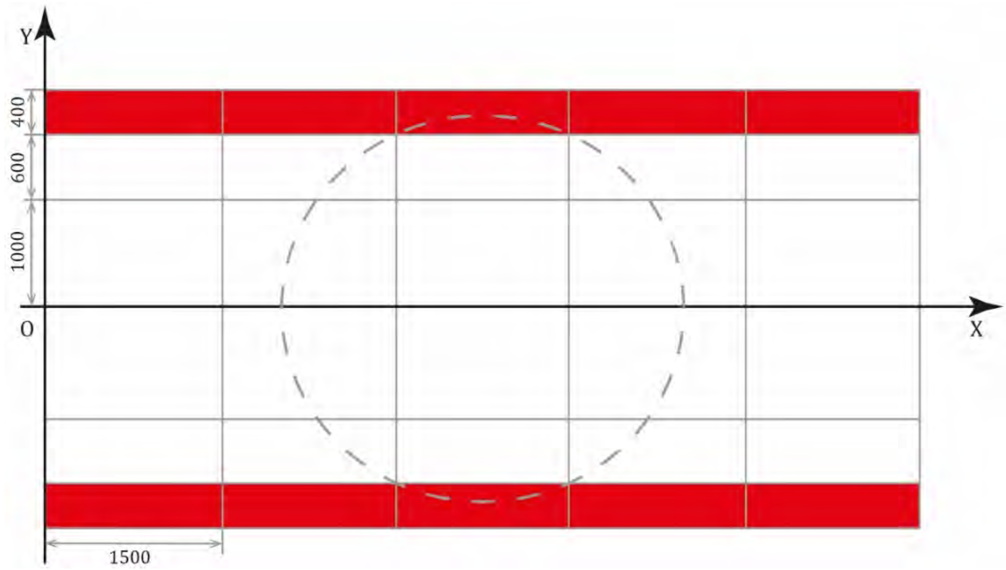

Figure 5-2. Schematic top view of the model plate setup in the model section. The longitudinal flow direction is from left to right (axis system represented in black) and the horizontal origin marked with O. Red shaded areas represent the smooth surface side corridors. Dimensions are given in millimetres and in model-scale.

5.3.3 Ridge geometries

Results from previous studies involving flows over idealised hills show that the most influential geometric parameters on the observed flows are the height (H) and the inclinations of windward (γ) and leeside (θ) slopes, as schematised in the cross-sectional view of a generic ridge displayed in Figure 5-3. Idealised hill geometries are frequently characterised by the aspect ratio, which relates H to the half-length (L_R) or the length (L). In the present investigation, the half-length is used to characterise the ridge geometries but is specified according to the length of the slopes. This with the purpose of maintaining equivalence between relative positions of different ridge geometries. This approach is further detailed in Chapter 7.

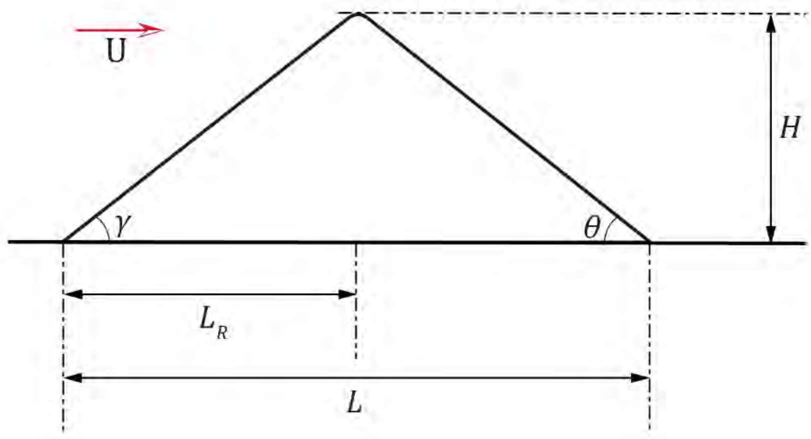

Figure 5-3. Geometric parameters of a generic ridge geometry viewed in the vertical plane (XZ). Longitudinal flow develops from left to right (as indicated by U).

Selections of ridge dimensions are limited by milling constraints and the cross-sectional blockage caused by the models. The surface resolution of the milling procedure is $5\ mm$ (diameter of the milling tool), corresponding to the horizontal length of the aforementioned surface pyramids. In order to preserve homogeneous roughness, without interrupted pyramids, all model dimensions (H and L) are multiples of $5\ mm$. The milling constraint also applies to the ridge slopes (γ and θ), playing a fundamental role in defining the permissible angles for the ridge models. The largest (or steepest) permissible angle for the slopes corresponds to 75°.

Selections of ridge heights initially consist of 80 and $200\ mm$ (model scale). Cross-sectional geometric blockage that occurs due to the wind tunnel wall imposition on the flow, together with the transversal blockage posed by the model in the wind tunnel test section, should be below a 5% threshold (VDI, 2000). Ridge heights are selected accordingly, the condition of geometric blockage fulfilled by both heights (maximum of $\approx 3.5\%$). Further reductions of transversal blockage are achieved through a model width reduction and side slope treatment (based on a cosine function), conceived by Erdmann (2017). However, the combination of longitudinal static pressure gradient analyses (Appendix B) and laser light sheet visualisations display excessive flow blockage produced by the higher ridge. Due to this constraint, the ridge investigation is focused on the lower height ridge, which fulfils geometric and flow blockage criteria. Three windward slopes are selected to assess slope effects on the flow:

- gentle slope: $\gamma = 10^{\circ}$;
- intermediate slope: $\gamma = 30^{\circ}$;
- steep slope: $\gamma = 75^{\circ}$.

These are built with two ridge models: symmetric ($\gamma = \theta = 30^{\circ}$) and non-symmetric ($\gamma = 10^{\circ}$ and $\theta = 75^{\circ}$). For a constant inflow direction, 180° rotations of the non-symmetric model result in a third ridge domain consisting of a steeper windward slope ($\gamma = 75^{\circ}$ and $\theta = 10^{\circ}$). Contemplating the eventual requirement for small amplitude variations of the inflow direction, the conceived ridge models fit within the wind tunnel turntable. Ridge models follow a nomenclature system with corresponding colour schemes, as defined in Table 5-1. Non-symmetric ridges are termed '*Type I'* (aspect ratio, $L/H \sim 6$) and given the suffix '*75'* or '*10'* for steep or gentle windward slopes (γ), respectively. Figure 5-4 displays a view of the *Type I-75* ridge model positioned in the wind tunnel, assuming inflow from the left. The same model corresponds to *Type I-10* when flipped horizontally (by 180°). The symmetric ridge is named '*Type II'* ($L/H = 3.5$) and presented in Figure 5-5. The colour scheme presented in Table 5-1 is used for the respective experimental results associated to each model, presented in Chapter 7. The *Type I-10* ridge geometry is subsequently used by Diezel (2019) to create v-shaped valleys on the long windward slope.

Table 5-1. Definitions and relevant dimensions of the model ridge geometries, using the symbols defined in Fig. 5-3.

ridge geometry	aspect ratio L/H $[-]$	ridge height H_{fs} $[m]$	ridge length L_{fs} $[m]$	windward slope inclination γ [°]	leeside slope inclination θ [°]	shape and colour assignment
Type I-75	5.9	80	475	75	10	
Type I-10	5.9	80	475	10	75	
Type II	3.5	80	280	30	30	

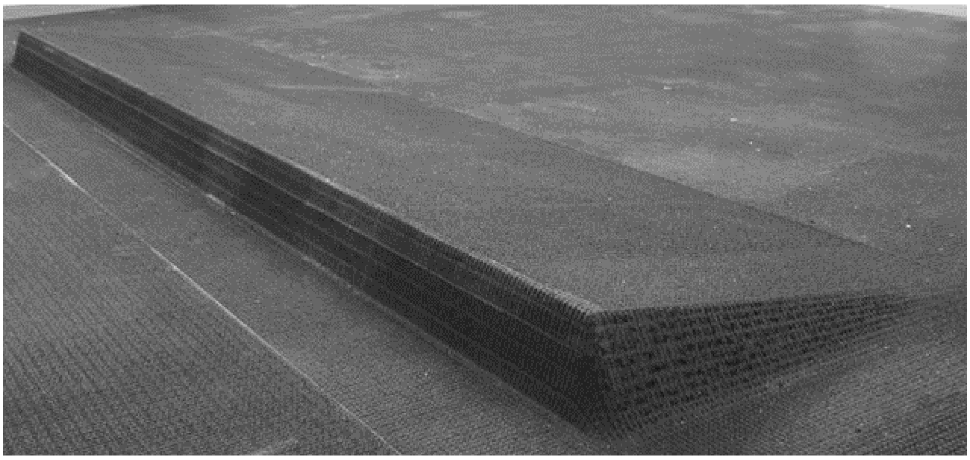

Figure 5-4. Lateral view of the non-symmetric ridge (*Type I*) mounted in WOTAN. The model corresponds to the *Type I-75* ridge when flow originates from the left. The same model corresponds to *Type I-10* ridge when rotated $180°$.

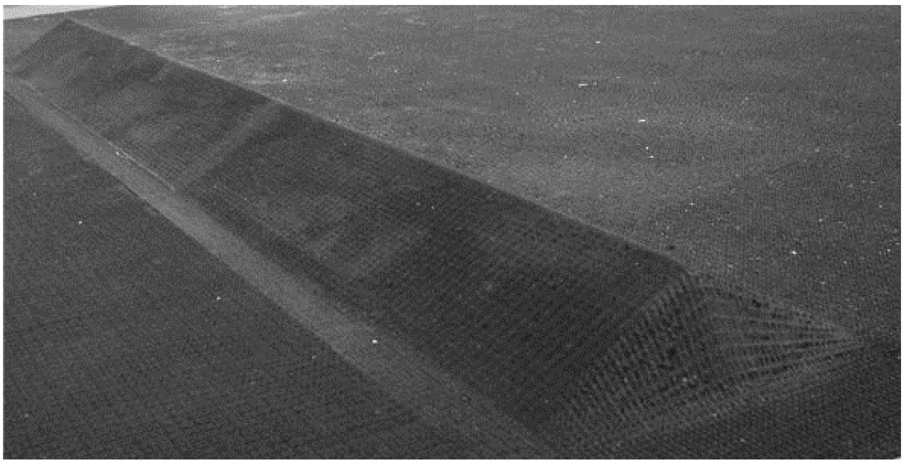

Figure 5-5. Lateral view of the symmetric ridge (*Type II*) mounted in WOTAN.

5.3.4 Valley geometries

Valleys are created using combinations of two equivalent ridge geometries defined earlier. This leads to three longitudinally symmetric valley geometries, defined as follows and schematised in Figure 5-6:

- Non-symmetric ridged valley with gentle slope ($\gamma = 10^{\mathrm{o}}$) on the windward side of the first ridge, hereby designated *Type I*;
- Non-symmetric ridged valley with steep slope ($\gamma = 75^{\mathrm{o}}$) on the windward side of the first ridge, defined as *Type II*;
- Symmetric ridged valley ($\gamma = \theta = 30^{\mathrm{o}}$) named *Type III*.

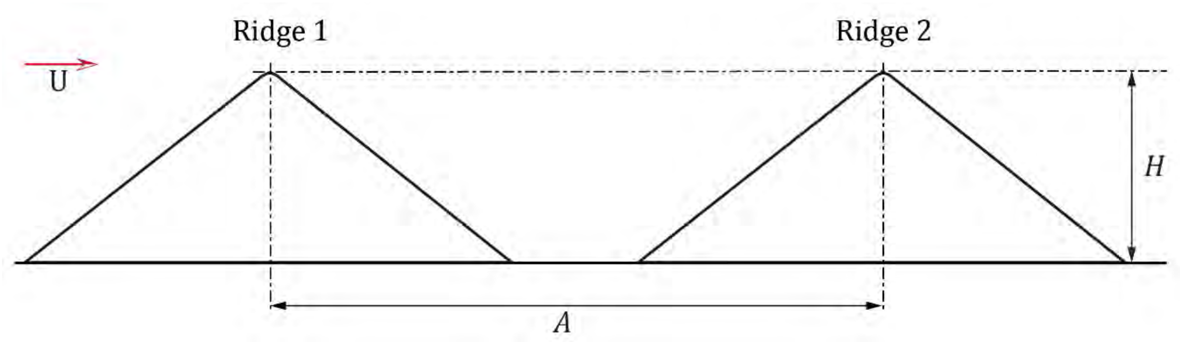

Figure 5-6. Geometric parameters of a generic valley geometry, as viewed in the vertical plane (UW). Longitudinal flow develops from left to right.

For the crossflow over the valleys of the present study, the valley width (A), distance between ridge crests (peak-to-peak), is varied systematically. Starting with the smallest values of each of the valley types, A is incremented by constant amplitudes of twice the ridge height or valley depth, $2H$. The smallest values of A are $4H$ for *Type I* and *Type III* valleys and $12H$ for *Type II*, the minimum width of the latter constrained by the inside slopes of the valley. Widths of *Type I* and *Type III* valleys are systematically varied to $12H$, equal to the smallest possible width of valley *Type II*. This results in thirteen valley models of the same depth as summarised in Table 5-2.

Table 5-2. Definitions and relevant dimensions of the model valley geometries for an assumed model scale of $\mathbf{1:1000}$, using symbols defined in Fig. 5-6.

valley geometry	valley depth $\boldsymbol{H}\ [\boldsymbol{m}]$	valley widths $\boldsymbol{A}$	shape and colour assignment
Type I		$4H$, $6H$, $8H$, $10H$ & $12H$	
Type II	80	$12H$, $14H$ & $16H$	
Type III		$4H$, $6H$, $8H$, $10H$ & $12H$	

5.3.5 Valley width modifications

For the construction of the valleys using ridge geometries, two approaches are possible: to build new models for each valley or to employ segments of flat terrain to construct valleys from existing parts. The first option provides more dimensionally precise models, milled on full model base plates without requiring further transformations. Additionally, this provides more robustness and resistance of the plates to sustaining deformations. However, the wider *Type I* valleys (more specifically, widths from $8H$ to $12H$) occupy longitudinal extensions that cannot fit on a single model plate, thus this modelling strategy would require a total of sixteen base plates containing twenty-six ridges.

Using terrain segments (strips) of differing lengths and constant width ($2\ m$) to create each valley can forfeit dimensional precision due to the additional cutting procedures and the resulting strips are more susceptible to undesired deformations. Nonetheless, applying this methodology is significantly more advantageous in terms of minimising the timescale required to build each valley. Another advantage of this approach is the ease of building the valleys in the wind tunnel, the relatively small and light strips only requiring one user to perform the model changes between each setup. To this effect, only one additional model of each ridge geometry (non- and symmetric) is required and the corresponding model plates of the existing ridges transformed into terrain strips. In order to fulfil all the proposed valley combinations, a total of eleven flat terrain strips of different lengths are required. Each of the combinations requires different strip setups for the inner valley section (i.e., the region between the ridges) as well as the outer valley section, downwind from the second ridge.

Segments associated to non-symmetric ridges provide the added complexity of pinpointing the exact location of the transition between flat terrain and $10°$ slope. This is reflected in the absolute (effective) valley widths measured for each valley, listed in Table 5-3. Figures 5-7 to 5-9 present lateral views of mock-ups of the smallest and largest widths of *Type I*, *Type II*, and *Type III* valleys, respectively.

Table 5-3. Effective valley widths of each valley type after systematic variation

valley geometry	dimensionless approximate widths	absolute widths $[\boldsymbol{m}]$
Type I	$4H$, $6H$, $8H$, $10H$ & $12H$	349 , 509, 669, 829 & 989
Type II	$12H$, $14H$ & $16H$	936, 1096 & 1256
Type III	$4H$, $6H$, $8H$, $10H$ & $12H$	320, 480, 640, 800 & 960

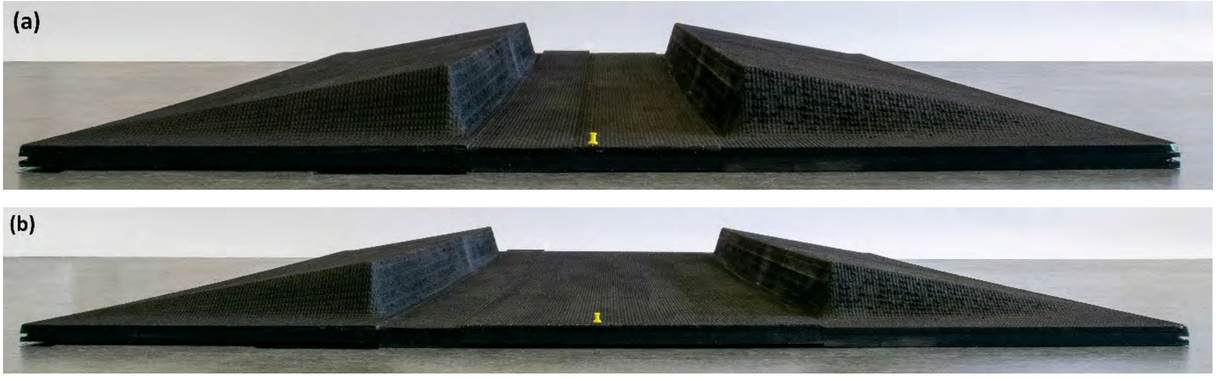

Figure 5-7. Lateral view of mock-up of *Type I* valleys of width $\mathrm{A} = 4\mathrm{H}$ (a) and $\mathrm{A} = 12\mathrm{H}$ (b). The yellow-coloured pin indicates the approximate mid-valley location.

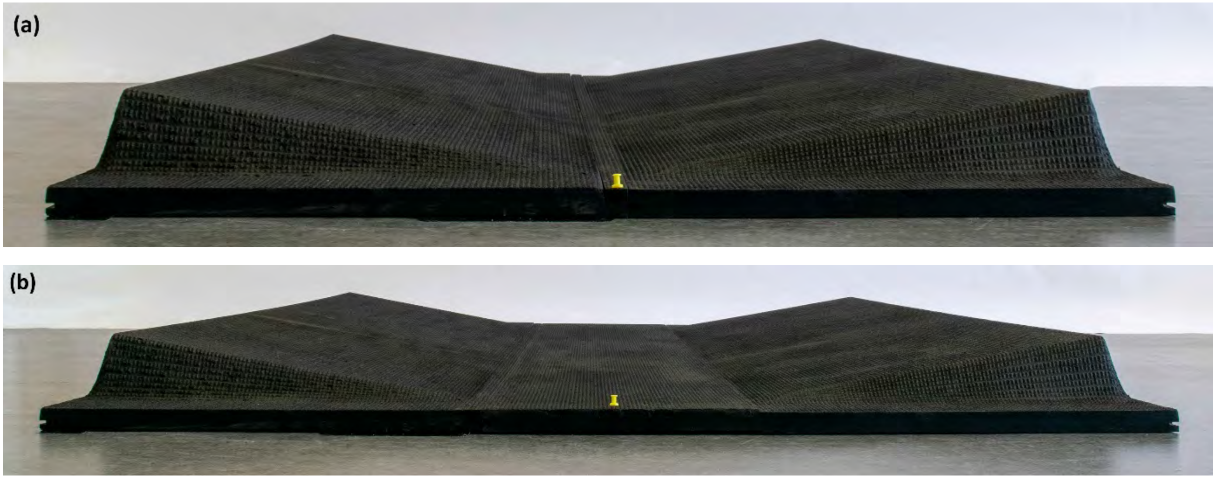

Figure 5-8. Lateral view of mock-up of *Type II* valleys of width $\mathrm{A} = 12\mathrm{H}$ (a) and $\mathrm{A} = 16\mathrm{H}$ (b). The yellow-coloured pin indicates the approximate mid-valley location.

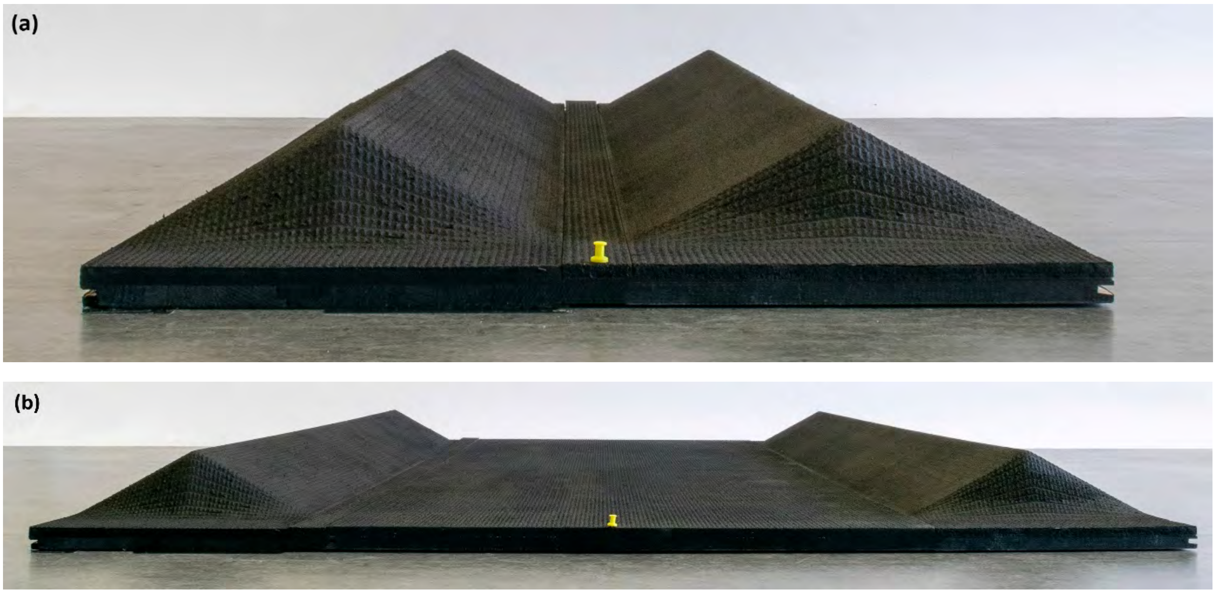

Figure 5-9. Lateral view of mock-up of *Type I* valleys of width $\mathrm{A} = 4\mathrm{H}$ (a) and $\mathrm{A} = 12\mathrm{H}$ (b). The yellow-coloured pin indicates the approximate mid-valley location.

5.3.6 Turbulence measurements over complex terrain with LDV

Several measurement techniques, such as LDV and hot-wire anemometry, are available for turbulence-resolving flow measurements at the EWTL. As discussed in Chapter 3, LDV provides higher temporal and spatial resolutions of the measurement data than alternative techniques used in wind tunnel modelling. Assuming a fixed spatial resolution of the measurement volume, the temporal resolution of the LDV data is less influential on the statistical representativeness of time-averaged flows than transient phenomena analyses. A meaningful transient analysis must contemplate the broadest range of temporal and spatial scales of flow turbulence. Higher measurement resolutions are a function of the quantity of detected samples (seeding particles) passing through the measurement volume, defined as the data rate. The larger the number of valid samples, the higher the measurement data rates.

Several adjustable measurement parameters also influence the data rate of LDV measurements (Dantec Dynamics, 2012). Sensitivity corresponds to the amplification of analog and digital measurement signals applied to each of the laser channels. Higher values of sensitivity typically lead to increased data rates but also increase the amount of non-valid burst signals to be rejected. The velocity span (bandwidth of the measurements) and the centre velocity (mean or most frequent measurement value) are associated to the expected velocities and contribute to higher data rates when correctly adjusted but can also disregard particles transiting at velocities outside the defined span, thus decreasing the data rate.

Data processing of the measured velocity dataset (continuous signal) consists in obtaining statistical estimates from reconstructed (discrete) datasets that are mainly influenced by the measurement data rates (Nobach, 1999). In the simplest form, flow statistics are represented by moments calculated from each measurement dataset. Higher order statistical moments are required for a thorough characterisation of flow turbulence, which requires a maximised reconstruction of the digital measurement signal (higher temporal resolution). This is dependent on the relationship between the measurement data rate and the Nyquist frequency of the signal.

The Burst Spectrum Analyser (BSA) software of the LDV supplies an indication of the validity of the measurement, which is an important measure of the data quality and can act in opposition to increases of data rates. The software provides a real-time display of the burst signal from each measurement channel during the measurement, which allows the user to monitor its quality. As well as the data rate, the quality of the measurement is dependent on high signal-to-noise ratios of the burst signals. Noise can be a significant source of measurement error and may arise from several sources of the measurement system. Each particle passing the laser measurement volume contains undesirable thermal and secondary electron noise from the detector (Ristic, 2007). Other sources of noise stem from velocity gradients within the measurement volume, signal processing and dirty airflows (Nobach, 1999; Ristic, 2007). The BSA software enables the user to tune the LDV measurement setup through the manipulation of the aforementioned parameters. These considerations are taken into account for the present experiments.

5.3.7 Data processing

Experimental data is processed using a software suite developed at the EWTL. Its basic functionality stems from the work of Fischer (2011). Most recent developments in the LDV data analysis were implemented by Schliffke & Wiedemeier (2018). This software package is built in Python (version 3.6) and computes all relevant mean flow and turbulence statistics from the raw measurement data series. Transit time weighting scripts provide signal statistics unbiased by varying data rates, developed and tested with data from the present experiments. With the exception of the aerodynamic surface roughness (z_0) and the profile exponent (α) of the velocity profiles, all mean data is processed with this software package. To avoid quantifications of z_0 and α that are locally affected by individual roughness elements or surface details, a dedicated software package developed at the EWTL (called PROFIT), is used. Transient data, expressed for the flows above valleys (Chapter 8), is processed using scripts developed within the scope of the thesis of Cheng (2019) and based on algorithms created for the data analyses of the present investigation. These scripts act as add-ons to the aforementioned software package of Schliffke & Wiedemeier (2018).

5.3.8 Flow coordinate systems

When interacting with terrain, the main flow direction varies with regard to the undisturbed horizontal approach flow. Flow unstably conforms to the underlying surface, leading to temporal and spatial variations of the directions of the resulting velocity vectors. This is relevant for flow measurements, for which the employed coordinate system may affect the results and is particularly influential above the slopes of the ridges. In defining the setup for measurements of flows over complex terrain, three approaches are available: Earth (fixed), flow-referenced (streamline), and hybrid coordinate systems.

The Earth coordinate system uses fixed settings regardless of the inclination of the underlying surfaces. This is suited to quantifying gravitational effects above complex terrain, which are vertical regardless of the surface geometry. Another example of the suitability of the Earth coordinate is flow characterisation for wind energy applications. Common wind turbines are mounted on vertical masts, their axis aligned longitudinally and independent of the inclination of the terrain. However, the Earth coordinate system fails to capture the maximal velocity of the flow, expected to follow the streamline direction translated by the reorientation of the velocity vectors with regard to the terrain. Differences between maximum magnitudes of the velocity field above ridge slopes and those of the horizontal direction increase with increasing slope inclinations. This has repercussions in terms of direct comparability with analytical theory and flat terrain data. There is no clear evidence of how this affects expressions of turbulence.

The flow-referenced coordinate system corrects the tilt of the streamline direction via data rotation. This enables direct comparisons with analytical theories and flat terrain data without the effects of sloping terrain (Kaimal & Finningan, 1994; Peña et al., 2019; Wilczak et al., 2001). The approach frequently involves applying a rotation matrix to make the raw measurement data parallel to the underlying slope or the velocity vector at the near-surface (Liu et al., 2012). The accuracy of this approach is dependent on the flow being parallel to the flow-referenced velocity vector. This can produce an adverse dependence on temporal and spatial variations of the flow (coordinate dependence on flow dynamics) when significant variations of the velocity vectors occur, thus may not hold for transient flows (Sun, 2007). Flow separation or torsion of the streamlines also affect flow characterisations using the flow-referenced system for 3D flows over orography (Kaimal & Finningan, 1994). Furthermore, observations of wake flows above leeside slopes of ridges indicate that streamlines are less likely to follow the surface inclination for unstable and neutral atmospheric stabilities (Menke et al., 2018). This can contribute to increases of inaccuracy of flow-referencing founded on the underlying slope inclination above these regions.

The hybrid coordinate system uses the streamline direction of the flow-referenced system as longitudinal component and the vertical direction of the Earth coordinate system (Kaimal & Finningan, 1994). For the present investigation, the Earth coordinate system is used. While forfeiting the direct comparability with longitudinal velcoties above flat terrain, it is unaffected by the occurrence of flow separation. This approach also minimises uncertainty propagation due to the 3D flow field data reconstruction from 2D measurements performed separately. In practical terms, this method has no repercussions in terms of providing data for numerical model validation.

Diezel (2019) provides an analysis of the effect of rotating data measured in the Earth coordinate system to the flow-referenced system. Coordinate transformation is made for flows measured above the crest of the *Type I-10* ridge of the present investigation, atop the gentle windward slope

(Table 5-1). Of the present ridge geometries, the *Type I-10* ridge is most feasible for coordinate rotation due to the proximity between flow data in fixed and rotated coordinate systems. A maximum tilt angle of $\approx 8°$ was observed between the streamline vector and the horizontal (fixed) direction at $z_{AT} = 12\ m$ (full-scale) above the crest of the ridge. Vertical turbulence components present the largest differences between fixed and rotated data, the largest differences observed for the mean vertical turbulent fluxes at heights up to ≈ 1.5 times that of the ridge ($\approx 1.5H$). The rotated data of the vertical velocity fluctuations increases to values outside the range of uncertainty of the fixed data, while streamwise and lateral components of both coordinate systems are contained within the reported confidence intervals.

6 THE MODELLED ABL

The present chapter characterises the modelled ABL flow, generated using the experimental setup outlined in the previous chapter. Quality assurance of the measurement data is documented in the first subchapter, prior to the description of the ABL flow. An adequately modelled ABL is achieved when flow conditions between inflow and model sections are consistent, assuming that flow similarity is already established. This is verified through the analyses of the two-dimensional (2D) mean flow characteristics of the ABL flow (in the vertical plane), presented in the second subchapter, with particular emphasis on the near-surface heights where shear dominates over buoyant turbulence production. Fundamental characteristics of the modelled ABL flow are briefly summarised at the end of the chapter. Unless specified otherwise, all dimensions used in the present chapter are presented in full-scale.

6.1 Data quality

The quality of the measurements depends on the aptitude of the experimental setup in providing representative data of scaled flows that are consistent with the prototype (full scale). The evaluation of the reliability of the measurement setup is an important measure of data quality assurance and associated uncertainties must be quantified. Adequate sampling times for each measurement point are required to ensure statistical representativeness of the mean data. This is provided by data convergence analyses of flow and turbulence parameters of the experimental setup used. Data uncertainties that result from repetitive measurements purposefully performed throughout the experimental campaign quantify data representativeness. Flow similarity between model and prototype is verified for the flat terrain reference scenario through Reynolds number (Re) independence tests. Pressure gradient analyses constitute further measures of quality, related to the modelled ABL flow and discussed in Appendix B.

6.1.1 Convergence

Wind tunnel flows are scaled spatially and temporally, the geometric scale also defining the time scale of the model flow. For identical wind speeds between model and full scale, geometric and time scales are identical. Accordingly, $1\,min$ at model scale ($\sim 1{:}\,1000$) corresponds to approximately $1000\,min$ ($\approx 16.7\,h$) at full-scale. Longer time series decrease statistical uncertainties and provide higher confidence intervals of fluctuating quantities. Thus, increasing measurement durations contributes to capturing low frequency fluctuations of the spectral distributions. The minimum point-specific sampling duration that provides adequate statistical representativeness of the mean flow parameters is determined through a temporal convergence test. This consists of measurements made over long intervals and at a comparatively high reference velocity ($U_0 \sim 7\ m/s$) at two streamwise locations ($X = 3500\ m$ and $4500\ m$) and three corresponding heights above the local surface ($Z = 30, 200$ and $450\ m$). For each convergence test, the time series is averaged independently over increasing time intervals. The scatter around the mean for all statistical moments and turbulence quantities is verified at every measurement point. A 5% ($\pm 2.5\%$) range around the mean of each parameter is defined as convergence criterion, consistent with typical studies of statistical convergence of time series. Figure 6-1 presents the convergence data for the mean dimensionless quantities of the UW measurement components at $Z = 30\ m$ above $X = 3000\ m$.

At this measurement position, the velocities are fastest to converge, the longitudinal component (U/U_0) at approximately 160 minutes (min) at full-scale (or 160 dimensionless time units) and the vertical component at roughly 357 min. The velocity fluctuations (standard deviations) take longer, $\approx 615\ min$ and $\approx 1075\ min$ for the streamwise (u_{std}) and vertical (w_{std}) components, respectively. The quantities that take the longest to converge are the dimensionless vertical fluxes ($u'w'/U_0^2$), convergence criterion reached after $\approx 2046\ min$, and the longitudinal integral length scales of turbulence (L_U^X) that exhibit the worst convergence properties at $\approx 2230\ min$. Using L_U^X as governing parameter in defining the sample period yields a measurement duration of at least $134\ s$ (model scale). For $u'w'/U_0^2$, the sampling time decreases to $\approx 122\ s$ but with a scatter of just over $\approx 8\%$ for L_U^X. The present convergence tests use a higher U_0 than that of the experimental campaigns. Assuming homogeneous seeding conditions, this corresponds to lower sampling rates than those observed for the lower U_0 of the experiments, thus measurements made with lower U_0 would be expected to converge quicker. A measurement period of $120\ s$, approximately $2000\ min$ ($\approx 33.3\ h$) at full-scale, is selected as temporally representative for all mean flow parameters. Similar results occur at the remaining measurement heights and above the second streamwise position, measurements made at higher altitudes converging quicker.

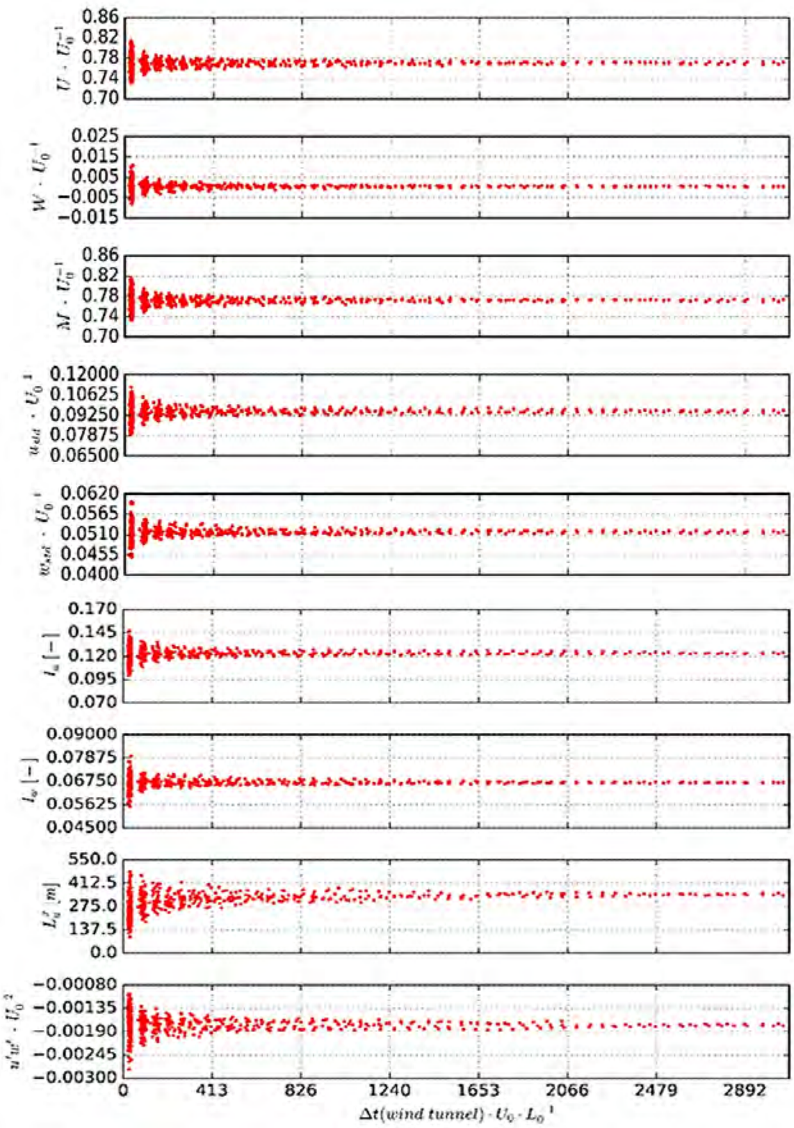

Figure 6-1. Temporal convergence data of the relevant mean flow parameters at $\mathrm{Z} = 30\ \mathrm{m}$ above $\mathrm{X} = 4500\ \mathrm{m}$ (full-scale). The abscissa is made of dimensionless time units (made dimensionless with reference velocity and length, the latter $1\ \mathrm{m}$) and the ordinate axes present each of the dimensionless flow parameters.

6.1.2 Repeatability

Measurement uncertainties arise from imperfections in the experimental setup, which lead to measurement errors. These can be systematic, meaning predictable and continuous throughout the measurement procedure (frequently known before the experiment), or random, corresponding to unpredictable spatial and temporal variations of the measured quantities. An appropriate statement of the uncertainty is an important measure of data quality and used to evaluate the reliability and comparability of the experimental results (with themselves or reference values), as well as the effectiveness of the experimental setups. A more detailed guide to general definitions regarding uncertainties in measurements is provided by JCGM 100:2008 (2010).

Several sources of uncertainty are perceptible within the experimental procedures of the present experiments. Flow measurement techniques are significant sources of uncertainty. Frequent pressure transducer calibrations minimise the systematic component of the uncertainty related to measurements with the Prandtl tube. Random effects, such as environmental conditions or different pressure ranges, ensure that exactitude (ideal zero uncertainty condition) cannot be achieved. Considerations regarding the calculation of the reference velocity (U_0) using Bernoulli's law include the propagation of uncertainties related to the measurements of each equation parameter. A similar logic applies to the LDV technique, with more sources of potential uncertainty due to its larger complexity. Furthermore, the traverse system used to position the LDV probe has an accuracy of $\approx 0.1\ mm$.

Accurate expressions of the overall measurement uncertainties require the quantification of all the individual uncertainties present in the measurement chain, which is very difficult to achieve. Repetitive measurements are used to provide an estimate of the statistical accuracy through the quantification of the statistical errors that arise due to uncertainties of the measurement setup. It is important to note that this provides a statistical measure of reproducibility or data uncertainty of the experimental setup. The efficiency of this approach depends on the quantity of repetition measurements, larger statistical representativeness obtained for larger amounts of data. In the case of 3D data measured separately for each of the 2D LDV probe alignments (UV/UW arrangements), two types of repetition are evaluated:

1. Repeatability in its pure sense – performing repetition measurements (UV <u>and</u> UW probe alignments) at the same location, followed by the quantification of the statistical distribution of the results as measure of the overall uncertainty.
2. Directional repeatability – using data separated by probe orientations (UV <u>or</u> UW settings) to provide a measure of reliability of the longitudinal components from each probe setting, measured twice at every measurement point (once for each of UV and UW).

Twenty repetition profile measurements are carried out above $X = 1000\ m$ at six heights (from 30 to $200\ m$). Of these, twelve are performed with UW settings and eight using the UV setup. For each measurement point, the absolute ranges of reproducibility of the dimensionless mean flow parameters are expressed as half of the difference between minimum and maximum observations (or bandwidth) of the repetition data. In regions of near-zero velocity, relative uncertainties may increase due to the small values of the corresponding divisors. This results in erroneously amplified quantifications of repetition uncertainty. Absolute quantifications of repeatability avoid the issue. The absolute uncertainties are divided into three height ranges (Δz_i). These are:

- $\Delta z_1 < 50\ m$,
- $50 \leq \Delta z_2 < 100\ m$,
- $\Delta z_3 \geq 100\ m$.

Absolute ranges of reproducibility of the dimensionless mean flow parameters, presented in Table 6-1 as function of the measurement height ranges, only apply to the measurements made for ABL flow characterisation. Further repetition analyses from measurements performed above the terrain features provide separate expressions of data uncertainty for ridges (Chapter 7) and valleys (Chapter 8). These express data uncertainties of the mean dimensionless longitudinal, lateral and vertical velocities (U, V and W, respectively), turbulence intensities (I_U, I_V and I_W), and velocity fluctuations (σ_U, σ_V and σ_W). Data uncertainties of the mean horizontal and vertical turbulent velocity fluxes ($u'v'$ and $u'w'$), and longitudinal integral length scales of turbulence (L_U^X) are also quantified. When applicable, data uncertainties of the flow parameters are made dimensionless with the reference velocity (U_0), those associated to length scales with the height of the ridges (H). The listed data uncertainties are represented by error bars in the subsequent plots. Data uncertainties associated to the longitudinal components (measured twice at each point) result from the combination of both sets of 2D data, whereas the lateral and vertical components result from a single measurement for each repetition.

Table 6-1. Data uncertainties of relevant mean dimensionless flow parameters of the modelled ABL flow above flat terrain as function of height ranges.

Height ranges (Δz_i)	Δz_1	Δz_2	Δz_3
U/U_0	± 0.0099	± 0.0084	± 0.0053
W/U_0	± 0.0018	± 0.0015	± 0.0013
σ_U/U_0	± 0.0021	± 0.0033	± 0.0018
σ_W/U_0	± 0.0008	± 0.0011	± 0.0007
I_U	± 0.0025	± 0.0042	± 0.0027
I_W	± 0.0011	± 0.0013	± 0.0010
$u'w'/U_0^2$	± 0.0002	± 0.0001	± 0.0001
L_U^X/H	± 0.3323	± 0.4330	± 0.5319

Larger absolute uncertainties of the mean velocities are generally found at the lowest height range (Δz_1). Inversely, uncertainties associated to the velocity fluctuations exhibit increases with height, the largest observed at the intermediate height range (Δz_2). The largest absolute deviations to the mean values, associated to the dimensionless integral length scales (L_U^X/H), increase with height. This is consistent with the theoretical predictions for which eddy sizes increase with height and, despite the lower turbulence intensity at these levels, lead to larger absolute variabilities of L_U^X at the higher altitudes.

Directional repeatability

The non-spherical shape of the LDV measurement volume (ellipsoid) implies that its different orientations (UV and UW modes) can lead to biased measurements of the respective longitudinal flow components. This arises from the perpendicular orientation between major axes of the 2D ellipses relative to the longitudinal inflow. The major axis of the longitudinal component of horizontal plane (UV) measurements is typically aligned with the larger gradients of flow velocity, perpendicular to the major axis of the vertical plane (UW) ellipse. This can cause increases of uncertainty of the longitudinal flow components, particularly when combining data from UV and UW measurements performed separately. Hence, the repeatability of the longitudinal velocities that result from the repetitive measurements with each of the probe orientations, designated as directional repeatability within the scope of this investigation, is a relevant measure of data quality. Directional repeatability is expressed as the cumulative relative frequency distribution of the differences between the longitudinal mean velocities (U) measured with the horizontal probe orientation (U_V) and the vertical setup (U_W). Figure 6-2a displays the (cumulative) relative frequency distribution of the difference between the longitudinal velocities measured with each LDV probe (measurement volume) orientation. Results indicate good agreement between UV and UW settings, all data contained within a $\approx 5\%$ bandwidth centred on zero.

6.1.3 Reynolds number independence

Flow similarity between model scale and prototype depends exclusively on the Reynolds number (Re). Larger scale turbulent eddies drive most flow phenomena in the ABL and their characteristics remain unaffected if the flow is fully turbulent (high enough Re) and the formation of laminar sublayers is minimised. Under these conditions, the modelled flow becomes independent of the inflow velocity and deemed independent for the larger scales of the flow (Townsend, 1976). Evaluation of Re independence consists of measuring time series of comparable statistical representativeness at a wide range of reference velocities (U_0). Accordingly, increases of U_0 are accompanied by decreases of the respective sampling durations. Sufficiently large U_0 provides virtually invariant longitudinal flow statistics, corresponding to Re independence of U_0 and the assurance that the flow is fully turbulent. Re independence is evaluated at one inflow position ($X = -560\ m$) and at two streamwise positions of the model section ($X = 3000$ and $4500\ m$), at two heights above the local surfaces ($Z = 50$ and $450\ m$). A bandwidth of 2% around the mean of the dimensionless longitudinal velocity fluctuations (σ_U/U_0) is defined as criterion for Re independence. Figure 6-2b presents the results obtained at the first model section position ($X = 3000\ m$). Shaded areas correspond to the 2% range around σ_U/U_0 and share the same colours based on measurement height. Re independent flow is achieved for all ranges of U_0 above the model section at the lower height ($Z = 50\ m$); whereas similarity is achieved starting at $U_0 \approx 3\ m/s$ at $Z = 450\ m$. Further downstream ($X = 4500\ m$), results are virtually identical. The homogeneously rough surface provides adequate levels of turbulence to maintain quasi-constant properties of flow similarity at a wide range of velocities. The roughened model surface minimises viscous sublayer effects and provides consistency with the approach flow conditions. In this context, a reference velocity of $U_0 \approx 5\ m/s$ is used for the present experiments. Considering the characteristic length scale equivalent to the ridge height ($L = 80\ mm$), Eq. (9) yields $Re \approx 28500$ ($\nu = 1.46 \times 10^{-5}$) for $U_0 = 5.2\ m/s$.

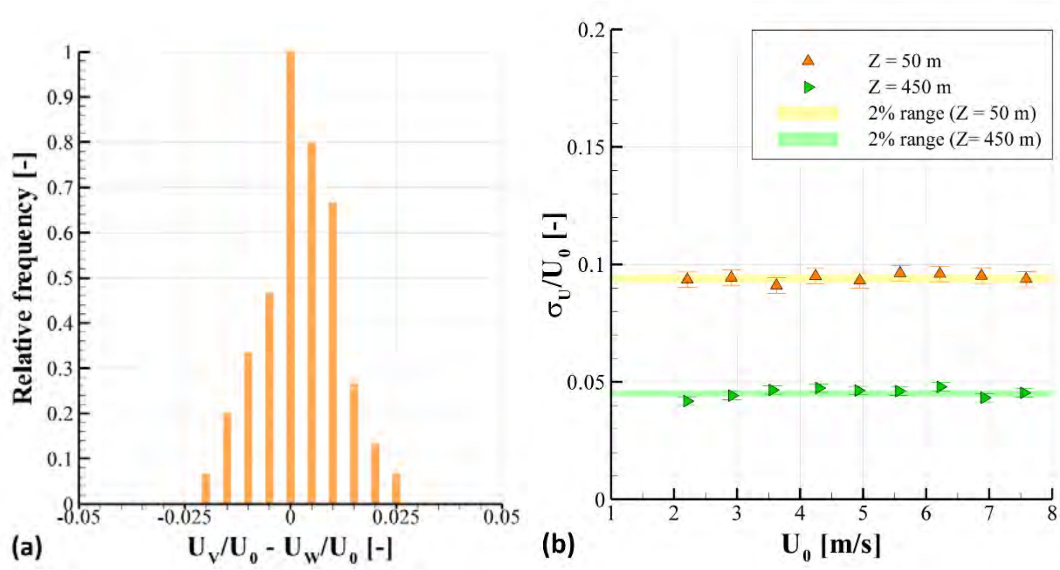

Figure 6-2. Relative frequency distribution of the differences between longitudinal velocity measurements made in the horizontal (UV) and vertical (UW) planes above flat terrain (a), and Reynolds number independence according to longitudinal velocity fluctuations at Z = 50 and 450 m above X = 3000 m (b). Shaded regions in (b) correspond to a ±2% bandwidth centred on the mean of the fluctuations of the reference velocities.

6.2 Characteristics of the modelled ABL flow

The modelled ABL flow is characterised through mean flow parameter analyses of the 2D (UW) measurements performed above the flat terrain. Results presented here are focused on two streamwise positions:

- Inflow position – located at $X = -560\ m$ (upstream from the model section).
- Model section position – located within the model section at $X = 3100\ m$ and corresponding to a position where the ridge models are later placed.

Data from the remaining streamwise positions is presented in Appendix C. Velocity profile measurements made above these positions verify the streamwise uniformity of the ABL flow characteristics and establish reference data for posterior comparisons with the complex terrain scenarios. Each of the profiles are sampled at the same heights above the local surface, most of which contained within the lowest $Z = 200\ m$ above the surface, where shear effects are more relevant for ABL flows. In the subsequent plots, data from the inflow position is represented in light blue colour and that of the model section position represented in red.

6.2.1 Velocity profiles

For neutrally stable ABL flows, the longitudinal velocity increases with height from zero (or height equivalent to the local aerodynamic roughness length, z_0) to the local maximum at levels above the atmospheric surface layer (ASL). Linear velocity profiles present a logarithmic shape (or linear trend when plotted semi-logarithmically). Figure 6.3a displays the vertical profiles of the mean dimensionless streamwise (U/U_0) and vertical (W/U_0) velocities at the two analyses positions. Separate abscissa axes correspond to each of the velocity components. Vertical profiles of U/U_0 at all streamwise measurement positions are displayed in Figure C1 (Appendix C). Linear profiles of U/U_0 exhibit larger velocities above the model section than the inflow position, the largest difference of about 10% being observed at the lowest height ($Z = 10\ m$). W/U_0 presents negative values that increase in magnitude with height, strong agreement being observed between the positions. This represents a weak descendent advection of momentum, which is overpowered by the larger horizontal momentum of the flow.

The observation of the semi-logarithmic profiles of U/U_0, displayed in Figure 6-3b, can enable an estimate of the ASL depth. Exponential-fit lines that correspond to the linear trend of measurements made in the lowest $Z = 75\ m$ above the surface, assist this observation. Data from the full range of measurement positions is presented in Figure C2 (Appendix C). Deviations from the respective trend-line above the inflow position are more pronounced than that of the model section. Data starts to diverge to non-linearity at heights greater than $Z = 100\ m$, indicating this to be the depth of the modelled ASL. Above the model section, deviations from linearity are more difficult to identify, data uncertainties intersecting the (red) trend-line for the full range of heights.

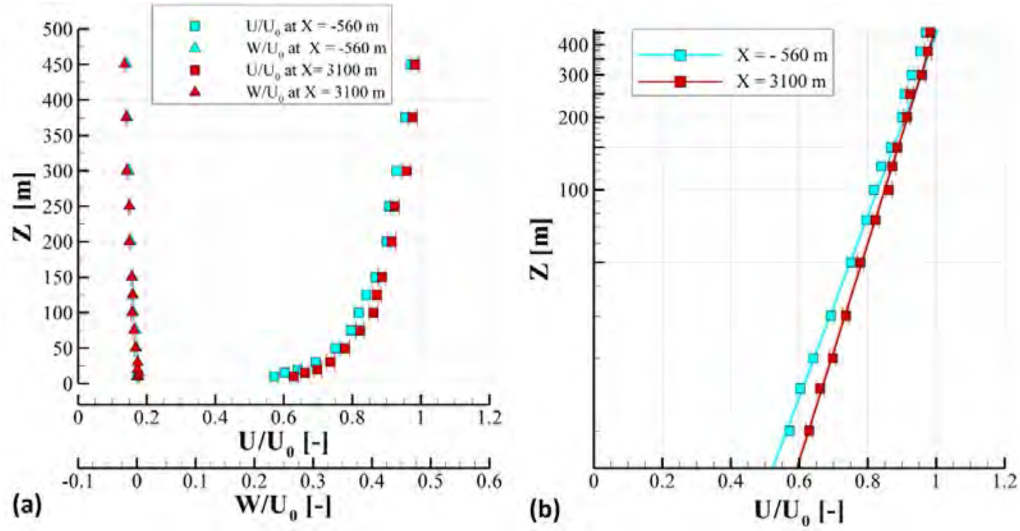

Figure 6-3. Linear vertical profiles of the mean dimensionless longitudinal and vertical velocities (a) and semi-logarithmic vertical profiles of the longitudinal velocity (b) of the modelled ABL flow above the two analyses positions ($\mathrm{X} = -560$ and 3100 m). Separate abscissa axes in (a) correspond to separate velocity components. Solid lines in (b) represent exponential fits of the data from the lowest $\mathrm{Z} = 75$ m above the surfaces.

Near-surface flows are dependent on the surface conditions, which are frequently quantified by the aerodynamic surface roughness length (z_0). z_0 cannot be measured but can be calculated (under equilibrium conditions) with the logarithmic formula for near-wall flows, Eq. (18). The formula is applicable to surface-related flow parameters (such as z_0 or the friction velocity, u_*) for heights contained within the ASL. Here, z_0 corresponds to the average of the lowest $Z = 75\ m$ of the profiles of U/U_0 (with $d_0 = 0$). ABL wind profiles are commonly characterised with the power law function that relates the local flow velocities with the heights above the ground, Eq. (17). This provides the value of the profile exponents (α) of the ABL flows. Here, mean values of α are calculated from data from $Z \leq 75\ m$. Estimates of the overall values of z_0 and α, averaged over all measurement positions, are presented below. Local values at each measurement position are listed in Table C4 (Appendix C).

$$z_0 = 0.025\ \pm 0.015\ [m]$$

$$\alpha = 0.14\ \pm 0.01$$

Values of both parameters are within the ranges of a moderately rough ABL flow, representing grass- or farmlands (VDI, 2000). This is supported by the observation of the semi-logarithmic relationship between z_0 and α, as proposed by Counihan (1975), presented in Figure 6-4a. The ratio of the modelled ABL flow is contained within the curves deduced from the reference data of Counihan (1972) and Davenport (1967) and within the 'moderately rough' category of z_0, corresponding to values between 10^{-2} and $10^{-1}\ m$ of the logarithmic abscissa. Thus, results are consistent with the findings related to U/U_0.

6.2.2 Vertical turbulent fluxes

Vertical turbulent velocity fluxes ($u'w'/U_0^2$) are expected to be near-constant with height within the fully developed ASL, assuming no occurrence of longitudinal pressure gradients (verified in Appendix B), and no thermal or Coriolis effects are present. At heights above the fully developed ASL, values of $u'w'/U_0^2$ tend towards zero until equalling zero at the height equivalent to the ABL depth (Snyder, 1981). In practice, $u'w'$ is assumed to be contained within a 10% range of the near-surface values, where longitudinal flow is horizontally homogeneous but far enough from the surface to avoid viscous sublayer effects. A $\pm 10\%$ range of the mean from the fluxes contained within the lowest $Z = 50\ m$ is applied as criterion for the present analysis and represented by the grey shaded area in Figure 6-4b, which displays the semi-logarithmic vertical profiles $u'w'/U_0^2$ above $X = 3100\ m$. Profiles of the inflow analysis position and the full range of longitudinal measurement positions are exhibited in Figure C3 (Appendix C). Heights at which data shifts outside the $\pm 10\%$ range of the mean are between $Z = 75$ and $150\ m$. Above, $u'w'/U_0^2$ clearly shifts towards zero. According to ABL flow theory, the depth of the ASL approximately corresponds to the lowest 10% of the ABL, which results in an ABL depth (δ) between $\delta = 750$ and $1500\ m$ (full-scale) for the modelled ABL flow. For easier interpretation, the ASL depth is assumed to be $\approx 100\ m$, resulting in $\delta \approx 1000\ m$ for the modelled ABL flow.

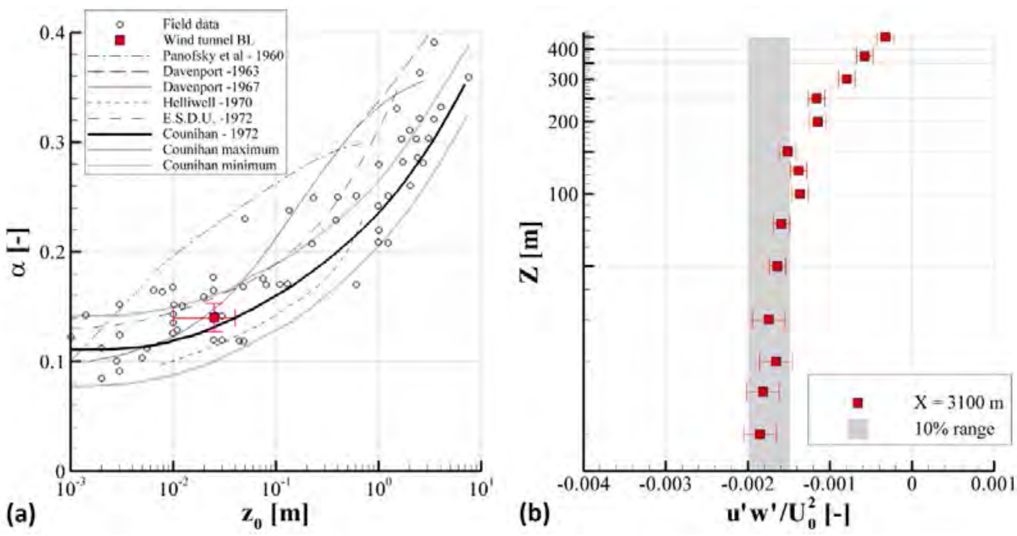

Figure 6-4. Semi-logarithmic relationship between aerodynamic surface roughness and profile exponent of the modelled ABL flow and reference values from the Literature (a), and semi-logarithmic vertical profile of the mean dimensionless turbulent velocity fluxes above $\mathbf{X = 3100\ m}$ (b). The shaded region in (b) delimits a $\pm\mathbf{10}\%$ range around the mean fluxes from the lowest $\mathbf{Z = 50\ m}$ above the surface.

6.2.3 Friction velocity, shear stress and roughness Reynolds number

Friction velocity (u_*) can be calculated using two approaches: through vertical fluxes, Eq. (19), or through the logarithmic formula for near-wall flows, Eq. (17). The second approach, which requires the quantification of z_0 and the fulfilment of assumptions regarding the ABL flow, is an indirect approach and only valid within the lowest $0.15 \times \delta$ (Snyder, 1981). Using both approaches, the modelled ABL flow yields $u_* \approx 0.2\, m/s$ for the ASL heights (assuming $\delta \approx 1000\, m$). Values of u_* above each of the longitudinal positions are in Table C5 in Appendix C, together with the resulting shear stresses (τ). Quantifications of z_0 and u_* enable the calculation of the roughness Reynolds number (Re_*), as expressed in Equation (26) where ν is the kinematic viscosity (VDI, 2000).

$$Re_* = \frac{u_* \times z_0}{\nu} \tag{26}$$

Assuming $\nu = 1.5 \times 10^{-5}\, m^2/s$ and constant, Eq. (26) yields an overall $Re_* \approx 0.4$. This fails to satisfy the condition stated in VDI (2000), $Re_* > 5$, which has no indication of the surface roughness condition. According to Bowen (2003), $Re_* \approx 0.4$ is within the expected values of the transition range of roughness ($0.2 < Re_* < 3$), indicating that a fully turbulent flow is likely but not guaranteed. The study conducted by Snyder & Castro (2002), dedicated to rough surface boundary layer flows, concludes that flow can be assumed fully turbulent for values of $Re_* \approx 1$. However, none of these studies are oriented to ABL flows over orography. Within this field, Meroney (1990) indicates that the relaxation of the condition of Eq. (26) to $Re_* \approx 0.4$ is permissible for ABL flows over complex terrain. Surface conditions of the present investigation are sufficiently rough to maintain a fully turbulent flow throughout the wind tunnel test section, as foreseen from the Reynolds number (Re) independence tests.

6.2.4 Turbulence intensity and velocity fluctuations

Figure 6-5 presents the vertical profiles of the mean longitudinal (I_U) and vertical (I_W) turbulence intensities above the analyses positions. Data from the full range of streamwise positions is in Figure C5 (Appendix C). Data from both components are fully contained within the moderately rough class and present larger intensities above the inflow position. I_U exhibits the largest differences between positions at heights below $Z = 150\, m$. The largest difference ($\approx 15\%$) is found at $Z = 10\, m$, data tending to converge at higher altitudes. Differences between the data obtained above each position also occur for I_W, a maximum $\approx 10\%$ difference observed at $Z = 10\, m$.

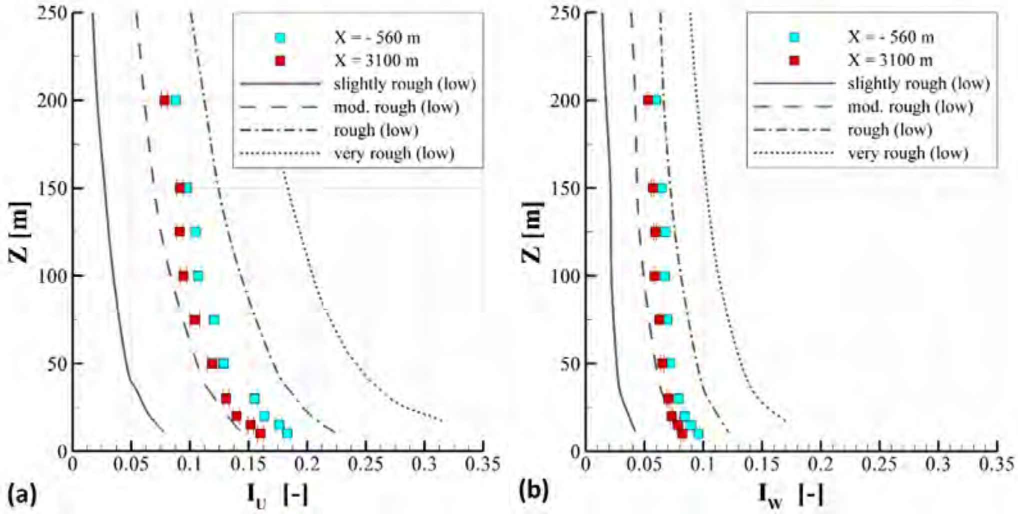

Figure 6-5. Vertical profiles of the longitudinal (a) and vertical (b) turbulence intensities of the modelled ABL flow above the two streamwise analyses positions ($\mathrm{X} = -560$ and 3100 m). Reference curves represent the lower bounds of roughness classes (VDI, 2000).

Turbulence of the individual velocity components can also be characterised by their velocity fluctuations (standard deviations), longitudinal (σ_U/U_0) and vertical (σ_W/U_0) components displayed in Figure 6-6. Differences between inflow and model sections are smaller than obtained for the turbulence intensities, $\approx 10\%$ the largest difference for σ_U/U_0 ($Z = 30\ m$). Profiles of σ_W/U_0 show closer agreement between positions. Fluctuation ratios (Table C6, Appendix C) exhibit the closest agreement with the theoretical predictions at the near-surface.

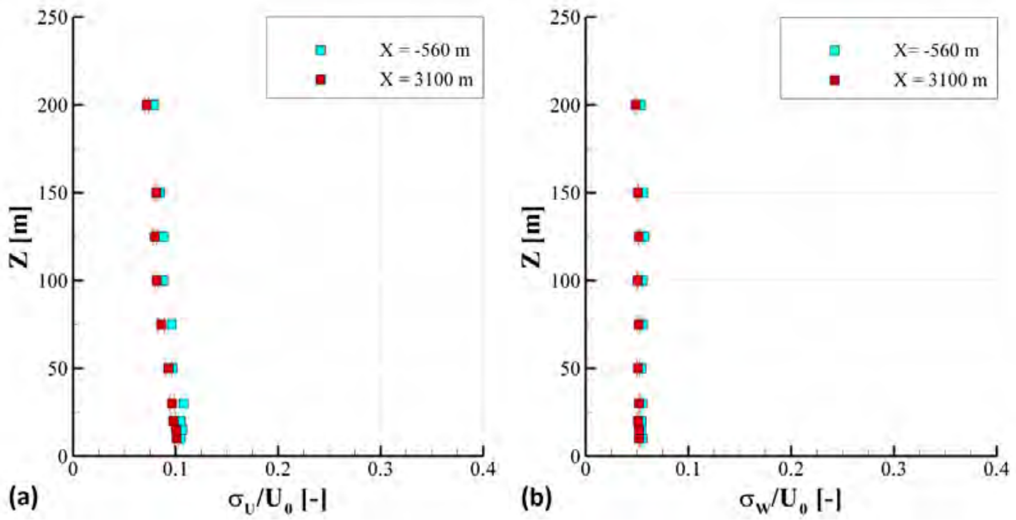

Figure 6-6. Vertical profiles of the longitudinal (a) and vertical (b) mean dimensionless turbulent velocity fluctuations of the modelled ABL flow above the two streamwise analyses positions ($\mathrm{X} = -560$ and 3100 m).

6.2.5 Longitudinal integral length scales of turbulence

Longitudinal integral length scales (L_U^X) provide an indication of the lengths of the most energetic eddies present in the longitudinal flow and are strongly dependent on the surface roughness at the lower altitudes of the ABL ($Z < 200$ to $300\ m$ according to Counihan, 1975). L_U^X typically decreases with increases of z_0, meaning that energy-intensive eddies are smaller above rougher terrains. Figure 6-7a displays the logarithmic vertical profiles of the dimensionless mean longitudinal integral length scales (L_U^X/H), made dimensionless via the height of the ridges (H), as function of the dimensionless height (Z/H).

The smallest energy-intensive eddies ($L_U^X \approx 80\ m$) are expectedly found at $Z/H \approx 0.13$ (or $Z = 10\ m$), where the best agreement with the reference data from Counihan (1975) is found. Values of the modelled surface roughness ($z_0 \approx 0.025\ m$) and those indicated by the reference lines in Fig. 6-7a exhibit the closest agreement at heights lower than $Z/H = 0.38$ ($Z = 30\ m$). At heights above, values of L_U^X tend to approximate those of a slightly rough ABL flow with $z_0 < 0.01\ m$. Similar results are obtained for the profiles above the remaining longitudinal measurement positions, displayed in Figure C7 (Appendix C). Based on the findings of Gillmeier (2014) and Erdmann (2017), this outcome corresponds to the effect of the employed geometric scale. The present results constitute a significant improvement to those obtained by Erdmann (2017), using a geometric scale of 1:1750, already an improvement over that of Gillmeier (2014) for a 1:3650 scale. Of all analysed mean flow parameters, L_U^X is typically the hardest to match relative to observations in nature (Snyder, 1981).

6.2.6 Lateral homogeneity

An additional measure of quality assurance of the modelled ABL flow is the verification of lateral symmetry of the flow. Lateral homogeneity tests are conducted at the two longitudinal analyses positions at every $\Delta Y = 200\ m$ span-wise position across the central $Y = 2000\ m$ of the wind tunnel cross-section (or up to $\pm 1000\ m$ from $Y = 0$). Figure 6-7b displays the resulting lateral profiles of the dimensionless longitudinal velocity (U/U_0) at $Z = 50\ m$. Differences between data exceed the range of uncertainty at five of the lateral positions: $Y = -400$, -200, 400, 600, and $800\ m$. The largest absolute differences with regard to the mean U/U_0 occur at $Y = 400\ m$ for the inflow position and at $Y = 600\ m$ above the model section with differences of $\approx 5\%$. Similar findings result from the lateral profiles of the mean longitudinal fluctuations (σ_U/U_0) at the same locations, which are displayed in Figure C8 (Appendix C).

Gillmeier (2014) observed a similar tendency for the inflow modelled without vortex generation (spires or trip barriers) and roughness elements in the same wind tunnel, observing a $\approx 5\%$ maximum shift with regard to the mean U/U_0. Erdmann (2017) made similar findings, albeit to a lesser extent, for the longitudinal components measured in the vertical plane (UW), thus without the added uncertainty that results from the LDV probe reorientation for horizontal plane (UV) measurements. Based on these findings, it can be speculated that the observed lateral inhomogeneities are an unavoidable consequence of the asymmetric wind tunnel hall. Thus, improvement of lateral flow symmetry could be achieved through the instalment of additional flow-straightening screens in the inlet region of the wind tunnel.

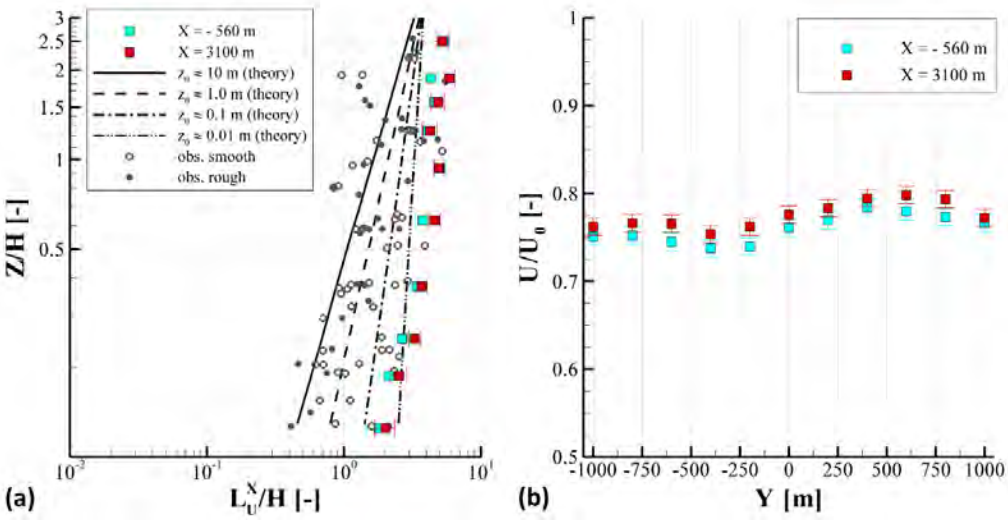

Figure 6-7. Logarithmic vertical profiles of the mean dimensionless longitudinal integral length scales of the modelled ABL flow with reference data from Counihan (1975) represented in black (a), and lateral profiles of the mean dimensionless longitudinal velocity of the modelled ABL flow at $\mathbf{Z = 50\ m}$ and at every $\mathbf{\Delta Y = 200\ m}$ until $\mathbf{Y = \pm 1000\ m}$ (b) above the two streamwise analyses positions ($\mathbf{X = -560}$ and $\mathbf{3100\ m}$).

6.2.7 Turbulence spectra

Distributions of the dimensionless longitudinal ($f \times S_{UU}/\sigma_U^2$) and vertical ($f \times S_{WW}/\sigma_U^2$) spectral energy at $Z = 30\ m$ are exhibited in Figure 6-8. Reference curves that originate from the data of the experimental investigations performed by Kaimal et al. (1972) and Simiu & Scanlan (1986) are included in the plots, the latter exclusively for $f \times S_{UU}/\sigma_U^2$. Both components of the spectra match well with the reference data, particularly within the inertial subrange where a slope of $\approx -2/3$ is verified. This is consistent with Kolmogorov's hypothesis for this frequency range, from which a $-5/3$ slope results from the product of the frequency with the energy spectra. Of the two spectral components, $f \times S_{UU}/\sigma_U^2$ exhibits the closest agreement with the Kolmogorov theory in the inertial subranges. At the smaller frequencies of the inertial subrange, $f \times S_{WW}/\sigma_U^2$ presents a steeper slope before tending to converge with the reference data at the larger frequencies. The close general agreement observed between the spectral distributions of the approach flow and model section locations indicates consistent turbulent energy distributions throughout the longitudinal extent of the flat terrain study domain.

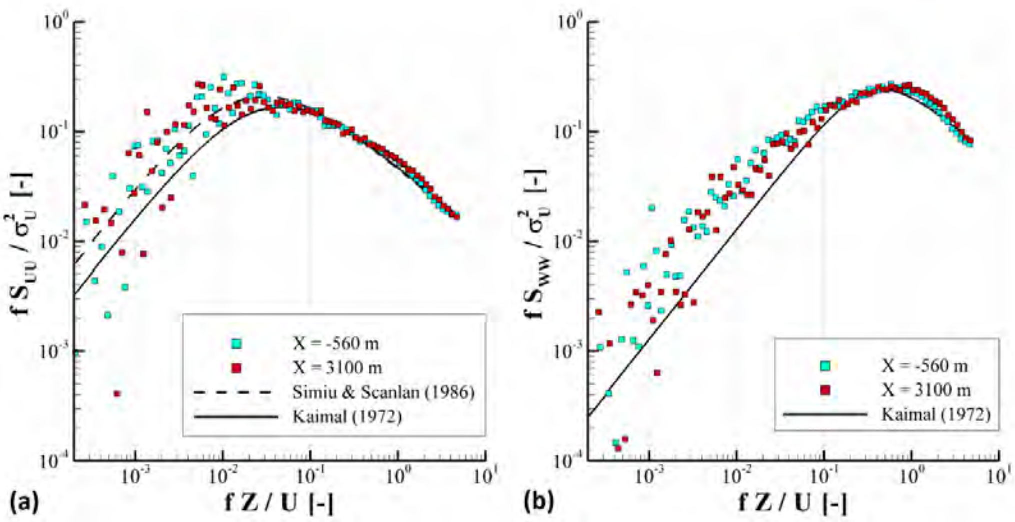

Figure 6-8. Spectral distributions of longitudinal (a) and vertical (b) turbulent energy at $\mathrm{Z} = 30\ \mathrm{m}$ above the two streamwise analyses positions ($\mathrm{X} = -560$ and $3100\ \mathrm{m}$). Black reference curves represent the data from the experiments of Kaimal (1972) and Simiu & Scanlan (1986).

6.3 Summary

The experimental flow setup, which is common to ridge and valley measurement campaigns and described in Chapter 5, results in a modelled ASL flow with a depth of $\approx 100\ m$. Assuming the 10% correspondence with regard to the ABL, this implies a theoretical ABL depth of $\delta \approx 1000\ m$. As ascertained from the mean velocity profiles, the modelled ABL flow is consistent throughout all of the longitudinal measurement positions of the wind tunnel. For all mean flow parameters, the vertical profiles display strong agreement between inflow and model section positions. Furthermore, the static pressure analysis (Appendix B) reveals that no significant longitudinal pressure gradients are observed. In terms of turbulence characteristics, the modelled ABL flow is verified to be fully turbulent (Reynolds number independent) and is categorised as moderately rough (corresponding to grass- or farmlands). Mean turbulence parameters exhibit general consistency with theoretical data, the integral length scales presenting the largest differences (to the data from Counihan, 1975). Longitudinal and vertical spectra display close agreement with the reference data, particularly within the corresponding inertial subranges.

7 FLOW OVER RIDGES

7.1 Introduction

Measurement positions and study subdomains of the ridge geometries (presented in Chapter 5) are defined and data quality assessments for the mean flows over ridges are made in the first part of the present chapter. The second subchapter presents the results for four main study subdomains related to each ridge geometry. It is important to note that this subchapter is focused on presenting the flow results, less emphasis being given to analyses and discussions of the observed phenomena. Relevant mean dimensionless flow parameters are presented using a systematic approach for three streamwise locations of each subdomain. In the perspective of numerical model validation, more flow field data from more measurement locations is available. An extensive subdomain-specific discussion of the flow over the ridges is reserved for the final subchapter.

7.2 Measurement positions

7.2.1 Study regions

The selection of the measurement positions is oriented to providing maximal information of the flow field. A more complete depiction of the flow addresses relevant topics associated to the main research questions and the additional measurement positions provide more data for numerical model validation. Region-specific analyses, to address the aims of the present investigation, drive the selection to separate each ridge domain into four subdomains. Following the longitudinal direction of the flow, the subdomains are:

- Upwind (abbreviated *UpW*) – flat terrain area upstream from the foot of the windward slope of the ridges.
- Windward slope (*WW*) – windward slope of the ridges (from the foot up until the crest).
- Leeside slope (*LW*) – leeside slope of the ridges (from the crest to the foot of the ridge).
- Downwind (*DW*) – flat terrain area downstream from the foot of the leeside slope.

Three streamwise positions establish the boundaries between each of the subdomains:

- Foot of the uphill slope (termed *B1*) – separating the *UpW* and *WW* subdomains.
- Crest (*Cr*) – dividing the two slopes of the ridges (*WW* and *LW);*
- Foot of the downhill slope (*B2*) – between *LW* and *DW*.

Figure 7-1 presents a schematic of the subdomains and boundaries of a generic ridge given the aforementioned nomenclature. Measurement positions are expressible in absolute or relative (dimensionless) coordinate systems. For the present investigation, focused on idealised terrain with re-scalable flow, the relative coordinate system is particularly beneficial for direct comparisons between corresponding positions of different ridge domains. Thus, all length and height positions use relative coordinates. For the ridge subdomains (*WW* and *LW*), the vertical (Z) and longitudinal (X) coordinates are non-dimensionalised according to the height (H) and the half-length (L_r) of the ridges, respectively. For the flat terrain subdomains (*UpW* and *DW*), both Z and X are non-dimensionalised with H. In line with the methods used in Literature, all absolute vertical measurement coordinates (z_i) correspond to heights above local terrain (vertical axis oriented towards the centre of the Earth).

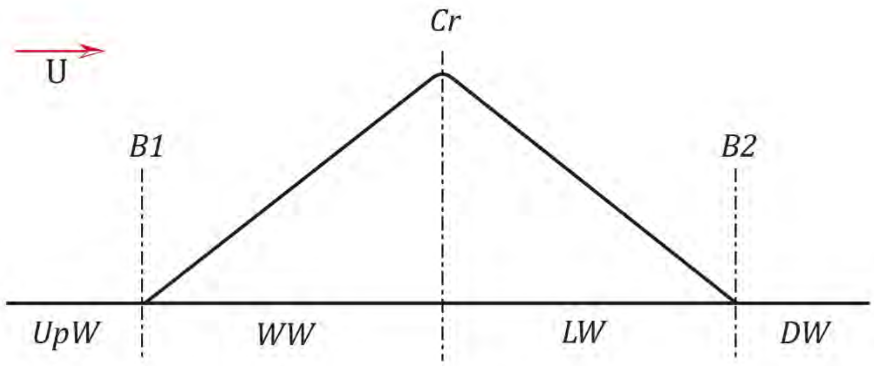

Figure 7-1. Study subdomains of a generic ridge. From left to right: Upwind (*UpW*), Windward slope (*WW*), Leeside slope (*LW*), and Downwind (*DW*). Subdomains are separated by the foot of the windward slope (*B1*), the crest (*Cr*), and the foot of the leeside slope (*B2*). Flow develops from left to right (as indicated by *U*).

7.2.2 Lateral and vertical coordinates

The selection of measurement heights aims to provide a larger density of near-surface locations but is restricted by the LDV probe interaction with model surfaces for vertical plane (UW) measurements. Seven heights above local terrain, ranging from $z_{AT} = 30$ to $200\ m$, are selected for the analyses and listed in Table 7-1. With the exception of lateral homogeneity tests, measurements are made in the lateral centreline aligned with the mean flow ($Y = 0$).

Table 7-1. Vertical positions of the ridge measurements in absolute and dimensionless coordinates. Coordinates are terrain-following (heights above local surfaces) and made dimensionless with ridge height ($\mathrm{H} = 80\ \mathrm{m}$).

dimensionless heights z_{AT}/H [−]	absolute heights z_{AT} [m]
0.38	30
0.63	50
0.94	75
1.25	100
1.56	125
1.88	150
2.5	200

7.2.3 Longitudinal coordinates

1.1.1.1 Upwind and downwind subdomains

The Upwind (*UpW*) region contemplates eight longitudinal positions starting with *B1* ($X = 0$ for this subdomain) and following the negative longitudinal direction (upstream). These positions are given the prefix '*UpW'* and the first five positions (*UpW1* to *UpW5*) are equidistant, with amplitude of $\Delta X \approx 0.8H$. The furthermost upwind position from *B1* is *UpW7*, distanced $X \approx -8H$ from *B1*. The downwind (*DW*) subdomain is symmetric to *UpW* and comprises the matching eight streamwise positions from *B2* onwards in the flow direction. Table 7-2 presents the positions of the *UpW* subdomain, those of the *DW* subdomain are presented in Table D1 (Appendix D).

Table 7-2. Dimensionless and absolute longitudinal coordinates of the measurement positions of the Upwind (*UpW*) subdomain. Coordinates are relative to the foot of the windward slope of the ridges (*B1*).

position	B1	UpW1	UpW2	UpW3	UpW4	UpW5	UpW6	UpW7
dimensionless coordinates $-(x/H)$ [−]	0	0.78	1.56	2.34	3.12	3.90	5.46	8.08
absolute coordinates $-x$ [m]	0	62.5	125	187.5	250	312.5	437	647

Flow observations with laser light sheet reveal larger flow effects downwind from the ridges than upwind. In order to capture these effects, an extended downwind subdomain comprises seven additional streamwise positions further downstream from the downwind subdomain (*DW*). Given the prefix '*DDW*', these positions are listed in Table 7-3. Experimental time constraints limit these positions to 2D measurements only (UW).

Table 7-3. Dimensionless and absolute longitudinal coordinates of the measurement positions of the Extended downwind (*DDW*) subdomain. Coordinates are relative to the foot of the leeside slope of the ridges (*B2*).

position	DDW1	DDW2	DDW3	DDW4	DDW5	DDW6	DDW7
dimensionless coordinates $\boldsymbol{x/H}$ $[-]$	10.7	13.3	15.9	18.5	21.1	23.7	26.3
absolute coordinates $\boldsymbol{x}$ $[\boldsymbol{m}]$	856	1064	1272	1480	1688	1896	2104

1.1.1.2 Windward and leeside slope subdomains

The windward slope (WW) subdomain includes nine longitudinal measurement positions (prefix 'WW') that start near the crest (*Cr*) and follow the negative longitudinal direction towards the foot of the ridge (*B1*), of coordinate $X = -L_R$, as listed in Table 7-4. These positions are non-dimensionalised with the ridge slope lengths (L_R), thus vary between 0 and 1. This approach has the purpose of providing direct comparability between the same relative positions of different ridges. For example, the relative mid-slope position of all ridges is $x/L_R = -0.52$, whereas the absolute coordinate changes between ridges. Positions of the leeside slope (*LW*) subdomain are symmetric to *WW*, following the flow direction downhill from *Cr* towards *B2*. The nine positions have the prefix '*LW*' and are presented in Table D2 (Appendix D). Due to the expected flow complexity in this region, *LW4* and *LW8* positions are singled out for data quality analyses.

Table 7-4. Dimensionless and absolute longitudinal coordinates of the measurement positions of the windward slope (*WW*) subdomain. Coordinates are relative to the crest of the ridges (*Cr*).

position		WW1	WW2	WW3	WW4	WW5	WW6	WW7	WW8	WW9
dimensionless coordinates $-(\boldsymbol{x/L_R})$ $[-]$		0.10	0.21	0.31	0.42	0.52	0.62	0.74	0.85	0.90
absolute coordinates $-\boldsymbol{x}$ $[\boldsymbol{m}]$	*Type I-75*	2.50	5.25	7.75	10.5	13.0	15.5	18.5	21.3	22.5
	Type I-10	45.0	94.5	139.5	189.0	234.0	279.0	333.0	382.5	405.0
	Type II	14.0	29.4	43.4	58.8	72.8	86.8	103.6	119.0	126.0

7.3 Data quality

7.3.1 Repeatability

With larger flow complexities expected above the ridges, data uncertainties associated to the undisturbed flow (Chapter 6) are expected to misrepresent the reproducibility of the measurement data obtained near the ridges. Thus, expressions of data uncertainty that capture additional uncertainties that may arise from the ridge measurements is warranted. The most accurate approach would consist of making several repetitions for every measurement point defined earlier, which is unrealistic. Limited quantities of repetitive measurements, performed above the crests (*Cr*) and two leeside slope positions (*LW4* and *LW8*), provide local measures of data reproducibility for the terrain positions expected to produce larger flow instabilities. The application of the data uncertainties from each streamwise position to neighbouring flow regions constitutes a balance between achievable and accurate expressions of reproducibility. At an average of just over four repetition profiles per streamwise position (total of 49 repetition profiles), with unevenly distributed amounts between each, these rely on a small repetition database. Nonetheless, the approach provides a more realistic expression of data uncertainties when compared to the ABL flow repetition data.

The resulting absolute data uncertainties are listed in Tables D3 to D5 (in Appendix D), classified by longitudinal position (*Cr*, *LW4* and *LW8*), ridge geometry, and by height range. For flow parameters or measurement heights with less than three repetitive measurement profiles, applied values of data uncertainty originate from the flat terrain repetition data. In such instances the affected values are shaded in grey in Tables D3 to D5. Expressions of the data uncertainty for each streamwise measurement position above the ridges originate from the nearest longitudinal position, for which repetitions are performed. Table 7-5 provides a summary of these topics, which includes a guide to the measurement positions and the corresponding sources of the data uncertainties for each in Appendix C.

Table 7-5. Positional assignments of the data uncertainties that originate from the repetitions above the ridge positions and presented in Appendix D.

Repetition position	Data uncertainties	Measurement region/positions
Cr	Table C3	*UpW*, *WW* and *Cr*
LW4	Table C4	*LW1* to *LW6*
LW8	Table C5	*LW7* to *LW9*, *DW*

In the context of directional repeatability, as defined in Chapter 6, Figure 7-2a presents the cumulative relative frequency distribution of the difference between the mean longitudinal velocities measured in vertical (UW) and horizontal (UV) planes. For comparison, the results of the directional repeatability obtained above flat terrain (Fig. 6-2a) are included. Due to the more complex nature of the flows above the ridges, differences between longitudinal components cover a wider range than those observed in Chapter 6. A fraction of these values falls outside the $\approx 10\%$ bandwidth centred on zero (marked in lighter shades of blue in Fig. 7-2a).

7.3.2 Reynolds number independence

Reynolds number (Re) independence is evaluated above four streamwise positions: *Cr*, LW4, *LW8* and a position contained within the downwind (*DW*) subdomain. The present assessment follows the same methodology as described in Chapter 6. Measurements are performed at two heights above the *Cr* and *DW* positions of each ridge ($z_{AT}/H = 0.63$ and 2.5) and three heights above *LW4* and *LW8* ($z_{AT}/H = 0.38$, 0.63 and 2.5). Results obtained above *LW8* of the *Type I-75* ridge are presented in Figure 7-2b. At all sampling heights, Re independence is verified starting at $U_o \approx 3.5\ m/s$. Similar outcomes are obtained above *Cr* and *DW*.

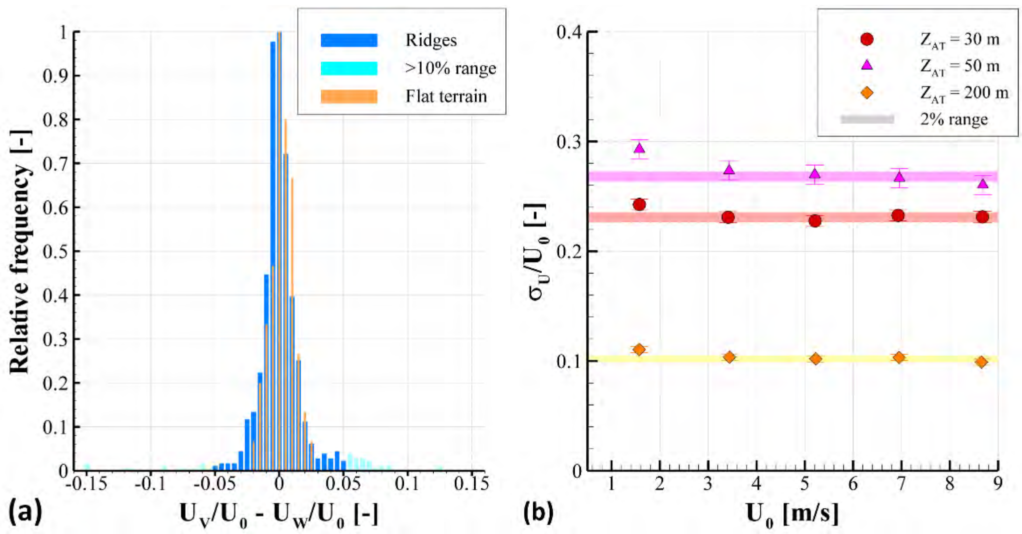

Figure 7-2. Relative frequency distribution of the differences between longitudinal velocity measurements made in the horizontal (UV) and vertical (UW) planes above the ridges (a), and Reynolds number independence data according to longitudinal velocity fluctuations at $z/H = 0.38$, 0.63 and 5.63 above *LW8* of the *Type I-75* ridge (b). Shaded regions in (b) correspond to a $\pm 2\%$ bandwidth centred on the mean fluctuations.

7.3.3 Lateral homogeneity

Lateral homogeneity evaluations result from measurements made at $z_{AT} = 50$ and $200\ m$ above *Cr, LW4* and *LW8* of each ridge, spanning from $Y = -600\ m$ to $600\ m$ (with increments of $\Delta Y = 200\ m$). Lateral profiles of the mean dimensionless longitudinal velocity (U/U_0) and velocity fluctuations (σ_U/U_0) of all ridge geometries at $z_{AT} = 50\ m$ are presented in Figure 7-3. Data from the flat terrain case is represented by the grey-coloured gradient symbols with a linear-fit line. Above *Cr*, both parameters exhibit similar laterally homogeneous trends to the flat terrain. Further downwind, the approach flow inhomogeneities are amplified by the terrain structures. This is translated by increases of variability between lateral positions observed for U/U_0, the largest above *LW4* of the *Type II* ridge. Above *LW8*, the largest absolute differences of U/U_0 compared to the approach flow are also those of the *Type II* ridge and the mean flow is reversed ($U/U_0 < 0$) above all lateral positions of *Type I-10* and *Type II* ridges. The largest difference between lateral profiles of σ_U/U_0 and flat terrain is found above *LW4* of the *Type I-75* ridge, with σ_U/U_0 approximately three times larger than that of the approach flow. At the same height above the crests of all ridge geometries (Figure D1, Appendix D), effects on the lateral homogeneity of both aforementioned parameters are expectedly less evident.

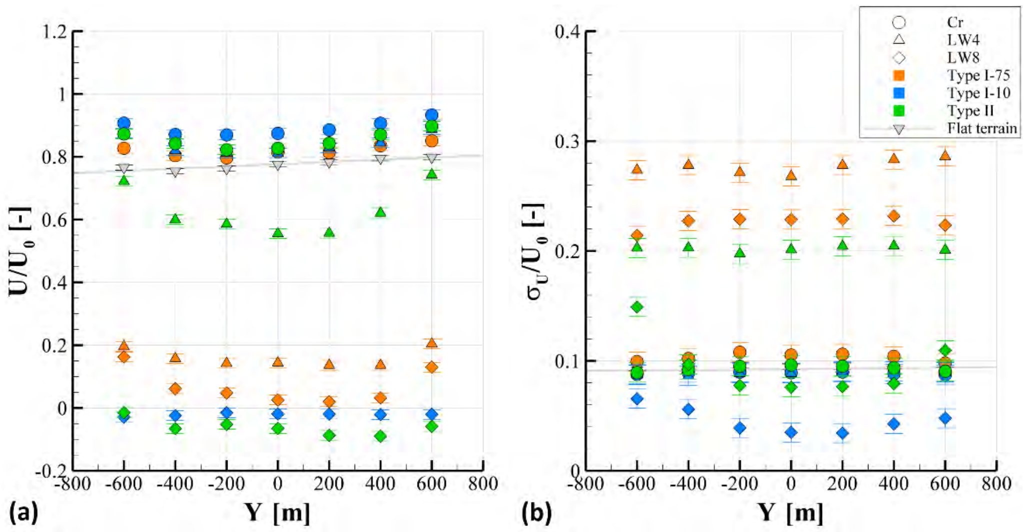

Figure 7-3. Lateral profiles of the mean dimensionless longitudinal velocities (a) and velocity fluctuations (b) at $z/H = 0.63$ above the crests (*Cr*) and leeside slope positions (*LW4* and *LW8*) of the ridges. Ridge data uses the colour scheme defined in Table 5-1 and undisturbed flow data is represented in grey.

7.4 Mean flow above ridges

For each flow subdomain, three streamwise positions are specified for analyses of the vertical profiles of the mean flow and two heights selected to ascertain the same parameters above all positions in the longitudinal direction: $z_{AT} = 50$ and $100\ m$ ($z_{AT}/H = 0.63$ and 1.25 , respectively). With the exception of unreachable measurement heights with the LDV probe for UW plane measurements, the longitudinal flow data corresponds to that obtained from combinations of 2D measurements made independently with UV and UW orientations. When no UW data is available, results originate from measurements made with the UV probe orientation. This has negligible influence on the representativeness or the comparability of the associated data, as ascertained from the directional repeatability analysis. This is particularly valid when no coordinate system rotations due to tilting are applied and the fixed coordinate system shared for both UV and UW measurements. All data presented here follows the nomenclature and colour schemes assigned in Table 5-1 (Chapter 5). Measurement heights (above local terrain) correspond to those listed in Table 7-1 and the longitudinal positions are defined in Tables 7-2 to 7-4. In the context of flows over orography, where regions of near-zero local mean velocity are expected, values of turbulence intensity can be amplified due to extremely small values of the divisors of Eq. (16), thus resulting in misleading quantifications of the local turbulence. Therefore, expressions of turbulence intensity are avoided here. In this regard, mean turbulent fluctuations provide more reliable quantifications. Flows above the crests are analysed together with the corresponding data from the valley measurements in Chapter 8.

7.4.1 Upwind subdomain

Analyses of the vertical profiles are centred on three longitudinal measurement positions: *UpW7*, *UpW3*, and *B1* (Table 7-2). Due to probe positioning constraints at the near-surface of the ridges, no vertical plane (UW) measurements are performed at $z_{AT}/H < 0.94$ downwind from *UpW4* and *UpW6* for *Type II* and *Type I-75* ridge domains, respectively.

Figure 7-4 displays the vertical and longitudinal profiles of the mean dimensionless longitudinal velocity (U/U_0). Deviations from the approach flow first become noticeable at $z_{AT}/H = 0.63$ above $x/H \approx -5.5$, where U/U_0 is outside the data uncertainty ranges for *Type I-10* and *Type I-75* ridges. These differences increase with proximity to the ridges, indicating a windward slope effect on the upwind flow that is maximum at the foot of the ridges ($x/H = 0$). Here, U/U_0 of the *Type I-75* ridge is approximately three times smaller than that of the *Type I-10* ridge. Plots of the mean dimensionless lateral (V/U_0) and vertical (W/U_0) velocities are in Figure D2 (Appendix D). V/U_0 is less affected by the ridges than the other components throughout the upwind subdomain. W/U_0 develops inversely to U/U_0, values increasing with proximity to the ridges and larger increases observed for steeper windward ridge slopes.

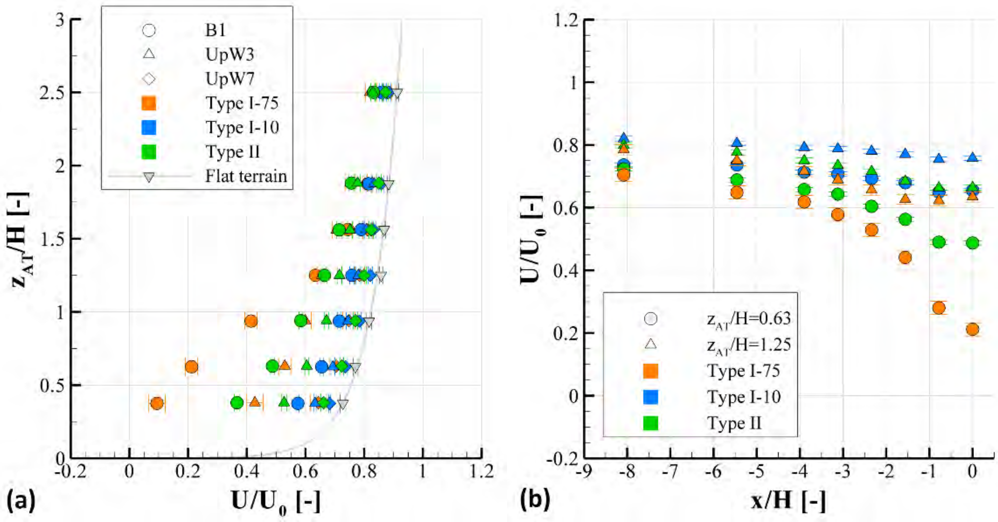

Figure 7-4. Vertical (a) and longitudinal (b) profiles of the mean dimensionless longitudinal velocity above the Upwind subdomain (*UpW*) of the ridges.

Figure 7-5 presents vertical and longitudinal profiles of the dimensionless mean longitudinal, lateral, and vertical velocity fluctuations. All components display increases relative to the undisturbed flow at near-surface and near-ridge locations, which are larger for increasing inclinations of the windward slopes. Hence, the maximum fluctuations are generally observed for the *Type I-75* ridge. Longitudinal fluctuations (σ_U/U_0) are affected further upwind than lateral and vertical components, specifically at $z_{AT}/H = 0.63$ above $x/H \approx -5.5$ where ridge data is first outside the confidence interval of the flat terrain. The maximum increase of σ_U/U_0 compared to the flat terrain data ($\approx 55\%$) is observed at $z_{AT}/H = 0.63$ above $x/H \approx -0.8$ of *Type I-75*. Maximum lateral fluctuations (σ_V/U_0) are observed for the same ridge geometry, the largest ($z_{AT}/H = 0.38$ above $x/H = 0$) over two times larger than the flat terrain. σ_V/U_0 is $\approx 60\%$ larger than the longitudinal component at the same location. From the data obtained at the permissible measurement heights, the vertical fluctuations (σ_W/U_0) are affected by the terrain closer to the ridges when compared to the previous components, namely at $z_{AT}/H = 0.94$ above $x/H \approx -2.3$ from the *Type I-75* ridge.

Figure 7-6 exhibits the average ratios of the mean longitudinal to lateral (σ_U: σ_V) and longitudinal to vertical (σ_U: σ_W) velocity fluctuations of the lowest $Z = 100\ m$ above the surface of the upwind subdomain. These are presented as function of the dimensionless streamwise length (x/H) of the upwind subdomain. Hollow symbols of the same colour as the corresponding ridge in Fig. 7-6b, represent positions lacking UW plane measurements at near-surface heights. Dashed (σ_U: σ_V) and dash-dotted (σ_U: σ_W) dark grey lines correspond to the reference data (as documented in VDI, 2000). Both ratios expectedly present the closest values to the reference relationship, $\sigma_U : \sigma_V : \sigma_W = 1 : 0.75 : 0.5$ (VDI, 2000), at the furthermost upwind positions from the ridges. With the exception of the *Type I-75* ridge, both ratios remain virtually unaffected by the proximity to the ridge location. This indicates that the longitudinal component of turbulence is dominant throughout the region upwind from *Type I-10* and *Type II* ridge geometries. Above the foot of the steepest windward slope (*Type I-75*), σ_V overpowers σ_U by $\approx 20\%$, corresponding to the largest increase of the upwind subdomain compared with the reference values.

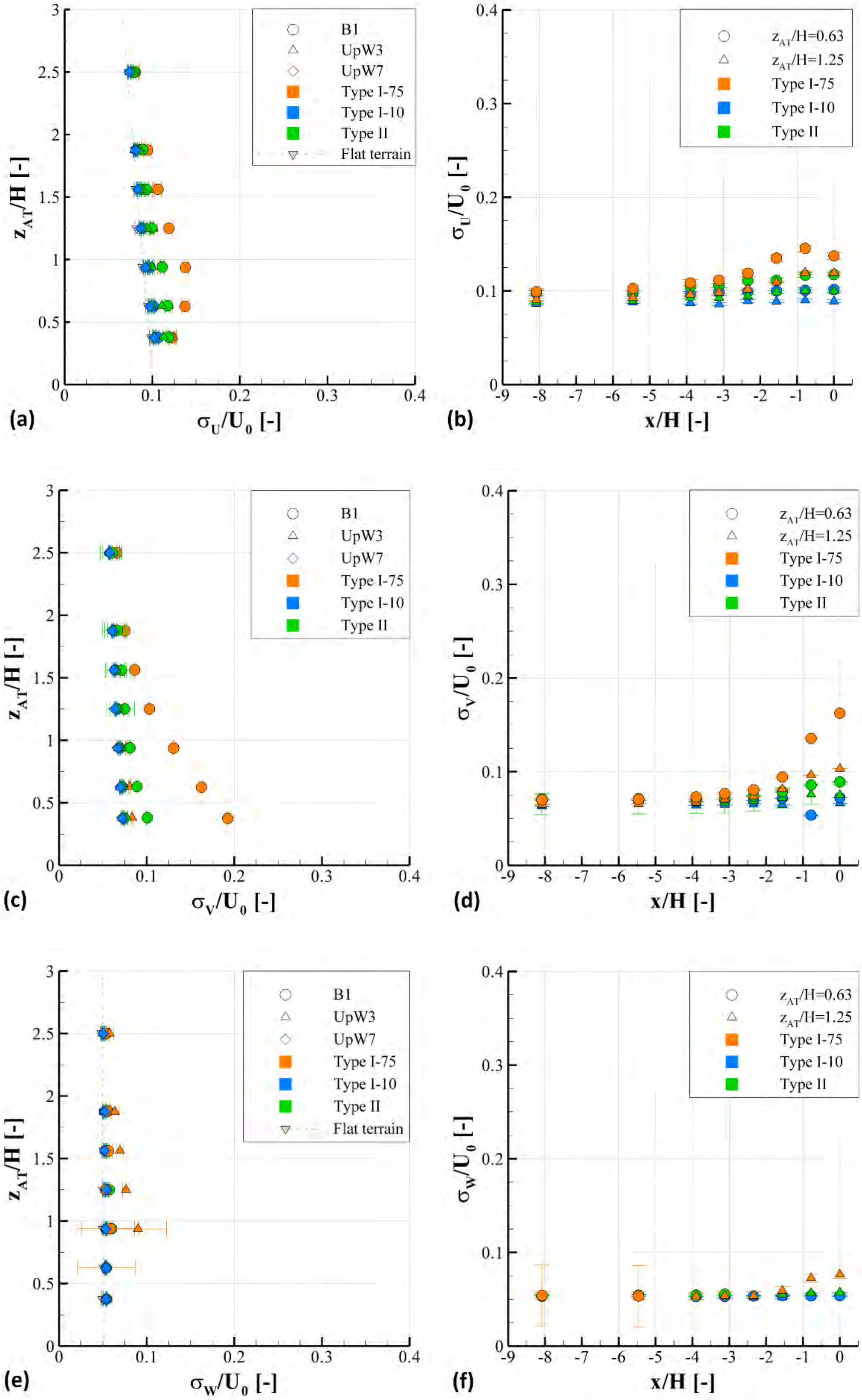

Figure 7-5. Vertical (a, c, e) and longitudinal (b, d, f) profiles of the mean dimensionless longitudinal (a, b), lateral (c, d), and vertical (e, f) velocity fluctuations above the Upwind subdomain (*UpW*).

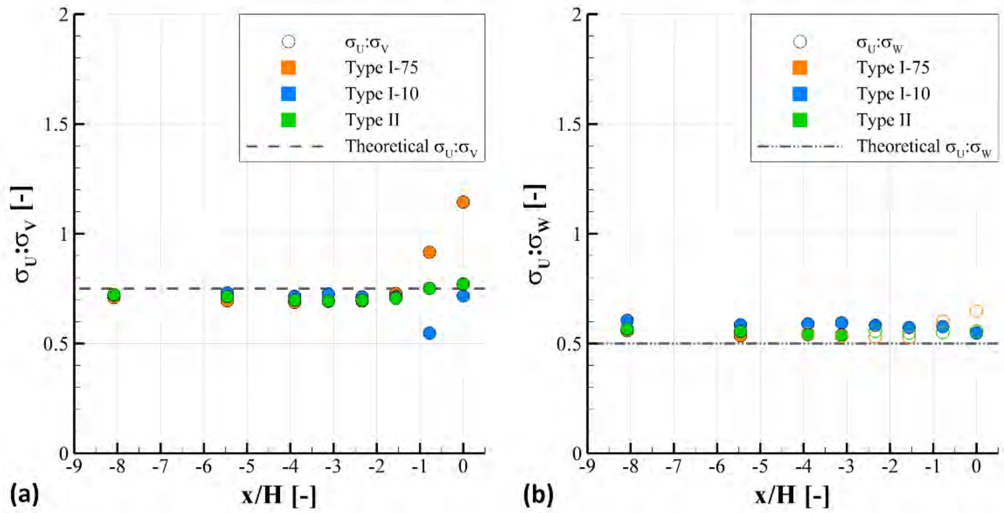

Figure 7-6 Longitudinal profiles of the average longitudinal to lateral (a) and longitudinal to vertical (b) ratios of velocity fluctuations from the lowest $100\,m$ above the Upwind subdomain (*UpW*). Reference values are represented by dark grey lines (VDI, 2000).

Figure 7-7 presents the profiles of the dimensionless longitudinal integral length scales (L_U^X/H) together with the longitudinal and lateral spectra at the lowest measurement height ($z_{AT}/H = 0.38$). Longitudinal spectra ($f \times S_{UU}/\sigma_U^2$) correspond to that obtained with the horizontal plane (UV) probe orientation. Distributions of longitudinal and vertical ($f \times S_{WW}/\sigma_U^2$) spectra, measured in the vertical plane (UW), are displayed in Figure D3 (Appendix D), together with the mean dimensionless fluxes. Reference data from the experiments of Kaimal (1972) and Simiu & Scanlan (1986) is represented in black. These are obtained above flat, homogeneous terrain, thus comparability with flows above the ridges is constrained. Nonetheless, these are represented for all plots of spectral distribution as visual aid for comparisons with the approach flow data. As observed in Chapter 6, the undisturbed flow spectra exhibit close agreement with these distributions.

L_U^X/H is most affected by the terrain at $z_{AT}/H = 0.38$ above $x/H = 0$ (*B1*), where the indicative length of the energy-intensive eddies exhibits a clear dependence on the inclination of the windward slopes. Accordingly, decreasing eddy lengths are observed for increasing steepness of the windward slopes. The smallest value of L_U^X/H is observed for the *Type I-75* ridge, whereas the profiles upstream from the *Type I-10* ridge present close agreement to the undisturbed flow (largest eddies). Above the streamwise positions nearest to the ridges, peaks of both spectra are more energetic than the flat terrain and reference data. The largest increases are found upstream from the *Type I-75* ridge, the strongest for the lateral components ($f \times S_{VV}/\sigma_U^2$) above *B1* (coarse twofold increase over the undisturbed flow). The peak of $f \times S_{UU}/\sigma_U^2$ at the same location occurs at a very distinct frequency. The peak energy frequency of the *Type I-75* ridge is shifted to larger ranges by roughly an order of magnitude. The vertical spectra ($f \times S_{WW}/\sigma_U^2$) are the least affected, but have limited data near to the ridges.

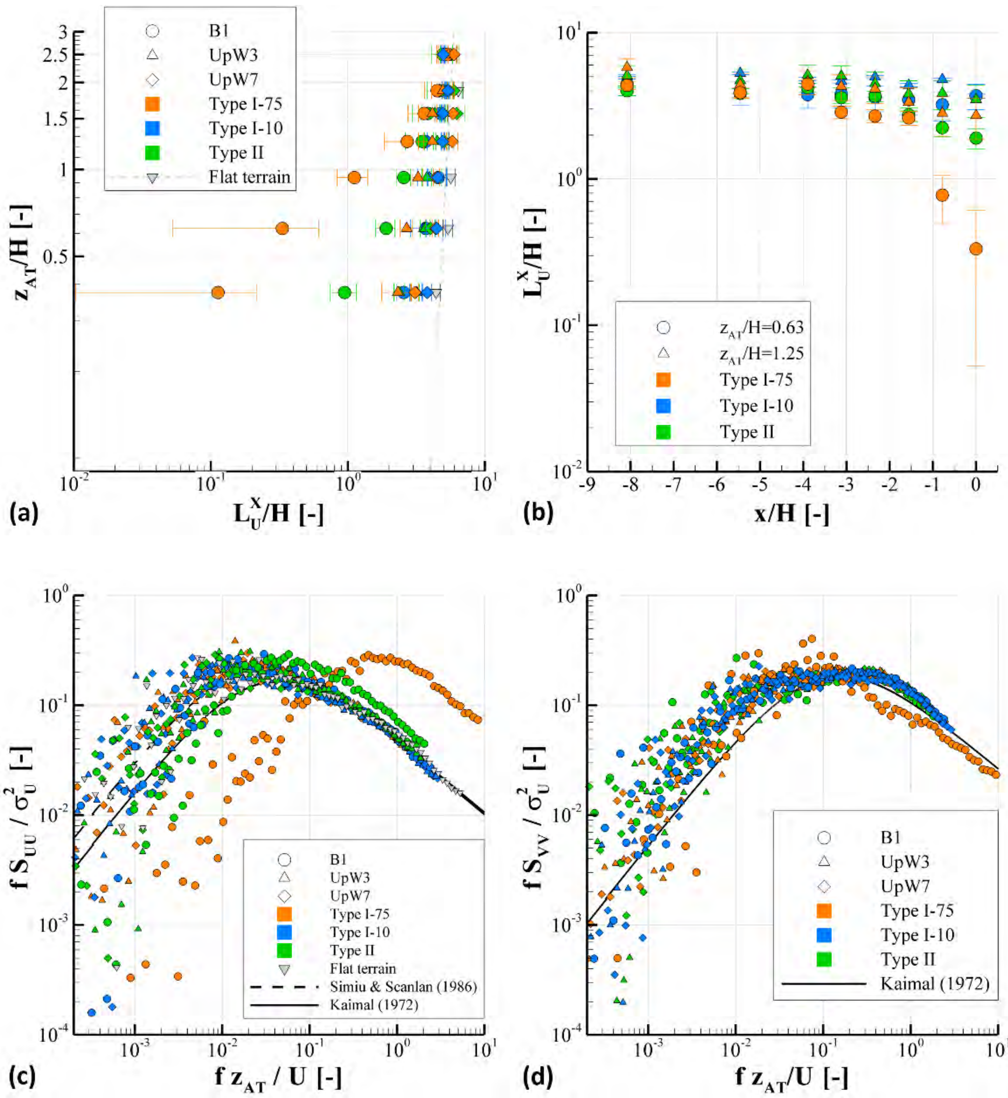

Figure 7-7. Vertical (a) and longitudinal (b) profiles of the mean dimensionless longitudinal integral length scales, and spectral distributions of longitudinal (c) and lateral (d) turbulent energy at $z/H = 0.38$ above the Upwind subdomain (*UpW*).

3D approach flow/reference data

Measurements performed for the ABL characterisation consist of vertical plane (UW) data only. To provide a more complete analysis of the effects of the terrain on turbulence, an approach flow scenario of 3D flow data is required. Using the data measured above one of the upwind subdomain positions, with flow virtually unaffected by the orography, as approach flow data is a worthwhile approach. The location where the flow is least affected by the ridges is the furthermost position ($x/H = -8.1$) from the *Type I-10* ridge. Thus, data from this position is adopted as approach flow reference case for the remainder of the ridge flow analyses.

7.4.2 Windward slope subdomain

Analyses are centred on three longitudinal measurement positions: *WW3*, *WW6*, and *WW9* (Table 7-4). Probe positioning constraints dictate that no UW component measurements are performed at $z_{AT}/H < 0.94$ from *WW9* to *WW7* and at $z_{AT}/H < 0.63$ between *WW6* and *WW5* above *Type II* and *Type I-75* ridges, respectively. Figure 7-8 presents the profiles of longitudinal (U/U_0) and vertical (W/U_0) velocity.

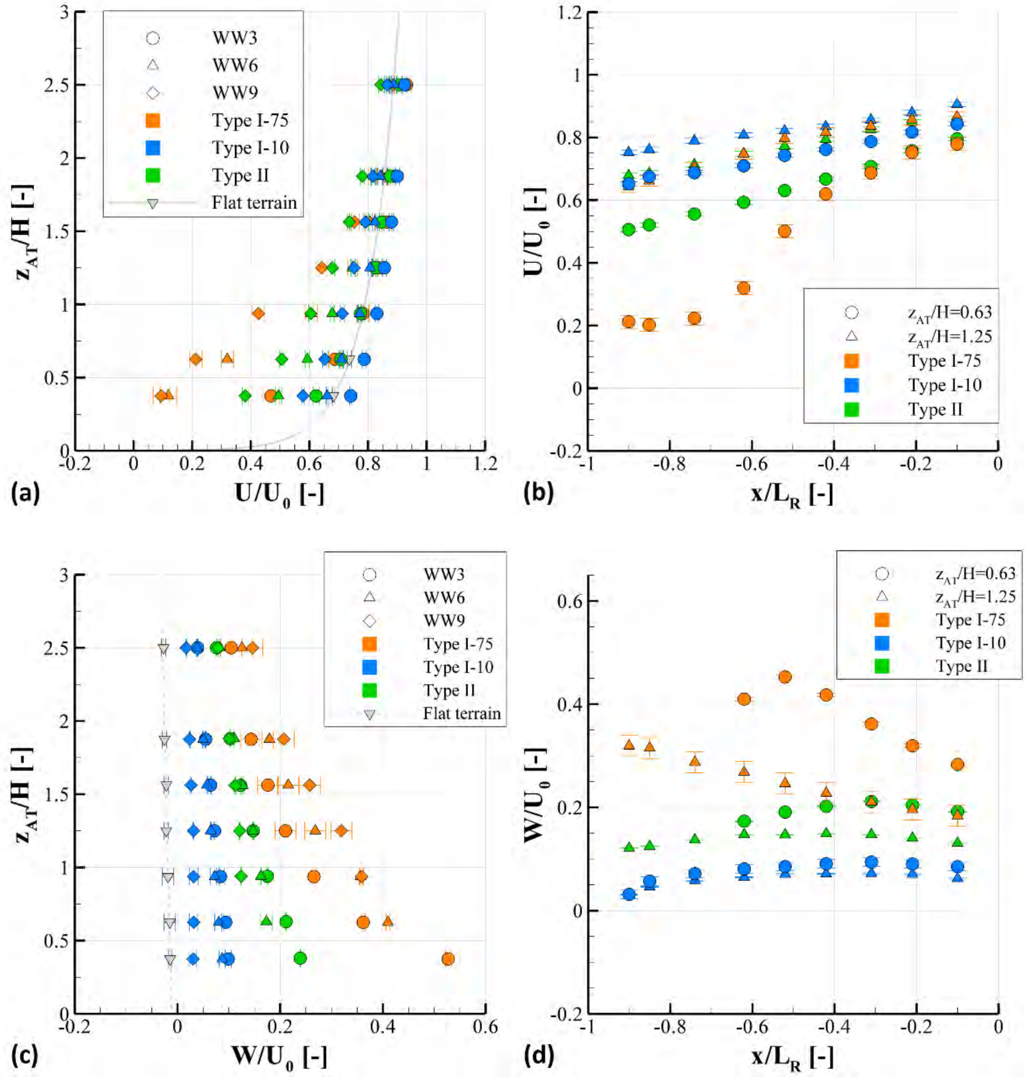

Figure 7-8. Vertical (a, c) and longitudinal (b, d) profiles of the mean dimensionless longitudinal (a, b) and vertical (c, d) velocities above the Windward slope subdomain (*WW*).

The largest differences of U/U_0 to the approach flow are observed at $x/L_R = -0.9$ (*WW9*), where a maximum seven-fold decrease is observed at $z_{AT}/H = 0.38$ of the *Type I-75* ridge. The maximum W/U_0 is found at $z_{AT}/H = 0.38$ above the near crest ($x/L_R = -0.31$, *WW3*) of the same ridge, with a nine-fold increase relative to the approach flow. Profiles of V/U_0 (Figure D4 in Appendix D) are virtually unaffected above the windward slope.

Figure 7-9 presents vertical and longitudinal profiles of all components of the velocity fluctuations above the windward slope positions. Longitudinal velocity fluctuations (σ_U/U_0) display closer agreement with the data from the near-ridge streamwise positions of the upwind subdomain. Accordingly, the largest intensities are observed for the *Type I-75* ridge. The maximum difference to the approach flow ($\approx 40\%$ increase) is observed at the furthermost position from the crest (above $x/L_R = -0.9$ or *WW9*). The most evident effects of the ridges on the lateral turbulence are those found at $z_{AT}/H = 0.38$ above $x/L_R \approx -0.6$ (*WW6*) of the same ridge geometry. Here, lateral velocity fluctuations (σ_V/U_0) increase a maximum of roughly twofold over the approach flow data. The largest magnitude of the vertical velocity fluctuations (σ_W/U_0) is observed at $z_{AT}/H = 0.38$ above $x/L_R \approx -0.3$ (*WW3*) of the *Type I-75* ridge and is $\approx 45\%$ smaller than that of σ_V/U_0 at the same position ($\approx 20\%$ smaller than σ_U/U_0).

Average ratios of longitudinal to lateral (σ_U: σ_V) and longitudinal to vertical (σ_U: σ_W) velocity fluctuations (from the lowest $Z = 100\ m$ above local terrain) are presented in Figure 7-10, as function of the dimensionless streamwise length (x/L_R). Both ratios generally present increases over those observed for the upwind subdomain. As with the previous subdomain, the largest ratios correspond to σ_U: σ_V of the *Type I-75* ridge. This is most prominent between $x/L_R = -0.9$ (*WW9*) and $x/L_R \approx -0.3$ (*WW3*), where lateral fluctuations overpower the longitudinal counterparts. Above the windward slopes, a maximum increase of $\approx 25\%$ of the lateral fluctuations over the longitudinal components is observed above $x/L_R \approx -0.6$ (*WW6*). Increases of the vertical fluctuations relative to the longitudinal components are relatively less expressive. For all streamwise positions of the windward slopes, the longitudinal fluctuations overpower the vertical components.

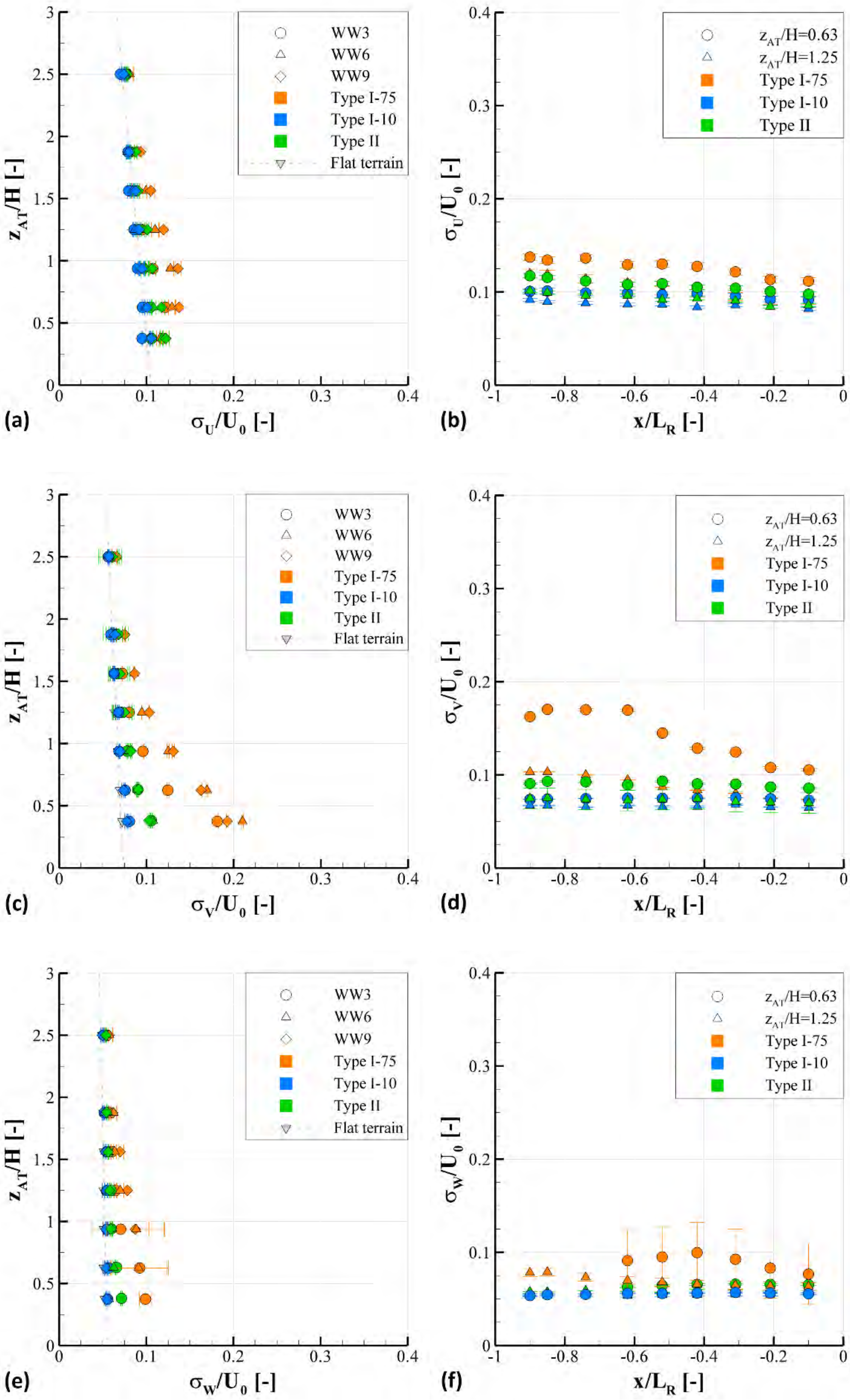

Figure 7-9. Vertical (a, c, e) and longitudinal (b, d, f) profiles of the mean dimensionless longitudinal (a, b), lateral (c, d), and vertical (e, f) velocity fluctuations above the Windward slope subdomain (*WW*).

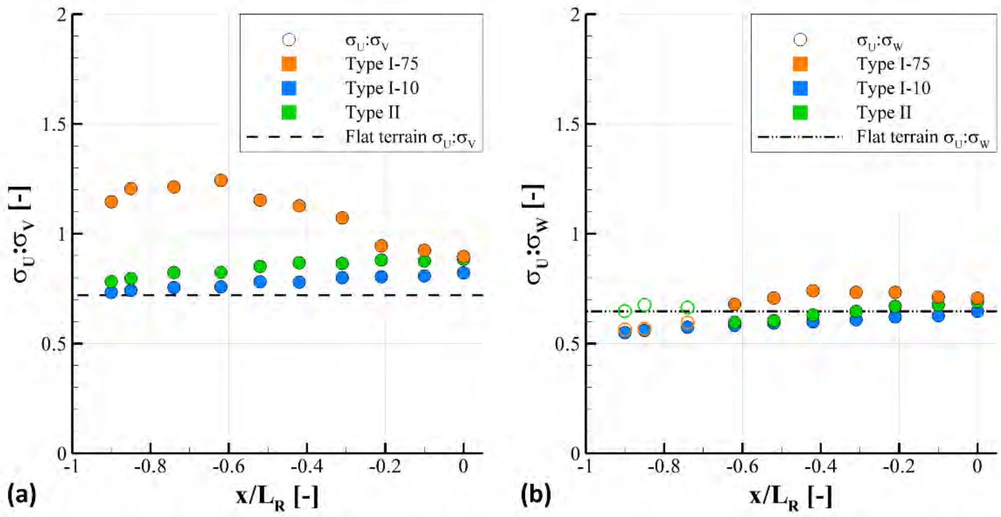

Figure 7-10. Longitudinal profiles of the average longitudinal to lateral (a) and longitudinal to vertical (b) ratios of velocity fluctuations from the lowest $\mathbf{Z} = \mathbf{100}$ m above the Windward slope subdomain (*WW*). Reference values are represented by dark grey lines (VDI, 2000).

Analogous trends are observed for integral length scales (L_U^X/H) and vertical fluxes ($u'w'/U_0^2$), which are displayed in Figure 7-11 together with the spectra at $z_{AT}/H = 0.38$. Decreases of L_U^X/H accompany increases of slope steepness at $z_{AT}/H \leq 0.94$. The largest differences to the approach flow data are those of the *Type I-75* ridge, the maximum found at $z_{AT}/H = 0.38$ above $x/L_R = -0.9$ (*WW9*) where L_U^X/H decreases roughly an order of magnitude. In terms of turbulent fluxes, $u'w'/U_0^2$ is more affected by the ridges than horizontal components ($u'v'/U_0^2$), displayed in Fig. D4 (Appendix D). The steepest windward slope produces the strongest effects on $u'w'/U_0^2$, translated by the increases of absolute values relative to the profiles of the other ridges and the approach flow. The maximum increase of $\left|u'w'/U_0^2\right|$ is observed at $z_{AT}/H = 0.94$ above $x/L_R = -0.9$ (*WW9*), at approximately threefold compared to the approach flow.

Spectral distributions resemble those of the near-ridge streamwise positions of the upwind subdomain. The longitudinal component ($f \times S_{UU}/\sigma_U^2$) also exhibits shifts of the reduced frequency of the peak energy to higher frequency ranges (over an order of magnitude) above all slope positions of the *Type I-75* ridge. Peak energy frequencies of lateral ($f \times S_{VV}/\sigma_U^2$) and vertical ($f \times S_{WW}/\sigma_U^2$) components are less affected. Profiles of $f \times S_{WW}/\sigma_U^2$ lack data from $x/L_R \approx -0.6$ (*WW6*) and $x/L_R = -0.9$ (*WW9*), thus inconclusive regarding the full extent of the windward slope effects on the vertical spectra.

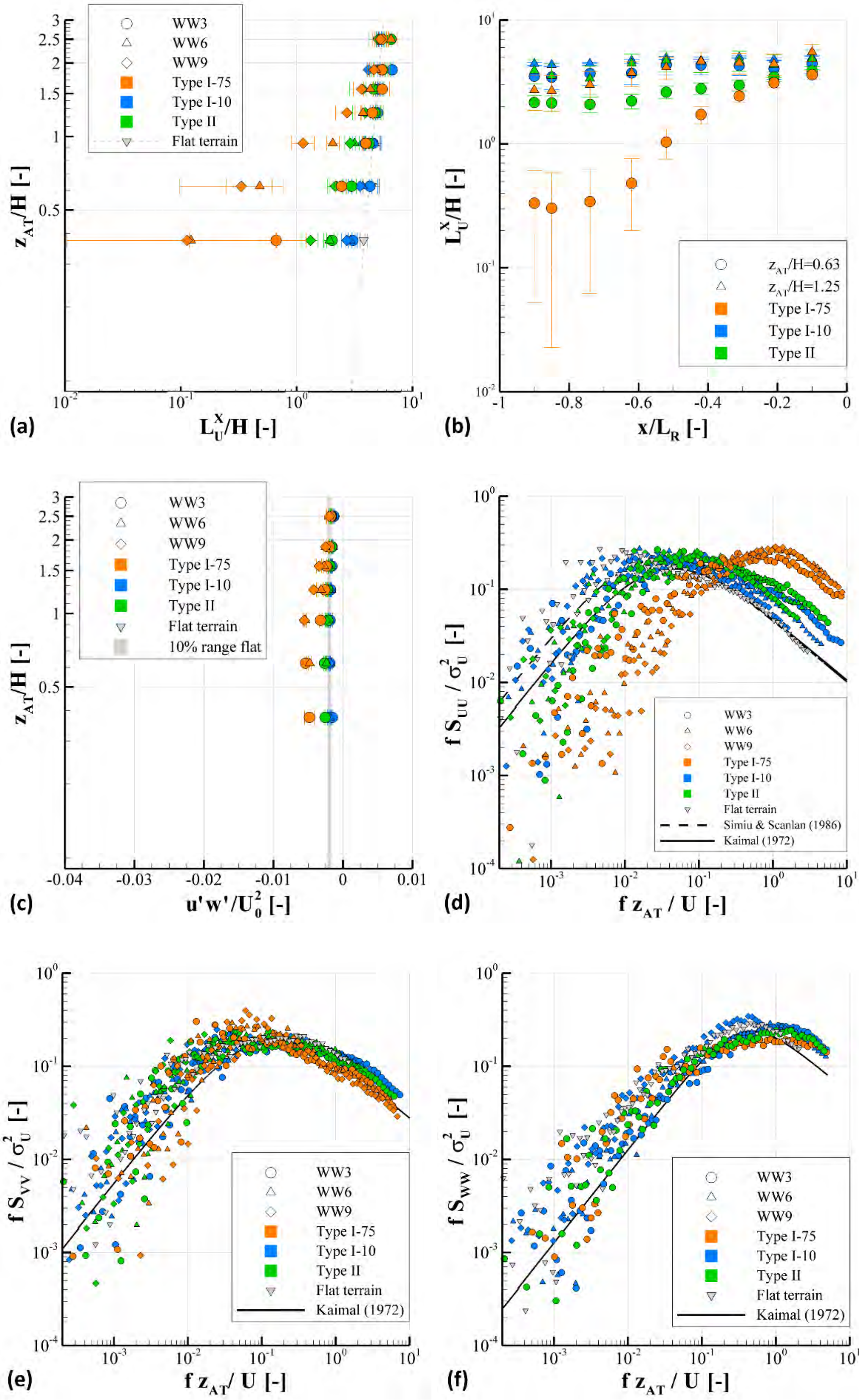

Figure 7-11. Vertical (a, c) and longitudinal (b) profiles of the mean dimensionless longitudinal integral length scales (a, b) and vertical turbulent fluxes (c), and spectral distributions of longitudinal (d) and lateral (e), and vertical (f) turbulent energy at $z/H = 0.38$ above the Windward slope subdomain (*WW*).

7.4.3 Leeside slope subdomain

Analyses are centred on the longitudinal measurement positions symmetric to the *WW* subdomain: *LW3*, *LW6*, and *LW9* (Table D2, Appendix D). Data uncertainties originate from the repetition measurements performed above the leeside slope positions, $x/L_R = 0.42$ (*LW4*) and $x/L_R = 0.85$ (*LW8*), of each ridge geometry. Thus, these are the most representative of all flow subdomains of the single ridges. Probe positioning constraints dictate that no vertical plane (UW) measurements are performed at $z_{AT}/H < 0.63$ above $x/L_R = 0.62$ (*LW6*) and downstream from this position for the *Type I-10* ridge.

The longitudinal velocity (U/U_0) is the most affected of the velocity components. In Figure 7-12, mean flow reversal ($U/U_0 < 0$) is observed at $z_{AT}/H = 0.38$ above all positions except nearest to the crest of the *Type II* ridge. The largest intensity of negative U/U_0 is observed for the *Type I-75* ridge above $x/L_R \approx 0.6$ (*LW6*). The lateral velocity (V/U_0) remains the least affected of the velocity components above the centreline of the leeside slope. The vertical component (W/U_0) is less influenced by the ridges than observed above the windward slope, as underlined by the smaller variability between data of the different ridges. Profiles of the *Type I-75* ridge exhibit downward vertical flow ($W/U_0 < 0$) that increases in magnitude with height and streamwise distance from the crest. Inversely, *Type I-10* and *Type II* ridges provoke upward flows at all heights of the profiles above the respective analyses positions.

All components increase relative to the previous subdomains, with larger gradients between consecutive heights and streamwise positions of the same profiles observed in Figure 7-13. Longitudinal fluctuations (σ_U/U_0) present the largest increases, a maximum of roughly threefold over the approach flow observed at $z_{AT}/H = 0.94$ above $x/L_R \approx 0.6$ (*LW6*) of the *Type I-75* ridge. At $z_{AT}/H \leq 0.63$, σ_U/U_0 is smaller than the reference data for *Type I-10* and *Type II* ridges, the largest decrease found at the furthermost positions from the crests. Longitudinal profiles display the closest agreement between data above $x/L_R = 0.1$ (*LW1*), following which σ_U/U_0 increases by over twofold at $z_{AT}/H = 0.63$ above $x/L_R \approx 0.2$ (*LW2*) of *Type I-75*. The maximum of the lateral fluctuations (σ_V/U_0) is at $z_{AT}/H = 0.63$ above *LW3* of the *Type I-75* ridge, with a coarse threefold increase over the approach flow at the same height. A strong increase of σ_V/U_0 ($\approx 85\%$) occurs between *LW1* and *LW2* at $z_{AT}/H = 0.63$. Above the same geometry, the largest vertical fluctuations (σ_W/U_0) with height and streamwise positions are observed. The maximum ($z_{AT}/H = 0.94$ above *LW6*) corresponds to a coarse fourfold increase compared to the approach flow (about two times larger than the maximum from the windward slope).

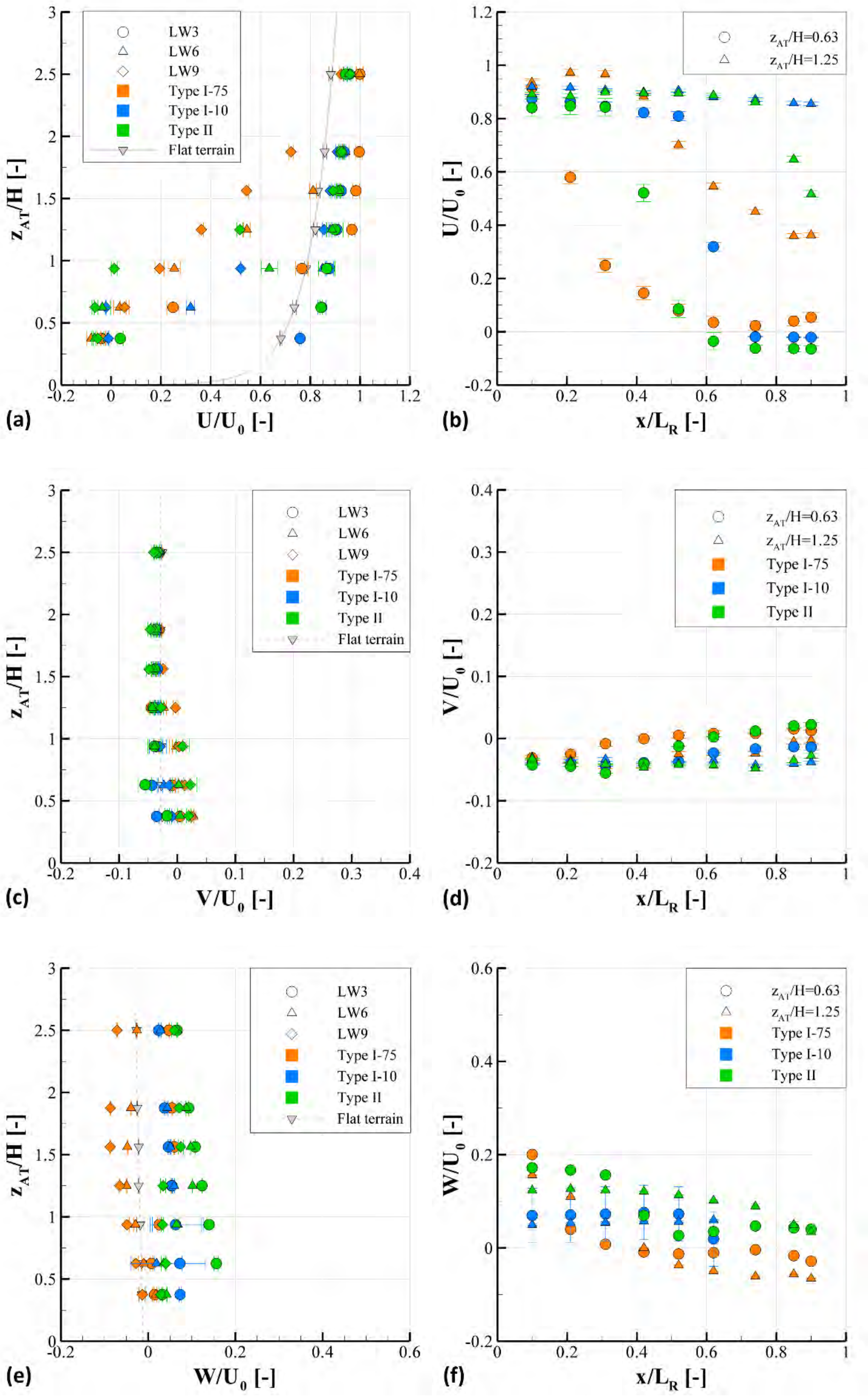

Figure 7-12. Vertical (a, c, e) and longitudinal (b, d, f) profiles of the mean dimensionless longitudinal (a, b), lateral (c, d), and vertical (e, f) velocities above the Leeside slope subdomain (*LW*).

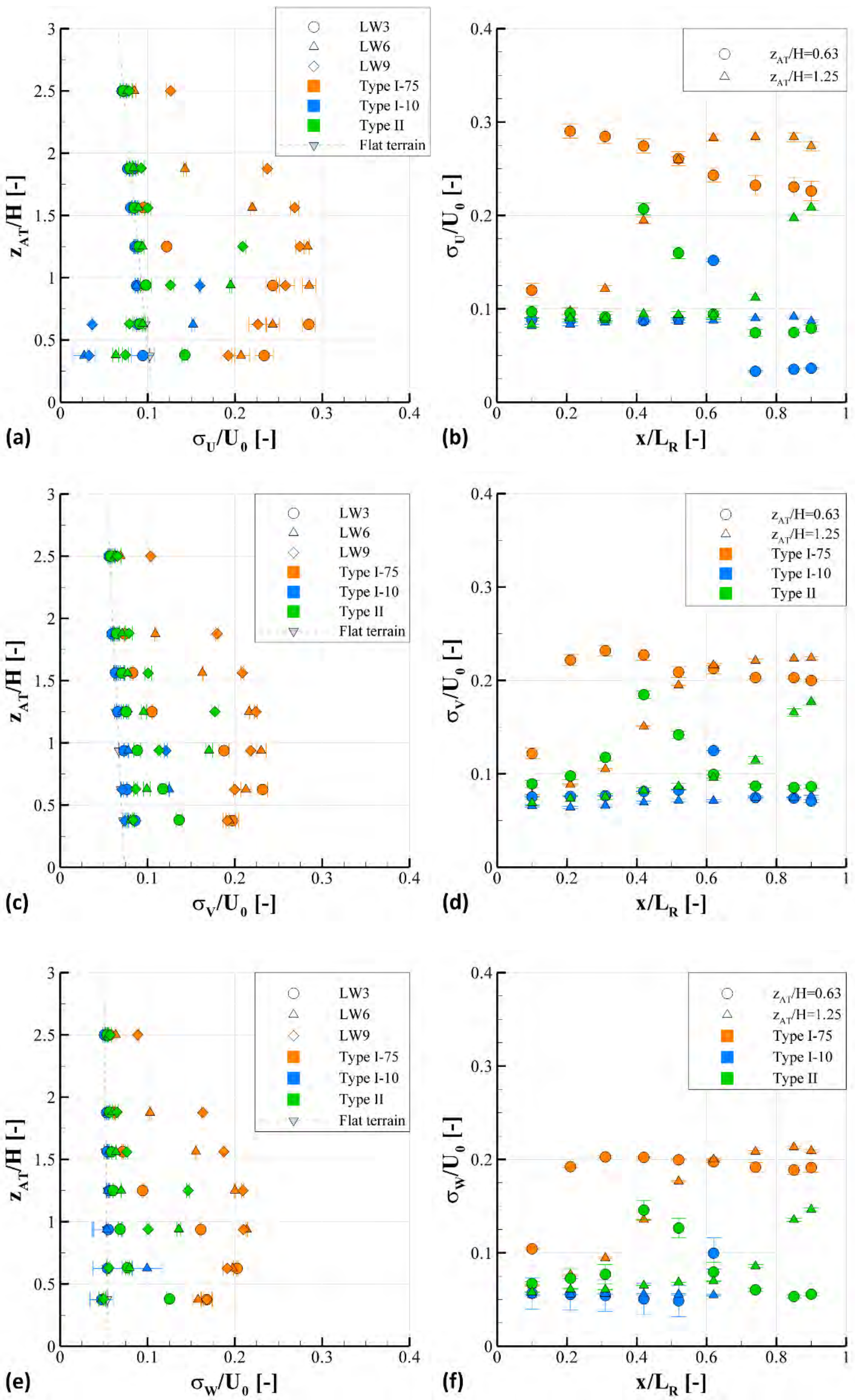

Figure 7-13. Vertical (a, c, e) and longitudinal (b, d, f) profiles of the mean dimensionless longitudinal (a, b), lateral (c, d), and vertical (e, f) velocity fluctuations above the Leeside slope subdomain (*LW*).

Ratios of the velocity fluctuations are presented in Figure 7-14. Ratios of the *Type I-10* ridge exhibit the largest gradients from $x/L_R \approx 0.3$ (*LW3*) onwards. The largest variations are observed for the longitudinal to lateral ratio (σ_U: σ_V), which increase $\approx 55\%$ between *LW3* and $x/L_R \approx 0.4$ (*LW4*). Longitudinal to vertical ratios (σ_U: σ_W) present closer agreement to the reference values.

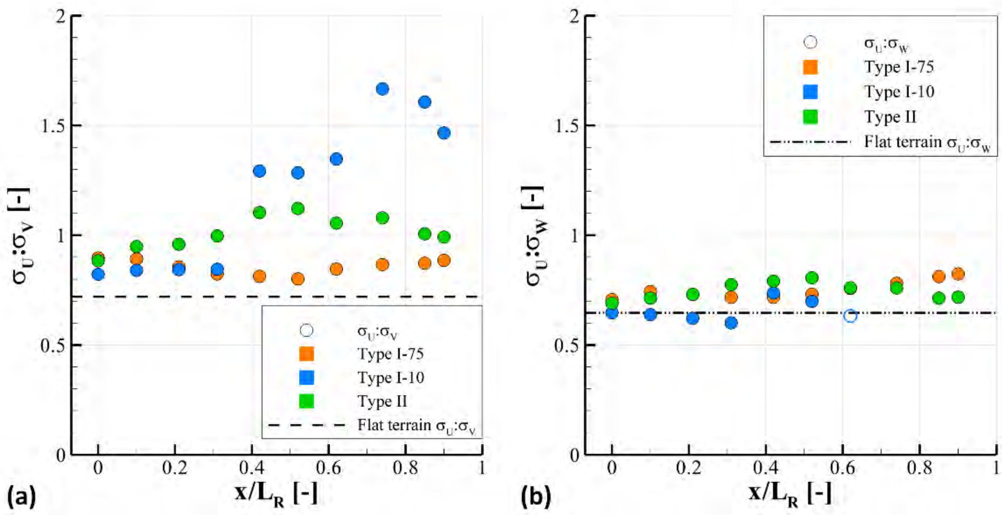

Figure 7-14. Longitudinal profiles of the average longitudinal to lateral (a) and longitudinal to vertical (b) ratios of velocity fluctuations from the lowest $\mathbf{Z = 100\ m}$ above the Leeside slope subdomain (*LW*). Reference values are represented by dark grey lines (VDI, 2000).

Integral length scales (L_U^X/H) and vertical fluxes ($u'w'/U_0^2$) are displayed in Figure 7-15 with the spectra at $z_{AT}/H = 0.38$. L_U^X/H exhibits larger scatter than for the previous subdomains, data spanning two orders of magnitude at $z_{AT}/H \leq 0.94$. The smallest energy intensive eddies are observed above $x/L_R \approx 0.3$ (*LW3*) of the *Type II* ridge, which also yields the highest extending effects, reaching up to $z_{AT}/H = 1.25$ above $x/L_R = 0.9$ (*LW9*). Vertical profiles of L_U^X/H are also characterised by sharp gradients (roughly two orders of magnitude) between consecutive heights of the same profile. $u'w'/U_0^2$ presents a maximum increase of roughly 15 times the approach flow (in magnitude) at $z_{AT}/H = 0.94$ above $x/L_R \approx 0.6$ (*LW6*) of the *Type I-75* ridge. $u'v'/U_0^2$ (Fig. D4, Appendix D) is also most affected by the *Type I-75* ridge, an increase of coarsely an order of magnitude relative to the approach flow being found at $z_{AT}/H = 0.63$ above *LW3*.

Spectra exhibit higher energy content than previously observed, with larger shifts of the respective peak energy frequencies to higher frequency ranges. The largest peak of longitudinal spectra ($f \times S_{UU}/\sigma_U^2$) is observed above *LW9* of the *Type II* ridge, approximately three times larger than the approach flow. With the exception of this position, peaks show shifts of at least an order of magnitude higher frequency ranges relative to the approach flow. Lateral spectra ($f \times S_{VV}/\sigma_U^2$) are relatively less affected, the inertial subrange is less inclined than predicted by the Kolmogorov theory. The most intense peaks of the vertical spectra ($f \times S_{WW}/\sigma_U^2$) occur above *LW3*, the maximum observed above the *Type II* ridge ($\approx 60\%$ increase over reference data).

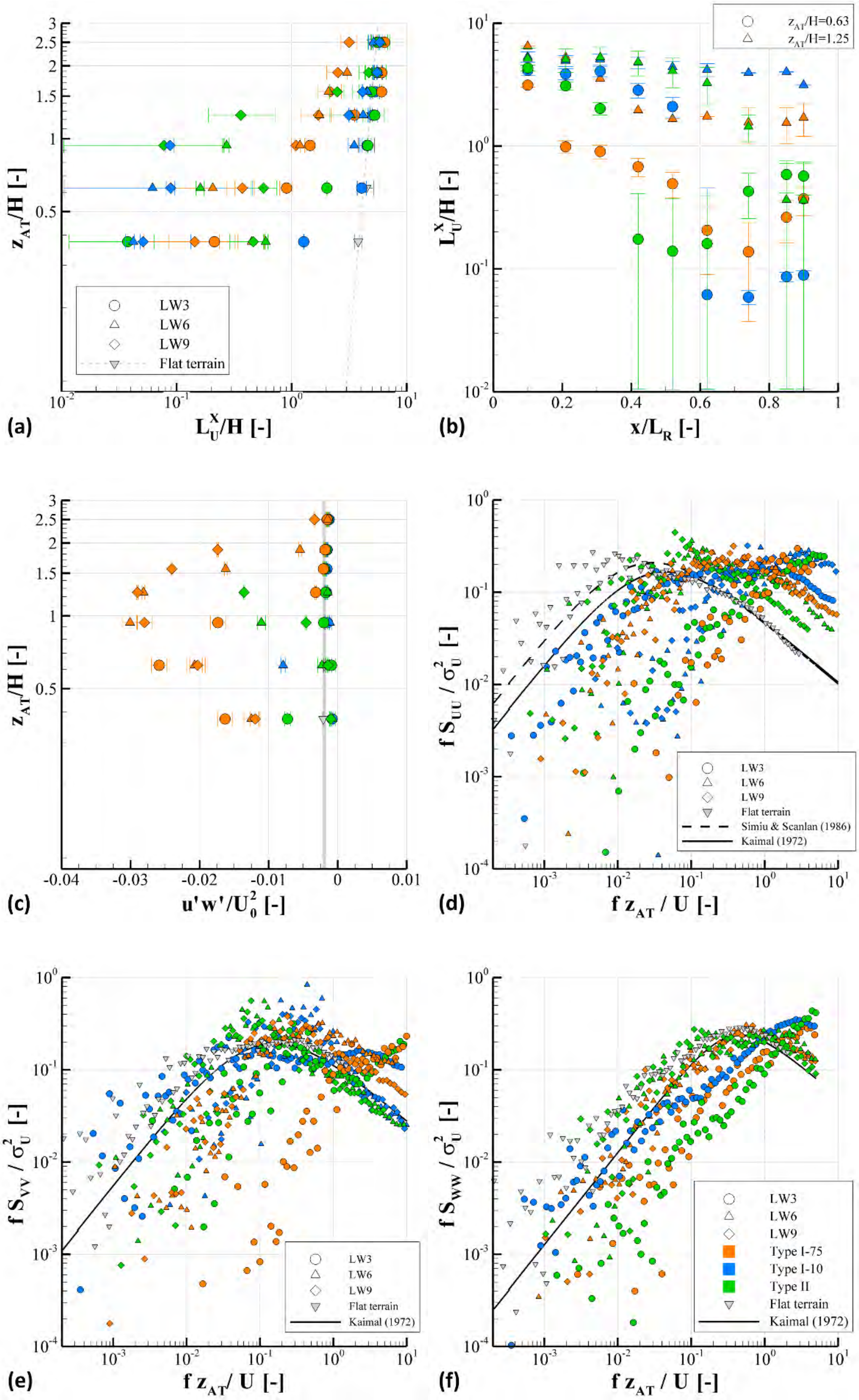

Figure 7-15 Vertical (a, c) and longitudinal (b) profiles of the mean dimensionless longitudinal integral length scales (a, b) and vertical turbulent fluxes (c), and longitudinal (d) and lateral (e), and vertical (f) spectra at $z/H = 0.38$ above the Leeside slope subdomain (*LW*).

7.4.4 Downwind subdomain

Analyses are centred on three longitudinal measurement positions that are symmetric to those of the Upwind (*UpW*) subdomain: *B2*, *DW3*, and *DW7* (Table D1, Appendix D). Probe and traverse system constraints rule out vertical plane (UW) measurements above *B2* of the *Type I-10* and *Type I-75* ridges, and horizontal plane (UV) measurements above *DW7* of *Type II*.

Figure 7-16 presents the profiles of the velocities. Flow reversal characteristics of the near-surface longitudinal velocities (U/U_0) continue downstream from all ridges. The maximum magnitude of flow reversal ($U/U_0 < 0$), observed at $z_{AT}/H = 0.38$ above $x/H \approx 2.3$ (*DW3*) downstream from the *Type II* ridge, is $\approx 50\%$ larger than the maximum observed above the leeside slope (*Type I-75* ridge). Lateral components (V/U_0) are the least affected, data from all ridges contained within the confidence intervals of the reference data above $x/H \approx 8.1$ (*DW7*). Vertical components (W/U_0) are most affected at the upper altitudes, those related to the *Type II* ridge exhibiting the clearest effects. This is highlighted by the larger gradients between successive longitudinal positions. Above the furthermost position (*DW7*), flows above all ridge geometries exhibit downward flow characteristics ($W/U_0 < 0$).

The largest magnitudes of all three components of the fluctuations, presented in Figure 7-17, are observed downstream from the *Type I-75* ridge, but general increases of magnitude compared to the leeside slope results are found for *Type I-10* and *Type II* ridges. The maximum longitudinal component (σ_U/U_0), observed at $z_{AT}/H = 1.25$ above $x/H = 0$ (*B2*) of *Type I-75*, constitutes an approximate threefold increase over the approach flow at the same height. As with the leeside slope, σ_U/U_0 of *Type I-10* and *Type II* ridges are smaller than the approach flow at the near-surface. The largest magnitudes of the lateral components (σ_V/U_0) is observed at $z_{AT}/H = 0.94$ above *B2* of the *Type I-10* ridge, consisting of a threefold increase over the approach flow data. This is $\approx 20\%$ smaller than the maximum value of σ_U/U_0 of the same ridge. Relatively undisturbed above the leeside slope, values of σ_V/U_0 downstream from the *Type I-10* ridge exhibit strong near-surface variations between $x/H \approx 2.3$ (*DW3*) and $x/H \approx 5.5$ (*DW6*). The most evident is observed at $z_{AT}/H = 0.63$, with σ_V/U_0 increasing to over twice the value of *DW3*. Vertical fluctuations (σ_W/U_0) are less affected downstream from the ridges. The maximum σ_W/U_0, found at $z_{AT}/H = 0.94$ above *DW3* of the *Type I-75* ridge domain, overpowers the approach flow data by roughly fourfold. At $z_{AT}/H = 0.63$ above *DW7*, σ_W/U_0 displays the largest deviations between data from different ridges of all components of fluctuations.

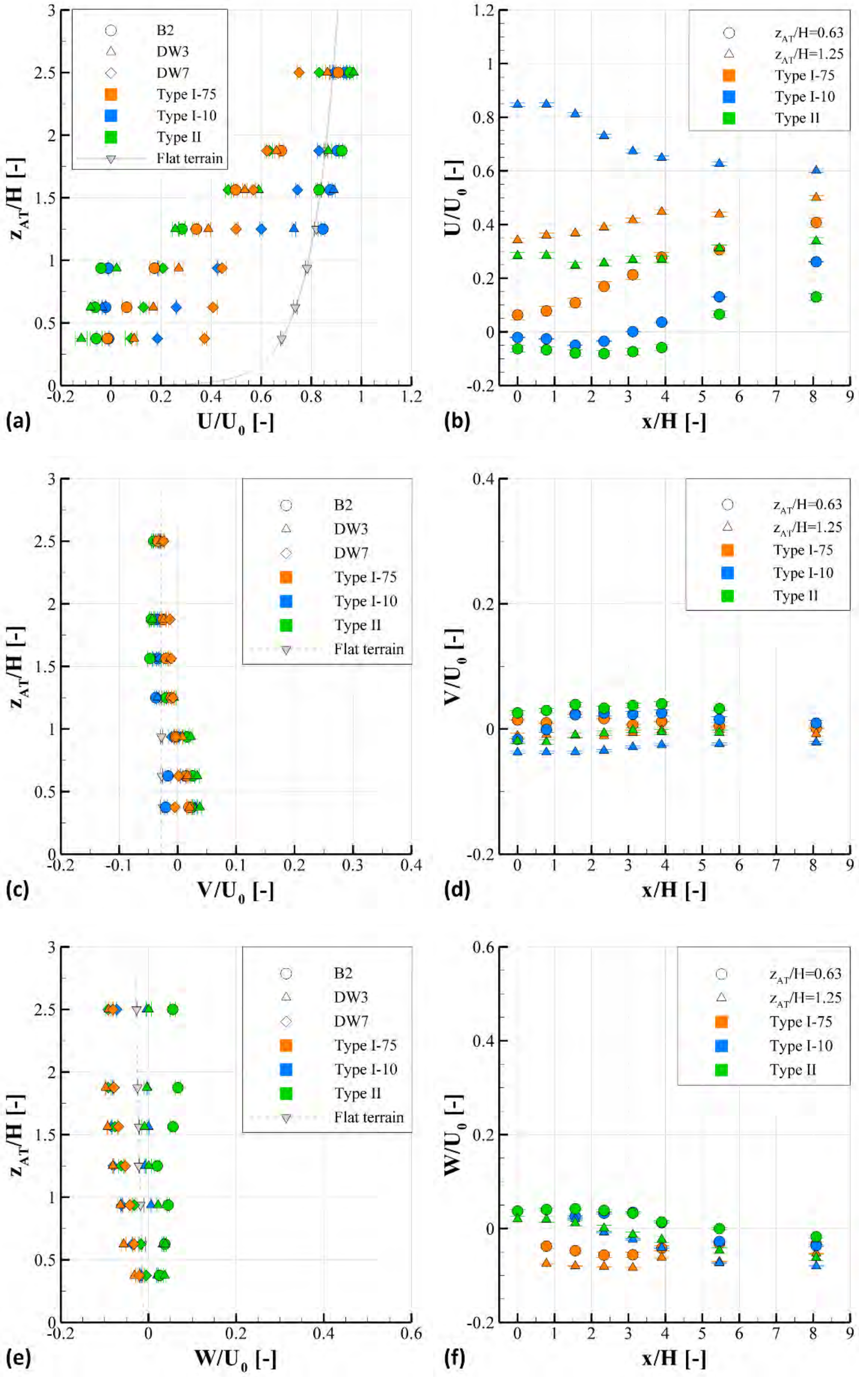

Figure 7-16. Vertical (a, c, e) and longitudinal (b, d, f) profiles of the mean dimensionless longitudinal (a, b), lateral (c, d), and vertical (e, f) velocities above the Downwind subdomain (*DW*).

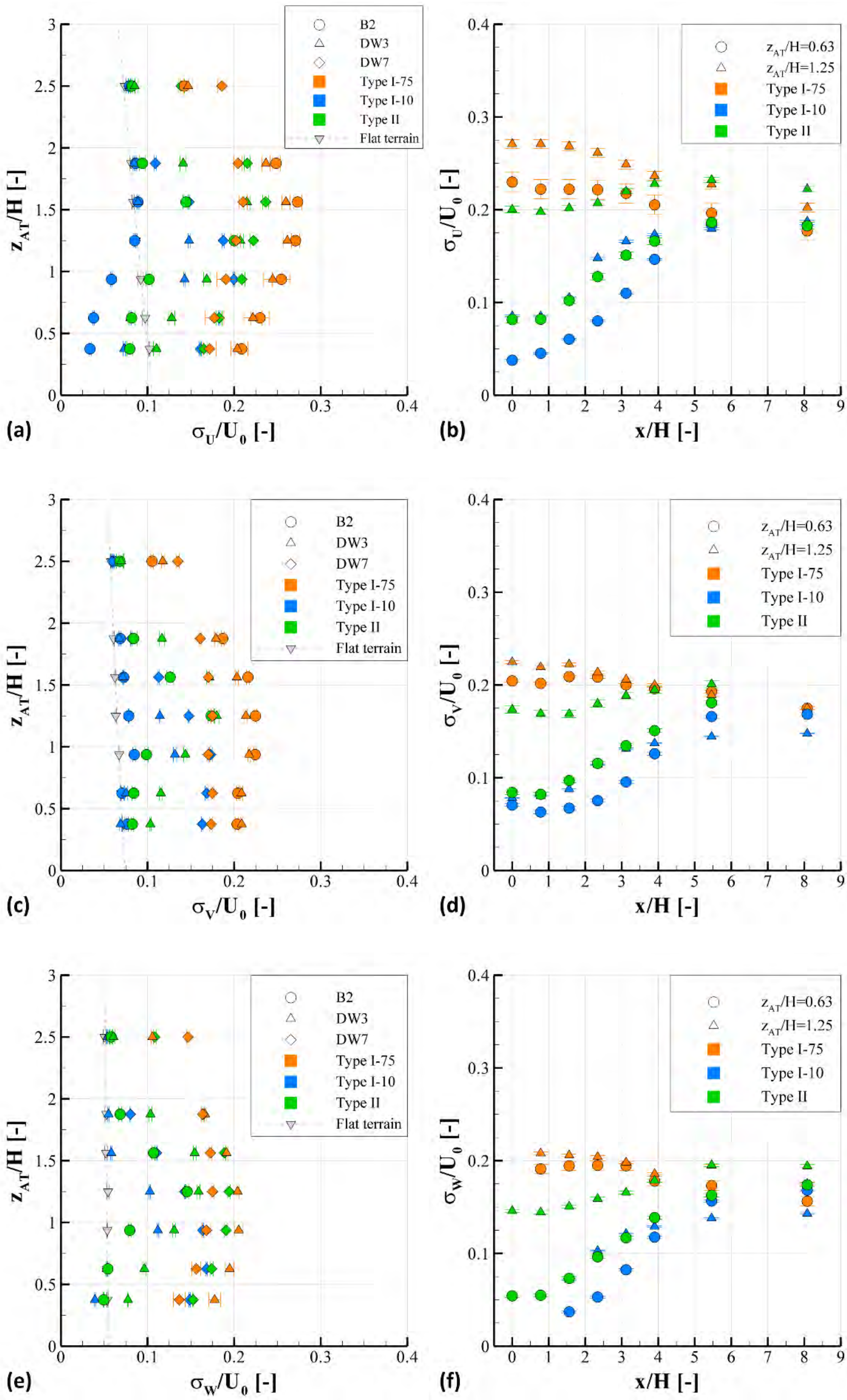

Figure 7-17. Vertical (a, c, e) and longitudinal (b, d, f) profiles of the mean dimensionless longitudinal (a, b), lateral (c, d), and vertical (e, f) velocity fluctuations above the Downwind subdomain (*DW*).

Average ratios of the longitudinal to lateral fluctuations, displayed in Figure 7-18a, are most affected above *B2*, the largest contribution of lateral over longitudinal components ($\approx 65\%$) being that of the *Type I-10* ridge. Longitudinal to vertical ratios ($\sigma_U{:}\,\sigma_W$) are relatively less affected (Fig. 7-18b), but tend to deviate from the reference value with increasing distances from the ridges.

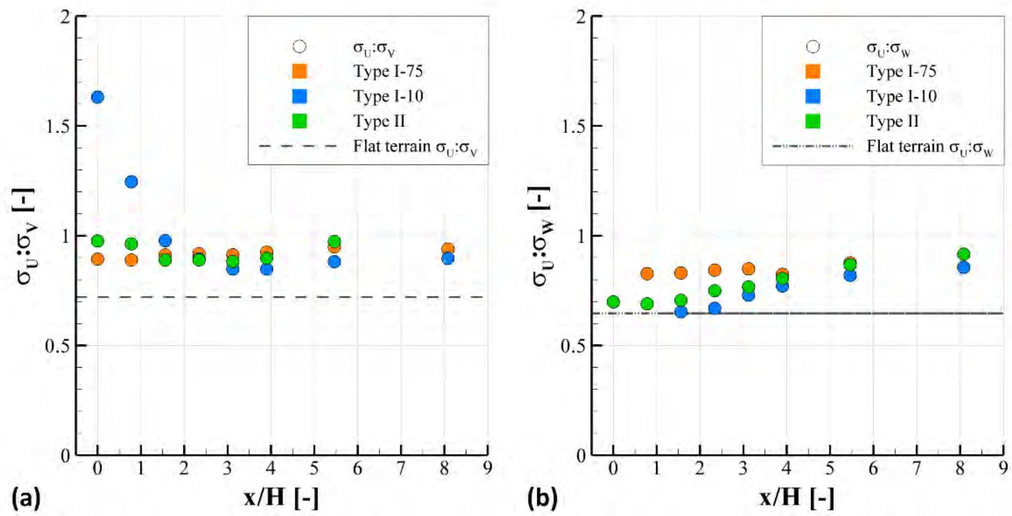

Figure 7-18. Longitudinal profiles of the average longitudinal to lateral (a) and longitudinal to vertical (b) ratios of velocity fluctuations from the lowest $\mathbf{Z = 100\ m}$ above the Downwind subdomain (*DW*). Reference values are represented by dark grey lines (VDI, 2000).

Integral length scales (L_U^X/H), displayed in Figure 7-19, generally increase compared to the leeside slope at $z_{AT}/H \leq 0.94$ and decrease above ($z_{AT}/H \geq 1.25$). The *Type I-75* ridge is an exception, a decrease of $\approx 40\%$ being observed at $z_{AT}/H = 0.38$ above $x/H = 0$ (*B2*). Profiles of the vertical fluxes ($u'w'/U_0^2$) exhibit larger differences to the approach flow than those of the leeside slope at $z_{AT}/H \geq 1.25$, the largest corresponding to about an order of magnitude above $x/H \approx$ 2.3 (*DW3*) of the *Type I-75* ridge. This is $\approx 10\%$ smaller than the maximum magnitude observed above the leeside slope. Horizontal fluxes (Figure D5, Appendix D) are less affected and differences to the approach flow tend to decrease with increasing downwind distances from the ridges.

Frequencies of the peak longitudinal spectra ($f \times S_{UU}/\sigma_U^2$) display closer agreement with the approach flow than above the leeside slopes. Frequency shifts are limited to *B2* of *Type I-75* and *Type II* ridges, with shifts of roughly two orders of magnitude to larger frequency ranges. The maximum spectra, observed above *DW3* of *Type I-10*, is $\approx 50\%$ larger than the maximum of the leeside slope of the same ridge. The maximum lateral spectra ($f \times S_{VV}/\sigma_U^2$) is $\approx 25\%$ larger than $f \times S_{UU}/\sigma_U^2$ above *B2* of *Type I-10*. Frequency shifts are restricted to *B2* of *Type I-75* (roughly two orders of magnitude). Frequency shifts of the peaks of the vertical components ($f \times S_{WW}/\sigma_U^2$) are to smaller frequency ranges above all positions except *B2* of *Type I-75*.

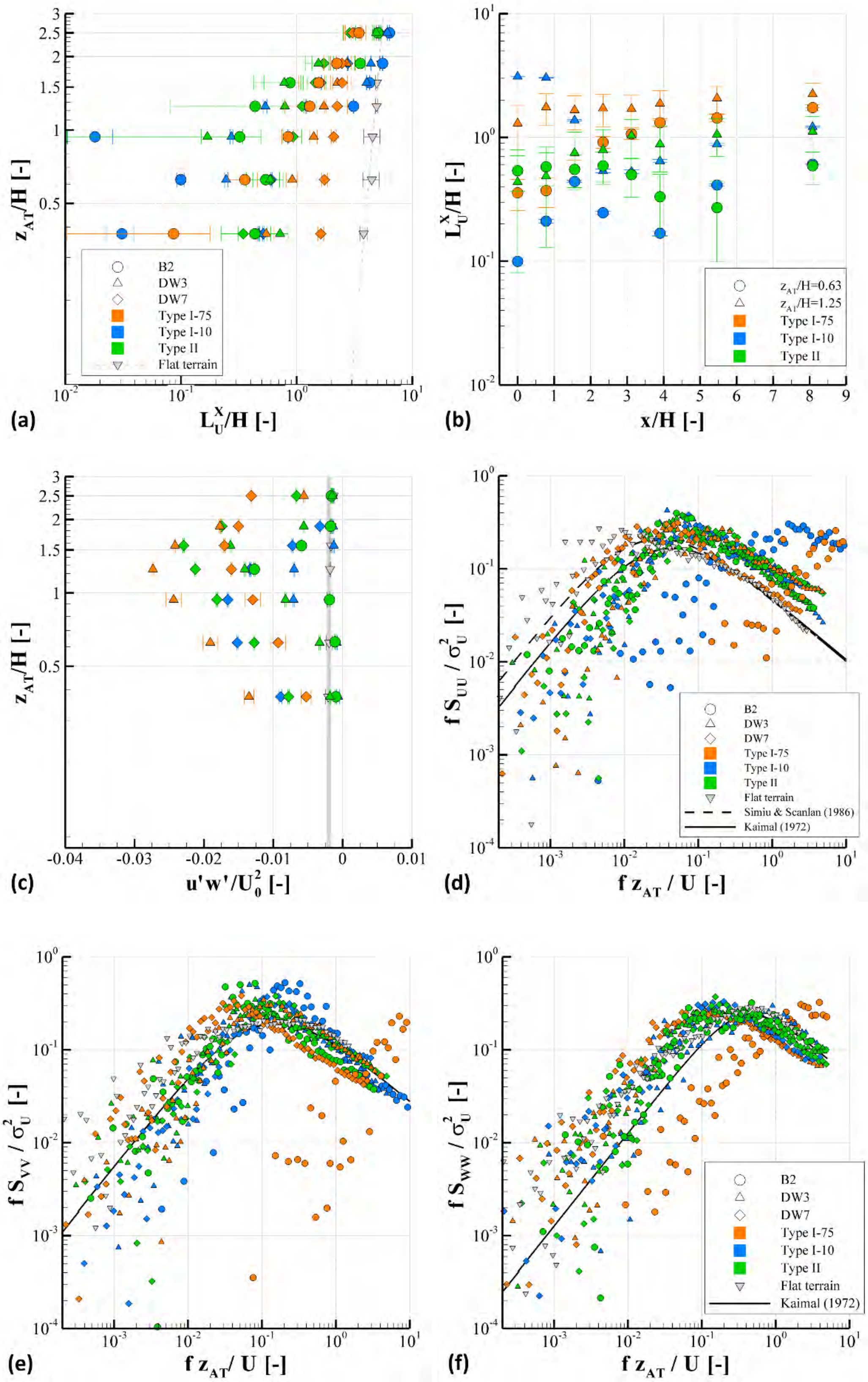

Figure 7-19. Vertical (a, c) and longitudinal (b) profiles of the mean dimensionless longitudinal integral length scales (a, b) and vertical turbulent fluxes (c), and spectral distributions of longitudinal (d), lateral (e), and vertical (f) turbulent energy at $z/H = 0.38$ above the analyses positions of the Downwind subdomain (*DW*).

7.4.5 Extended downwind subdomain (DDW)

Analyses are centred on three longitudinal measurement positions: *DDW2*, *DDW4*, and *DDW6*. Only vertical plane (UW) measurements are made above this subdomain, no measurements being performed above the furthermost position (*DDW7*) from the *Type I-10* ridge (beyond the reach of the traverse system). Velocities present closer agreement to the approach flow than above the downwind subdomain, as observed in Figure 7-20. Longitudinal velocities (U/U_0) exhibit larger deviations than the vertical components (W/U_0). The maximum difference of U/U_0 is observed at $z_{AT}/H = 0.38$ above $x/H \approx 13$ (*DDW2*) of the *Type II* ridge ($\approx 50\%$ decrease from the approach flow). W/U_0 presents close agreement to the reference data, the closest observed at $z_{AT}/H = 0.38$, where all results are contained within the confidence intervals regardless of the ridge types or longitudinal distances from the ridges.

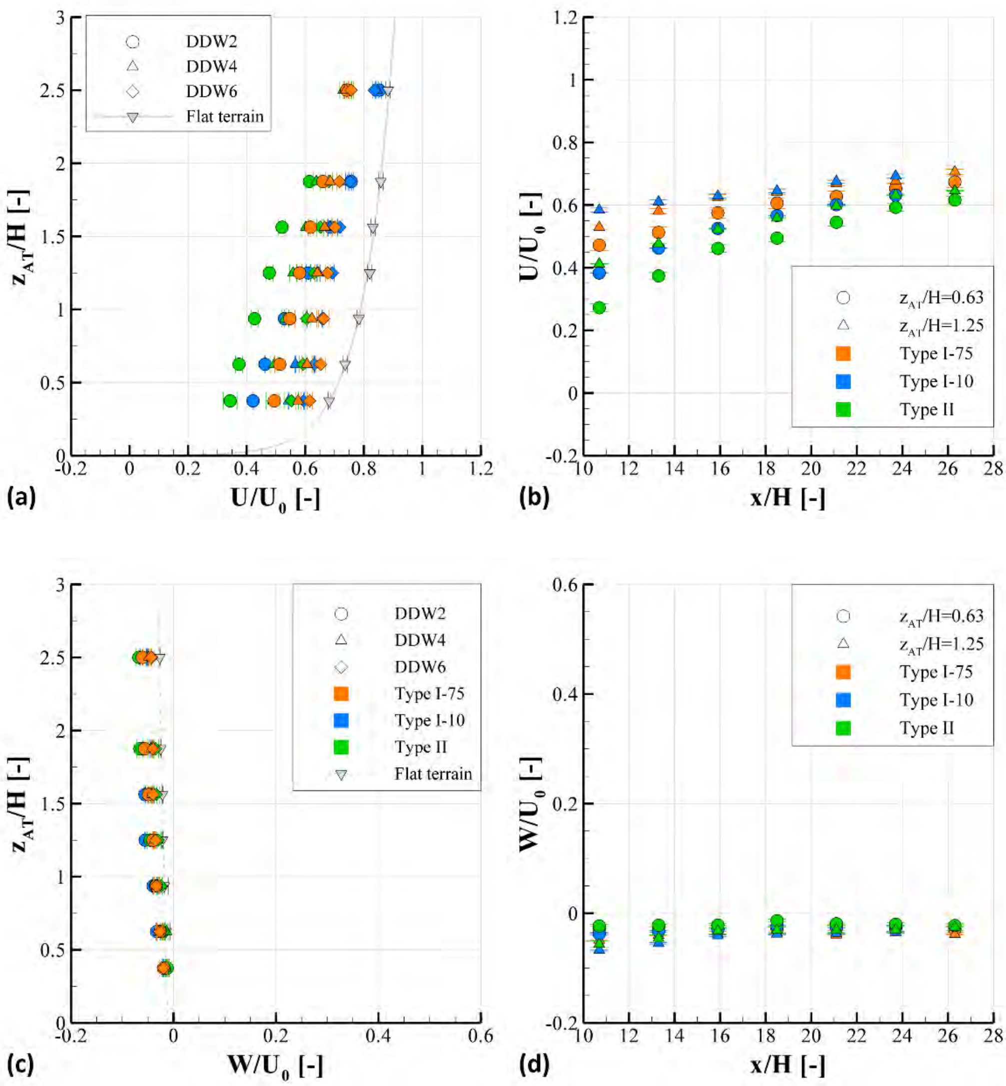

Figure 7-20. Vertical (a, c) and longitudinal (b, d) profiles of the mean dimensionless longitudinal (a, b) and vertical (c, d) velocities above the Extended downwind subdomain (*DDW*).

Longitudinal velocity fluctuations (σ_U/U_0), in Figure 7-21, present the closest agreement with the approach flow at $z_{AT}/H = 0.38$ above $x/H \approx 26$ (*DDW7*) of the *Type I-10* ridge, where σ_U/U_0 is $\approx 10\%$ larger than the inflow. Data convergence between *Type I-75* and *Type II* ridges is observed above *DDW7.* The maximum σ_U/U_0 is observed for the *Type II* ridge at $z_{AT}/H = 1.56$ above $x/H \approx 13$ (*DDW2*), over twice that of the reference data. The largest magnitudes of the vertical fluctuations (σ_W/U_0) are also observed above *DDW2* of the *Type II* ridge, a maximum threefold increase relative to the approach flow found at $z_{AT}/H = 1.56$. Ratios of longitudinal to vertical fluctuations (Fig. D5, Appendix D) tend to converge with increasing distances from the ridges.

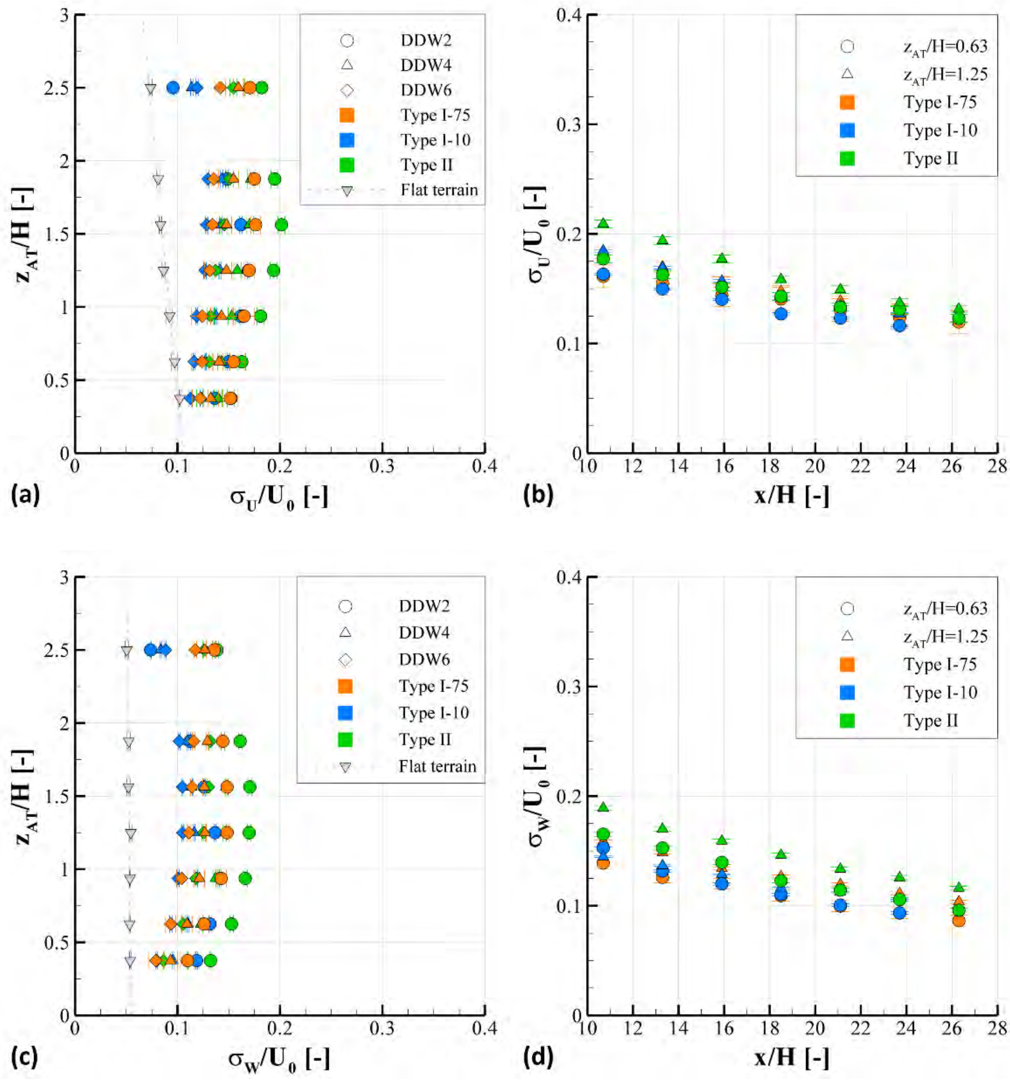

Figure 7-21. Vertical (a, c) and longitudinal (b, d) profiles of the mean dimensionless longitudinal (a, b) and vertical (c, d) velocity fluctuations above the Extended downwind subdomain (*DDW*).

Integral length scales (L_U^X/H) are less affected by height variations and exhibit near-constant offsets to the approach flow, as perceived in Figure 7-22. Closer agreement is observed downwind from the *Type I-75* ridge, the closest at $z_{AT}/H = 0.38$ above *DDW6* where L_U^X/H is $\approx 40\%$

smaller than the approach flow. Vertical fluxes ($u'w'/U_0^2$) present the largest absolute increases compared to the reference data at $z_{AT}/H \geq 1.25$, the maximum of about an order of magnitude observed at $z_{AT}/H = 1.56$ above *DDW2* of *Type II*. Inversely, $u'w'/U_0^2$ achieves convergence with the flat terrain at $z_{AT}/H = 0.38$ above the furthermost downwind distances (*DDW7*) from all ridges. Longitudinal spectra ($f \times S_{UU}/\sigma_U^2$) exhibit the closest agreement between ridge datasets and to the approach flow than the vertical counterparts ($f \times S_{WW}/\sigma_U^2$). Peaks of $f \times S_{UU}/\sigma_U^2$ overpower the peak of the approach flow (maximum of about twofold above *DDW2* of *Type II*). Peaks of $f \times S_{WW}/\sigma_U^2$ occur at smaller frequency ranges than the approach flow. This is most significant above *DDW2* of the *Type II* ridge, where the peak occurs at a frequency of roughly an order of magnitude smaller than the approach flow.

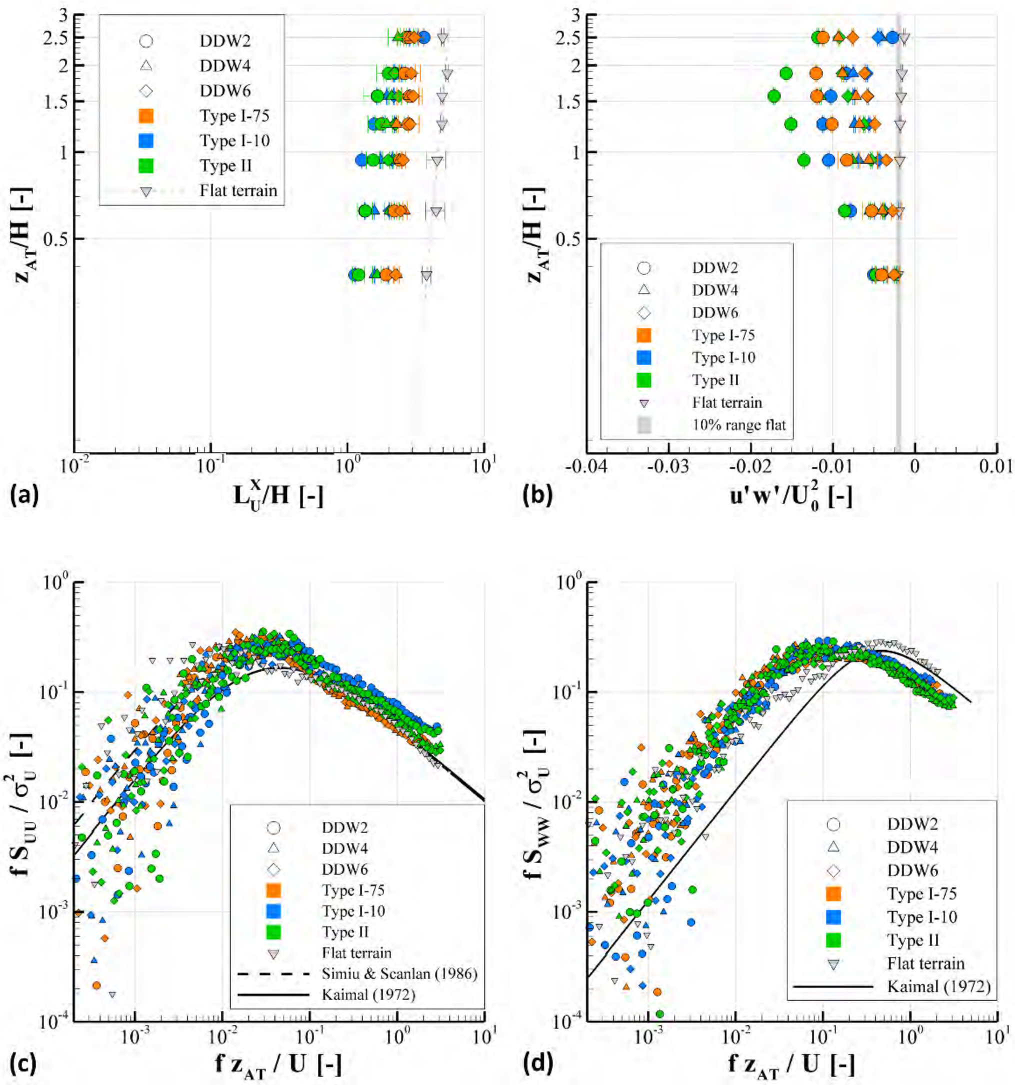

Figure 7-22. Vertical (a, b) profiles of the mean dimensionless longitudinal integral length scales (a) and vertical turbulent fluxes (b), and spectral distributions of longitudinal (c), and vertical (d) turbulent energy at $z/H = 0.38$ above the Extended downwind subdomain (*DDW*).

7.5 Summary

Main findings regarding mean flow interactions with the ridges are summarised and discussed. This discussion is region-specific and addresses the flow subdomains (defined in Fig. 7-1) in the same order as presented in the previous subchapter.

7.5.1 Upwind subdomain

Flows are expectedly the least affected of all subdomains of the ridges. Maximal effects of the orography on the flow (or differences to the approach flow) are observed in the immediate longitudinal vicinity of the ridges, at heights nearest to the surface. Mean velocities exhibit the largest sensitivity of all mean parameters, as highlighted by the larger upstream distances where differences to the approach flow profiles are first observed. Upstream effects of the ridges on the mean turbulence are comparatively less expressive than the velocity. When deviations of the turbulence parameters from the reference data are noticeable, these occur at closer distances to the ridges than for the velocities. These trends mirror findings made in the Literature. For example, Cao & Tamura (2006) and Gong & Ibbetson (1989) report decreases of longitudinal velocity and increases of the corresponding fluctuations relative to the approach flows at the foot of symmetric ridges. In particular, the longitudinal velocity profile obtained above *B1* of the *Type I-10* ridge is consistent with the vertical profiles obtained above the ridge ($\gamma \approx 14°$) modelled by Gong & Ibbetson (1989).

Inclinations of the windward slope (γ) of the ridges are clearly influential on the turbulence upstream from the ridges. Increases in slope steepness result in larger deviations from the approach flow characteristics. Of the mean turbulence parameters, this is most evident from the profiles of the mean velocity fluctuations and the vertical fluxes. Upwind distances from the ridges where the approach flow is affected also increase with increasing slope steepness. This is ascertained from the longitudinal distances where effects of the ridges on the upwind mean flow parameters first become evident at two measurement heights above the terrain: $z_{AT}/H = 0.63$ and 1.25, in Table 7-6. Effects of the ridges on the velocities and velocity fluctuations are assumed when values fall outside a 10% bandwidth centred on the corresponding mean value of the approach flow data. Effects are presumed when data falls outside the confidence intervals of the reference flow data for fluxes and integral length scales. Mean velocities are affected furthermost from all the ridges and distances increase with increasing windward slope inclinations. The turbulence statistics also exhibit slope dependence, albeit at shorter distances from the ridges.

Differences between the heights at which ridge effects first occur are smaller when compared to slope effects.

Table 7-6. Dimensionless longitudinal positions of the Upwind subdomain (*UpW*) where ridge effects are first observed for each mean flow parameter, at $\mathrm{z/H} = \mathbf{0.63}$ and $\mathbf{1.25}$ for all ridge domains.

	heights above local terrain					
	$z_{AT}/H = 0.63$ ($z_{AT} = 50\ m$)			$z_{AT}/H = 1.25$ ($z_{AT} = 100\ m$)		
	Type I-75	***Type I-10***	***Type II***	***Type I-75***	***Type I-10***	***Type II***
$\boldsymbol{U/U_0}$	5.46	2.34	5.46	5.46	1.56	3.90
$\boldsymbol{V/U_0}$	5.46	3.12	5.46	5.46	2.34	5.46
$\boldsymbol{W/U_0}$	5.46*	3.12	3.90**	5.46	2.34	3.90
$\boldsymbol{\sigma_U/U_0}$	3.90	no effect	3.90	3.90	no effect	3.90
$\boldsymbol{\sigma_V/U_0}$	3.12	0.78	2.34	3.90	0	3.90
$\boldsymbol{\sigma_W/U_0}$	5.46*	no effect	3.90**	2.34	no effect	1.56
$\boldsymbol{u'w'/U_0^2}$	3.90	no effect	3.90**	3.12	no effect	2.34
$\boldsymbol{u'v'/U_0^2}$	1.56*	no effect	0.78	62.5	no effect	no effect
$\boldsymbol{L_U^X/H}$	3.12	0.78	1.56	1.56	0	1.56

7.5.2 Windward slope subdomain

Flows maintain similar windward slope inclination dependences as those observed at the near-ridge of the upwind subdomain, but generally exhibit larger deviations compared to the reference data. Flows decelerate relative to the approach flow near the foot of the ridges, the magnitudes of which are dependent on the slope inclination. Longitudinal (U/U_0) and vertical (W/U_0) components of the mean velocity exhibit opposite developments throughout the uphill positions, U/U_0 increases (accelerates) and W/U_0 decreases with decreasing distances to the crests (*Cr*). Similar tendencies are observed above the 2D ridges modelled by Cao & Tamura (2006), Gong & Ibbetson (1989), and Loureiro et al. (2008).

With the exception of the longitudinal integral length scales (L_U^X/H), all mean turbulence parameters exhibit increases in magnitude compared to the corresponding approach flow characteristics. L_U^X/H tends to decrease relative to the approach flow values, energy-intensive eddies decreasing with increases of slope steepness. The dependence of the mean turbulence on the slope inclination is expectedly stronger than observed upwind from the ridges, as exemplified by the larger magnitudes of turbulence data of the steepest slope ($\gamma = 75°$) relative to the smallest inclination ($\gamma = 10°$). Flow above the latter provides the closest resemblance to the approach flow characteristics, data generally contained within the related confidence intervals This mirrors the trends of longitudinal turbulence (mean fluctuations) above the corresponding windward slope positions of the ridges used by Cao & Tamura (2004) and Takahashi et al. (2002), both with small inclinations of the slopes ($\gamma \approx 16°$ and $\approx 18°$, respectively). The lateral velocity fluctuations produce the largest increases of magnitude compared to the approach flow above the steepest slope, overpowering the longitudinal counterpart at the near-surface. This indicates the transferral of longitudinal turbulent energy to lateral directions due to streamwise flow blockage posed by the steep slope ($\gamma = 75°$). Increases of the peak magnitudes of lateral spectral energy relative to those of the longitudinal components support this observation.

Maximum differences of the mean flow parameters compared to the reference data provide further evidence of the influence of the inclination of the slope on the uphill flows, data from $z_{AT}/H = 0.63$ listed in Table 7-7. The largest differences between the horizontal components are observed at the furthermost positions from the crests, whereas the maximum differences between vertical components occur at near-crest locations.

Table 7-7. Maximum absolute differences between ridge and approach flow datasets at $\mathrm{z/H} = \mathbf{0.63}$ above the Windward slope subdomain (*WW*) and corresponding dimensionless longitudinal positions.

	Reference data	Type I-75		Type I-10		Type II	
		maximum difference	position ($-x/L_R$)	maximum difference	position ($-x/L_R$)	maximum difference	position ($-x/L_R$)
$\boldsymbol{U/U_0}$	0.737	−0.535	0.85	−0.085	0.90	−0.231	0.90
$\boldsymbol{V/U_0}$	−0.027	+0.005	0.52	+0.004	0.10	−0.008	0.62
$\boldsymbol{W/U_0}$	−0.014	+0.467	0.52*	+0.108	0.31	+0.225	0.31*
$\boldsymbol{\sigma_U/U_0}$	0.097	+0.040	0.90	−0.004	0.21	+0.020	0.90
$\boldsymbol{\sigma_V/U_0}$	0.070	+0.100	0.85	+0.006	0.31	+0.023	0.52
$\boldsymbol{\sigma_W/U_0}$	0.051	+0.049	0.42*	+0.006	0.31	+0.015	0.31*
$\boldsymbol{u'w'/U_0^2}$	−0.0019	−0.0044	0.42*	+0.0002	0.10	−0.0009	0.31*
$\boldsymbol{u'v'/U_0^2}$	−0.0003	+0.0006	0.90	−0.0006	0.10	−0.0005	0.90
$\boldsymbol{L_U^X/H}$	4.435	−4.132	0.85	−0.977	0.85	−2.350	0.74

7.5.3 Leeside slope subdomain

The largest increases of turbulence compared to the approach flow are generally observed above the leeside slopes. Similar to the previous subdomain, the majority of the maximum differences to the approach flow are observed at the furthermost streamwise locations from the crests. This is exemplified by the maximum differences of the turbulence parameters relative to the reference data (at $z_{AT}/H = 0.63$), displayed in Table 7-8. The main modification from the mean flows above the windward slopes is the occurrence of flow separation at the crests of all ridges and the generation of recirculation zones above the leeside slopes (extending into the downwind subdomain). Flow dynamics within these wake regions are dominated by turbulence. This replicates the findings of Cao & Tamura (2006), Kim et al. (1997), Loureiro et al. (2008), and Takahashi et al. (2002), for example, all reporting the creation of recirculation zones downstream from the crests of 2D ridges. While significantly affected above the leeside slope, no longitudinal flow reversal characteristics are observed above the ridge modelled by Gong & Ibbetson (1989).

Table 7-8. Maximum absolute differences between ridge and approach flow datasets at $\mathrm{z/H} = \mathbf{0.63}$ above the Leeside slope subdomain (*LW*) and corresponding dimensionless longitudinal positions.

	Reference data	**Type I-75**		**Type I-10**		**Type II**	
		maximum difference	position (x/L_R)	maximum difference	position (x/L_R)	maximum difference	position (x/L_R)
$\boldsymbol{U/U_0}$	0.737	−0.714	0.74	−0.758	0.90	−0.801	0.90
$\boldsymbol{V/U_0}$	−0.027	+0.042	0.85	+0.013	0.90	+0.049	0.90
$\boldsymbol{W/U_0}$	−0.014	+0.214	0.10	+0.090	0.42*	+0.186	0.10
$\boldsymbol{\sigma_U/U_0}$	0.097	+0.192	0.21	+0.055	0.74	+0.109	0.42
$\boldsymbol{\sigma_V/U_0}$	0.070	+0.162	0.31	+0.055	0.62	+0.115	0.42
$\boldsymbol{\sigma_W/U_0}$	0.051	+0.152	0.31	+0.048	0.62*	+0.095	0.42
$\boldsymbol{u'w'/U_0^2}$	−0.0019	−0.0240	0.31	−0.0059	0.62*	−0.0107	0.42
$\boldsymbol{u'v'/U_0^2}$	−0.0003	−0.0032	0.31	−0.0004	0.62	+0.0001	0.52
$\boldsymbol{L_U^X/H}$	4.435	−4.297	0.74	−4.376	0.74	−4.296	0.52

Recirculation zones of the flows in the vertical (UW) planes above the leeside slopes are characterised by longitudinal mean flow reversal ($U/U_0 < 0$), first observed at $z_{AT}/H = 0.38$ above $x/L_R \approx 0.3$ downstream from the crests of *Type I-10* and *Type I-75* ridges (above $x/L_R \approx 0.4$ for *Type II*). Turbulence characteristics of the recirculation zones are dependent on inclinations of both slopes. Larger windward slope inclinations (γ) lead to increases of all components of the mean turbulence, indicating that the effects of the windward slope on the dynamics of the recirculation zones dominate relative to those produced by the leeside slope. Accordingly, the largest increases of the turbulence parameters relative to the reference data correspond to the steepest windward slope.

Horizontal flow separation generated at the side slopes of the ridges is a common characteristic of flows above 3D hills (Chapter 4). Increases of the differences of the lateral velocities relative to the reference data in Table 7-8 indicate the occurrence of horizontal flow separation. This is most notable on the flows above the leeside slopes of *Type I-75* and *Type II* ridges, where lateral flow reversal relative to the previous subdomains is observed. Lateral components of the velocity fluctuations strongly overpower the longitudinal components at $z_{AT}/H \leq 1.25$ above the leeside slopes of *Type I-10* and *Type II* ridges. This indicates the occurrence of horizontal flow separation at the side slopes (at $Y \approx \pm 845\ m$), which produce increases of lateral turbulence above the centreline of the measurements ($Y = 0$). This trend is consistent with that reported by Hansen & Cermak (1975), who observe that flow separation affects the flow along the centreline of a 3D hill. Peaks of lateral spectra also overpower the longitudinal counterparts above the leeside slopes of these ridges, which supports these findings. Shifts of the peaks of longitudinal spectral energy at $z_{AT}/H = 0.38$ to higher frequency ranges, exclusive to the *Type I-75* ridge above the previous subdomains, extend to all ridge geometries above the leeside slope. These are also observed for lateral and vertical spectral distributions, in particular at the streamwise location nearest to the crests ($x/L_R \approx 0.3$), but less expressive than the frequency shifts of the longitudinal components. Further discussions on this topic are reserved for Chapter 9.

7.5.4 Downwind and extended downwind subdomains

Recirculation zones of all ridges prolong into the downwind region. Within this subdomain, longitudinal flow reversal characteristics cease first for *Type I-75* at $X \approx 2H$ from the foot of the leeside slope (*B2*). This is outlasted by the longitudinal flow reversal of the other ridges, which extend to $X \approx 8H$ from *B2*. This outlasts the recirculation zones obtained by Loureiro et al. (2008), only restricted to the leeside slope of 2D ridges, but is more consistent with the findings of Cao & Tamura (2006) and Takahashi et al. (2002), which present longitudinal flow reversal at distances up to $X \approx 5H$ and $\approx 6H$ (respectively) downwind from the ridges. Based on negative velocities at $z_{AT}/H = 0.38$, the largest absolute length of the recirculation zones (X_{RZ}) is observed for *Type II* with $X_{RZ} \approx 9H$. This is followed by the lengths of the recirculation zones of *Type I-75*, $X_{RZ} \approx 7.5H$, and *Type I-10*, with $X_{RZ} \approx 6.5H$. The estimated length of the recirculation zone of *Type II* is in good agreement with that of a triangular 2D ridge of similar slopes ($\gamma \approx 30°$) modelled by Snyder & Britter (1987), who report separated flow that lasts up to $X \approx 8H$ from the crest.

The largest magnitudes of all components of the velocity fluctuations are observed above the streamwise positions downwind from the *Type I-75* ridge. Increases of turbulence relative to the leeside slope and the maxima of the turbulence parameters of the *Type I-10* ridge are found at the furthermost positions from the ridge. Maximum differences to the approach flow at $z_{AT}/H = 0.63$, in Table 7-9, exemplify these characteristics. The largest absolute increases of fluxes are observed at the furthermost longitudinal position from the landforms ($X = 8H$), which demonstrates that the full extent of effects on turbulence are not captured within the downwind subdomain, thus outlasts the upwind effects. This justifies the supplemental measurements performed above the extended downwind subdomain.

Table 7-9. Maximum absolute differences between ridge and approach flow datasets at $\mathbf{z/H = 0.63}$ above the Downwind subdomain (*DW*) and corresponding dimensionless longitudinal positions.

	Reference data	Type I-75		Type I-10		Type II	
		maximum difference	position (x/H)	maximum difference	position (x/H)	maximum difference	position (x/H)
$\boldsymbol{U/U_0}$	0.737	-0.674	0	-0.787	1.56	-0.819	2.34
$\boldsymbol{V/U_0}$	-0.027	$+0.051$	1.56	$+0.053$	3.90	$+0.067$	3.90
$\boldsymbol{W/U_0}$	-0.014	$+0.043$	2.34*	$+0.048$	3.12**	$+0.056$	1.56
$\boldsymbol{\sigma_U/U_0}$	0.097	$+0.133$	0	$+0.087$	5.46	$+0.089$	5.46
$\boldsymbol{\sigma_V/U_0}$	0.070	$+0.139$	1.56	$+0.098$	8.08	$+0.111$	5.46
$\boldsymbol{\sigma_W/U_0}$	0.051	$+0.144$	2.34*	$+0.117$	8.08**	$+0.123$	8.08
$\boldsymbol{u'w'/U_0^2}$	-0.0019	-0.0184	8.08*	-0.0133	8.08**	-0.0108	8.08
$\boldsymbol{u'v'/U_0^2}$	-0.0003	-0.0021	8.08	-0.0012	8.08	$+0.0012$	2.34
$\boldsymbol{L_U^X/H}$	4.435	-4.078	0	-4.333	0	-4.164	5.46

The full available longitudinal distance downwind from the ridges ($X \approx 26H$) is short of capturing the location where turbulence parameters achieve full convergence with the approach flow. The closest agreement to the vertical profiles of the approach flow is generally observed nearest to the surface. Above the furthermost downwind position, turbulence parameters achieve the closest agreement between different ridge domains, in particular at $z_{AT}/H \leq 1.25$. This indicates negligible slope effects with regard to the blockage caused by the ridges, which supports the lack of agreement with the reference data. The same conclusion is reached by Arya & Gadiyaram (1986), who observe independence of mean turbulence in the far-wake of 3D hills relative to the slopes. Above the furthermost positions from the ridges, the flow of the *Type I-75* ridge is closest to readjusting to the approach flow characteristics (particularly integral length scales and vertical fluxes). Oppositely, the *Type II* ridge presents the largest differences to the approach flow. This is better understood from the minimum differences of the mean flow parameters for each ridge domain relative to the reference data at $z_{AT}/H = 0.63$, displayed in Table 7-10.

Table 7-10. Minimum absolute differences between ridge and approach flow datasets at $\mathrm{z/H} = \mathbf{0.63}$ above the Extended downwind subdomain (*DDW*) and corresponding dimensionless longitudinal positions.

	Reference data	**Type I-75**		**Type I-10**		**Type II**	
		minimum difference	position (x/H)	minimum difference	position (x/H)	minimum difference	position (x/H)
$\boldsymbol{U/U_0}$	0.737	−0.064	26.3	−0.106	23.7*	−0.121	26.3
$\boldsymbol{W/U_0}$	−0.014	−0.012	21.1	−0.009	23.7*	+0.005	18.5
$\boldsymbol{\sigma_U/U_0}$	0.097	+0.023	26.3	+0.019	23.7*	+0.026	26.3
$\boldsymbol{\sigma_W/U_0}$	0.051	+0.035	26.3	+0.043	23.7*	+0.045	26.3
$\boldsymbol{u'w'/U_0^2}$	−0.0019	−0.0006	26.3	−0.0018	23.7*	−0.0009	26.3
$\boldsymbol{L_U^X/H}$	4.435	−1.541	26.3	−2.410	23.7*	−2.281	26.3

8 FLOWS OVER VALLEYS

The present chapter is focused on the analyses of flows over idealised symmetric 3D valleys. The generated inflow boundary conditions are identical to the ridge campaign. A valley crossflow is modelled, with the valley axis oriented perpendicular to the mean approach flow direction. Valley experiments are focused on assessing the influence of the valley width on turbulence through systematic variations of constant amplitude. With the aim of providing further insight into terrain-induced turbulence characteristics, emphasis is also given to exploring transient analyses of the measurement data. This requires changes to the LDV setup to provide higher temporal resolutions than those obtained above the ridges. These are discussed in the first subchapter. This is followed by the verification of an equivalent modelled ABL flow relative to the single ridges. Measurement locations of the flows over valleys are presented in the third subchapter and data repeatability evaluated in the fourth. Following a different approach to Chapter 7, data analyses of the flows over valleys are centred on four specific longitudinal measurement points: the crests of the two ridges, the mid-valley location, and the furthermost downwind position from the valleys. Starting with the analyses of the flows above the crests of the first ridges, the fifth subchapter presents the results of the mean flows at these locations. The feasibility of transient turbulence data analyses from the present measurements is explored in the subsequent subchapter. This is followed by a discussion of the main findings in the final subchapter.

8.1 Experimental setup

The experimental setup for the valley campaign is generally identical to that of the ridge campaign. However, there are three major changes for the valley setups:

1. Position of the terrain-occupying model plate is shifted one plate ($\Delta x = 1500\ m$) upwind.
2. LDV probe is realigned for vertical plane (UW) measurements.
3. LDV settings are adjusted to maximise measurement data rates.

The first change arises from the insufficient allowable measurement distance downwind from the single ridges and enables measurements further downwind from the second ridge of the valleys. The quasi-identical mean flow characteristics over successive longitudinal positions above flat terrain (verified in Chapter 6) demonstrate that this change has minimal impact on the direct comparability between data from both experimental campaigns.

LDV probe positioning constraints near the surfaces of the ridge models result in the inability of performing UW measurements at $z_{AT} < 30\ m$. For the valleys, this issue is more significant due to the presence of the second ridge, which renders near-surface UW component measurements effectively impossible within the inner valley regions (particularly for the smaller valley widths). The vertical alignment of the probe with regard to the longitudinal direction, as exhibited in Figure 8-1, enables it to reach lower heights. With this alignment, the probe is only limited by its length in the longitudinal flow direction, equivalent to the probe diameter ($\approx 4\ cm$). With this approach, UW measurement heights as low as $z_{AT} = 12\ m$ (full-scale) are reachable.

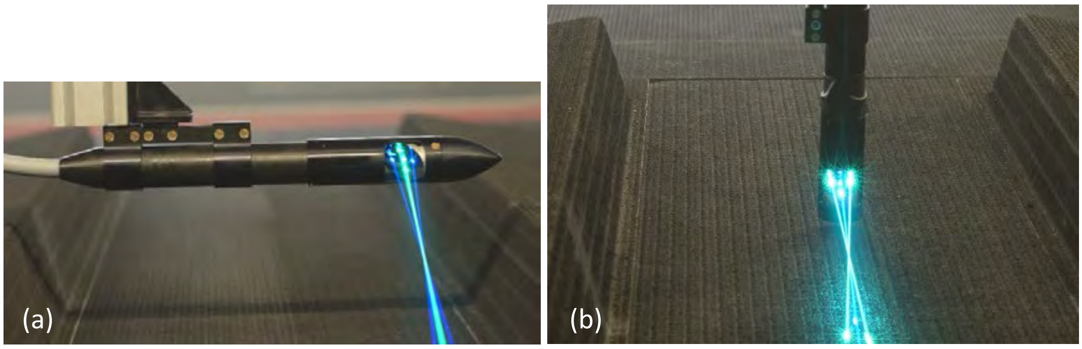

Figure 8-1. Horizontal (a) and vertical (b) LDV probe alignments above the inner valley of the same valley geometry.

The rationale behind the third change stems from the need to increase the resolution of the data to enable transient flow analyses. Flow measurements can be observed in real-time by the corresponding BSA software feature that resembles an oscilloscope displaying the amplitude of the filtered signal as function of its duration. This signal also contains inherent noise that is not removable (discussed in Chapter 5). When the velocity is very close to zero, burst amplitudes of the velocity readings can have similar magnitudes to those generated by noise. This affects the accuracy of time-dependent, small-scale turbulence measurements. To provide reliable time-dependent data, adjustments are made to the LDV settings to optimise the burst signal quality for the specific flow characteristics of the near-surface heights. This also yields larger data rates, which boosts the resolvability of smaller scales of turbulence. This setup is later applied by Diezel (2019) for the experiments related to flows over v-shaped valleys.

8.2 The modelled ASL

Reference measurements performed above flat, homogeneous terrain serve to evaluate if the modelled ASL flow characteristics are comparable to those of the single ridges. Vertical plane (UW) flows are sampled above the model section at equivalent heights to those of Chapter 6 with the LDV probe using the standard horizontal alignment (as in Fig. 8-1a). The present measurement position shifts upwind by $\Delta X = 1500\ m$ relative to the setup from the single ridges. This is motivated by the change of the terrain-occupying model plate. With this positional shift, relative positions of the terrain model location, are retained between ridge and valley setups.

8.2.1 Data quality

Direct comparability between mean data from both experimental campaigns requires the same temporal resolution of the measurements. Therefore, convergence tests are not repeated and the same measurement duration of two minutes (or approximately thirty-three hours at full-scale) is applied for the valley measurements.

As with the ridges, data uncertainties of the mean flow parameters result from repetition measurements performed at the same position under different conditions. 33 repetition measurement profiles (14 with UV and 19 with UW settings) are performed throughout the present campaign at the same longitudinal position ($X = 700\ m$) and for three heights ($Z = 12$, 50, and $100\ m$). Only 6 of the UW repetition profiles correspond to the vertical LDV probe alignment, whereas the remaining 13 are made with the horizontal alignment. Data uncertainties are categorised into the same three measurement height ranges (Δz_i) as those defined in Chapter 6. The resulting absolute data uncertainties are presented in Table E1 (Appendix E). As with the previous analyses, data uncertainties associated to the longitudinal flow components result from the combination of UV and UW measurements. Results exhibit increases of data uncertainty associated to the longitudinal components of the present setup compared to the single ridges.

Reynolds number (Re) independence tests also fulfil flow similarity criteria in equivalent terms to the flow above the single ridges. Within the scope of the valley campaign, no terrain-related similarity tests are performed. This is motivated by the Re independence previously verified above the crests and leeside slopes of the single ridges from which the present models originate.

8.2.2 ABL flow characteristics

Sharing the same inflow setup and surface conditions as the previous campaign, the modelled ABL flow of the valleys expectedly presents the same characteristics as those observed in Chapter 6. Vertical profiles of the UW mean flow parameters are presented in Figures E1 and E2 in Appendix E. Results compare data obtained at equivalent streamwise positions between the valleys and the single ridges. The largest deviations between setups are those of the longitudinal velocity, a maximum decrease of $\approx 10\%$ observed for the valley setup at $Z = 10\ m$. Vertical fluxes exhibit close agreement between experimental setups, the valley setup yielding a modelled ASL flow assumed $\approx 100\ m$ deep. Flow characteristics are consistent with moderately rough classed ABL flows, with $z_0 \approx 0.08\ m$ and $\alpha \approx 0.17$. Mean velocity fluctuations and integral length scales exhibit data convergence between setups at all heights.

8.3 Measurement positions

8.3.1 Study regions

Following a similar approach to that of the ridges, three subdomains represent the valley flows:

- Upwind – area upwind from the crest of the first ridge in the longitudinal flow direction.
- Inner valley – region between (and including) the ridge crests.
- Downwind – starting downwind from the crest of the second ridge in the longitudinal direction and extending to the furthest downwind position attainable with the traverse system.

8.3.2 Measurement positions

Every vertical profile of the valley measurements contains eight heights ranging from $z_{AT} = 12$ to $200\ m$ above local terrain, as presented in Table 8-1. Every measurement is made above the same centreline (symmetry plane) as the single ridges ($Y = 0$).

Table 8-1. Vertical coordinates of the valley measurements in absolute and dimensionless coordinates. Coordinates are above local surfaces and made dimensionless with valley depth ($\mathrm{H} = \mathbf{80\ m}$).

dimensionless heights z_{AT}/H $[-]$	absolute heights z_{AT} $[m]$
0.15	12
0.25	20
0.38	30
0.63	50
0.94	75
1.25	100
1.88	150
2.5	200

1.1.1.3 Upwind and Downwind subdomains

The upwind subdomain begins at the crest of the first ridge (hereby designated *Cr1*) and includes up to four upstream positions: the mid-slope (equivalent to *WW5* from the ridges), the foot of the windward slope of the first ridge (*B1*) and at distances $X = H$ and $2H$ upstream from *B1*. Due to the limited effects observed upwind from the single ridges, only measurements upwind of the smaller width valleys are made. This is intended to capture effects caused by the second ridge on the flow upwind from the first ridge. Equivalence between flow characteristics above the crests of the single ridges and *Cr1* of the present campaign indicates minimal effects of the second ridge on the mean flows upwind from the valleys. Therefore, upwind region analyses are neglected in the scope of this thesis.

The downwind subdomain begins at the crest of the second ridge (named *Cr2*) and contemplates the leeside mid-slope (equivalent to *LW5* of the single ridges), the downhill foot of the second ridge (*B2*) and seven downwind longitudinal distances from *B2* ranging from $X = H$ to $X = 32H$. Measurements made at the two furthermost distances from the valleys ($X = 24H$ and $32H$) are exclusively in the vertical plane (UW). Within the scope of the present thesis, only data from the furthermost downwind position (named *DW7*), located at $X = 32H$ from *B2*, is analysed.

1.1.1.4 Inner valley subdomain

In order to evaluate flows at corresponding locations between different valleys, the longitudinal measurement points originate from the mid-valley point (designated *MV*). Measurement positions are then defined moving upwind and downwind in constant amplitudes ($\Delta X = H$), starting from the mid-valley (*MV*). For all valleys, this procedure is performed upwind from *MV* until the crests of the first ridges (*Cr1*) or until a maximum amplitude of $\Delta X = 5H$ upstream from *MV* is reached. This approach is taken under the assumption that the mean flow upwind from *MV* exhibits the same characteristics as downwind from the corresponding single ridges for large valley widths. Downwind from *MV*, data from all corresponding positions ($\Delta X = H$) until the crests of the second ridges (*Cr2*) are sampled. The analyses of the flows above the inner valley subdomain are centred on three of the aforementioned positions: *Cr1*, *Cr2*, and *MV*.

8.4 Data repeatability

Less repetitive measurements are made for the valleys than for the single ridges. Thus, data uncertainties for the mean valley flow parameters rely on different sources. In the context of providing adequate measures of reproducibility in the absence of dedicated repetition data, three different approaches can be used: the same uncertainties from the ridge repetitions, the present repetitive uncertainties, or a mixture of both. The only repetition datasets associated to orography, data from the ridges are observed to affect the reproducibility of the measurements. Therefore, data uncertainties associated to valley measurements would expectedly increase with regard to those of the present ABL flow. Data uncertainties of the ridges do not contemplate the changes made to the present setup, also expected to affect the reproducibility of the valley measurements. Thus, the method likely to provide the most reliable data uncertainties is the combination of both aforementioned repetitive measurement datasets.

When using the data uncertainties of the single ridges, the adopted values of uncertainty of the valley data originate from equivalent positions of the ridges. Furthermore, correspondence between valley and ridge types is maintained for all cases. Table E2 (in Appendix E) presents the resulting data uncertainties above *Cr1* and Table E3 those for the remaining analyses positions (*MV*, *Cr2*, and *DW7*). The majority of the corresponding data uncertainties ($\approx 80\%$ of all values) originate from the present ASL repetitive measurements, particularly those of the longitudinal components. This indicates a misalignment of the vertical probe setting relative to the longitudinal direction for vertical plane (UW) measurements.

The assessment of the directional repeatability of the terrain measurements uses data from 1844 measurement positions (3D). This includes both instances of the probe orientations for UW measurements, 1547 of the measurements performed with the vertical probe orientation and 297 with the standard horizontal orientation, the latter downwind from the valleys. Figure E3 (in Appendix E) displays the relative frequencies of the differences between longitudinal velocities (U/U_0) measured in both planes (Fig. E3a), and of the vertical plane (UW) measurements made with horizontal and vertical probe alignments (Fig. E3b). UW measurements made with the vertical probe alignment exhibit large shifts of the data relative to the horizontal setup. This is a clear indication of an undesired tilt of the probe relative to the perpendicular direction of the flow, resulting in an oblique ellipsoid with regard to the main flow direction. The data uncertainties presented above contemplate this effect.

3D approach flow/reference data

Following the same approach as the single ridges, data from the furthermost upstream position from the least inclined windward slope (*Type I*), termed *UpW2* and located $X = 2H$ upstream from the foot of the first ridge, is used as 3D approach flow case. As observed in Chapter 7, flow disturbances upwind from the corresponding single ridge (*Type I-10*) are negligible with regard to the inflow characteristics of the model section. Resulting profiles of the vertical plane mean flow parameters are in Figures E4 to E6 in Appendix E. The best agreement between datasets is observed for the velocity fluctuations, both components converging at all heights of the respective vertical profiles. Vertical fluxes and integral length scales exhibit similar shapes between the three data sources. Hence, *UpW2* is suitable in providing reference data for the valley measurements.

8.5 Mean flows over valleys

Characteristics of the mean flows above both crests (*Cr1* and *Cr2*), the mid-valley (*MV*), and the furthest downwind location from the valleys (*DW7*) are analysed here.

8.5.1 Crest of first ridge (*Cr1*)

Vertical profiles of the longitudinal and vertical flow parameters obtained above *Cr1* are displayed in Figures 8-2 (*Type I* valleys) to 8-4 (*Type III*). Data related to the corresponding single ridges is represented by dark grey square symbols. Results of the lateral flow parameters and the distributions of spectral energy at the lowest measurement height above local terrain ($z_{AT}/H = 0.15$) are in Figures E7 and E8 in Appendix E. Speed-up relative to the approach flow is observed above *Cr1* of all ridge geometries and the maximal increases of longitudinal velocity (U/U_0) are observed at $z_{AT}/H = 0.15$, the largest of which corresponds to *Type III* ($\approx 45\%$) and followed by *Type I* ($\approx 40\%$) and *Type II* ($\approx 25\%$) valleys. Thus, windward slope inclinations clearly affect the speed-up characteristics above the crests. Slopes also influence the vertical velocities (W/U_0), a maximum increase (roughly two orders of magnitude) observed for *Type II*.

Effects of the slope are also observed for the velocity fluctuations, but generally less expressive than the velocities. Longitudinal components (σ_U/U_0) increase relative to the reference data for *Type II* (maximum of $\approx 20\%$ at $z_{AT}/H = 0.15$) but decreases for *Type I* (decrease of $\approx 15\%$) and *Type III* ($\approx 10\%$) valleys. The predominance of the steep slope of *Type II* also extends to lateral and vertical fluctuations, both presenting maximum increases of roughly twofold relative to the approach flow. With the exception of *Type II*, vertical fluxes and integral length scales present broad agreement with the approach flow. Longitudinal and lateral spectra present small increases of peak energy (maximum $\approx 10\%$) relative to the reference data for *Type II* and *Type III* valleys, while peaks of the vertical components of the same geometries decrease (maximum of $\approx 30\%$ for *Type III*). Shifts of the frequencies of the spectral peaks to higher ranges (roughly an order of magnitude) are observed for longitudinal and vertical components, whilst those of the lateral spectra exhibit shifts to smaller frequency ranges.

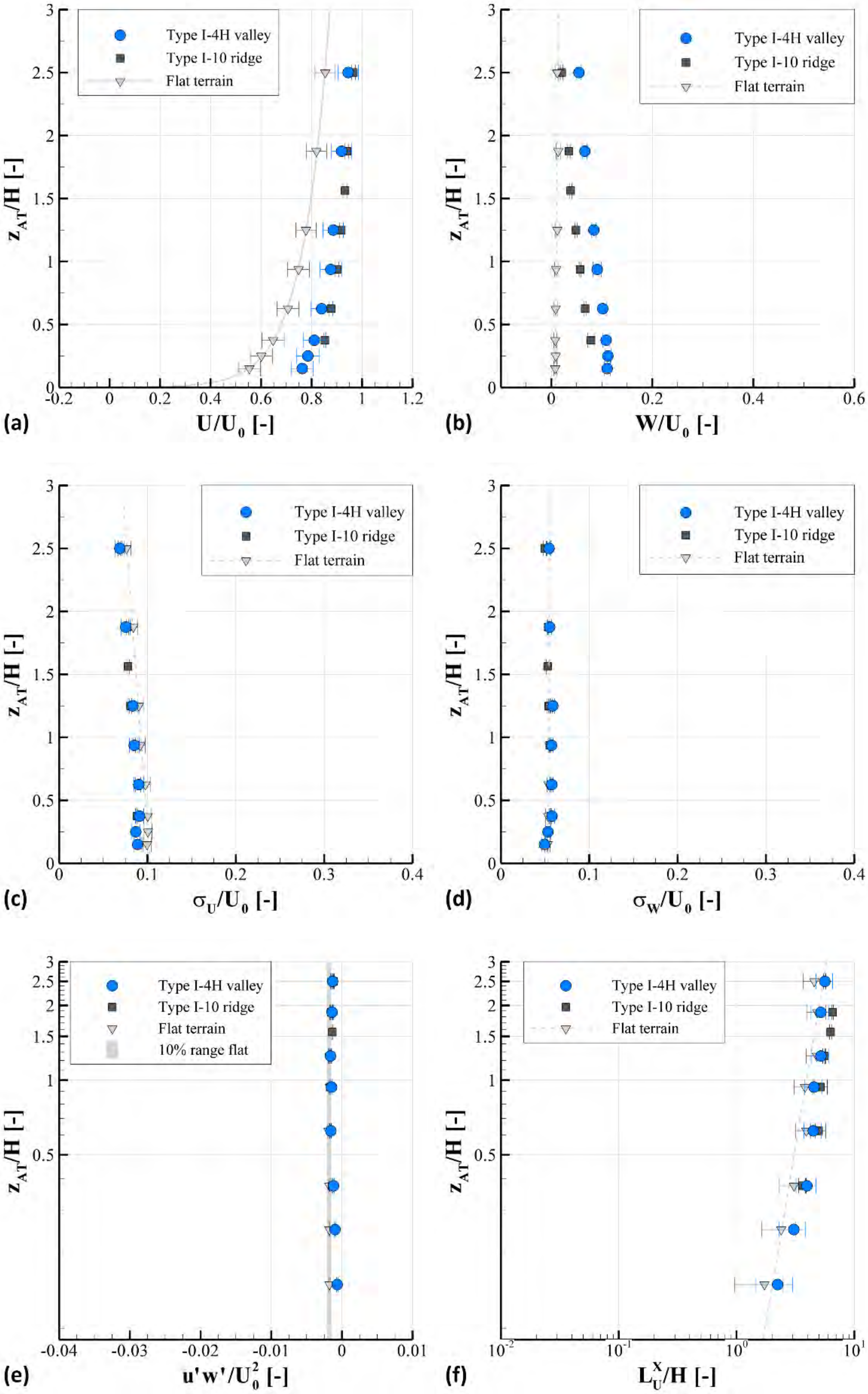

Figure 8-2. Vertical profiles of the mean dimensionless longitudinal (a, c, f) and vertical (b, d, e) velocities (a, b), velocity fluctuations (c, d), turbulent fluxes (e), and integral length scales (f) above the crests of the first ridge of valley *Type I* and ridge *Type I-10*.

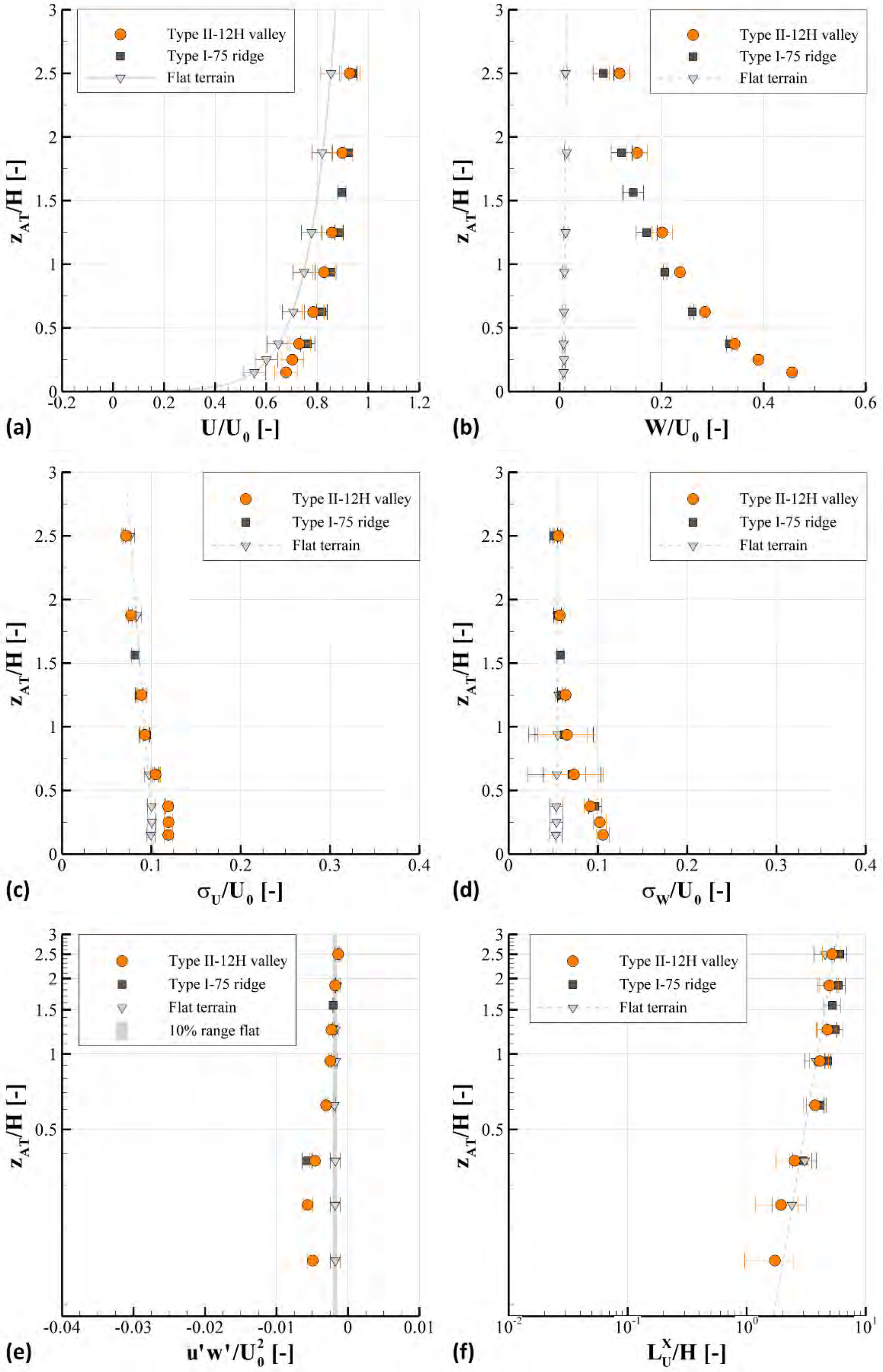

Figure 8-3. Vertical profiles of the mean dimensionless longitudinal (a, c, f) and vertical (b, d, e) velocities (a, b), velocity fluctuations (c, d), turbulent fluxes (e), and integral length scales (f) above the crests of the first ridge of valley *Type II* and ridge *Type I-75*.

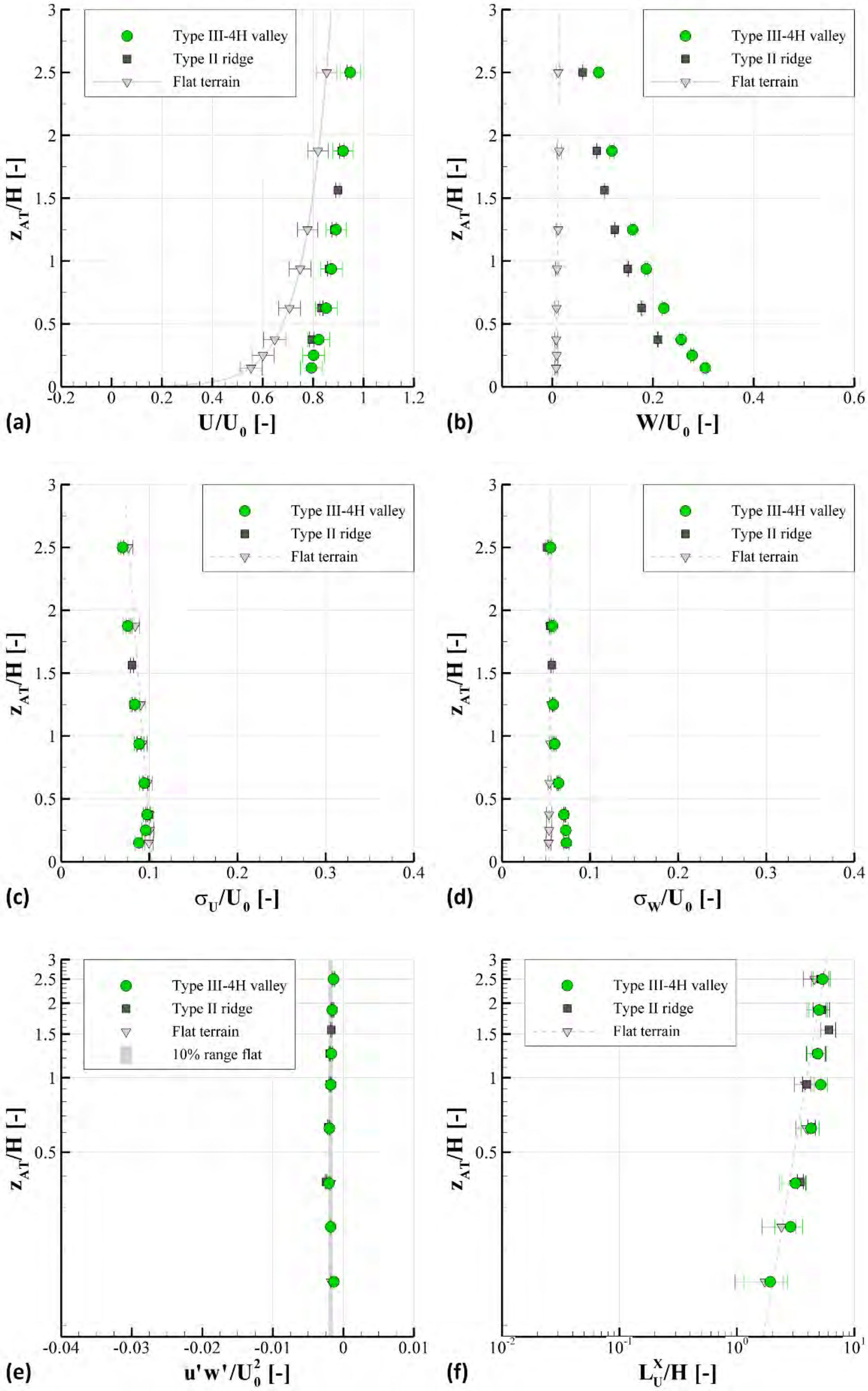

Figure 8-4. Vertical profiles of the mean dimensionless longitudinal (a, c, f) and vertical (b, d, e) velocities (a, b), velocity fluctuations (c, d), turbulent fluxes (e), and integral length scales (f) above the crests of the first ridge of valley *Type III* and ridge *Type II*.

8.5.2 Mid-valley (MV)

Vertical profiles of the mean velocities and fluctuations above *MV* of *Type I* are displayed for all valley widths in Figure 8-5. In general, profiles of the mean flow parameters resemble that of $x/H \approx 2$ (*DW3*) downwind from the corresponding single ridge, *Type I-10* (Fig. 7-16). Accordingly, an inflection point of the vertical profiles of the longitudinal velocity (U/U_0) is observed at approximately ridge height ($z_{AT}/H < 1.25$). At heights below this point, longitudinal flow deceleration relative to the approach flow is maximal with reversal of U/U_0 at the near-surface. Above, profiles of U/U_0 tend to converge with the reference flow data. This behaviour is consistent with the existence of a steady recirculation zone in the wake region downstream from the first ridge, which is bounded by free shear layer flow above (Kaimal & Finnigan, 1994). Effects of the variations of valley width on U/U_0 are most evident at $z_{AT}/H = 0.94$, where the maximum U/U_0, of the largest width ($A = 12H$), is $\approx 90\%$ larger than the minimum ($A = 4H$). Lateral and vertical components are relatively less affected.

Effects of the terrain on the velocity fluctuations are restricted to $z_{AT}/H \leq 1.25$, the dominant magnitudes corresponding to the largest valley widths. Maximum increases over the approach flow of about twofold and threefold are observed for longitudinal (σ_U/U_0) and lateral (σ_V/U_0) components (respectively) of $A = 10H$ ($z_{AT}/H = 0.94$). The maximum increase of roughly threefold of the vertical component (σ_W/U_0) is found for $A = 12H$ ($z_{AT}/H = 0.63$). σ_U/U_0 of the smallest width ($A = 4H$) is smaller than the approach flow at $z_{AT}/H \leq 0.63$. A maximum decrease of $\approx 20\%$ from the approach flow data is observed at $z_{AT}/H = 0.25$. σ_V/U_0 and vertical (σ_W/U_0) components exhibit similar width dependencies to σ_U/U_0, the largest scatter between data observed at $z_{AT}/H = 0.63$.

Mean fluxes and integral length scales are presented in Figure 8-6, together with the spectra at $z_{AT}/H = 0.15$. The largest increases of the vertical fluxes ($u'w'/U_0^2$) relative to the approach flow are found at $z_{AT}/H = 0.94$ and the maximal width dependence observed at $z_{AT}/H = 0.63$, where roughly an order of magnitude separates $u'w'/U_0^2$ of $A = 4H$ and $A = 12H$. Integral length scales (L_U^X/H) decrease relative to the approach flow, the largest decreases found at $z_{AT}/H = 0.63$, as is the largest width dependence of L_U^X/H. Here, L_U^X/H of $A = 6H$ decreases over two orders of magnitude with regard to the approach flow and $\approx 90\%$ compared to $A = 12H$. Spectra exhibit a clear width dependence of the peak energy frequencies. Longitudinal ($f \times S_{UU}/\sigma_U^2$) and vertical ($f \times S_{WW}/\sigma_U^2$) peaks occur at roughly an order of magnitude larger frequencies than the reference data, while peaks of the lateral components ($f \times S_{VV}/\sigma_U^2$) shift to smaller frequency ranges for all widths except $A = 4H$ and $12H$.

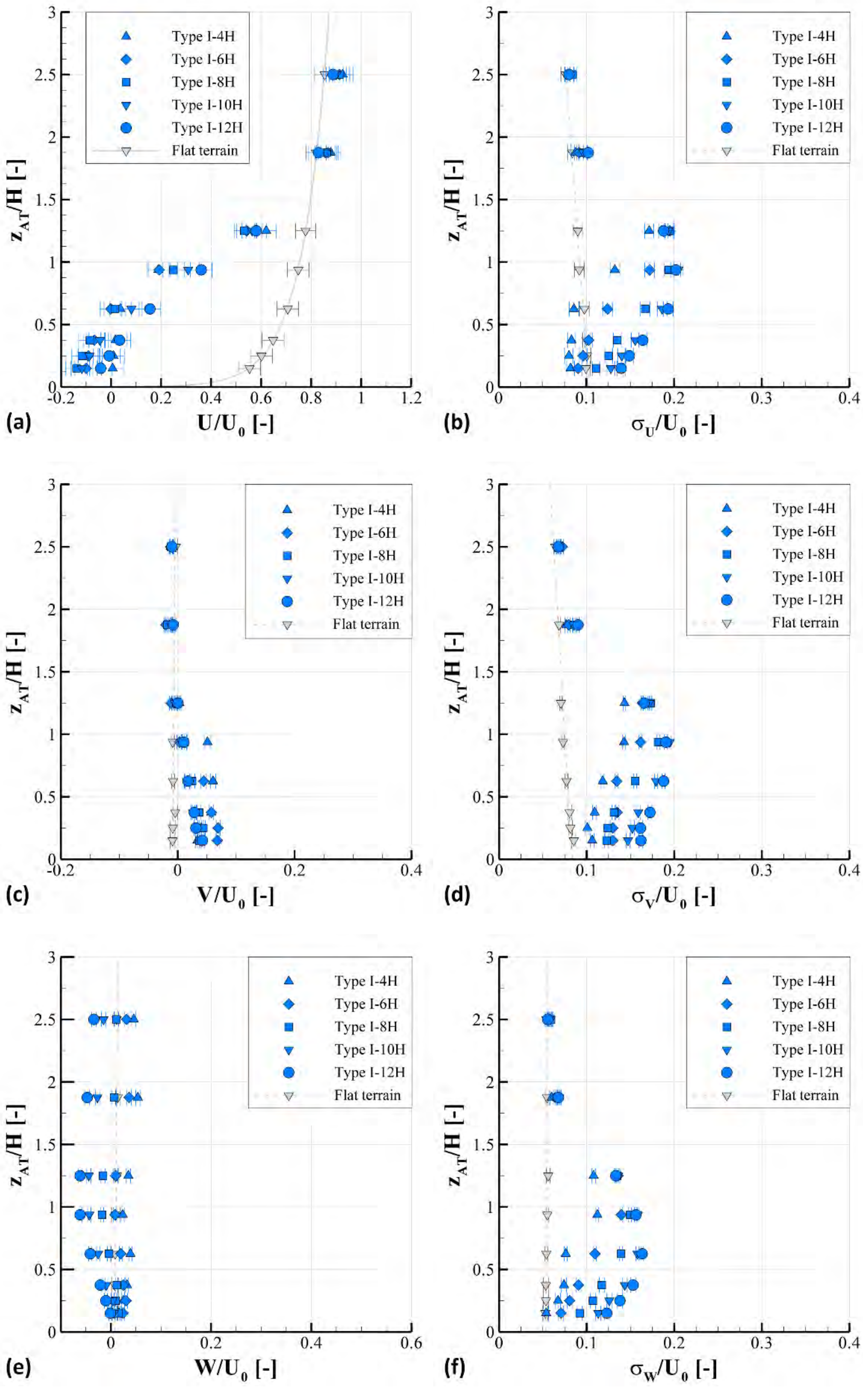

Figure 8-5. Vertical profiles of the mean dimensionless longitudinal (a, b), lateral (c, d), and vertical (e, f) velocities (a, c, e) and velocity fluctuations (b, d, f) above the mid-valley (*MV*) of *Type I* valleys.

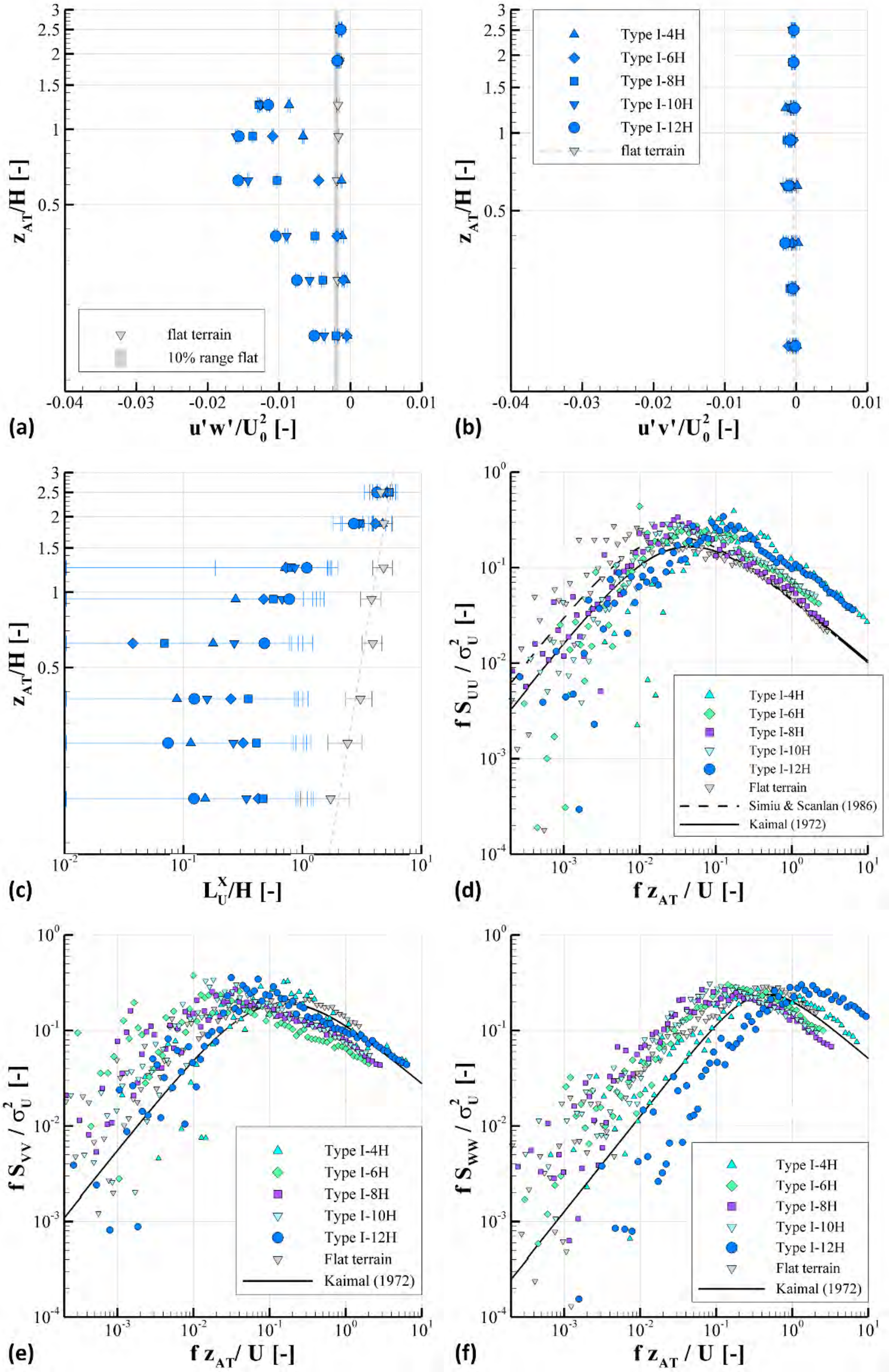

Figure 8-6. Vertical profiles of the mean dimensionless vertical (a) and horizontal (b) turbulent fluxes and integral length scales (c), and spectral distributions of longitudinal (d), lateral (e), and vertical (f) of turbulent energy at $z/H = 0.15$ above the mid-valley (*MV*) of *Type I* valleys.

Velocities and velocity fluctuations of *Type II* valleys are presented in Figure 8-7. Velocity profiles generally resemble those obtained above $x/H \approx 8$ (*DW7*) of the *Type I-75* single ridge. Reversal of longitudinal velocity (U/U_0) occurs at $z_{AT}/H \leq 0.38$ for $A = 12H$ and $14H$, less so for $A = 16H$. This indicates longitudinal proximity to the end of the recirculation zone generated by the first ridge for the valley of largest width. *Type II* valleys are less affected by valley width modifications relative to the other geometries. A near-constant difference of $\approx 70\%$ is observed between minimum and maximum U/U_0 ($A = 12H$ and $16H$, respectively). Profiles of all components of the fluctuations resemble those obtained above $x/H \approx 2$ (*DW3*) of *Type I-75* (Fig. 7.17). Longitudinal fluctuations (σ_U/U_0) present the largest increases over the reference data, the maximum roughly threefold at $z_{AT}/H = 1.25$ ($\approx 30\%$ larger than the maximum of *Type I*). Similarly, the largest increases of the lateral components (σ_V/U_0) over the approach flow are also found at $z_{AT}/H = 1.25$, the maximum of which about threefold ($A = 14H$). Effects of the width modifications are clearest at $z_{AT}/H = 0.63$, where σ_V/U_0 of $A = 14H$ overpowers $A = 12H$ by $\approx 15\%$. The largest valley width dependence of the vertical components (σ_W/U_0) is observed at $z_{AT}/H = 0.38$, where the maximum ($A = 16H$) constitutes a $\approx 15\%$ increase over the minimum ($A = 12H$).

Figure 8-8 exhibits the profiles of fluxes and integral length scales, together with the spectral distributions at $z_{AT}/H = 0.15$. The largest increases of magnitude of the vertical fluxes ($u'w'/U_0^2$) over the reference data are observed at $z_{AT}/H = 1.25$, the maximum roughly an order of magnitude. The maximal effect of the valley width modifications is observed at $z_{AT}/H = 0.63$, where the maximum ($A = 16H$) is $\approx 40\%$ larger than the minimum ($A = 12H$). At the same height, the largest width dependence of the profiles of L_U^X/H is also observed. Roughly an order of magnitude separates the minimum ($A = 12H$) and the maximum ($A = 16H$), the latter roughly an order of magnitude smaller than the approach flow data. Peak energy frequencies of the spectra are more affected by *Type II* above *MV* than by *Type I* valleys. This is most evident for the energy peaks of $A = 16H$, the peak of the longitudinal spectra ($f \times S_{UU}/\sigma_U^2$) occurring at roughly two orders of magnitude larger frequency than that of the reference data. In terms of energy content, the largest peak of $f \times S_{UU}/\sigma_U^2$ ($A = 12H$) corresponds to an increase of $\approx 60\%$ compared to the approach flow. Frequencies of the lateral spectra ($f \times S_{VV}/\sigma_U^2$) exhibit shifts of about an order of magnitude to smaller ranges relative to the reference data, except for $A = 16H$ that occurs at a larger frequency. A maximum increase of $\approx 95\%$ is observed for the peak of $f \times S_{VV}/\sigma_U^2$ of $A = 14H$ over the approach flow. All peaks of vertical spectra ($f \times S_{WW}/\sigma_U^2$) occur at frequencies contained within the same order of magnitude as the approach flow, the largest difference between peak frequencies corresponding to a $\approx 70\%$ decrease for $A = 12H$.

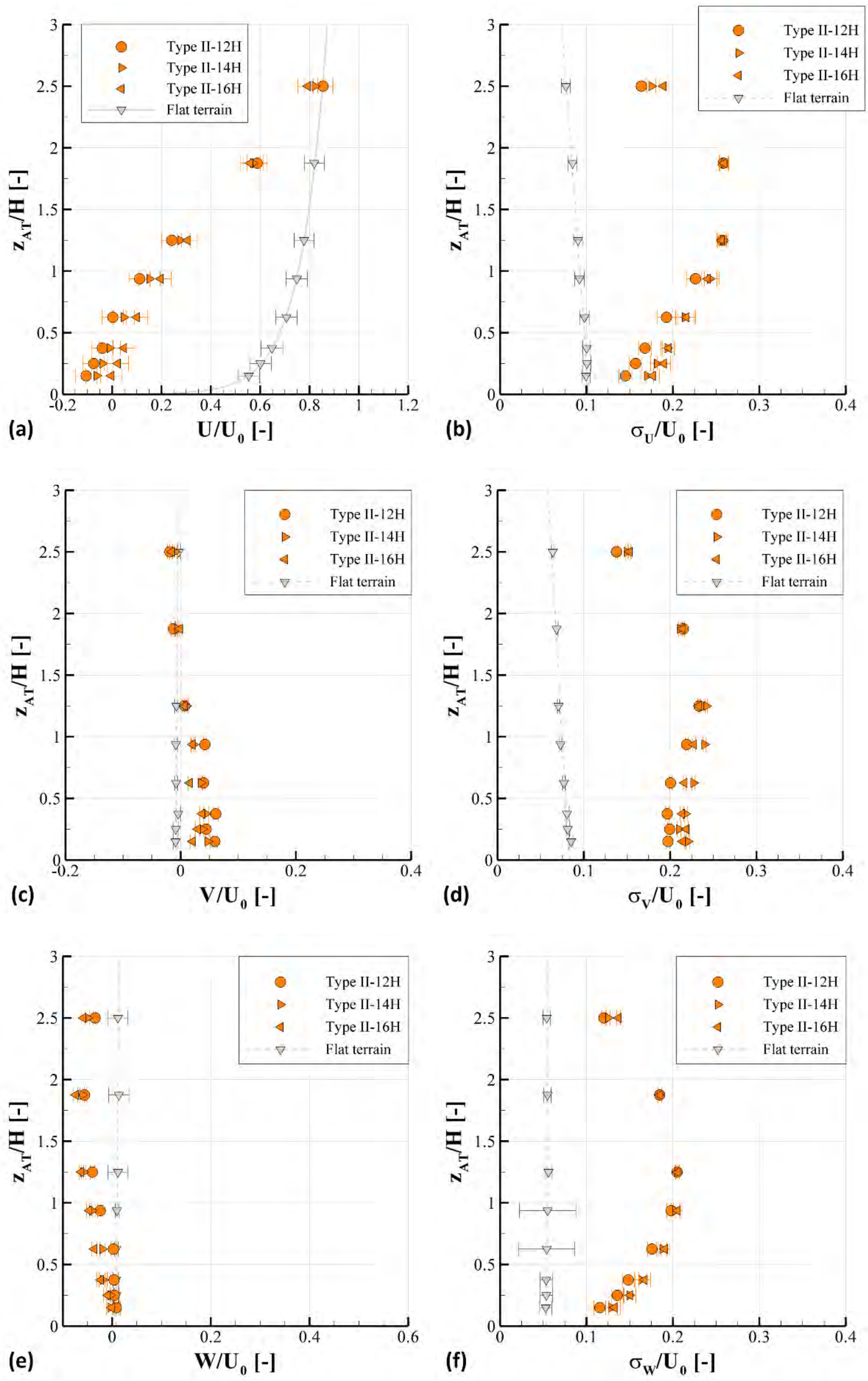

Figure 8-7. Vertical profiles of the mean dimensionless longitudinal (a, b), lateral (c, d), and vertical (e, f) velocities (a, c, e) and velocity fluctuations (b, d, f) above the mid-valley (*MV*) of *Type II* valleys.

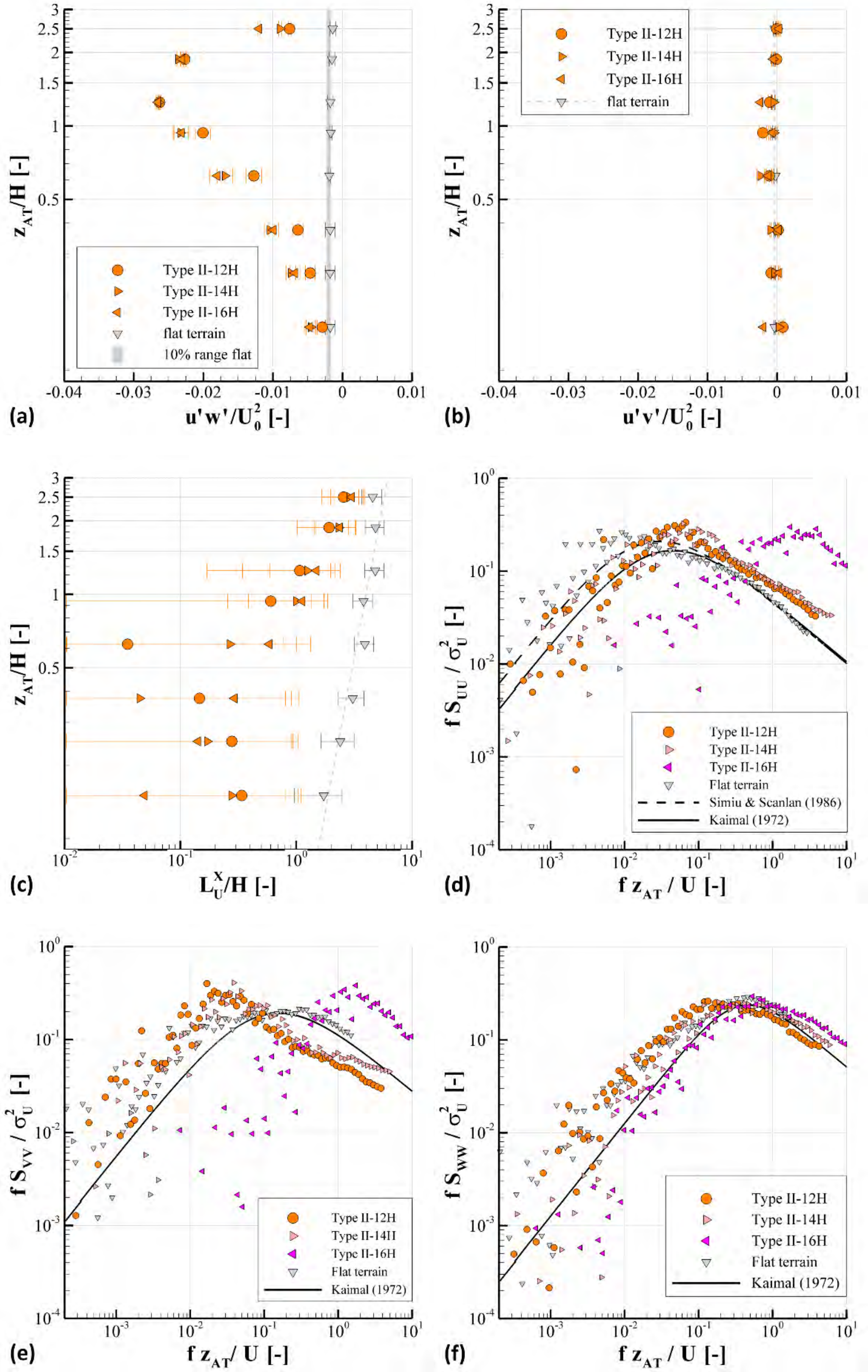

Figure 8-8. Vertical profiles of the mean dimensionless vertical (a) and horizontal (b) turbulent fluxes and integral length scales (c), and spectral distributions of longitudinal (d), lateral (e), and vertical (f) of turbulent energy at $z/H = 0.15$ above the mid-valley (*MV*) of *Type II* valleys.

Mean velocity and fluctuation profiles of *Type III* valleys are displayed in Figure 8-9. Profiles of the longitudinal velocities (U/U_0) exhibit similar characteristics to those observed at $x/H \approx 2$ (*DW3*) of the corresponding single ridge (Fig. 7-16). Reversal of U/U_0 occurs at $z_{AT}/H \leq 0.38$ for all valley widths, the magnitude of which is the largest observed of all valley types. Opposing the trends observed for the previous valleys, the maximum negative U/U_0 corresponds to the largest valley width ($A = 12H$). Relevant differences to the other valley geometries are also observed for lateral velocities (V/U_0), profiles exhibiting larger valley width dependence at $z_{AT}/H \leq 0.38$. Vertical velocities (W/U_0) are less affected at the near-surface. Velocity fluctuations follow the same width dependence as observed for the other valleys, the largest intensities observed for $A = 12H$. The largest magnitudes of all components are observed at $z_{AT}/H = 1.25$ and the most evident valley width dependence found at $z_{AT}/H = 1.88$. The maximum of the longitudinal fluctuations (σ_U/U_0) is $\approx 5\%$ smaller than that of *Type II* ($\approx 20\%$ larger than *Type I*). Similarly, the maximum lateral (σ_V/U_0) and vertical (σ_W/U_0) components are $\approx 10\%$ smaller than that of *Type II* ($\approx 10\%$ larger than *Type I*). The largest variability between data from different widths corresponds to a coarse twofold increase observed between minimum ($A = 4H$) and maximum ($A = 12H$) values of σ_W/U_0 at $z_{AT}/H = 1.88$.

Mean fluxes and integral length scales, as well as the spectra, are displayed in Figure 8-10. Vertical fluxes ($u'w'/U_0^2$) are smaller (in magnitude) than those of *Type II* (maximum decrease of $\approx 15\%$) and larger than *Type I* (maximum of $\approx 40\%$). The largest effects of the width modifications are observed at $z_{AT}/H = 1.88$, an order of magnitude separating maximum ($A = 12H$) and minimum ($A = 4H$) absolute values of $u'w'/U_0^2$. Horizontal fluxes ($u'v'/U_0^2$) are virtually invariant with height and less affected by valley width modifications. Integral length scales (L_U^X/H) present the closest general agreement to the approach flow characteristics. Spectral distributions are the least affected by the modifications of valley widths. This is highlighted by the agreement between peak energy frequencies of longitudinal ($f \times S_{UU}/\sigma_U^2$) and vertical ($f \times S_{WW}/\sigma_U^2$) spectra, unobserved for the previous valleys. The largest difference between peaks of $f \times S_{UU}/\sigma_U^2$ corresponds to the increase of $\approx 55\%$ that occurs between minimum ($A = 6H$) and maximum ($A = 12H$) values. The lateral spectra ($f \times S_{VV}/\sigma_U^2$) is the only component with frequency shifts of the energetic peaks of (at least) an order of magnitude, to smaller frequency ranges than the peaks of the approach flow. Valley width modification effects are translated by the increase of $\approx 90\%$ between smallest ($A = 4H$) and highest ($A = 12H$) energy peaks.

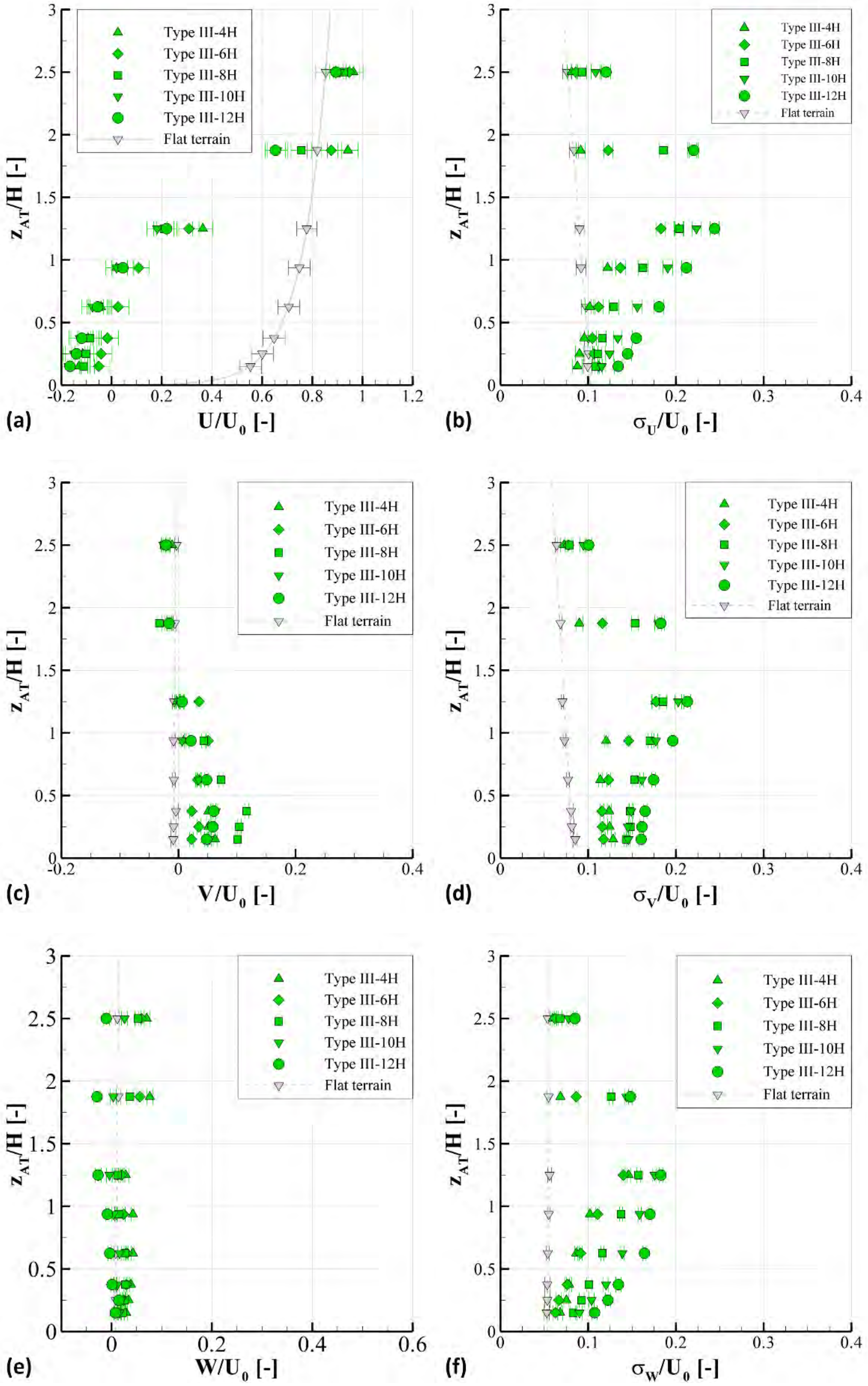

Figure 8-9. Vertical profiles of the mean dimensionless longitudinal (a, b), lateral (c, d), and vertical (e, f) velocities (a, c, e) and velocity fluctuations (b, d, f) above the mid-valley (*MV*) of *Type III* valleys.

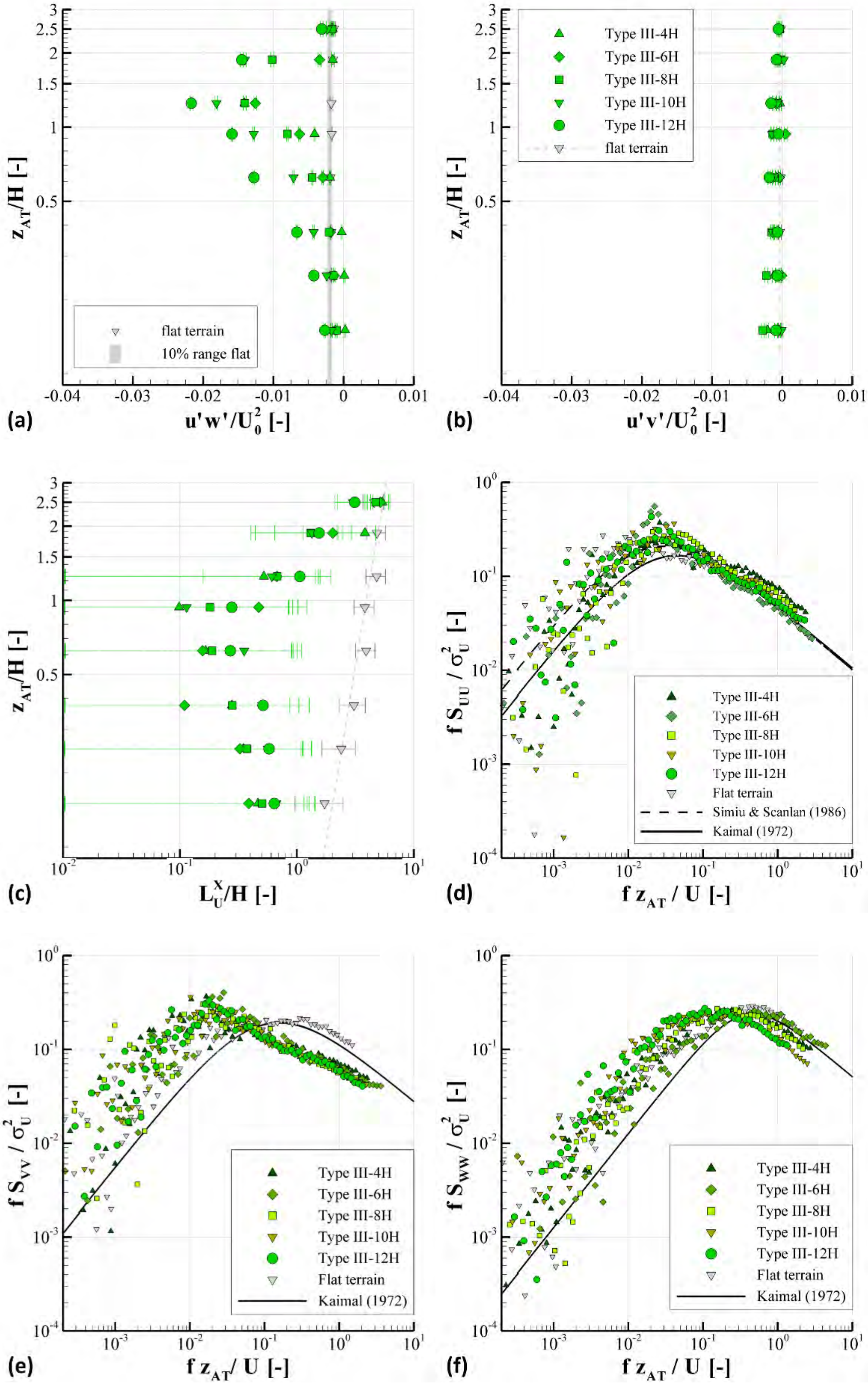

Figure 8-10. Vertical profiles of the mean dimensionless vertical (a) and horizontal (b) turbulent fluxes and integral length scales (c), and spectral distributions of longitudinal (d), lateral (e), and vertical (f) of turbulent energy at $z/H = 0.15$ above the mid-valley (*MV*) of *Type III* valleys.

8.5.3 Crest of second ridge (*Cr2*)

Results of the flows above the crest of the second ridge (*Cr2*) are analysed using the data from the crest of the first ridge (*Cr1*), together with the approach flow, as reference. Profiles from the crests are not directly comparable, as these do not share the same windward slopes due to the symmetric nature of the valleys. Data from *Cr1* serves as indication to how the flow develops between crests of the valleys. Results obtained for mean lateral and vertical velocities (V/U_0 and W/U_0), as well as the turbulence parameters less affected by the valleys ($u'v'/U_0^2$ and the spectral distributions) are in Figures E9 to E11 in Appendix E.

Profiles of flow parameters of *Type I* valleys are presented in Figure 8-11. Smaller speed-ups of the longitudinal velocities (U/U_0) are observed above the second crest (*Cr2*), in particular at $z_{AT}/H \leq 1.25$. Vertical velocities (W/U_0) exhibit the largest dependence of all velocity components on the valley widths at $z_{AT}/H = 0.15$, where the maximum ($A = 12H$) overpowers the minimum ($A = 4H$) by roughly threefold. All components of the velocity fluctuations increase relative to the first crest (*Cr1*). The largest increase of the longitudinal component (σ_U/U_0) is approximately twofold over *Cr1*, observed at $z_{AT}/H = 0.63$ of $A = 8H$. The largest increases relative to *Cr1* are observed for the lateral fluctuations (σ_V/U_0), the maximum constituting an approximate threefold increase over *Cr1* ($z_{AT}/H = 0.15$ of $A = 12H$). An increase of $\approx 65\%$ of σ_V/U_0 of $A = 12H$ over the minimum ($A = 4H$) corresponds to the clearest valley width modification effect, observed at the same height. This also constitutes an increase of $\approx 35\%$ over the maximum value of σ_U/U_0 above *Cr2*. The largest increases of σ_W/U_0 relative to the data from *Cr1* are observed at $z_{AT}/H = 0.15$ where a coarse fourfold increase over *Cr1* is observed for $A = 10H$.

The largest magnitude of the vertical fluxes ($u'w'/U_0^2$) corresponds to an increase of roughly an order of magnitude relative to *Cr1* for $A = 10H$ ($z_{AT}/H = 0.38$). Valley width variations are most influential at $z_{AT}/H = 0.63$, where an approximate twofold increase between minimum ($A = 4H$) and maximum ($A = 8H$) magnitudes is observed. Integral length scales (L_U^X/H) exhibit a maximum decrease of approximately fourfold from *Cr1* being observed for $A = 4H$ ($z_{AT}/H = 0.38$). The clearest dependence on the valley widths is observed at $z_{AT}/H = 1.25$, where the largest L_U^X/H ($A = 4H$) represents an increase of about twofold over the smallest ($A = 10H$). Peaks of longitudinal spectra ($f \times S_{UU}/\sigma_U^2$) exhibit increases in frequency of roughly an order of magnitude relative to the approach flow. The maximum energy peak corresponds to an increase of $\approx 85\%$ over the approach flow and is observed for $A = 8H$. Lateral ($f \times S_{VV}/\sigma_U^2$) and vertical ($f \times S_{WW}/\sigma_U^2$) spectra present closer agreement with the approach flow.

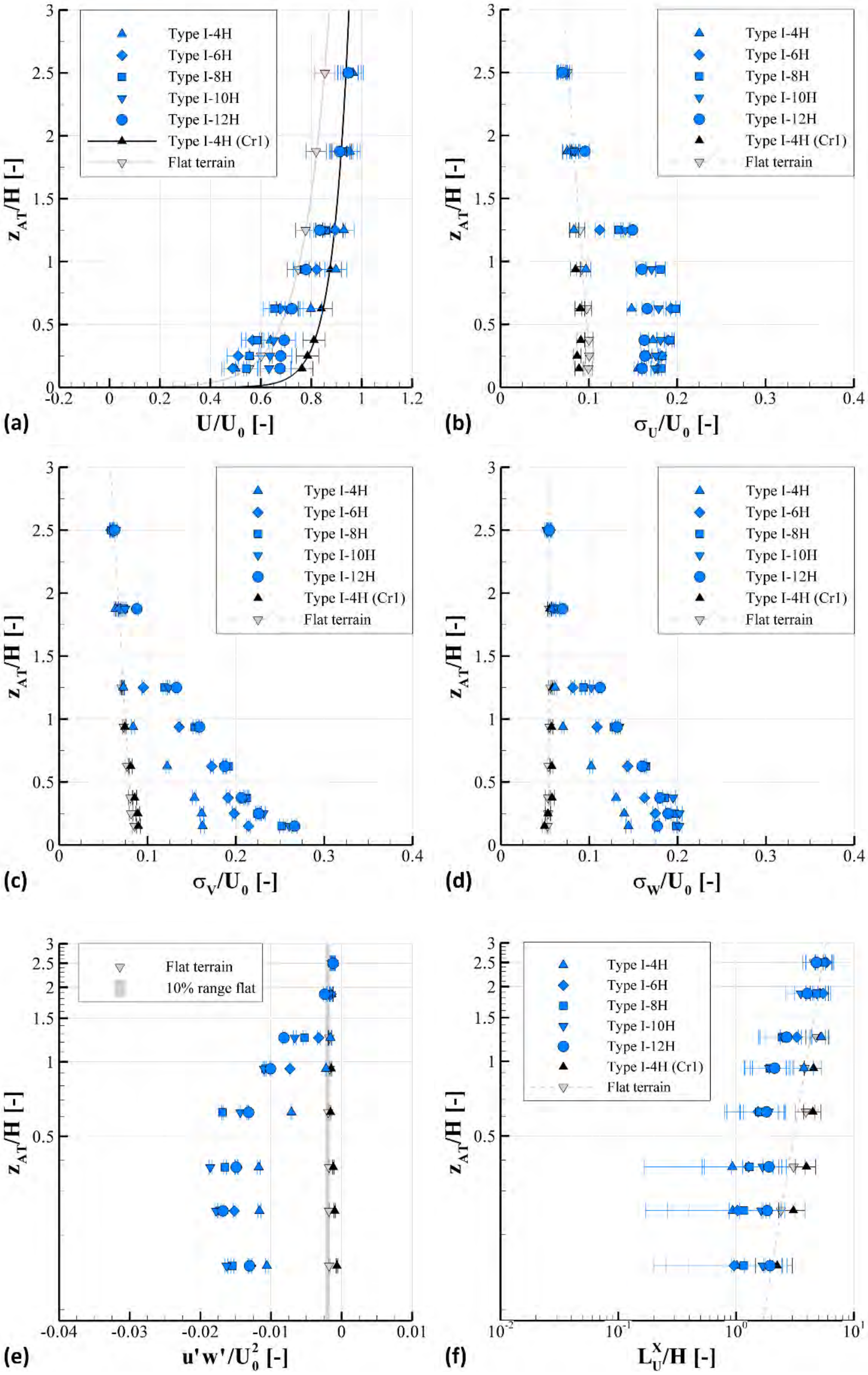

Figure 8-11. Vertical profiles of the mean dimensionless longitudinal velocities (a), longitudinal (b), lateral (c), and vertical (d) velocity fluctuations, vertical turbulent fluxes (e), and integral length scales (f) above the crest of the second ridge (*Cr2*) of *Type I* valleys.

Vertical profiles of *Type II*, presented in Figure 8-12, are less affected by the valley width changes than the other geometries. The largest decrease of longitudinal velocity (U/U_0) relative to the first crest (*Cr1*) is the $\approx 30\%$ decrease observed at $z_{AT}/H = 0.63$ above $A = 12H$. The largest effects of the width modifications are found at $z_{AT}/H = 0.38$, where the maximum U/U_0 ($A = 16H$) overpowers the minimum ($A = 12H$) by $\approx 20\%$. Lateral velocities (V/U_0) are less affected in terms of magnitude but exhibit lateral flow reversal relative to the approach flow (and *Cr1*) at $z_{AT}/H \leq 1.25$. Vertical velocities (W/U_0) exhibit the largest differences compared to *Cr1*, a maximum relative decrease of $\approx 90\%$ observed at $z_{AT}/H = 0.15$ of $A = 12H$. Opposing the findings made above the mid-valley, the smallest width ($A = 12H$) produces the largest magnitudes of velocity fluctuations at $z_{AT}/H \leq 1.25$. The maximum increase of the longitudinal fluctuations (σ_U/U_0) relative to *Cr1* is just over twofold ($z_{AT}/H = 1.25$). The largest effect of the valley width variations corresponds to the $\approx 30\%$ increase between $A = 12H$ and $16H$. Lateral fluctuations (σ_V/U_0) produce maximum increases of over twofold from the reference data at $z_{AT}/H = 0.15$, where σ_V/U_0 overpowers σ_U/U_0 ($\approx 15\%$). Vertical components (σ_W/U_0) exhibit the closest agreement to the data from *Cr*1 at $z_{AT}/H = 0.15$. The clearest dependence on the valley width is translated by the $\approx 25\%$ increase between $A = 12H$ and $16H$.

The largest difference between vertical fluxes ($u'w'/U_0^2$) of both crests corresponds to that of $A = 12H$ at $z_{AT}/H \leq 0.94$. At heights above, maximum increases of $u'w'/U_0^2$ of over an order of magnitude are observed for $A = 12H$ at $z_{AT}/H = 1.25$. Profiles of the integral length scales (L_U^X/H) present the closest agreement to *Cr1* at the near-surface heights, convergence achieved between datasets at $z_{AT}/H = 0.15$. The largest decrease of $\approx 55\%$ relative to *Cr1* is observed for $A = 12H$ ($z_{AT}/H = 1.25$). Valley width modifications produce negligible effects on L_U^X/H, data from all heights contained within the respective confidence intervals. Spectral distributions also exhibit negligible width modification effects, strong agreement between all components being observed at the inertial subranges. For the longitudinal component ($f \times S_{UU}/\sigma_U^2$), a maximum increase of $\approx 60\%$ over the approach flow peak spectra ($A = 16H$) is accompanied by a frequency shift of roughly an order of magnitude to higher ranges. Maximum peaks of lateral ($f \times S_{VV}/\sigma_U^2$) and vertical ($f \times S_{WW}/\sigma_U^2$) spectra, observed for $A = 16H$ and $A = 14H$ (respectively) occur within the same order of frequency as the approach flow. Peaks of $f \times S_{VV}/\sigma_U^2$ of $A = 16H$ overpower the peak energy of the reference data by $\approx 90\%$ (and the maximum $f \times S_{UU}/\sigma_U^2$ by $\approx 25\%$).

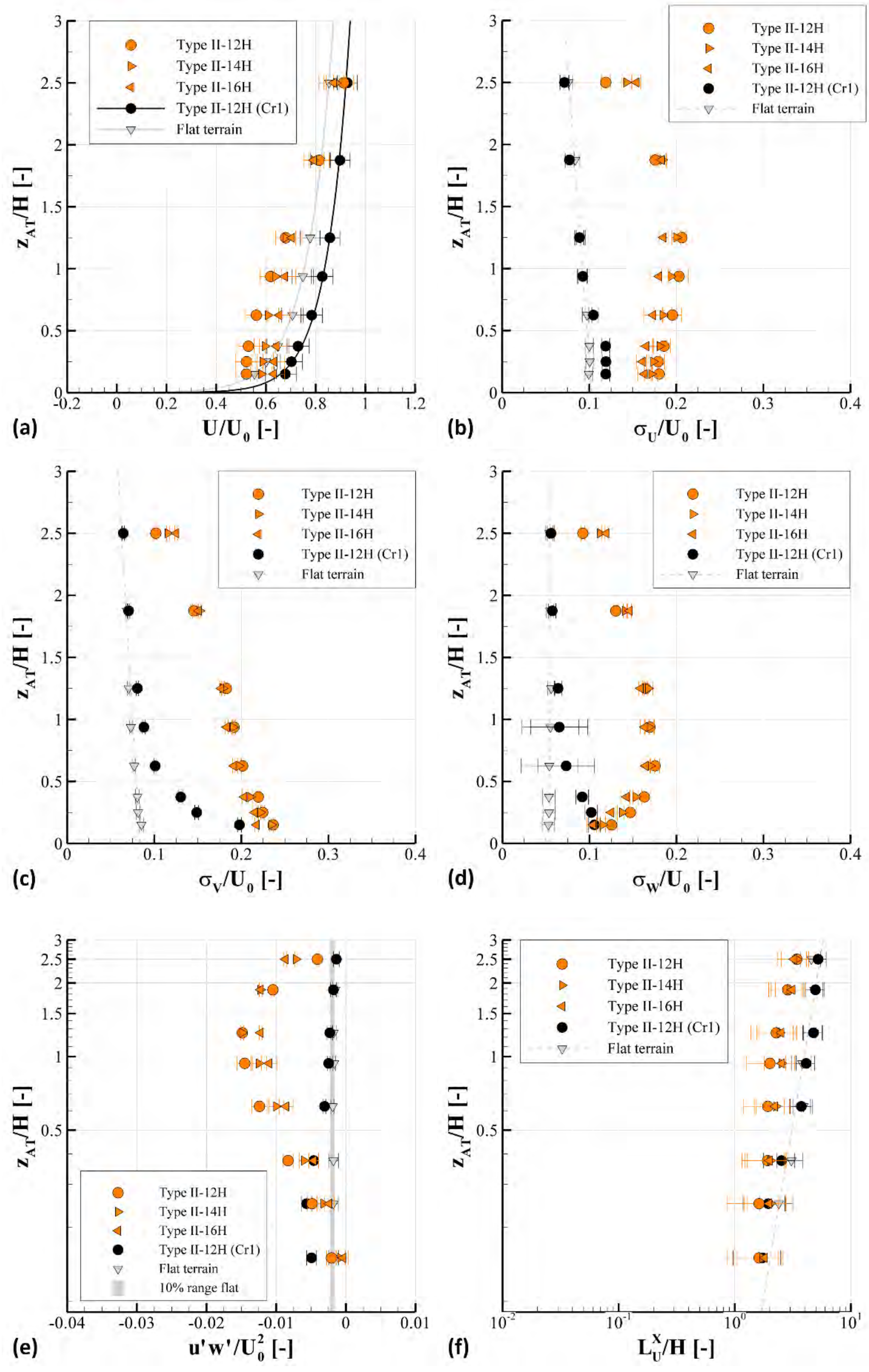

Figure 8-12. Vertical profiles of the mean dimensionless longitudinal velocities (a), longitudinal (b), lateral (c), and vertical (d) velocity fluctuations, vertical turbulent fluxes (e), and integral length scales (f) above the crest of the second ridge (*Cr2*) of *Type II* valleys.

Vertical profiles of *Type III* valleys are presented in Figure 8-13. Longitudinal velocities (U/U_0) display the largest decreases of all valley geometries relative to the first crest (*Cr1*), a maximum $\approx 70\%$ decrease observed at $z_{AT}/H = 0.15$ of $A = 4H$. As with *Type II* valleys, lateral flow reversal ($V/U_0 > 0$) relative to the approach flow (and *Cr1*) is found at $z_{AT}/H \leq 0.63$. Valley width changes are more influential on V/U_0 than for the previous valley geometries, an order of magnitude separating minimum and maximum values ($A = 6H$ and $12H$, respectively) at $z_{AT}/H = 0.25$. Vertical velocities (W/U_0) present decreases relative to *Cr1* at all heights. Downward flow characteristics ($W/U_0 < 0$) is observed for $A = 4H$ at $z_{AT}/H \leq 0.63$, whereas upward vertical flow is observed for the other widths. Longitudinal fluctuations (σ_U/U_0) present a maximum increase of roughly threefold relative to *Cr1* for $A = 10H$ at $z_{AT}/H = 1.25$. The maximal effects of the width modifications are found at the same height, the maximum σ_U/U_0 (observed for $A = 10H$) over twice the minimum ($A = 4H$). The maximum increase of the lateral components (σ_V/U_0) compared to *Cr1* is over twofold for $A = 12H$ ($z_{AT}/H = 0.15$). As with the previous valley domains, the maximum σ_V/U_0 overpowers the largest magnitude of σ_U/U_0 (by a maximum of $\approx 20\%$). The largest effects of the valley width variations on σ_V/U_0 are also observed at $z_{AT}/H = 1.25$, an increase of roughly threefold observed between extrema ($A = 4H$ and $10H$). Vertical components (σ_W/U_0) present a maximum increase of over threefold relative to *Cr1* for $A = 12H$ at $z_{AT}/H = 0.63$. Width modification effects are most evident at $z_{AT}/H = 1.25$, where the maximum ($A = 12H$) overpowers the minimum ($A = 4H$) by over threefold.

Vertical fluxes ($u'w'/U_0^2$) also exhibit the largest increases (in magnitude) over the approach flow of all valley geometries. The maximum is observed for $A = 10H$ ($z_{AT}/H = 0.94$) and corresponds to an increase of roughly an order of magnitude. The largest effects of the valley width variations on $u'w'/U_0^2$ are found at $z_{AT}/H = 1.25$, where an approximate order of magnitude separates the minimum and maximum ($A = 4H$ and $10H$, respectively). Integral length scales (L_U^X/H) exhibit the largest decreases compared to *Cr1* at $z_{AT}/H = 0.63$, where a decrease of $\approx 75\%$ is observed for $A = 4H$ ($\approx 70\%$ relative to the approach flow). As with the previous valley geometries, effects of the width modifications are less expressive on L_U^X/H. Peaks of the longitudinal spectra ($f \times S_{UU}/\sigma_U^2$) of all widths present increases of frequency of about an order of magnitude over the approach flow. The maximum peak is observed for $A = 12H$ and corresponds to an increase of $\approx 80\%$ over the approach flow ($\approx 45\%$ over the smallest peak, of $A = 4H$). Maxima of the lateral components ($f \times S_{VV}/\sigma_U^2$) occur at closer frequency ranges to that of the approach flow. The maximum $f \times S_{VV}/\sigma_U^2$, observed for $A = 4H$, corresponds to a $\approx 55\%$ increase over that of the approach flow. Distributions of the vertical components ($f \times S_{WW}/\sigma_U^2$) provide the closest agreement with the approach flow.

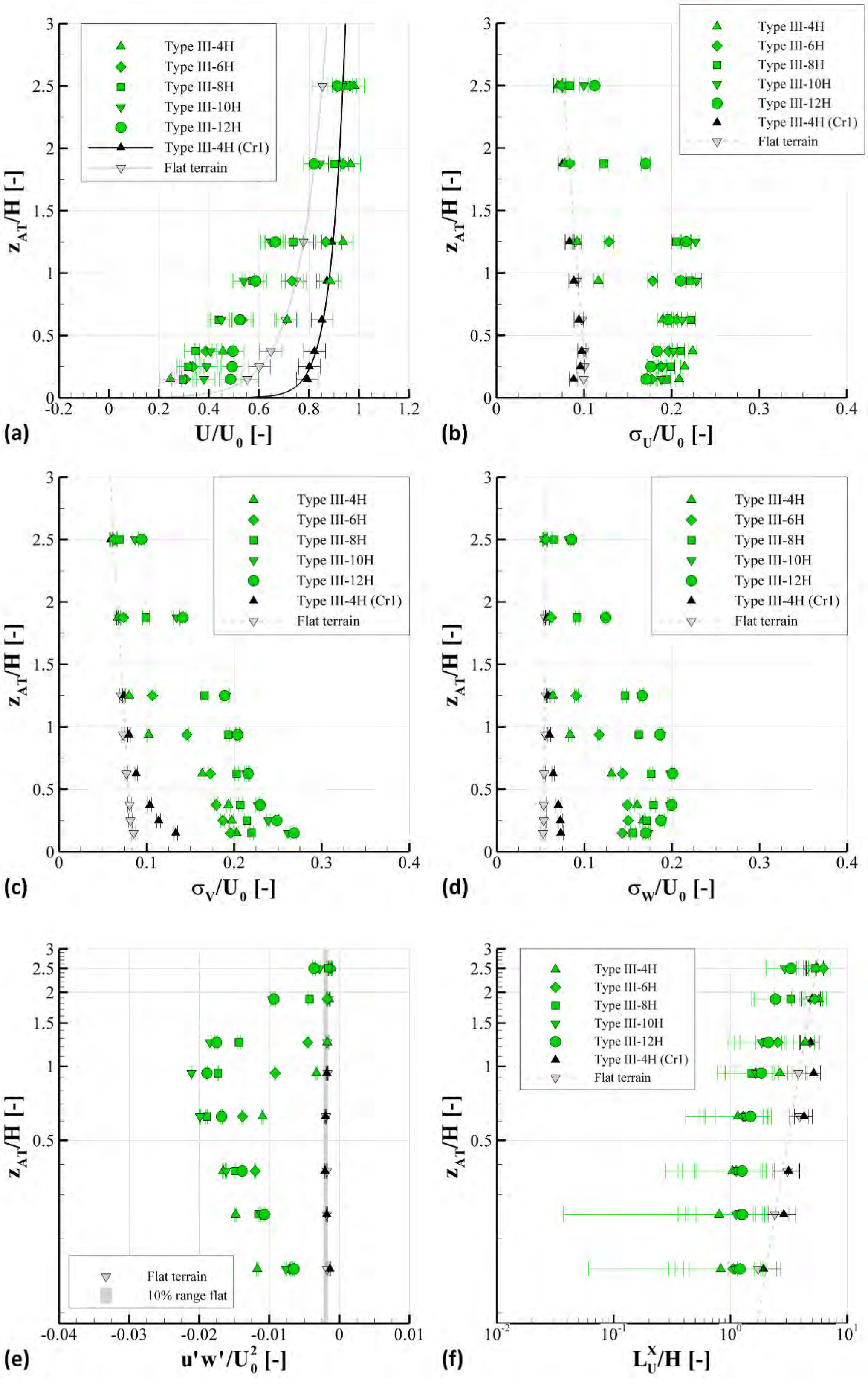

Figure 8-13. Vertical profiles of the mean dimensionless longitudinal velocities (a), longitudinal (b), lateral (c), and vertical (d) velocity fluctuations, vertical turbulent fluxes (e), and integral length scales (f) above the crest of the second ridge (*Cr2*) of *Type III* valleys.

8.5.4 Downwind (*DW7*)

This analysis focuses on the furthermost downwind position from the valleys, $X = 32H$ (*DW7*), where only vertical plane (UW) measurements are performed. Due to similar flow characteristics between geometries, only the results from the most affected of the flows (*Type III* valleys) are presented here. Data from the remaining valleys is in Figure E12 to E14 (Appendix E). Figure 8-14 displays the mean velocities and velocity fluctuations. When contemplating ranges of data uncertainty, mean parameters exhibit general convergence between the valley widths at all heights of the respective profiles. Thus, flow is independent of the valley width modifications for all valley types. Longitudinal velocities (U/U_0) replicate approach flow characteristics at $z_{AT}/H \leq 0.25$ and longitudinal fluctuations (σ_U/U_0) exhibit convergence between all datasets at $z_{AT}/H \leq 0.63$.

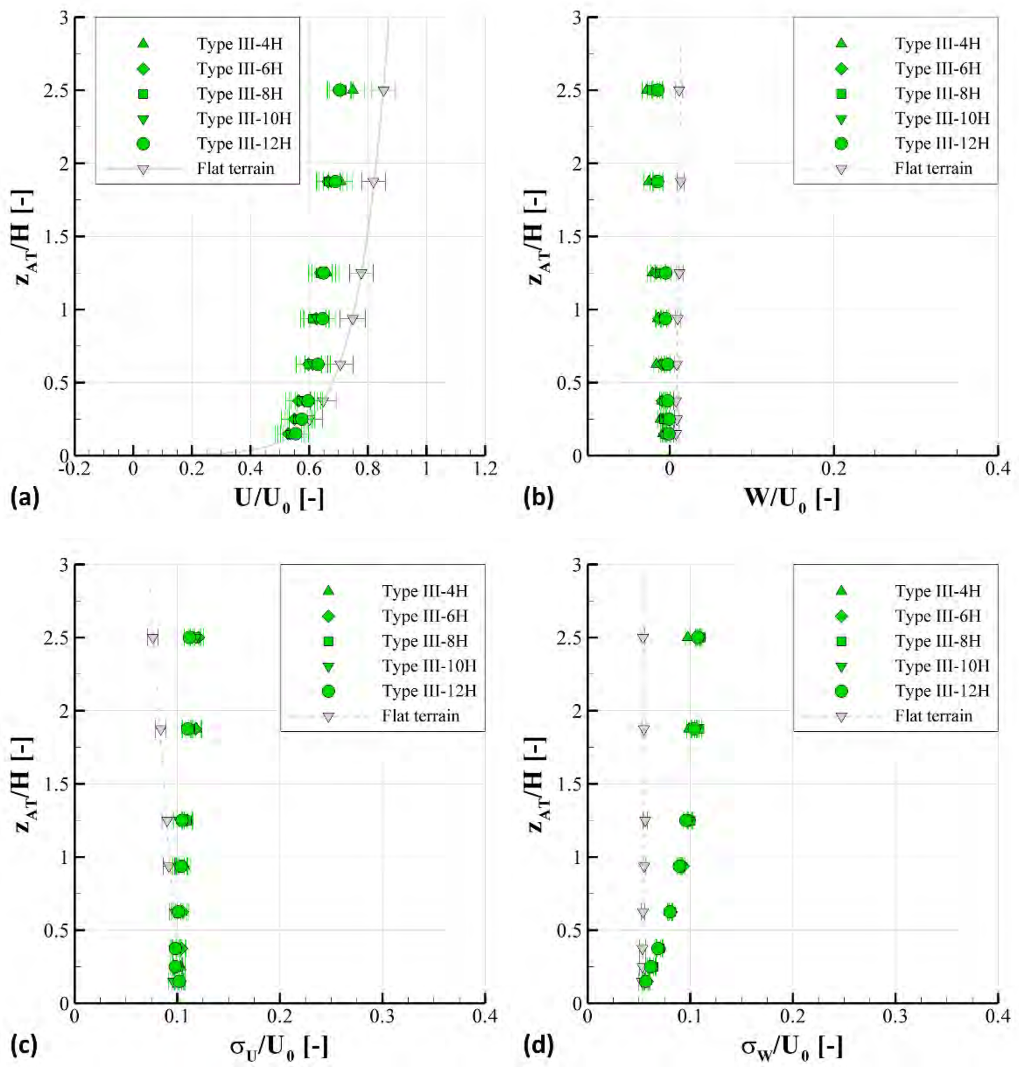

Figure 8-14. Vertical profiles of the mean dimensionless longitudinal (a, c) and vertical (b, d) velocities and velocity fluctuations above the furthermost downwind position (*DW7*) from *Type III* valleys.

Vertical fluxes and integral length scales are presented in Figure 8-15 with the spectra. Convergence between datasets of the fluxes outlasts in altitude that of the mean fluctuations. However, the closest agreement of all parameters with the approach flow is achieved for the integral length scales, as demonstrated by the convergence for the full range of measurement heights. Both components of the spectra exhibit close agreement with the approach flow, maxima of all valleys occurring within the same order of magnitude as the reference data but presenting shifts to smaller frequencies. Data from all valley widths exhibit convergence within the inertial subrange of both components of the spectra.

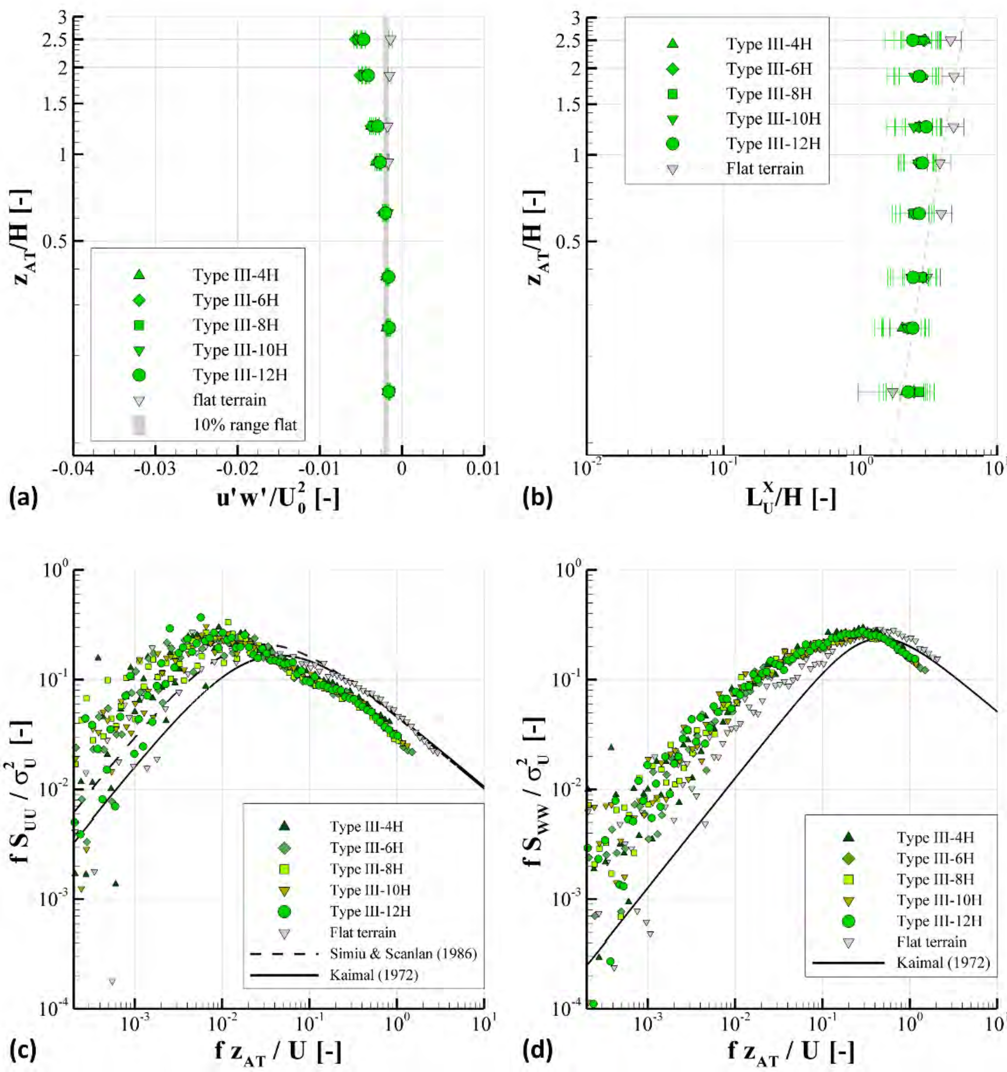

Figure 8-15. Vertical profiles of the mean dimensionless vertical turbulent fluxes (a) and integral length scales (b) and spectral distributions of longitudinal (c) and vertical (d) turbulent energy at $z/H = 0.15$ above the furthermost downwind position (*DW7*) from *Type III* valleys.

8.6 Transient flow above valleys

Time-averaged turbulence quantities alone are insufficient for the characterisation of complex flows, such as ABL flows over orography. Statistical descriptions can misrepresent strong flow gradients or short-lived flow phenomena. In addition, the increasing applicability of LES approaches demands more qualified data for validation of the corresponding numerical models. This dictates that time-dependent (transient) turbulence parameters be quantified, as discussed in Chapter 5. Transient phenomena related to the flows above valleys are explored here.

The adequacy of the experimental data for transient flow analyses is dependent on the temporal resolution of the measurements, which is influenced by the data rate of the LDV. Increases of measurement data rates are obtained with changes made to the LDV settings, introduced earlier. Transient flow analyses consist of the quantification of velocity fluctuations (magnitude and frequency) and gustiness. These entail the characterisation of turbulent flow features over shorter time intervals contained within each measurement of $\Delta t = 120\ s$ duration (model-scale). Accordingly, results are rescaled in time via the application of different reference velocities to the dimensionless measured time series. At a temporal scale of $1{:}\,1000$, the pointwise measurement time corresponds to just over thirty hours at full scale.

8.6.1 Gustiness

Gust factors of the longitudinal components of the wind vectors ($G_{T,\tau}$) are calculated via Eq. (23), using gust durations of $\tau = 3s$ and sampling periods of $T = 1800\ s$ (half-hour averages), at full scale. All gust factors ($G_{T,\tau} > 1$) are computed and the maxima of all sampling periods (T) averaged for each measurement position. Figure 8-16 exhibits the data from the crests of all valleys. Above the first crest (*Cr1*), small differences are observed between valley types. Above the crest of the second ridge (*Cr2*), gusts expectedly increase at $z_{AT}/H \leq 0.63$. The maximum is observed at $z_{AT}/H = 0.15$ of the smallest width ($A = 4H$) of *Type III*, with an increase of $\approx 20\%$ over that of *Cr1*. While following similar trends to those observed by Letson et al. (2019), the present gust data is less expressive than the $\approx 50\%$ increases of $G_{T,\tau}$ reported between the crests of the ridges at Perdigão. Dependence on the valley widths is maximal for *Type III* at $z_{AT}/H = 0.15$, a $\approx 10\%$ increase observed between $A = 12H$ and $4H$ (minimum and maximum $G_{T,\tau}$, respectively). Analyses of gustiness above the inner valley are restricted by the near-zero and negative averages of U/U_0 at $z_{AT}/H \leq 1.25$, which lead to amplified and unrealistic quantifications of $G_{T,\tau}$.

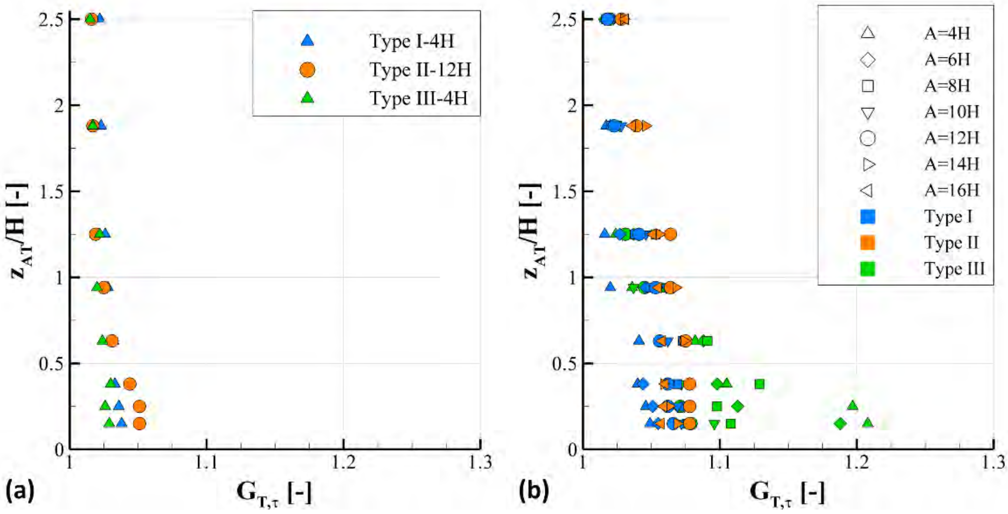

Figure 8-16. Vertical profiles of the longitudinal gust factors above the crests of the first (a) and second (b) ridges of all valley geometries.

8.6.2 Transient fluctuations

Transient velocity fluctuations, corresponding to the fluctuating parts of the instantaneous velocities defined by Eq. (10), are evaluated here. Under this rationale the dimensionless longitudinal fluctuations of each valid sample (u'/U_0), contained within each sampling period T, correspond to the difference between the measured instantaneous (u) and mean ($\bar{u}$) longitudinal velocities. Lateral (v'/U_0) and vertical (w'/U_0) fluctuations are obtained using the same approach. For each sampling period of $T = 1800\ s$, the average fluctuations of each component are computed.

Figure 8-17 displays the transient dimensionless longitudinal fluctuations (u'/U_0) above the crests and mid-valley (*MV*). Lateral and vertical components are in Figures E15 and E16 (Appendix E). u'/U_0 is predominantly near-zero above the first crest (*Cr1*), limited effects of the windward slope are perceived from marginal increases of u'/U_0 at $z_{AT}/H \leq 1.25$ of *Type II*. Above *MV* and the second crests (*Cr2*), results are characterised by larger scatter and distinct height trends between positions, the latter resembling the respective mean fluctuations. Larger magnitudes and variability of all components of the transient fluctuations between different valley widths are observed at $z_{AT}/H \leq 0.63$ above *Cr2* and at $z_{AT}/H \geq 0.94$ above *MV*. The maximum u'/U_0, observed above *MV* of *Type II* (at $z_{AT}/H = 1.88$), is $\approx$ 50% larger than the maxima of v'/U_0 (also of *Type II*) and w'/U_0 (*Type III*). Similarities to the width variation trends set by the mean fluctuations are restricted to equivalent heights of maximum bandwidths between minimum and maximum values above *MV* of *Type I* and *Type III* valleys.

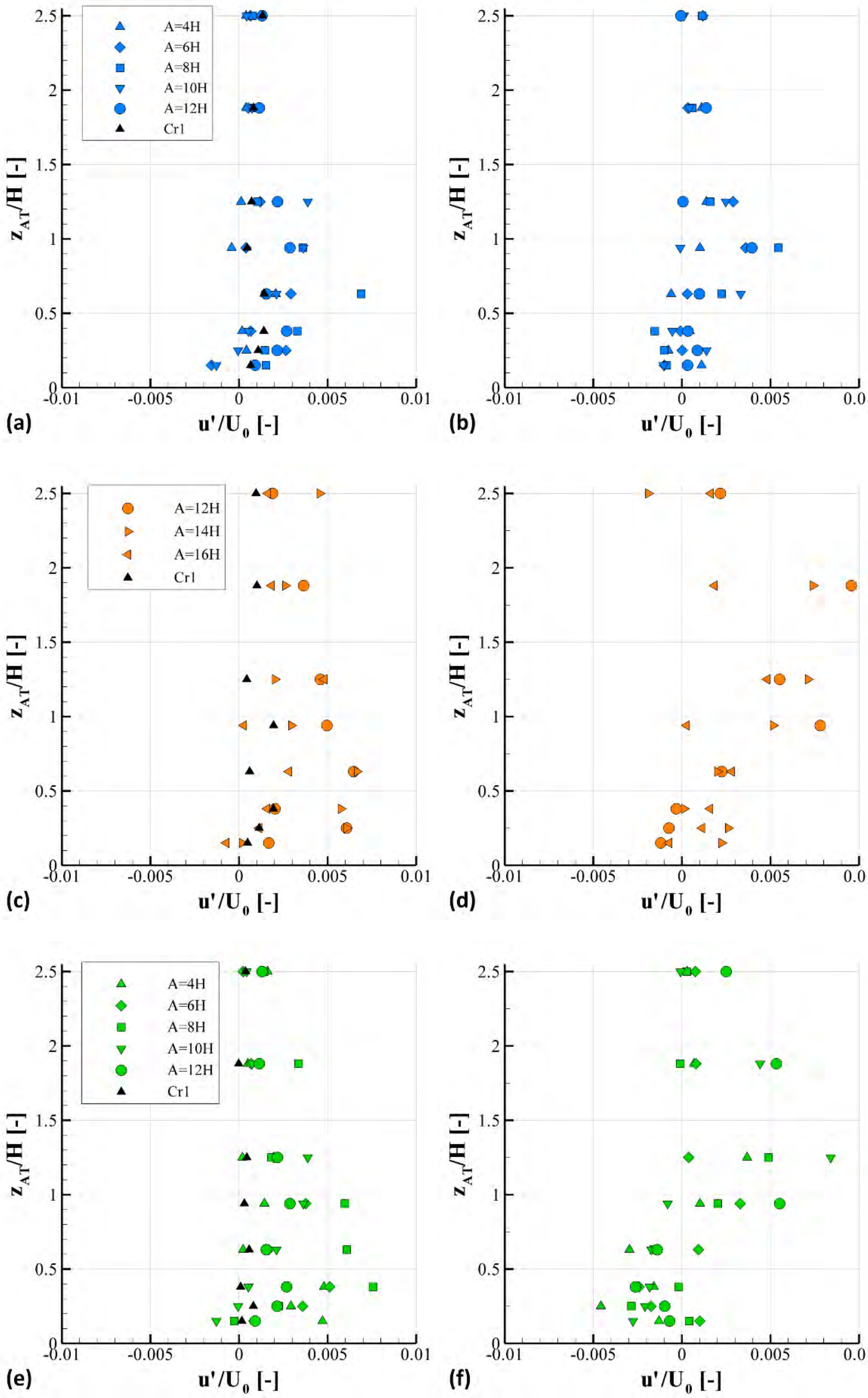

Figure 8-17. Vertical profiles of the dimensionless transient longitudinal fluctuations above the crests (a, c, e) and mid-valley (b, d, f) of *Type I* (a, b), *Type II* (c, d), and *Type III* (e, f) valleys. For all valley types, data from the crest of the first ridge is presented in black colour. Plots on the right (b, d, f) have symbol correspondence with the left.

8.6.3 Frequencies of transient fluctuations

Analyses of the frequencies at which each sampled velocity surpasses the averaged transient velocity fluctuations serves as measure of the intermittency of the flow turbulence above the orography. Frequencies at which each valid longitudinal sample (u) are larger than the average (σ_U) of each sampling period ($T = 1800\ s$) is obtained above the crests and mid-valley of each valley geometry. Lateral (v') and vertical (w') fluctuation frequencies result from the same method. Figure 8-18 presents the vertical profiles of the longitudinal components of all valleys. Lateral and vertical fluctuations are in Figures E17 and E18 (Appendix E).

Based on the present results, the intermittency of the fluctuations is virtually unaffected by the valleys. Above the first crests (*Cr1*), frequencies are generally near-invariant with height for all valleys. Above the crests of the second ridges (*Cr2*) similar frequencies to those of *Cr1* are found. Effects of the valley width modifications on the frequencies are more perceivable than differences between valley types or profile heights. The largest scatter between minimum ($A = 12H$) and maximum ($A = 6H$) frequencies is observed at $z_{AT}/H = 2.5$ of *Type III* valleys. Frequencies of the fluctuations above the mid-valley (*MV*) are less expressive than above *Cr2*, results indicating minimal effects due to the variation of valley widths and geometries. Similar findings are made from the profiles of the frequencies of lateral and vertical fluctuations (Appendix E).

Results display significant differences when compared to the variations of the magnitudes of the corresponding mean velocity fluctuations, analysed earlier. This is most evident from the relative height independence of the current frequencies with regard to the clear variations of the mean fluctuations at the corresponding positions. When applying the same method to express the frequencies at which each instantaneous velocity surpasses twice the averaged fluctuations ($u > 2 \times \sigma_U$), frequencies of the fluctuations decrease by roughly an order of magnitude but maintain the same positional and height trends as those presented here. This would indicate that the ABL flow characteristics override the effects of intermittency due to the presence of orography at the applied temporal scale. As this has no correspondence with the results from the mean flows or the laser light-sheet visualisations, insufficient temporal resolutions are more likely. Under this rationale, the measurement data fails to capture the smaller scales of turbulence, expectedly more intermittent. Thus, geometric scaling is inadequate for meaningful intermittency analyses from the present time series.

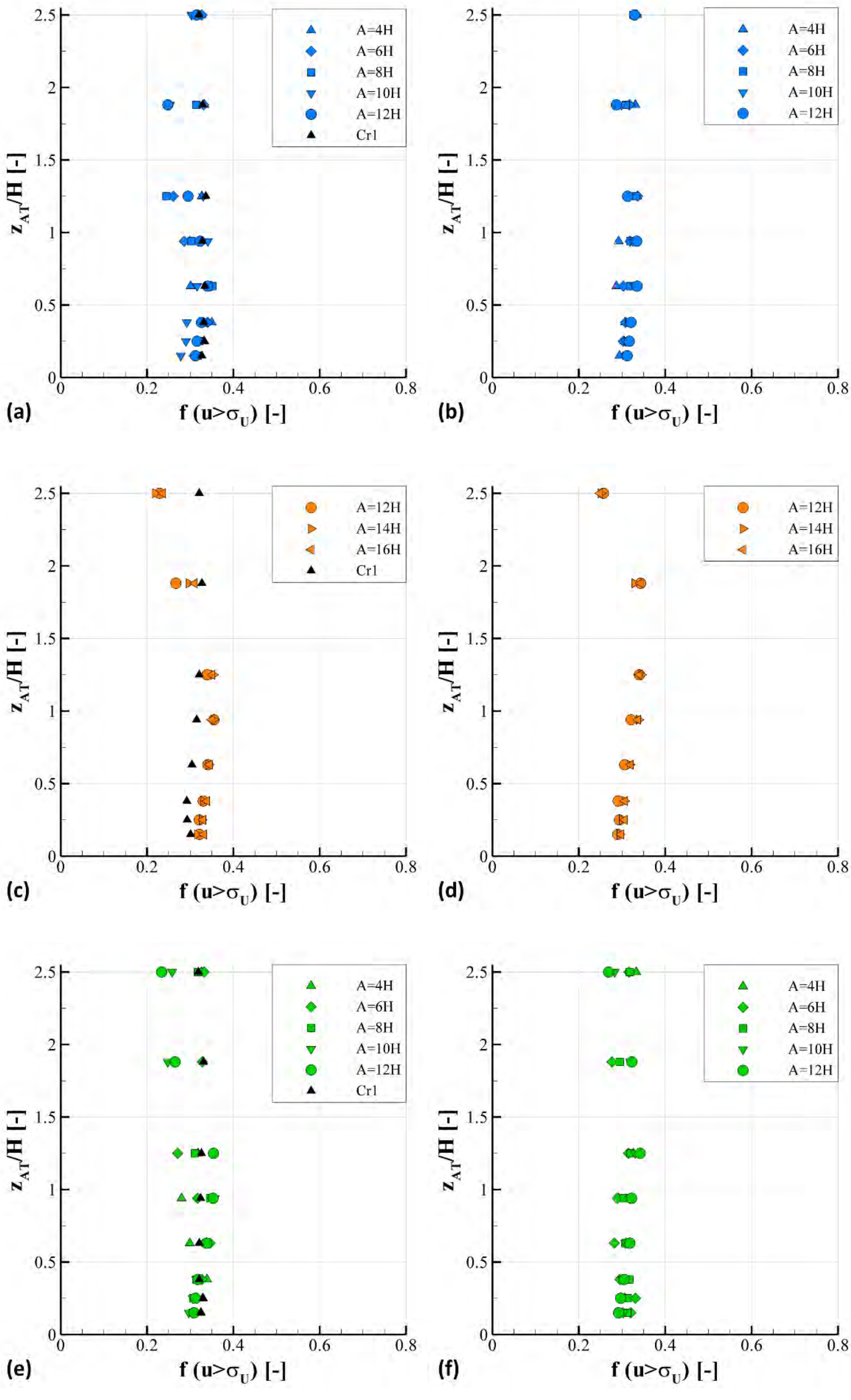

Figure 8-18. Vertical profiles of the frequencies at which the longitudinal velocities are larger than the averaged transient longitudinal velocity fluctuations above the crests (a, c, e) and mid-valley (b, d, f) of *Type I* (a, b), *Type II* (c, d), and *Type III* (e, f) valleys. For all valley types, data from the crest of the first ridge is presented in black colour.

8.7 Summary

The most relevant findings regarding flows over the analyses positions of the valleys are discussed here. First, the observed flow characteristics above the crests of the two ridges (*Cr1* and *Cr2*) and the mid-valley location (*MV*) are addressed. This is followed by a discussion centred on the specific effects of the modifications of valley types (slope effects) and valley widths on near-ground flow dynamics.

8.7.1 Crest flows

1.1.1.5 Crest 1 (Cr1)

Mean flows above the crests of the first ridge mirror characteristics extensively reported in the Literature for single ridges, namely maximum longitudinal velocities (for example, Ayotte & Hughes, 2004; Cao & Tamura, 2007; Lubitz & White, 2007). This is expected due to channelling of the flow in the vertical plane bounded by the underlying surface below and capped by the stronger flow momentum from higher altitudes. Present results indicate that these increases are strongly dependent on the inclination of the windward slopes (γ) and the height above local terrain (z_{AT}). It is important to point out that results are presented in the Earth coordinate system (discussed in Chapter 5), thus independent of the alteration of the streamline flow direction that is modified by the terrain. Differences between the coordinate systems are discussed in Chapter 9.

Turbulence characteristics are the least expressive of all analyses positions, as evidenced by the smallest differences of the mean parameters relative to the approach flow or the smaller variations of the gustiness and transient fluctuations compared to the inner valley and crests of the second ridges. The least affected turbulence parameters are the horizontal fluxes and the integral length scales. This indicates that the energy-intensive longitudinal eddies are of equivalent lengths to those of the approach flow, regardless of the inclination of the windward slopes. The influence of the windward slopes on the flows is translated by the maximal intensities the mean velocity fluctuations occurring atop the steepest windward slope (*Type II*). Inversely, the mean turbulence parameters atop the gentle slope (*Type I*) are less impacted. At the near-surface, mean longitudinal fluctuations are smaller than the approach flow data for *Type I*. Cao & Tamura (2007) make similar findings, attributing this to flow laminarisation due to rapid distortion. This has no correspondence from the vertical components and flow similarity tests yield fully turbulent flows above the same location. Furthermore, the longitudinal components of the spectra at $z_{AT}/H = 0.15$ above the crests present increases of peak energy relative to the approach flow distribution. Hence, the small velocity fluctuations are more indicative of the dampening of longitudinal turbulence due to minimal disturbances caused by the gentle windward slope and the extended length of this slope compared to the others. This enables an ample distance for the flow to stabilise (whilst turbulent).

1.1.1.6 Crest 2 (Cr2)

Inflow characteristics of the second ridges are generally governed by the perturbations posed by the first and expectedly mirror the wake flow characteristics obtained downwind from the corresponding single ridges. Thus, inflow profiles of the second ridges are dependent on the valley geometries but are also strongly influenced by the valley widths. Flows above the crests of the second ridges, which exhibit significant increases of turbulence from those observed above the first ridges. Consequently, smaller accelerations of the longitudinal velocity compared to the first crests are observed at the near-surface. These are accompanied by increases of the lateral and vertical components. Between these mean velocities, the vertical components are more affected above the crests and present the clearest effects of the inclination of the windward slopes of the second ridges.

The largest increases of mean turbulence between crests are those of the lateral velocity fluctuations. This indicates that the increases of lateral turbulence observed downwind from the single ridges (Chapter 7) extend to the second ridges of all valleys and overpower the longitudinal counterparts at the near-surface. Accordingly, lateral fluctuations display general increases from those observed above the mid-valley of all valley types. Further support is provided by the larger intensities of the peaks of lateral spectra compared to those of the longitudinal components (at $z_{AT}/H = 0.15$) and by the increases of the horizontal fluxes between consecutive crests (in absolute values). Perhaps the largest difference between the vertical profiles of the mean turbulence parameters above each crest are the heights at which the maximum turbulence is observed. The aforementioned maxima of the lateral turbulence parameters occur at the lowest height above local terrain, which mirrors the findings made above the first crests. Opposing this, the maxima of the longitudinal and vertical components are found at higher altitudes above the second crests. These findings indicate that the inflow conditions of the second ridge overpower those of the surface roughness when compared to the flows above the first ridges, where surface conditions drive the largest increases of all components of the mean turbulence at heights nearest to the surface.

The maxima of the mean vertical fluxes (in magnitude) are observed at altitudes that generally coincide with the maxima of the mean longitudinal fluctuations. These heights tend to increase with increasing windward slope inclinations of the first ridges. Mean integral length scales exhibit closer agreement with the data from the crests of the first ridges, as highlighted by the general data convergence between crests. The maxima of the transient longitudinal velocity fluctuations and gust factors occur at lower heights than the mean velocity fluctuations. This indicates that short-lived peaks of near-surface turbulence are smoothed out through time-averaging. However, this can also be due to inadequate temporal resolutions of the transient flow parameters.

8.7.2 Flows above the mid-valley

Profiles of the mean velocities closely resemble those of the downwind subdomain of the corresponding single ridges. These are characterised by the existence of flow recirculation zones, which are capped by free shear flow characteristics. This is demonstrated by the inversion of the profiles of the longitudinal velocity at altitudes above ridge height ($z_{AT}/H \geq 1.25$). The altitudes of the corresponding inflection points are dependent on both slopes of the first ridges. Heights below the inflection points are contained within the recirculation zones of all ridge geometries. At the near-surface, reversal of the mean longitudinal velocity is generally observed for all valley geometries and is also influenced by the valley widths. Vertical velocities exhibit downward flow momentum that is generally maximal (in magnitude) at heights above the inflection points of the profiles of the longitudinal counterparts. Increases of the lateral velocities are observed at heights nearest to the surface, indicating the influence of the lateral flow from the side slopes (discussed in Chapter 7). The maximum lateral velocities correspond to those of the smallest widths.

Profiles of the mean turbulence characteristics of the flows above the mid-valley also resemble those of the flows downwind from the single ridges, but present some differences. These are related to the altitudes at which maximum differences relative to the approach flow are observed. These are found at different altitudes above the mid-valley than those observed for the downwind subdomain of the single ridges. Noteworthy differences in the magnitudes of the extrema of the mean turbulence parameters compared with the data downstream from the single ridges are also observed, albeit these are less frequent than the differences associated to the altitudes of maximal turbulence. These differences indicate that the flows above the inner valleys are influenced by the presence of the second ridge further downstream and these are dependent on the valley geometries and widths. For example, the maxima of all components of the velocity fluctuations and the vertical fluxes of the smallest valley widths of *Type I* ($A = 4H$ and $6H$) occur at a higher altitude than the larger widths, where the maxima are found at the same altitude as the downwind data from the corresponding single ridge (above the inflection points of the velocity profile). This indicates that the respective recirculation zone (downwind from the first ridge) is intersected by the second ridge of the smaller width valleys and the large bulk of turbulent flow momentum bypasses the inner valleys, only a small fraction being redirected into the inner valley upon interaction with the second ridge. However, these turbulence characteristics have no correspondence from the equivalent valley widths of *Type III*, indicating the influence of the windward slopes on this behaviour. Integral length scales are the most affected of the mean turbulence parameters, the largest differences to the approach flow data frequently being found at different heights from the observations of the single ridges. Spectral distributions also exhibit differences to those of the downwind subdomain of the single ridges. Most notably, shifts of the frequencies of peak energy are more recurrent above the mid-valley.

8.7.3 Effects of valley width

The effects of the systematic modifications (constant amplitude) made to the valley widths are most evident above the mid-valley and crests of the second ridges. Width variation effects on upwind (invariance of the flow characteristics above the crests of the first ridges) and extended downwind flows are restrained. The exception to these observations corresponds to *Type II* valleys, corresponding profiles being less sensitive to the valley width modifications.

Mean vertical velocities are the most sensitive to the variations of valley widths, as evidenced by changes between upward and downward vertical flows for different widths. For example, upward flows are observed above the mid-valley position of the smaller width valleys of *Type III* ($A = 4H$, $6H$, and $8H$), whereas downward flows occur for the larger widths. This indicates that the characteristics of the recirculation zones, developed above the inner valley regions, are influenced by the width modifications. This is supported by the longitudinal flow reversal characteristics observed at the near-surface above the same regions. At the lowest height ($z_{AT}/H = 0.15$), the magnitudes of negative longitudinal velocity tend to increase with increases of valley width. This can be verified through the lengths of the recirculation zones (based on reversed mean longitudinal flow observations at $z_{AT}/H = 0.15$), displayed in Table 8-2 as function of the valley depth (H). Lengths of the recirculation zones tend to increase with valley widths until reaching a threshold from which lengths remain invariant with successive increases of the widths. This threshold roughly indicates the downstream distances from the first ridges at which the recirculation zones extend without the interference from the second ridges. The lengths of the recirculation zones are generally half the width of the corresponding valleys, which is consistent with the findings of Menke et al. (2019) who observe a similar average extension of the recirculation zones from the field measurements at Perdigão.

Table 8-2. Approximate streamwise length of the recirculation zones based on observations of negative mean longitudinal velocity at $z/H = 0.15$ above the inner valley positions.

Geometries	Valley widths (A)						
	$4H$	$6H$	$8H$	$10H$	$12H$	$14H$	$16H$
Type I	$2H$	$5H$	$6H$	$6H$	$6H$	–	–
Type II	–	–	–	–	$5H$	$5H$	$5H$
Type III	$2H$	$4H$	$5H$	$6H$	$6H$	–	–

Mean turbulence is also affected by the valley width modifications, as evidenced by the aforementioned variations of altitude at which the maxima of turbulence above the mid-valley are found. Turbulence data generally presents the largest differences to the approach flow profiles for the largest valley widths. At the near-surface, increases of lateral turbulence components relative to the longitudinal counterparts are influenced by the width modifications, as highlighted by the turbulence ratios in Tables E4 and E5 (Appendix E). For all valleys, mean lateral velocity fluctuations overpower the longitudinal components above the mid-valley and the differences are maximal for the smallest widths (Table E4). This is consistent with the amplification of lateral turbulence through channelling of the horizontal flow in-between the ridges, an effect dampened with increasing valley widths. For *Type I* and *Type II* valleys, the larger dependence of the turbulence parameters on the valley widths is observed above the mid-valley. This is verified by the larger scatter of the mean turbulence parameters, as result of the changes in width, compared with the data from the crests of the second ridges. Inversely, turbulence characteristics of *Type III* valleys are more width-dependent above the crests of the second ridges. This is clear from the data presented in Table 8-3, which lists the maximum scatter (differences between extrema) of the mean turbulence parameters of each valley geometry.

Table 8-3. Maximum absolute differences between extreme values of mean turbulence parameters resulting from the valley width modifications of each valley type above the mid-valley and the crest of the second ridge.

	Type I		**Type II**		**Type III**	
	Mid-valley (*MV*)	Crest 2 (*Cr2*)	Mid-valley (*MV*)	Crest 2 (*Cr2*)	Mid-valley (*MV*)	Crest 2 (*Cr2*)
$\Delta(\boldsymbol{\sigma_U/U_0})$	0.109	0.066	0.033	0.023	0.131	0.135
$\Delta(\boldsymbol{\sigma_V/U_0})$	0.071	0.105	0.028	0.023	0.093	0.111
$\Delta(\boldsymbol{\sigma_W/U_0})$	0.088	0.064	0.019	0.027	0.081	0.103
$\Delta(\boldsymbol{u'w'/U_0^2})$	0.015	0.010	0.005	0.005	0.013	0.018
$\Delta(\boldsymbol{L_U^X/H})$	2.89	2.13	0.56	0.57	2.56	3.36

8.7.4 Effects of valley type

Effects of the valley geometries on the flows are most evident above the crests and the inner valley locations. This is evidenced by the differences between the shapes of the respective vertical profiles related to different valley types. However, these observations include the joint effects of the valley types and the width modifications. An understanding of the exclusive contributions of the valley geometries on the flows can be gained through the assessment of the flows associated to the common width ($A = 12H$), which are discussed here. Vertical profiles of the mean flow parameters, obtained above the mid-valley, the crest of the second ridge, and above the furthermost downwind position are in Figures E19 to E23 (Appendix E).

For the majority of mean turbulence parameters, the largest differences between valley geometries are observed above the mid-valley at heights above the valley depth ($z_{AT}/H \geq 1.25$). Least affected by the width modifications, *Type II* presents the largest general differences to the approach flow turbulence data. Thus, the windward slope of the first ridges exerts a predominant effect on the flows above the mid-valley locations. This extends to the crests of the second ridges, where increases of the mean longitudinal velocity relative to the approach flow profile are exclusive to *Type I*. These are accompanied by the smallest values of mean longitudinal velocity fluctuations, which indicates that the influence of the slopes of the first ridges on the longitudinal flows overpowers the effects produced by the windward slope of the second ridges above the crests of the second ridges. Oppositely, the maximum of the vertical velocity fluctuations at the near-surface above the crest of the second ridge of *Type I* overpowers those of the other valley geometries, indicating the stronger effect of the steep windward slope of the second ridge on the vertical turbulence. Effects of the valley geometries on the turbulence are exemplified by the maximum scatter between profiles of the mean turbulence parameters associated to each valley type, presented in Table 8-4. Larger differences between extrema of the valleys of constant width provide evidence that valley geometries are more influential on the mean turbulence than the width modifications (Table 8-3) above the mid-valley and the opposite occurs above the crests of the second ridges.

Table 8-4. Maximum absolute differences between extreme values of mean turbulence parameters resulting from the valley type modifications, at constant valley width ($\mathrm{A} = 12\mathrm{H}$), above the mid-valley, the crest of the second ridge, and the furthermost downwind position.

	Mid-valley (*MV*)	**Crest 2** (*Cr2*)	**Downwind** (*DW7*)
$\Delta(\boldsymbol{\sigma_U}/\boldsymbol{U_0})$	0.156	0.081	0.011
$\Delta(\boldsymbol{\sigma_V}/\boldsymbol{U_0})$	0.125	0.059	–
$\Delta(\boldsymbol{\sigma_W}/\boldsymbol{U_0})$	0.117	0.061	0.019
$\Delta(\boldsymbol{u'w'}/\boldsymbol{U_0^2})$	0.021	0.010	–
$\Delta(\boldsymbol{u'v'}/\boldsymbol{U_0^2})$	0.002	0.004	–
$\Delta(\boldsymbol{L_U^X}/\boldsymbol{H})$	1.59	1.71	–

9 DISCUSSION

With the extensive and systematic datasets analysed in the preceding chapters, it is possible to address the research questions discussed in Chapter 1 and other topics related to near-surface wind interactions with orography. In each of the following subchapters, the research questions are addressed first. These are followed by considerations regarding the sensitivity of common turbulence parameters to flows over orography and the influence of the coordinate system used for turbulence measurements above terrain.

9.1 Upwind and downwind terrain effects

Previous studies reported in the Literature conclude that the upwind and downwind distances where idealised 2D hills affect the flow are dependent on terrain height and geometry (Chapter 4). While the present data inhibits evaluations of the influence of the ridge height (due to the excessive flow blockage posed by the higher ridge), slope effects are evident on the observed extents of terrain-induced turbulence both upwind and downwind from the landforms.

9.1.1 Upwind effects

Upwind disturbances caused by both terrain features on the mean flow parameters are restricted to short distances from the landforms and dependent on the inclination of the windward slopes of the ridges (or first ridges of the valleys). As observed in Chapter 7, the full extent of the upwind effects is contained within the corresponding flow subdomain (upwind subdomain) and flow disturbances are most evident for the steepest windward slope ($\gamma = 75°$). Equivalent findings are also made upwind from the first ridge of the smallest width valleys. The close agreement observed between the flow characteristics above the crests of the first ridges of the valleys and that of the corresponding single ridges indicates that the presence of the second ridge has virtually no effect on the flow upwind of the first.

Mean velocities exhibit the largest sensitivity to the presence of the orography further downwind. This is evidenced by the effects on all components of the mean velocities being felt further upwind from the ridges than those of the turbulence parameters. Deviations between approach flow and upwind velocities are first observed at up to $X \approx -6H$ from the foot of the steep windward slope. Similar slope dependences are observed for the mean turbulence parameters, albeit at closer streamwise distances from the terrain and at lower heights above the surface compared to the findings for the mean velocities. Mean velocity fluctuations are affected at further distances from the terrain than the fluxes, integral length scales, and the spectra. Longitudinal and vertical components of the fluctuations are the most sensitive. The earliest effect of the ridges on the mean fluctuations, at roughly $X \approx -5H$, is observed for the vertical component upstream from the steepest windward slope. Vertical effects on the turbulent fluctuations reach a maximum height of $z_{AT}/H \approx 2$. In terms of magnitude, lateral components are the most affected. At the near-surface, these overpower the longitudinal counterparts upstream from the steepest windward slope. The longitudinal blockage posed by the steeper slopes drives the increases of lateral and vertical turbulence intensities.

Turbulent fluxes are the least sensitive to the presence of the landforms further downwind, in particular the horizontal components. Starting at distances up to $X = -4H$, the effects of the inclinations of the windward slope are more evident on the vertical components of the fluxes. Furthermore, results indicate that the constant flux characteristics of the ASL are lost at distances from the terrain that increase with slope steepness. Effects of the ridges on the integral length scales are observed as far upstream as $X = -3H$ from the steep slope. Mean turbulence parameters are expectedly least affected upwind from the ridges with the smallest windward slope inclination ($\gamma = 10°$).

9.1.2 Downwind effects

Downwind flow turbulence overpowers in magnitude and outlasts in altitude and distance those observed upwind from the orography. The most prominent effects on the downwind flows are observed nearest to the landforms and are dependent on both slopes of the ridges. This is supported by the occurrence of flow separation at the crest of the gentle windward slope ($\gamma = 10°$), regardless of the agreement with the approach flow characteristics throughout the uphill positions. Thus, flow separation and recirculation characteristics are attributed to the influence of the steep leeside slope ($\theta = 75°$) of this ridge. Recirculation zones are generated at the crests of all ridges and the lengths of these are driven by the inclinations of the windward slopes. Increasing inclinations of the slopes result in increases of turbulence and decreases in the length of the recirculation zones.

The influence of the orography on turbulence deteriorates with increasing downwind distances. Above the furthermost downwind positions, the closest agreement to the reference data is observed. However, convergence between terrain and approach flow datasets is never achieved. Above the furthermost downwind position from the single ridges, $X \approx 26H$, data convergence with the approach flow is confined to the mean vertical fluxes and exclusively at the lowest measurement height ($z_{AT}/H = 0.38$). The extended downstream length of the valley domains provides improvements in levels of agreement with the approach flow turbulence data, particularly at $z_{AT}/H \leq 1.25$ above $X \approx 32H$. Near-constant vertical fluxes, contained within a layer of depth $Z = 50$ to $75\ m$ above the surface and displaying convergence with the approach flow, are consistent with an ASL of smaller depth than above flat terrain (Chapter 6). Longitudinal turbulence components exhibit the closest agreement with the approach flow, integral length scales achieving full convergence at all heights of the vertical profiles and longitudinal velocity fluctuations obtaining convergence with the inflow data at $z_{AT}/H \leq 0.94$. Valley type (slope) and width dependences are minimal at the furthermost downwind location.

9.2 Influence of geometric parameters

Within the vicinity of orography, there is a clear effect of the terrain geometries on all mean flow parameters. Maximum differences to the approach flow characteristics tend to increase with increasing slope steepness. This is valid for ridges and valleys, for which slope effects are also observed at upwind and extended downwind locations from the landforms. Windward slopes drive the largest increases of mean flow turbulence, which are observed downstream from the crests. This applies to the characteristics of flow separation and the subsequent recirculation zones. Above the leeside slopes, flow perturbations caused by the windward slope are unadjusted to the underlying surface and amplified by the added disturbance caused by the leeside slope. Nonetheless, effects of the orography on the turbulence above the leeside slopes are dominated by the inclination of the windward slopes. Larger inclinations of the windward slopes also govern the increases of lateral and vertical turbulence, particularly downstream from the crests.

Turbulence above the valleys is also dominated by the inclination of the windward slopes of the first ridges. This is evidenced by the maximum effects on turbulence corresponding to the valleys of constant width ($A = 12H$), for which the largest magnitudes of turbulence are observed above the mid-valley. These effects overpower those caused by the systematic width variations of each valley type at this location. Inflow conditions of the second ridges of the valleys are strongly affected by the flow recirculation zones, in turn driven by the geometries of the first ridges. However, the influence of the valley widths gains greater relevance on the flows above the second ridges. For the smaller width valleys, the second ridge intersects the same recirculation zones from the other valley widths at different locations. Thus, effects of the valley width modifications gain prominence. This is demonstrated by the largest variabilities between turbulence datasets that originate from the width variations of the same valley type, observed above the crests of the second ridges.

9.3 Surface heterogeneities versus orography

The present measurement data is limited in providing direct quantifications of the influence of orography compared with surface heterogeneities (changes in roughness) on turbulence. However, it can provide some indications towards which exerts the strongest influence on flows over orography. Regions upwind from the crest of the gentle windward sloped ridge correspond to those with the closest characteristics to the flat terrain, which shares the same homogeneous surface characteristics as the surfaces of the orography. As observed from the analyses made upwind from the respective single ridge (*Type I-10*), mean turbulence parameters are contained within the confidence intervals of the approach flow data until the transition to the windward slope. Above this slope, increases of turbulence relative to the flat terrain are observed. The only geometric difference between ridge and flat terrain surfaces is the $10°$ slope, which indicates that these increases are generated by orography. Thus, orography exerts greater influence on mean flow turbulence than the homogeneous roughness.

In the absence of terrain features, individual surface heterogeneities (single changes in roughness) above flat terrain provoke flow inhomogeneities that tend to readjust to the changes of the underlying surface rapidly (Antonia & Luxton, 1971; Wood, 1982). Following a tenfold step increase of roughness length (z_0), Cheng & Castro (2002) observe that a distance equivalent to at least 300 times the larger value of z_0 is required before the log-law profiles adjust to the flat surface. Downwind from the present orography, the effect of all ridges on turbulence extends beyond $X \approx 32H$, which is two orders of magnitude larger than the prediction of Cheng & Castro (2002). This supports the hypothesis of orography being more influential on the flow than surface heterogeneities. However, the present orography would constitute a step change of over 3000 under this rationale. Thus, larger ranges of impact due to the model height alone would be expected.

Verifications of z_0 above the regions upwind from the single ridges provide further insight into the exclusive contribution of the orography. In the eventuality of the effect of the ridges on the flow being smaller than the surface roughness, values of z_0 would expectedly remain stable (at least within the same roughness class) throughout this region. Applying the logarithmic law of the wall, Eq. (17), to the measurement data from the lowest $Z = 100\ m$ above the surface at each of the longitudinal locations of the region upwind from the gentle sloped ridge yields the results listed in Table 9-1. Values of z_0 are accompanied by those of the profile exponent (α), calculated from Eq. (18) using the same measurement data. Increases of z_0 and α with decreasing upwind distances from the ridge indicate increases in turbulence due to the orography. This occurs despite the vertical velocity profiles generally maintaining the same logarithmic shape throughout the upwind subdomain and a near-zero longitudinal pressure gradient near the transition to the windward slope. Previous studies centred on the effects of a single roughness step change above flat surfaces suggest that flow disturbances start above the surface heterogeneity, but present negligible upwind influence on the respective flows (Antonia & Luxton, 1971; Cheng & Castro, 2002; Wood, 1982). According to the data from Table 9-1, even the expectedly least impactful of the ridge geometries also disturbs the flows upstream from its location. Starting with similar values to flat terrain at the furthermost distances (moderately rough ASL), values of z_0 and α increase with proximity to the ridge resulting in very rough or rough ASL characteristics according to z_0 or α, respectively, at the foot of the ridge ($x/H = 0$).

Table 9-1. Average aerodynamic roughness and profile exponent from the lowest $Z = 100\ m$ above all streamwise positions of the upwind subdomain of the *Type I-10* ridge and respective roughness classes.

$-(x/H)$	surface roughness z_0 $[m]$	profile exponent α	roughness class
8.08	0.08	0.15	moderately rough
5.46	0.04	0.14	
3.90	0.08	0.15	
3.12	0.12	0.17	rough
2.34	0.18	0.18	
1.56	0.21	0.18	
0.78	0.62	0.23	very rough
0	0.70	0.22	

Further evidence for the dominance of orography over surface heterogeneities on turbulence originates from the data obtained from the high and low surface details of the same study domain performed by Erdmann (2017). Mean turbulence data shows agreement between heterogeneous ($\approx 7.5\ m$ horizontal grid resolution) and homogeneous ($\approx 1150\ m$) surfaces at the majority of the measurement locations. While the small model scale ($1{:}\,1750$) and limited measurement locations result in low temporal resolutions and fail to capture significant gradients across small distances, these findings do indicate that orography exerts more influence on flow dynamics. The study of the flow over Bolund Hill, performed by Petersen (2013) at the EWTL, also compares two models of distinct geometric resolution at a larger scale than that of the present investigation ($1{:}\,250$). Flows above a very coarse model, consisting of a terraced contour (step-like) geometry of perpendicular edges and a fine model, using smoothened and detailed surfaces, are compared. Strong dependence of flow characteristics on the existing surface heterogeneities is observed.

However, direct comparisons are hampered by differences in geometric shapes of the model hills and the strong effects of the sharp edges of the contoured terrace surface of the coarse model.

Following studies of flow over 2D hills with different homogeneous surface roughness conditions (two homogeneous roughness lengths, z_0), results from Cao & Tamura (2006) and Loureiro et al. (2007 and 2008) lead to similar conclusions. Despite the absence of surface heterogeneities, the flow differences caused by the distinct z_0 are evident but limited to the magnitudes of the mean flow parameters and flow separation characteristics. The presence of hills changes the shapes of the vertical profiles as well as the magnitudes, which indicates a stronger influence of the orography. Britter et al. (1981) provide comparisons between homogeneous and heterogeneous surfaces of a 2D hill, the surface heterogeneity case corresponding to a step change in roughness from rough to smooth layouts upwind from the hill. A major finding of the study is the occurrence of flow separation for the rougher arrangement and no flow separation for the smooth surface.

9.4 Orography classification based on flow turbulence

Based on the results of the present investigation, classifications of terrain types according to effects produced on the flow turbulence are unfeasible. Upwind and crest turbulence features are shared between the present ridges and valleys. As discussed earlier, similar downwind turbulence characteristics are also observed between the different landforms. Thus, clear distinctions between turbulence characteristics from ridge and valley flows cannot be made for the majority of the flow regions. The exception to the above observations corresponds to the flows above the second ridges of the valley domains. Mean and transient flows are characterised by strong increases of near-surface turbulence and consequent modifications of the respective vertical profiles that have no correspondence with the low levels of turbulence obtained above the crests of the first ridges. This arises from the strong disturbances caused by the first ridge, which shape the inflow profiles of the second. Resulting turbulence characteristics are unmatched throughout the study domains of the single ridges, thus are exclusive to valley flows. These characteristics can be classified as valley flow features, but only within the region englobing the second ridges and their immediate downwind vicinity.

It is important to point out that the present discussion is founded on equivalent geometries between idealised ridges and valleys. Distinctions between flow characteristics of both terrain types are strongly constrained. The terrain geometries are over-simplified and too similar to provide a more realistic assessment of flow characteristics that are specific to given terrain types. Similar considerations can be made for the data from the study of Diezel (2019), which uses an equivalent geometry for the v-shaped valleys and a different direction of the main flow relative to the orography. A more complete answer requires larger differences to exist between ridge and valley geometries to generate more distinguishable terrain-specific effects on flows.

9.5 Sensitivity of turbulence parameters

Relevant findings regarding the sensitivity of turbulence parameters, frequently used to quantify turbulence, to flows over orography can be made from the present data. The applicability of turbulence intensities, obtained via Eq. (16), is constrained due to local terrain effects. Small mean velocities result in amplified quantifications of all components of the turbulence intensity, most evident above the leeside slopes and downwind regions of the terrain features of the present investigation. Erroneous quantifications ($> 100\%$) would be observed for longitudinal and lateral components of all ridge domains. An alternative approach, involving the mean reference (U_0) or friction (u_*) velocities at these locations, could lead to significantly decreased quantifications of the turbulence intensity due to the relatively small absolute values of the local velocity fluctuations. Hence, it is recommended that expressions of the turbulence intensity are avoided when characterising flows over complex terrain. This is also valid for the gust factors ($G_{T,\tau}$) of the transient analyses of the valley flows, where the near-zero mean velocities ($\overline{U_T}$) related to the near-surface heights of the inner valley positions can result in over-quantifications of gustiness.

As evidenced by the data from Table 9-1, the roughness length (z_0) is dependent on the near-surface characteristics of the flow. Classic predictions of z_0 result from observations made above flat surfaces with homogeneous roughness, corresponding to flow equilibrium conditions with the underlying surfaces. Values of z_0 obtained through the law of the wall, Eq. (17), are observed to strongly fluctuate throughout the terrain domains. This includes the upwind region, where results indicate that the smallest disturbances are sufficient to generate local flow imbalances that (unrealistically) amplify the values of z_0. This is exemplified for the upwind region of the gentle windward slope ridge (*Type I-10*) in Table 9-1, where z_0 achieves values consistent with very rough ABL flows upwind from the ridge. This indicates a lack of applicability of the law of the wall for flows over orography. A similar rationale can be made for the profile exponent (α), obtained from the exponential function at the same height range as z_0. Values of α corresponding to that of very rough ABL flows are also observed at the same upwind distances from the respective ridges, thus exhibit similar sensitivity to the presence of the ridges as z_0.

Further evidence of this originates from the comparison of friction velocities (u_*), obtained through the vertical turbulent fluxes, as in Eq. (19), and using the law of the wall. Table 9-2 presents the mean values of u_* above the foot of each ridge and above flat terrain, calculated using both approaches. Values of u_* obtained from the separate approaches display significant differences, which increase with windward slope inclinations due to the slope influence on the law of the wall (as with z_0). Values obtained from the vertical fluxes present relatively smaller increases due to the ridge slopes.

Table 9-2. Mean friction velocities from the lowest $Z = 100\ m$ above the foot of the windward slopes ($-x/H = 0$) of all ridges and flat terrain calculated via the law of the wall and the vertical turbulent fluxes.

friction velocity	Type I-75	Type I-10	Type II	Flat terrain
$\boldsymbol{u_*}$ (law of the wall) $[\boldsymbol{m/s}]$	0.92	0.32	0.51	0.21
$\boldsymbol{u_*}$ (vertical fluxes) $[\boldsymbol{m/s}]$	0.31	0.23	0.26	0.22

Re-applying the law of the wall to calculate z_0 above the same position of the single ridges using u_* obtained from the fluxes yields less exaggerated values of z_0: $\approx 6\ m$ (*Type I-75* ridge), $\approx 0.2\ m$ (*Type I-10*) and $\approx 0.7\ m$ (*Type II*). Under this approach, values of z_0 range from the lower bounds of a rough ASL (*Type I-10*) to the lower bound of a very rough ASL (*Type II*), whereas that of the steep windward slope (*Type I-75*) continues to exceed the upper limit of the latter roughness class.

Spectral distributions of turbulent energy at the heights nearest to the surface exhibit significant shifts of the frequencies of peak energy compared to the approach flow and the data from Kaimal (1972) and Simiu & Scanlan (1986). These occur despite the related probability density functions exhibiting normal distributions, without excessive skewness or bi-modal distributions. This indicates that the observed frequency shifts are motivated by the orography. Similar trends are reported by Cao & Tamura (2006), shifts of frequency of over an order of magnitude relative to the inflow being observed downstream from hills. Liu et al. (2019) also report shifts of the wavenumbers of the peaks of the spectra between the modelled LES flows above the crest and above two locations downstream of a 3D hill. These findings are generally consistent with those made from the present data.

Frequency shifts are largest at locations where the orography is observed to exert the strongest effects on the mean turbulence parameters, most notably downstream from the crests of the ridges. This corresponds to the turbulent wake region generated by the ridges, where flow recirculation occurs and sharp gradients of the mean wind velocities are observed. Profiles of the integral length scales indicate strong decreases of the energy-intensive eddy lengths relative to the approach flow. This is consistent with the observations made with the laser-light sheet within the wake regions downstream from the crests of the ridges. At the near-surface immediately downwind from the ridges, frequent ejections of small longitudinal eddies from the more energetic recirculation zones (containing larger, more steady eddies) are observed. These follow the reversed flow and, depending on the inclination of the slopes, move uphill the leeside slope towards the crests while successively being broken down by the interactions with the surfaces. The frequency shifts could also arise from different inclinations of the mean velocity vectors relative to the approach flow. Shifts are largest for steeper slopes, as supported by the observations upwind from the single ridges where only the steepest windward slope produces evident frequency shifts.

9.6 Effects of the coordinate system

Earth (fixed) and flow-referenced coordinate systems for flows above landforms have benefits and drawbacks, as discussed in Chapter 5. Differences between these approaches can be evaluated through rotated quantifications of the present measurement datasets to the flow-referenced system, using the script of Diezel (2019). The 2D data is rotated (independently) according to horizontal and vertical angles from the absolute zero of the lateral and vertical components of the velocity, respectively ($V = W = 0$), as outlined by Kaimal & Finningan (1994), for example. Results of transformations performed for mean velocities, velocity fluctuations and spectra above the slopes of the single ridges are analysed in Appendix F.

The flow-referenced coordinate system is best suited for expressions of the mean longitudinal velocity, as observed from the data of the steepest windward slope. This is particularly valid at heights nearest to the surface where larger differences between the directions of the mean velocity vectors of both coordinate systems are found. As expected, the flow-referenced data captures the largest magnitudes of the mean velocity. Thus, the rotation of the measurement data to the flow-referenced system is most advantageous. However, the same is not verified for the mean velocity fluctuations. While the rotated data produces the largest magnitudes of the vertical fluctuations, the largest magnitudes of the longitudinal components are observed for the Earth coordinate system. The inverse is observed above the equivalent relative slope positions of the leeside slope of the same ridge. Transformations of the spectra to the flow-referenced system result in similar distributions to those obtained in the Earth coordinate system. These are observed to maintain the shifts in frequency of the peaks of longitudinal and lateral spectra above the leeside slope obtained in the Earth coordinate system. Thus, the frequency shifts are broadly independent of the coordinate systems used.

Differences between fixed and rotated turbulence data are slope-dependent, the largest differences expectedly found downwind from the crests of the ridges. Flow instabilities at these locations lead to significant fluctuations of the directions of the transient velocity vectors, which may result in relevant inaccuracies of the time-averaged directions of the mean velocity vectors. For example, directions of the transient vertical plane velocity vectors observed at the near-surface above $X = 2H$ downwind from the ridge with the steep leeside slope fluctuate up to roughly $\pm 40°$ from the mean orientation. Smaller differences between the orientations of the mean horizontal velocity vectors above the centreline ($Y = 0$) dictate that lateral fluctuations are less affected by the coordinate system. However, the independent rotation of measured 2D data via different angles for horizontal and vertical planes results in different quantifications of the longitudinal components. This renders the flow-referenced coordinate system inept for constructions of 3D flow characteristics from 2D measurements. Furthermore, larger contributions from the side slopes can result in acceleration of lateral flows. This is exemplified by the increases of mean lateral velocity observed within the inner valley regions in Chapter 8. Rotation of the data to flow-referenced coordinates fails to quantify the stronger contributions from the lateral flow at such locations.

The present investigation highlights the relevance of the employed coordinate systems for characterisations of flows over orography. Flow-referenced coordinates are most advantageous in quantifying the largest magnitudes of longitudinal (streamline) velocities. However, the strongest magnitudes of turbulence fail to be quantified above the windward slopes. This indicates that the directions of maximal turbulent momentum are not parallel to the streamline velocity vectors. Similar observations are made from the transformations of the leeside slope turbulence data. Further analyses of the influence of the coordinate systems on the turbulence characteristics downstream from the single ridges or the within the inner valley regions can provide further insight into the adequacy of the flow-referenced coordinate system for flow recirculation characteristics. A third approach consists of maintaining the vertical coordinate of the Earth coordinate system and transforming the horizontal coordinates to the flow-referenced system (Kaimal & Finningan, 1994). However, this implies that the resulting flow axes are not perpendicular and the aforementioned larger contributions from the side slopes are still neglected. Furthermore, this method has limited applicability in terms of potential setups for measurements with LDV defined with the hybrid coordinate system.

10 CONCLUSIONS

It is well understood that orography influences local (up to mesoscale) meteorology, which in turn can affect the accuracy of numerical weather predictions. The advent of nesting procedures, which incorporate outputs of small-scale models into inputs of larger scale weather forecasting models, is known to provide better result accuracy. Ever-increasing computational developments have aided the development of such procedures, but demands for improved predictability of the smaller scale phenomena overpower this growth. The understanding of atmospheric flow interactions with complex terrain plays a significant role in the precision of downscaling approaches. Not only is this relevant for general weather forecasting, but also in applications concerned with sustainability, such as wind engineering or air quality.

Motivated by wind energy applications, microscale studies of flows are predominantly focused on expressing the speed-up as quantifier of the potential gains in wind speed above orography. While the linear theory has provided satisfactory predictions above gentle-sloped orography, it is inadequate for turbulence characterisations and breaks down when flow separation takes place. Large costs related to wind farms imply that accurate predictions of the impact of turbulence on the performance and durability of the associated infrastructures must be well understood before on-site installation can take place. Such requirements have led to CFD methods becoming the main numerical tool for flow predictions, their accuracy limited by the available computational capacities that govern the resolutions (grid sizes) of the simulations and the lack of adequate validation data. Increases of spatial and temporal resolutions of numerical models also mean that sub-grid effects become more evident and require understanding.

Data from field campaigns and physical models has been used to validate microscale numerical models. Field campaigns provide realistic data, no modelling assumptions being required, but are limited by large costs and unsteady meteorological conditions. Appropriate terrain sites for field campaigns require well defined inflow conditions and isolated landforms, not frequent in nature. Physical modelling campaigns have the benefit of fully controllable inflow conditions, but limited in the resolvability of the small structures of scaled flows and simultaneously replicating all contributions to the real-world flows. However, scaled turbulent flows that statistically resemble the full-scale counterparts can be achieved under the fulfilment of flow similarity criteria. In the present chapter, a summary of the flows over the idealised orography is made. This is followed by a discussion regarding potential enhancements to the current investigation.

10.1 Flow turbulence over orography

When comparable, the majority of mean flow trends of the present investigation replicate those reported in the relevant Literature. Orography affects surface layer flow turbulence and the largest effects of the idealised landforms on turbulence are nearest to the surface. This is verified by the largest increases of the magnitudes of the turbulence parameters with regard to the undisturbed flow. Upwind from the terrain features, the inclination of the windward slopes governs the intensities of the increases of turbulence relative to the inflow. According to the results obtained for the single ridges, turbulence parameters are first affected at upstream distances equivalent to approximately four times the ridge height ($X = -4H$) and up to altitudes equivalent to roughly two times the ridge height ($Z \approx 2H$). These observations are made upwind from the steepest windward slope, for which surface layer characteristics (constant vertical fluxes) are the earliest to be lost at $X \approx -2H$.

The exclusive effects of the windward slope are maintained up to the crests, downstream from which flow separation and consequent recirculation (reversed flow) originate for all geometries. Lengths and turbulence magnitudes of the recirculation zones are primarily dependent on the windward slopes, but also influenced by the inclination of the leeside slopes. Steeper windward slopes tend to produce smaller lengths and larger heights of the recirculation zones, together with larger magnitudes of turbulence. Relative to the regions upwind from the crests, magnitudes of the turbulence parameters increase above the leeside slopes and nearby downstream locations from the single ridges (or the first ridge of the valleys), where the maxima of the majority of turbulence parameters are observed. Also downstream from the crests, strong increases of lateral turbulence indicate the effect of the side slopes of the ridges on the turbulence above the centreline of the terrain ($Y = 0$). Within the vertical recirculation zones, these overpower the longitudinal contributions on the turbulent fluctuations.

With increasing downwind distances from the orography, magnitudes of all turbulence parameters decay and start to converge towards the approach flow characteristics. At the furthermost locations, effects of terrain types (valleys or ridges) and geometric parameters (ridge slopes and valley widths) on the turbulence are less expressive compared with the blockage induced by the presence of the landforms. Vertical profiles of the mean turbulence parameters fail to fully replicate those of the approach flow at the furthermost downwind location of both experimental campaigns: $X = 32H$ from the foot of the leeside slope of the second ridge of the valleys. The closest agreement with the approach flow is observed at the near-surface heights and for the longitudinal turbulence parameters. For valley flows, the presence of the second ridges has virtually no effect on the turbulence upwind from the crests of the first ridges. Thus, increases in turbulence of these flows are governed by the inclination of the windward slopes of the first ridges. Within the inner valley regions upwind from the second ridge, vertical profiles of the turbulence parameters strongly resemble those of the downwind region of the single ridges and the windward slope of the first ridge determines the inflow characteristics of the second ridge. These are also strongly affected by the modifications made to the valley widths, decreasing instabilities of the longitudinal inflow profiles of the second ridges result from increasing valley widths. Upwind from the second ridges, increases of lateral and decreases of vertical components of turbulence accompany decreases of the valley widths. This relationship is inverted for the lateral components above the second ridges.

10.2 Recommendations for further studies

To different degrees, the data from the present investigation addresses the research questions outlined in Chapter 1. While robust conclusions can be made regarding the upwind effects of the terrain or the effects of the ridge slopes and valley widths on the turbulence, for example, other topics fail to be thoroughly addressed. Discussions on complementary work to address these topics and potential additions or enhancements to the experimental and measurement setups are made here.

Downwind effects of orography

The full extent of the terrain effects on the downwind turbulence fails to be captured within the available model section of the wind tunnel, particularly at the upper altitudes of the vertical profiles. Stronger agreement with the inflow turbulence characteristics results from the additional $X \approx 6H$ of the furthermost downstream positions from the valleys relative to the single ridges. This indicates proximity to the location where the inflow profiles are fully recuperated. In order to assess this, a further upstream shift of the orography-containing model plates can be made to the model setups, as performed prior to the valley campaign. For purposes of comparability with the present data, the modelled inflow characteristics that result from this modification must match those of the present experimental setups.

Influence of surface heterogeneities

As discussed in Chapter 9, the most influential between surface heterogeneities and orography on the flow turbulence cannot be comprehensively ascertained from the present data. Direct methods to evaluate this require terrain models with heterogeneous surface roughness that enable a quantification of the exclusive effects of these relative to the orography. A complementary study of the present investigation could involve the evaluation of the effects of roughness transitions on the current terrain scenarios with added surface roughness. A feasible exercise consists of evaluating the disturbances posed by a steep change in surface roughness above the current flat terrain scenario, at the same locations and with the same inflow characteristics as the present terrain models. Quantifications of the effects of surface heterogeneities relative to the orography could be accomplished through the comparison of the resulting turbulence characteristics with the current data. Extending this approach to the landform models would provide a detailed understanding of the combined influence of surface heterogeneities and orography on the turbulence.

Additional terrain geometries

Studies of additional terrain geometries, which supplement the present investigation, can provide further insights into flow interactions with orography. Effects of specific geometric parameters that are influential (according to findings in the Literature) on flows over complex terrain, unaddressed by the data from the present investigation, should constitute a next step of additional research. In particular, systematic variations of the heights and leeside slopes of the current single ridges would be most relevant in this regard. The former should use terrain heights that are close to those of the current ridges and flow blockage effects should be minimised. Effects produced by the windward slopes of the present ridges are well established from the data and generally outweigh those of the leeside slopes. Quantifications of the exclusive influence of the leeside slopes on the flows should consist of modifications to the inclinations of the leeside slopes whilst maintaining the windward slope features constant.

An overview of all the complex terrain models related to the current research effort reveals a significant gap of model complexity between the present single, idealised terrain geometries and the structured terrain model of Hainich National Park (Erdmann, 2017). As well as bridging the levels of flow complexity between these terrain models, studies of flow interactions with additional orography could also provide further insight into how transitions between different terrain types affect turbulence and enable assessments of the transferability of the present data to other landforms. The next level of complexity should consist of single 3D ridges and valleys based on real-world orography. In a perspective of obtaining maximised comparability with the data from the present investigation, these should use the same geometric scale.

Transient flow analyses

Increased measurement data rates gained with the adjustment of the LDV settings prior to the valley campaign are insufficient to provide adequate temporal resolutions to characterise the smaller turbulence structures for transient flow analyses (Chapter 8). The next measure to enhance the data rates of the measurements above orography should consist of LDV measurements made in non-coincidence mode with the Prandtl tube reference measurements. Under this approach, all particles transiting through the measurement volume are sampled regardless of the reference measurement status. Further increases of data rate can be achieved by increasing the volumes of seeding and the laser voltage of the LDV. However, particle agglomeration can occur from over-seeding and should be minimised. Furthermore, higher voltages at near-surface locations increase the potential to damage the photomultiplier of the laser system through light backscatter. Joint time-frequency data analyses can provide further insight regarding the effects of orography on near-surface turbulence, in particular its temporal propagation. Similarly, wavelet analyses can be applied with the purpose of enabling coherent structure identification.

Coordinate system

The optimal choice between Earth and flow-referenced coordinate systems is non-trivial in the context of characterising flow turbulence above orography. Different results are observed between rotated longitudinal components measured at the same locations in horizontal and vertical planes. This arises due to the different inclinations of the horizontal and vertical streamwise velocity vectors and implies that lateral and vertical components cease to be perpendicular. Robust conclusions regarding the suitability/reliability of rotated coordinate systems for turbulence characterisations of flows above the present landforms cannot be made. This can be further evaluated through 3D measurements in the flow-referenced system. These should be focused on near-surface heights above select locations of the present datasets. This requires a pre-determination of the full range of streamline orientations at every desired measurement point, followed by the adjustment of the longitudinal measurement volume axis accordingly. This can be achieved through construction of streamlines from consecutive measurements, reorienting the LDV probe in the direction of the resulting vector after each.

Alternative characterisations

Flow measurements, such as those of the present investigation, provide the most complete data for turbulence characterisations. However, supplemental data from measurements of other parameters can shed further light on flow dynamics over orography and are rarely investigated in the Literature. Air quality analyses, based on concentration measurements that fulfil Froude number (Fr) similarity, can provide more details of the turbulence structure of the flows. To build on the present datasets, these should be focused on the regions downwind from the crests of the single ridges (crests of the first ridges of the valleys). Flow measurements, coupled with the scalar characterisations, should use the Earth or the hybrid coordinate system (Chapter 9). Buoyancy occurs vertically regardless of the inclinations of the underlying surfaces. Consequently, the vertical axis cannot be rotated. Downwind from the crests of the ridges, surface pressure measurements through static pressure taps mounted in the terrain models can enable more complete characterisations of the recirculation zones through adverse pressure gradients. Effects of atmospheric stability on the terrain flows of the present investigation can also be explored using the stratification wind tunnel of the EWTL. This would provide data on thermally-induced turbulence of flows with near-neutral stabilities, which could be coupled with the mechanically-induced turbulence data of the present investigation.

APPENDIX A – ATMOSPHERIC BOUNDARY LAYER FLOW MODELLING

Laser-Doppler velocimetry (LDV)

A one-component LDV system typically consists of a monochromatic, temporally coherent laser source split into two beams (via beam splitting) with light intensities that present a Gaussian shape (Molki et al., 2013; Vetrano & Riethmuller, 2010). A transmitter focuses and intersects the beams at a fixed distance, the focal length (Molki et al., 2013). This creates a superimposition of fixed-frequency waves in the measurement volume, forming an equally-spaced interference fringe pattern of parallel dark/bright sections (Ruck, 1991; Vetrano & Riethmuller, 2010). Fringe spacing (Δx) is dependent on the wavelength (λ) and the semi-angle formed between laser beams (φ), being given by the following relationship (Ruck, 1991).

$$\Delta x = \frac{\lambda}{2sin\varphi}$$

Light backscatter caused by the particles transiting through the measurement volume creates frequency shifts (Δf) detected by the system optics and correspond to the velocity components that are perpendicular to the fringe arrangement ($u_{\perp}$). Perpendicular velocity components are computed as follows (Ruck, 1991).

$$u_{\perp} = \Delta f \Delta x = \frac{\lambda \Delta f}{2sin\varphi}$$

The frequency shift alone produces identical signals when particles move in the forward or backward (reversed flow) direction, creating a directional ambiguity problem. To overcome this, LDV systems typically employ a Bragg cell to produce an additional constant frequency shift between the laser beams to distinguish negative velocities from the positive velocities.

To perform 3D measurements using a 2D LDV, the probe is aligned horizontally or vertically with the main flow component (longitudinal). This results in two independent samples of the longitudinal flow component for each measurement position. For horizontal plane (UV) measurements, the measurement volume is generated directly below the probe laser optics. This enables measurements at most (if not all) heights above the terrain models. The same does not apply for vertical plane (UW) measurements, for which the measurement volume is generated horizontally from the probe (transversal direction). This creates difficulties in positioning the probe without contact with the surfaces for near-surface measurements, particularly for complex terrain models which have a significantly larger horizontal extension than buildings present in urban domains, for example.

A useful approach that allows the measurement volume to be positioned at lower heights is to rotate the LDV probe, generating the measurement volume obliquely relative to the probe position. The laser fringe pattern is not perpendicular with the flow, which creates a velocity measurement offset. The larger the rotation angle the more the fringe pattern becomes oblique with respect to the flow, the particles take longer to pass through the measurement volume and the system measures smaller velocities than the actual particle velocities. Measurement compensation, through the application of a transformation factor (TF) to the measured UW velocities is required. TF is dependent on the amplitude of probe rotation (θ), which is calculated through trigonometric relationships (in this case the tangent) for the right triangle created between the horizontal focal length (b) and the height offset (a).

$$TF = \frac{1}{\cos\theta} = \frac{1}{\cos\left(tg^{-1}\left[\frac{a}{b}\right]\right)}$$

The applicability of this approach is constrained by the uncertainty created by high values of TF, which are most accurate when $= 1$ (horizontal alignment of the probe and measurement volume perpendicular to the flow components). Higher amplitudes of rotation lead to greater uncertainties of the resulting measurements ($TF > 1$). With the aim of limiting increases in measurement uncertainty to a minimum ($\leq \pm 2\%$), θ is limited to a maximum angle of $\approx 15^{\circ}$ for the UW measurement setups of the present investigation.

In turbulent flows of higher complexity, particle velocity statistics are not true representations of the mean velocities of the flow, i.e., the velocity distributions do not correspond to Eulerian averages and are distorted (George, 1988; Nobach, 1999). This arises due to particles transiting the measurement volume at different velocities, resulting in biases of flow statistics that are commonly computed with normal arithmetic averages from the following relationships for the mean ($\bar{u}$) and the variance ($\overline{\sigma_u^2}$) of each sampled particle i, respectively (George, 1988; Nobach, 1999).

$$\bar{u} = \frac{1}{N}\sum_{i=1}^{N} u_i$$

$$\overline{\sigma_u^2} = \frac{1}{N-1}\sum_{i=1}^{N}(u_i - \bar{u})^2$$

Biased statistics can be minimised through the application of weighting procedures for each measured value of velocity, thus providing a more reliable quantification of the mean flow characteristics. These include velocity weighting (only for 1D flows and noise sensitive), arrival time weighting (dependent on very high data rates for reliability) and transit time weighting (Nobach, 1999). Gillmeier (2014) provides a detailed discussion regarding each of these methods and their suitability for measurements of flows over very small scale orography.

For the present investigation, all associated mean flow parameters use transit time weighting. Transit (or residence) time weighting uses the time that each particle i requires to pass through the measurement volume (Δt_i), which must be determined independently from the Doppler shift and is dependent on constant particle concentrations (uniform scattered particle distributions in space) for maximised accuracy (George, 1988; Nobach, 1999). For this weighting technique, the average flow statistics correspond to those calculated using the following formulae for the mean and variance, respectively.

$$\bar{u} = \frac{\sum_{i=1}^{N} u_i \Delta t_i}{\sum_{i=1}^{N} \Delta t_i}$$

$$\overline{\sigma_u^2} = \frac{\sum_{i=1}^{N} (u_i - \bar{u})^2 \Delta t_i}{\sum_{i=1}^{N} \Delta t_i}$$

Numerical modelling of ABL flows

Predictions of fluid flows and heat transfer by means of numerical modelling is vastly applied in a wide variety of engineering and scientific sectors. This has been strongly driven by the advent of high-performance computational processing capacities, under continuous improvement, resulting in increased volumes of mathematical operations in shorter times. In essence, numerical modelling consists of the resolution of the Navier-Stokes Equation (NSE) for each cell of a user-defined computational grid with sets of user-specified flow parameters. Numerical models are structured codes of numerical algorithms that compute fluid flows. Typical methods of numerical modelling involve three major phases:

- Pre-processing – the modeller specifies the geometry (computational domain), generates the computational grid (division of the domain into cells), specifies boundary conditions at cells closest to the domain boundaries, and defines the fluid properties to be modelled.

- Processing – the numerical algorithm (also called solver) solves the virtual flow field using one of three main numerical solution techniques (finite difference, finite element, or spectral methods).
- Post-processing –numerical results and statistics are observed using visualisation tools.

The main problem of modelling turbulent flows resides in the dominance of non-linear effects and the requirement to accurately account for the contributions of all scales in the spectrum. In terms of numerical accuracy, the optimal size of a typical study domain should be larger (at least one order of magnitude) than the turbulent energy-intensive scales (larger eddies), while the numerical grid should present a high enough resolution to calculate the smallest relevant length scales of the flow (Zhiyin, 2015). Such requirements tend to be computationally intensive, particularly for larger study domains. These demand more grid cells, which increases the number of cell-specific calculations required for the simulation.

Different turbulence closure methods deal with the non-linear, multi-scale effects. Their main limitation is related to capturing the contributions of all scales in the spectrum with sufficient accuracy. Closure models can be classified according to the number of transport equations that are solved in addition to the NSE, ranging from approximate (steady-state) to highly rigorous (3D transient over entire spectrum).

The specification of boundary conditions also influences the outcome of numerical turbulence modelling, the most relevant for the present investigation being the surface condition. Numerical models typically employ wall functions to quantify the effects of the surface that are implicitly resolved in the flow simulations, corresponding to details that are not contemplated by the computational domains. This is due to their small dimensions relative to the grid size or as consequence of being contained in regions of lower priority that are minimised in order to reduce the computational requirements of processing (such as inflow regions). Wall functions used to replicate these effects on the near-surface flows are commonly based on the law of the wall (Eq. 17, Chapter 2) and are expressed in terms of surface roughness, typically by the roughness length (z_0) for ABL flow modelling. This can be disadvantageous for coarser grid resolutions, resulting in larger inaccuracies of the applied wall functions due to the near-wall gradients of flow and turbulence variables that are not captured by the simulations (sub-grid scale).

Numerical modelling of the atmospheric boundary layer (ABL) is typically more complex than for common engineering applications. As well as orography, surface heat and moisture exchanges with the atmosphere, the non-continuous nature of the incoming atmospheric flows, and Earth's rotation (Coriolis forces) are strongly influential on ABL flows. Due to the typical grid scales being orders of magnitude larger than the turbulent energy length scales, mesoscale modelling typically has limited flow turbulence modelling capabilities (Stull, 2000; Wyngaard, 2004). A common practice to achieve higher accuracy of numerical mesoscale predictions is to couple them with smaller scale numerical models, typically microscale models nested in mesoscale models. This provides more precise input boundary conditions for the larger scale simulations. In typical microscale numerical modelling, turbulence is extremely influential and must be modelled. The most traditional microscale modelling approach is to resolve turbulence using linear eddy viscosity based closures, which in turn provide a variety of turbulence "resolving" models (Hanjalic & Kenjeres, 2008). There are three main numerical methods used to solve the incompressible NSE at microscale: direct numerical simulation (DNS), large-eddy simulation (LES) and Reynolds-averaged Navier-Stokes (RANS).

Based on the Reynolds decomposition, steady-state RANS has been the most widely applied of the methods to numerically simulate ABL flows. It is characterised by statistical steadiness (stationarity) of flow conditions, with time averaging of the full spectrum of turbulent scales over an infinite 1D interval (Kempf, 2008; Salim et al., 2011). The main advantage of RANS is computational economy and speed of simulation, however it tends to use oversimplified (namely, first order closure) turbulence models that result in increasing losses of accuracy with increasing flow complexity, such as higher Reynolds numbers (Hanjalic & Kenjeres, 2008). Steady RANS is incapable of simulating unsteady flow phenomena and only provides statistical estimates of turbulent transport quantities. Increases in computational capacity have enabled developments to RANS methods and approaches that contemplate non-linear effects, such as unsteady RANS (URANS) and hybrid RANS/LES, have been proposed. URANS consists of the addition of an unsteady term to the momentum equation and processing through ensemble averaging to resolve partial time derivatives (finite time interval averaging) using the same turbulence models as steady RANS (Hanjalic & Kenjeres, 2008). Hybrid RANS/LES methods consist of the partial averaging of the NSE using URANS near walls and LES for the remaining study domain. This corresponds to a lower dependence on the turbulence models than pure URANS while requiring equivalent computational efforts.

DNS is the most recent of the aforementioned methods and is the only one with potential to provide a complete description of a turbulent flow through the resolution of the NSE at all scales of motion, including the smallest dynamically significant length-scales, without closure requirements (Moin & Mahesh, 1998). However, DNS is significantly more expensive than RANS and LES and requires super-computing capabilities for more complex flows. In the context of ABL flow investigations, characterised by high levels of turbulence and extensive study domains, DNS is presently an unrealistic alternative to RANS or LES for large study domains.

Considered the successor to RANS-based methods, LES aims to model flows with a complexity that is solely dependent on the numerical resolution, thus independent of Re (Berselli et al., 2005). The method was proposed as early as 1963 by Smagorinski for atmospheric predictions and had its first thorough application by Deardorff (1970) for the investigation of turbulent shear flow within a channel at very high Reynolds numbers (Berselli et al., 2005; Zhiyin, 2015). LES is more realistic than RANS, providing time-dependent (transient) information about the flow field due to its spatial filtering methods. This provides the capability to replicate complex, unsteady ABL flow phenomena for which RANS methods inherently fail. LES consists of separating the flow into small and large scales of turbulent motion through explicit or implicit spatial filtering, which is performed over a volume related (frequently equal) to the local grid size or required level of resolution (Germano, 1992). The larger eddies associated to the high energy scales of turbulent motion are computed directly from the NSE and the smaller unresolved ones, the sub-grid scale (SGS) eddies, modelled under the assumption that the smaller scales of turbulence tend to be more isotropic and homogeneous (self-similar) than the larger ones (Sorbjan, 2004; Zhiyin, 2015).

Several SGS models have been developed since the advent of LES, the majority based on the eddy viscosity of stress tensors (in turn based on the Boussinesq turbulent viscosity hypothesis). These have been found to work well with most fully turbulent flows, in which large fractions of the total turbulent kinetic energy can be resolved. However, for applications in which complex geometries and very high Reynolds numbers are a factor there is a requirement for more accurate SGS models (Zhiyin, 2015). An additional feature that reinforces this requirement is that Smagorinsky-based SGS models are absolutely dissipative, thus optimised for so called 'forward scatter' predictions (energy transfer from large to small scales) but cannot predict 'backscatter' flows (energy transfer from small to large scales) associated to intermittent fluctuations of SGS stresses (Berselli et al., 2005; Sorbjan, 2004). As well as SGS modelling, the selection of spatial filters and corresponding parameters (radius and shape parameters) is influential on result accuracy. Therefore, these are expected to assume greater importance as LES develops.

APPENDIX B – LONGITUDINAL PRESSURE GRADIENTS

Results of flow measurements can be severely influenced by flow blockage effects that create undesirable and unrealistic pressure gradients that should be minimised, if not maintained at zero. The dimensionless longitudinal pressure gradient (p_*) between different streamwise positions (Δx) should satisfy the condition expressed below (VDI, 2000). p_* is dependent on the depth of the modelled ABL (δ) and the corresponding streamwise velocity at the same height (u_δ), as well as the density of the air (ρ).

$$p_* = \frac{\left({}^{\partial p}/_{\partial x} \times \delta \right)}{\left({}^{\rho}/_{2} \times u_\delta^2 \right)} \leq 0.05$$

Static pressures in the streamwise flow direction are evaluated at eleven pairs of pressure taps located at each of the wind tunnel sidewalls at equidistant streamwise locations ($\Delta x \sim 1.5\ m$, model-scale), each at heights of approximately $1.5\ m$ from the wind-tunnel floor. These measurements are performed for the flat terrain and the $H = 200\ mm$ high (model-scale) ridge, contemplating both extremes in terms of expected minimal and maximal flow blockage due to the presence of the terrain models.

The traverse system, expected to affect the results due to its close proximity to the pressure intake heights, is initially at its home position ($X_{ms} \sim 15\ m, Y_{ms} \sim -1.6\ m$). For the calculation of p_*, δ is assumed to be $1\ m$ (model-scale) and the constant air density (ρ) considered $1.2\ kg/m^3$. To ascertain the combined effect of the ridge and the traverse system on p_*, further measurements are performed at the most relevant longitudinal positions, i.e., $7.5 \leq X_{ms} \leq 15\ (m)$. The traverse system is moved to a longitudinal position above the location of the ridge crest (between pressure taps at $X_{ms} = 10.5\ m$ and $12\ m$). The combined effect of the ridge model and the traverse system above the centreline position ($Y = 0\ m$) is also checked.

Figure B1 presents the absolute values of p_* (or $\|p_*\|$) taken at each streamwise position with the traverse system located at the home switch position. Results relative to the measurements with the traverse system located at the home position are presented in Fig. B1a, and those with the traverse located upstream (or above the ridge crest position) are presented in Fig. B1b. The latter includes the static pressure data from both span-wise traverse system locations ($Y_{ms} \sim -1.6\ m$ and $Y_{ms} = 0\ m$). At all streamwise positions and for both model scenarios of Fig. B1a, p_* is contained within the 5% threshold and the presence of the largest ridge alone has a negligible effect. The ridge combined with the traverse, in Fig. B1b, produces values of p_* that exceed the condition expressed above, increasing to $\approx 9\%$ with the traverse located at $X_{ms} = 12\ m$ and $Y_{ms} \sim -1.6\ m$. With the shift of the traverse to $Y_{ms} = 0\ m$, p_* decreases to $\approx 6\%$. Thus, the higher ridge ($H = 200\ mm$) leads to prohibitive increases of flow blockage and cannot be assumed meaningful, despite the acceptable geometric blockage.

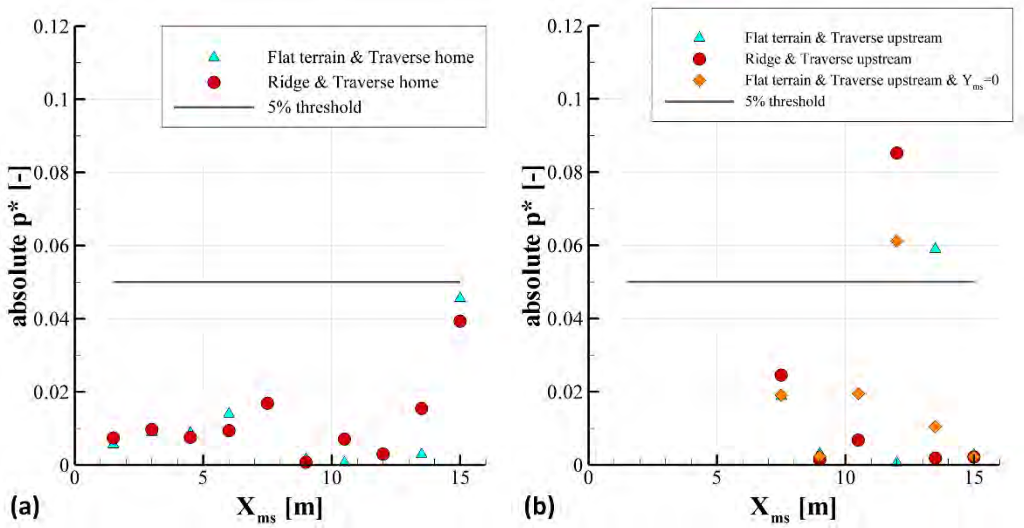

Figure B1. Longitudinal static pressure at every $\Delta X = 1.5\ m$ for flat terrain and ridge of $H = 200\ mm$ (model scale) with traverse system located at the longitudinal home position (a) and above the crest of the ridge (b). The reference line corresponds to the 5% limit as defined in VDI (2000).

APPENDIX C – INFLOW AND FLAT TERRAIN CHARACTERISTICS

Table C1. Experimental setups used for ABL flow of present investigation (dimensions in model-scale).

	Large scale turbulence generation	Small scale turbulence generation	Ceiling adjustment
1	Saw-tooth1	-	Setup 1
2	Saw-tooth2	-	Setup 1
3	Saw-tooth1	6 mm chains ($\Delta x = 50\ cm$)	Setup 1
4	Barrier1	6 mm chains ($\Delta x = 50\ cm$)	Setup 1
5	-	6 mm chains ($\Delta x = 50\ cm$)	Setup 1
6	Saw-tooth1	6 mm chains ($\Delta x = 25\ cm$)	Setup 2
7	-	6 mm chains ($\Delta x = 25\ cm$)	Setup 2
8	Barrier1	6 mm chains ($\Delta x = 25\ cm$)	Setup 2
9	Barrier1	4 mm chains ($\Delta x = 50\ cm$)	Setup 2
10	None used	4 mm chains ($\Delta x = 50\ cm$)	Setup 2
11	Saw-tooth1	4 mm chains ($\Delta x = 50\ cm$)	Setup 2
12	Isosceles spires 1	4 mm chains ($\Delta x = 50\ cm$)	Setup 2
13	Isosceles spires 2	4 mm chains ($\Delta x = 50\ cm$)	Setup 2
14	Isosceles spires 3	4 mm chains ($\Delta x = 50\ cm$)	Setup 2
15	Isosceles spires 4	4 mm chains ($\Delta x = 50\ cm$)	Setup 2
16	Isosceles spires 5	4 mm chains ($\Delta x = 50\ cm$)	Setup 2
17	Isosceles spires 6	4 mm chains ($\Delta x = 50\ cm$)	Setup 2
18	Isosceles spires 7	4 mm chains ($\Delta x = 50\ cm$)	Setup 2
19	Isosceles spires 8	4 mm chains ($\Delta x = 50\ cm$)	Setup 2
20	Isosceles spires 8	4 & 6 mm chains ($\Delta x = 25\ cm$)	Setup 2
21	Isosceles spires 7	4 & 6 mm chains ($\Delta x = 25\ cm$)	Setup 2
22	Isosceles spires 7	4 & 6 mm chains ($\Delta x = 20\ cm$)	Setup 2
23	Isosceles spires 9	4 & 6 mm chains ($\Delta x = 25\ cm$)	Setup 2
24	Isosceles spires 9 & Barrier1	4 & 6 mm chains ($\Delta x = 25\ cm$)	Setup 2
25	Isosceles spires 10	4 & 6 mm chains ($\Delta x = 25\ cm$)	Setup 2
26	Isosceles spires 10	4 & 6 mm chains ($\Delta x = 25\ cm$)	Setup 3

Table C2. Spire setups as function of height and quantities used (dimensions in model-scale).

Isosceles spires 1	8 x 75 cm + 10 x 50 cm
Isosceles spires 2	10 x 50 cm + 8 x 28 cm
Isosceles spires 3	5 x 55 cm + 10 x 50 cm + 8 x 28 cm
Isosceles spires 4	10 x 50 cm + 12 x 28 cm
Isosceles spires 5	19 x 28 cm
Isosceles spires 6	10 x 50 cm + 19 x 28 cm
Isosceles spires 7	29 x 28 cm
Isosceles spires 8	25 x 28 cm
Isosceles spires 9	33 x 28 cm
Isosceles spires 10	31 x 28 cm

Table C3. Three-dimensional coordinates of the flat terrain measurement positions at full-scale.

X_{fs} $[m]$	Y_{fs} $[m]$	Z_{fs} $[m]$
-560		10
-500		15
0 (transition to flat terrain)		20
500		30
1000		50
1500		75
2000	0	100
2500		125
3000		150
3100		200
3500		250
4000		300
4500		375
		450

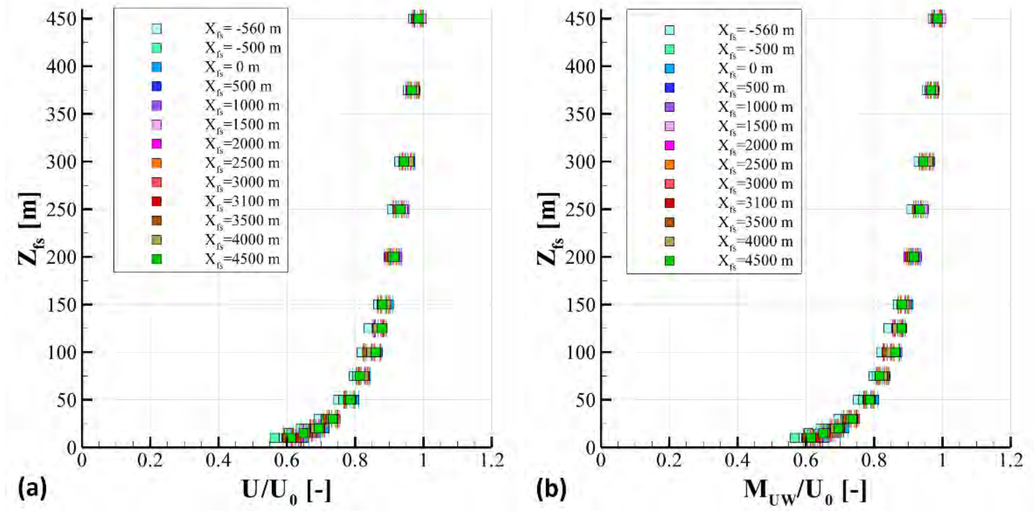

Figure C1. Vertical profiles of the mean dimensionless longitudinal velocity (a) and UW velocity magnitude (b) of the modelled ABL flow above the full range of streamwise measurement positions.

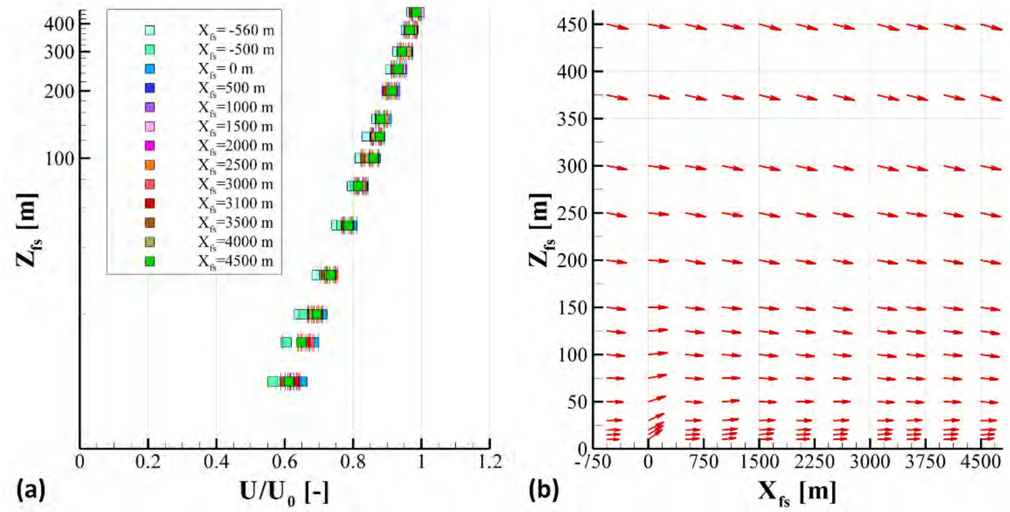

Figure C2. Semi-logarithmic vertical profiles of the mean dimensionless longitudinal velocity (a), and vertical UW velocity vector field (b) of the modelled ABL flow above the full range of streamwise measurement positions.

Table C4. Roughness lengths and profile exponents of the vertical profiles of the mean longitudinal velocity of the lowest $Z = 75$ m at all streamwise measurement positions above flat terrain.

X_{fs} [m]	z_0 [m]	α
-560	0.07	0.17
-500	0.02	0.13
0	0.01	0.12
500	0.02	0.14
1000	0.01	0.13
1500	0.02	0.14
2000	0.02	0.15
2500	0.04	0.14
3000	0.02	0.14
3100	0.02	0.14
3500	0.04	0.15
4000	0.03	0.15
4500	0.02	0.14
Mean	0.02	0.14
Uncertainty	0.015	0.013

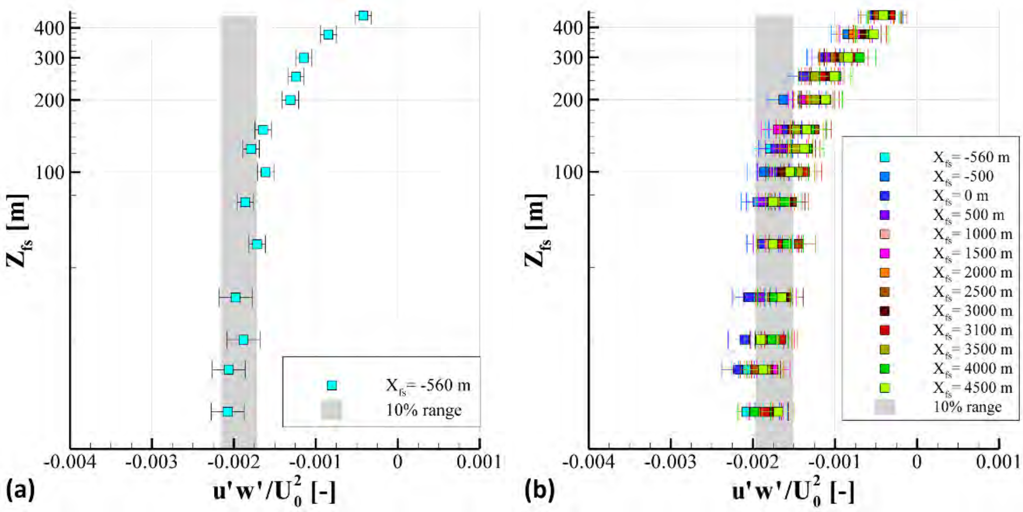

Figure C3. Semi-logarithmic vertical profiles of the mean dimensionless turbulent velocity fluxes above the inflow section position (a) and the full range of streamwise measurement positions above flat terrain. Shaded regions delimits a $\pm 10\%$ range around the mean fluxes from the lowest $Z = 50$ m above $X = -560$ m (a) and $X = 3000$ m (b).

Table C5. Local friction velocities, calculated via Equation (19) and shear stresses (τ) and averaged for the lowest $Z = 100\ m$ as function of longitudinal measurement position.

X_{fs} [m]	-560	0	500	1000	1500	2000	2500	3100	3500	4000	4500	Mean
$u_*[m/s]$	0.24	0.19	0.21	0.19	0.21	0.20	0.23	0.21	0.22	0.22	0.20	0.21
$\tau\ [N/m^2]$	0.07	0.04	0.05	0.04	0.05	0.05	0.06	0.05	0.06	0.06	0.05	0.05

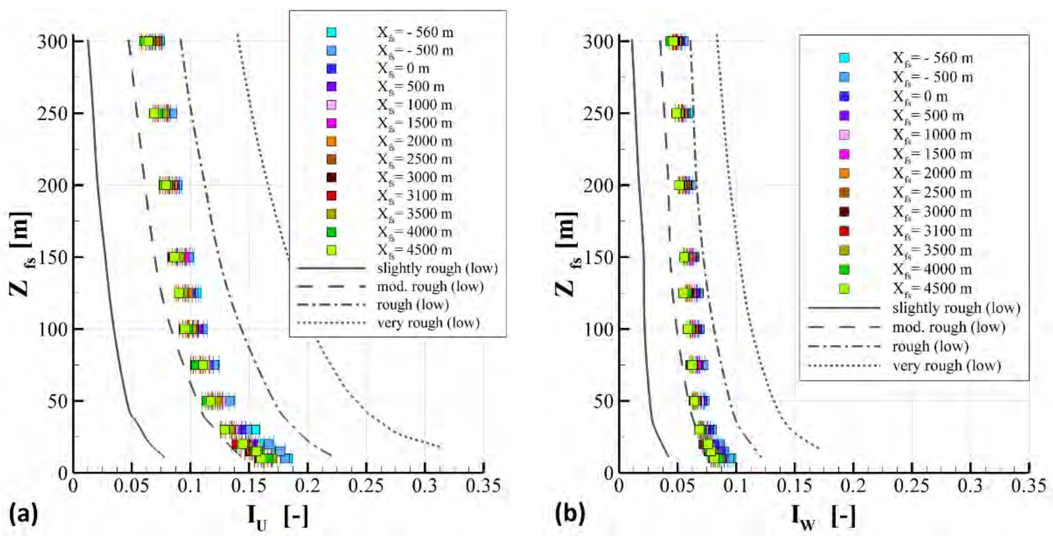

Figure C4. Vertical profiles of the longitudinal (a) and vertical (b) turbulence intensities of the ABL flow above the full range of streamwise positions. Reference curves represent the lower bounds of roughness classes (VDI, 2000).

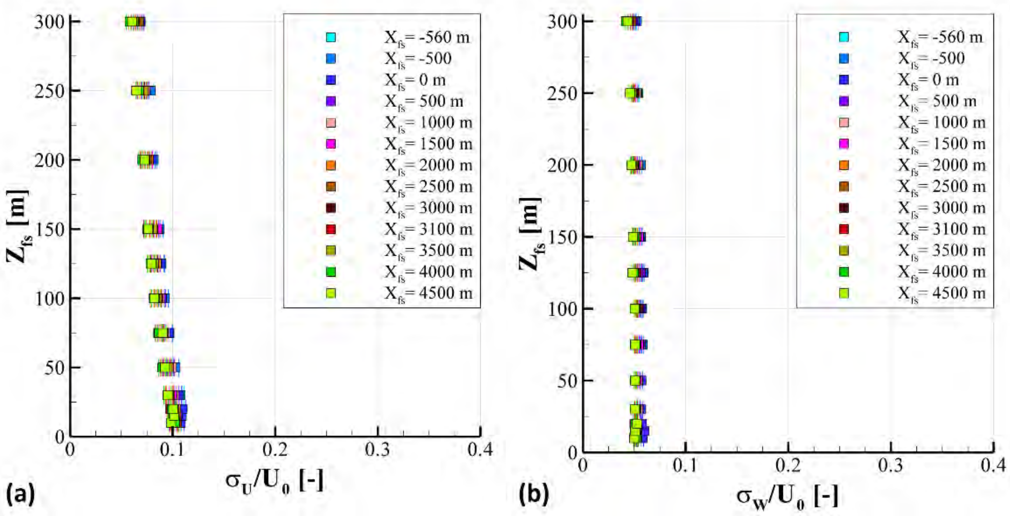

Figure C5. Vertical profiles of the longitudinal (a) and vertical (b) mean velocity fluctuations of the modelled ABL flow above the full range of streamwise positions.

Table C6. Average ratios of longitudinal to vertical velocity fluctuations for the measurement heights contained within the lowest $Z = 100$ m above the full range of longitudinal positions.

	X_{fs} [m]	-560	0	1000	1500	2000	2500	3100	3500	4000	4500	Mean
Z_{fs} [m]	10	0.53	0.54	0.50	0.49	0.53	0.50	0.51	0.51	0.51	0.51	0.51
	15	0.51	0.55	0.50	0.50	0.51	0.50	0.52	0.51	0.50	0.50	0.51
	20	0.52	0.52	0.49	0.50	0.51	0.51	0.52	0.52	0.52	0.53	0.51
	30	0.51	0.54	0.53	0.51	0.52	0.54	0.54	0.53	0.54	0.53	0.53
	50	0.56	0.58	0.54	0.56	0.53	0.56	0.55	0.54	0.56	0.55	0.55
	75	0.58	0.58	0.59	0.61	0.57	0.58	0.60	0.56	0.59	0.56	0.58
	100	0.63	0.64	0.62	0.63	0.62	0.63	0.62	0.60	0.61	0.62	0.62
$Z \leq 100\ m$		0.55	0.56	0.54	0.54	0.54	0.55	0.55	0.54	0.55	0.54	0.55
all heights		0.64	0.64	0.63	0.63	0.62	0.63	0.63	0.62	0.62	0.62	0.63

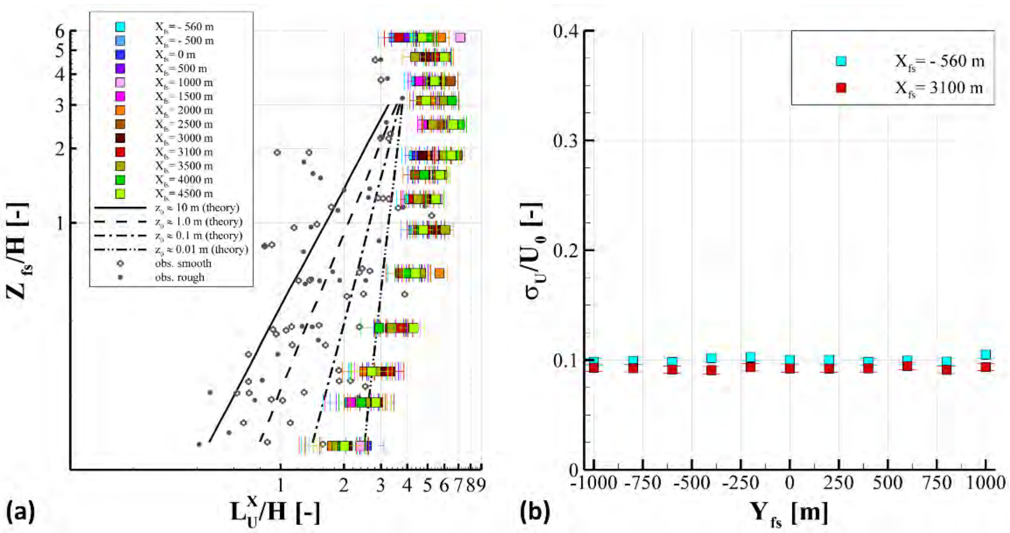

Figure C6. Logarithmic vertical profiles of the mean dimensionless longitudinal integral length scales of the modelled ABL flow above the full range of streamwise positions (a), and lateral profiles of the mean dimensionless longitudinal velocity fluctuations of the modelled ABL flow at $Z = 50$ m above the two streamwise analyses positions and at every $\Delta Y = 200$ m until $Y = \pm 1000$ m (b).

APPENDIX D – FLOWS OVER RIDGES

Table D1. Longitudinal measurement positions of the downwind subdomain (DW) in relative and absolute coordinates. Relative coordinates are non-dimensionalised with ridge height.

Position	*B2*	*DW1*	*DW2*	*DW3*	*DW4*	*DW5*	*DW6*	*DW7*
x/H $[-]$	0	0.78	1.56	2.34	3.12	3.90	5.46	8.08
x $[m]$	0	62.5	125	187.5	250	312.5	437	647

Table D2. Longitudinal measurement positions of the leeside slope subdomain (LW) in relative and absolute coordinates. Absolute coordinates are dependent on ridge type and relative coordinates are non-dimensionalised with ridge half-length.

Position		*LW1*	*LW2*	*LW3*	*LW4*	*LW5*	*LW6*	*LW7*	*LW8*	*LW9*
x/L_R $[-]$		0.10	0.21	0.31	0.42	0.52	0.62	0.74	0.85	0.90
x $[m]$	*Type I-75*	2.50	5.25	7.75	10.5	13.0	15.5	18.5	21.3	22.5
	Type I-10	45.0	94.5	139.5	189.0	234.0	279.0	333.0	382.5	405.0
	Type II	14.0	29.4	43.4	58.8	72.8	86.8	103.6	119.0	126.0

Table D3. Data uncertainties of mean dimensionless flow parameters above the crests of each of the ridges as function of height ranges. Uncertainties shaded in grey originate from the corresponding flat terrain repetitive measurements.

height ranges (Δz_i)	Δz_1			Δz_2			Δz_3		
	TI-75	TI-10	TII	TI-75	TI-10	TII	TI-75	TI-10	TII
U/U_0	± 0.0279	± 0.0035	± 0.0098	± 0.0209	± 0.0067	± 0.0067	± 0.0162	± 0.0076	± 0.0081
V/U_0	± 0.0040	± 0.0040	± 0.0040	± 0.0005	± 0.0018	± 0.0018	± 0.0011	± 0.0025	± 0.0009
W/U_0	± 0.0055	± 0.0062	± 0.0005	± 0.0036	± 0.0082	± 0.0011	± 0.0204	± 0.0009	± 0.0001
σ_U/U_0	± 0.0038	± 0.0007	± 0.0017	± 0.0036	± 0.0030	± 0.0024	± 0.0043	± 0.0014	± 0.0017
σ_V/U_0	± 0.0010	± 0.0010	± 0.0010	± 0.0012	± 0.0001	± 0.0008	± 0.0002	± 0.0006	± 0.0011
σ_W/U_0	± 0.0071	± 0.0007	± 0.0009	± 0.0326	± 0.0006	± 0.0010	± 0.0042	± 0.0016	± 0.0001
$u'v'/U_0^2$	± 0.0001	± 0.0001	± 0.0001	± 0.0001	± 0.0001	± 0.0001	± 0.0001	± 0.0001	± 0.0001
$u'w'/U_0^2$	± 0.0007	± 0.0001	± 0.0001	± 0.0002	± 0.0001	± 0.0001	± 0.0004	± 0.0001	± 0.0001
L_U^X/H	± 0.5470	± 0.2746	± 0.2022	± 0.2802	± 0.7261	± 0.3034	± 0.8582	± 0.1186	± 0.8688

Table D4. Data uncertainties of mean dimensionless flow parameters above the near-crest leeside slope position (LW4) of each of the ridges as function of height ranges. Uncertainties shaded in grey originate from the corresponding flat terrain repetitive measurements.

height ranges (Δz_i)	Δz_1			Δz_2			Δz_3		
	TI-75	TI-10	TII	TI-75	TI-10	TII	TI-75	TI-10	TII
U/U_0	± 0.0190	± 0.0042	± 0.0048	± 0.0249	± 0.0164	± 0.0327	± 0.0134	± 0.0061	± 0.0076
V/U_0	± 0.0030	± 0.0042	± 0.0051	± 0.0046	± 0.0012	± 0.0001	± 0.0038	± 0.0030	± 0.0011
W/U_0	± 0.0048	± 0.0023	± 0.0010	± 0.0036	± 0.0585	± 0.0052	± 0.0010	± 0.0013	± 0.0002
σ_U/U_0	± 0.0103	± 0.0128	± 0.0034	± 0.0075	± 0.0014	± 0.0062	± 0.0018	± 0.0015	± 0.0034
σ_V/U_0	± 0.0072	± 0.0008	± 0.0037	± 0.0058	± 0.0002	± 0.0039	± 0.0006	± 0.0013	± 0.0031
σ_W/U_0	± 0.0059	± 0.0134	± 0.0037	± 0.001	± 0.0168	± 0.0022	± 0.0008	± 0.0007	± 0.0002
$u'v'/U_0^2$	± 0.0001	± 0.0001	± 0.0001	± 0.0002	± 0.0001	± 0.0001	± 0.0003	± 0.0001	± 0.0001
$u'w'/U_0^2$	± 0.0011	± 0.0002	± 0.0004	± 0.0011	± 0.0003	± 0.0006	± 0.0002	± 0.0001	± 0.0001
L_U^X/H	± 0.1270	± 0.0062	± 0.0260	± 0.1160	± 0.3935	± 0.0133	± 0.0001	± 0.5053	± 1.106

Table D5. Data uncertainties of mean dimensionless flow parameters above the downstream leeside slope position (LW8) of each of the ridges as function of height ranges. Uncertainties shaded in grey originate from the corresponding flat terrain repetition measurements.

height ranges (Δz_i)	Δz_1			Δz_2			Δz_3		
	TI-75	TI-10	TII	TI-75	TI-10	TII	TI-75	TI-10	TII
U/U_0	±0.0089	±0.0015	±0.0232	±0.0173	±0.0012	±0.0121	±0.0083	±0.0066	±0.0120
V/U_0	±0.0041	±0.0023	±0.0031	±0.0010	±0.0046	±0.0034	±0.0042	±0.0017	±0.0039
W/U_0	±0.0083	±0.0018	±0.0028	±0.0055	±0.0015	±0.0026	±0.0008	±0.0013	±0.0060
σ_U/U_0	±0.0075	±0.0013	±0.0036	±0.0104	±0.0009	±0.0036	±0.0048	±0.0012	±0.0035
σ_V/U_0	±0.0017	±0.0010	±0.0010	±0.0014	±0.0017	±0.0021	±0.0016	±0.0006	±0.0039
σ_W/U_0	±0.0069	±0.0008	±0.0005	±0.0050	±0.0011	±0.0018	±0.0014	±0.0007	±0.0017
$u'v'/U_0^2$	±0.0001	±0.0001	±0.0001	±0.0005	±0.0002	±0.0003	±0.0001	±0.0001	±0.0001
$u'w'/U_0^2$	±0.0007	±0.0002	±0.0001	±0.0011	±0.0001	±0.0001	±0.0001	±0.0001	±0.0001
L_U^X/H	±0.0916	±0.0082	±0.1230	±0.1005	±0.0076	±0.1719	±0.5061	±0.0183	±0.3562

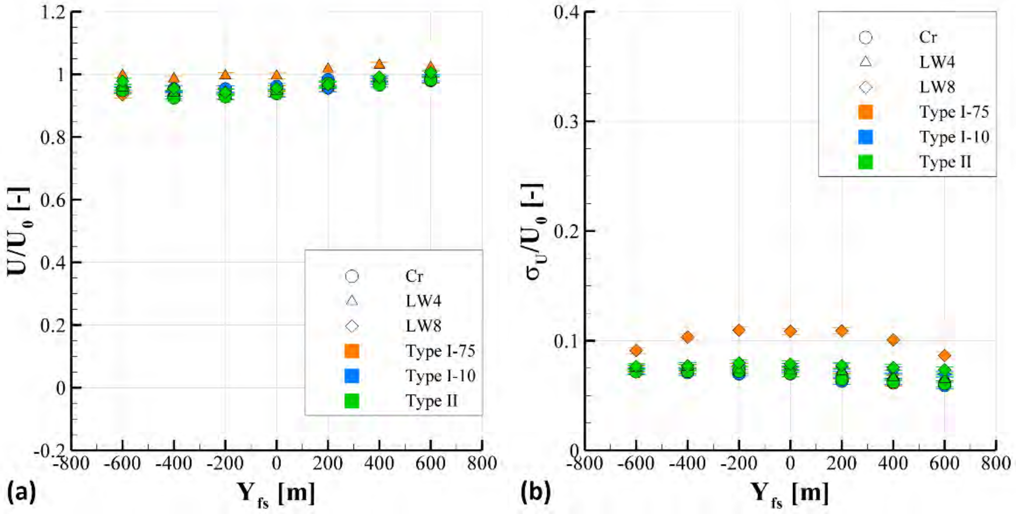

Figure D1. Lateral profiles of the mean dimensionless longitudinal velocities (a) and velocity fluctuations (b) at $z/H = 2.5$ above the crests (Cr) and leeside slope positions (LW4 and LW8) of the ridges. Ridge data uses the colour scheme defined in Table 5.1 and flat terrain data is represented in grey.

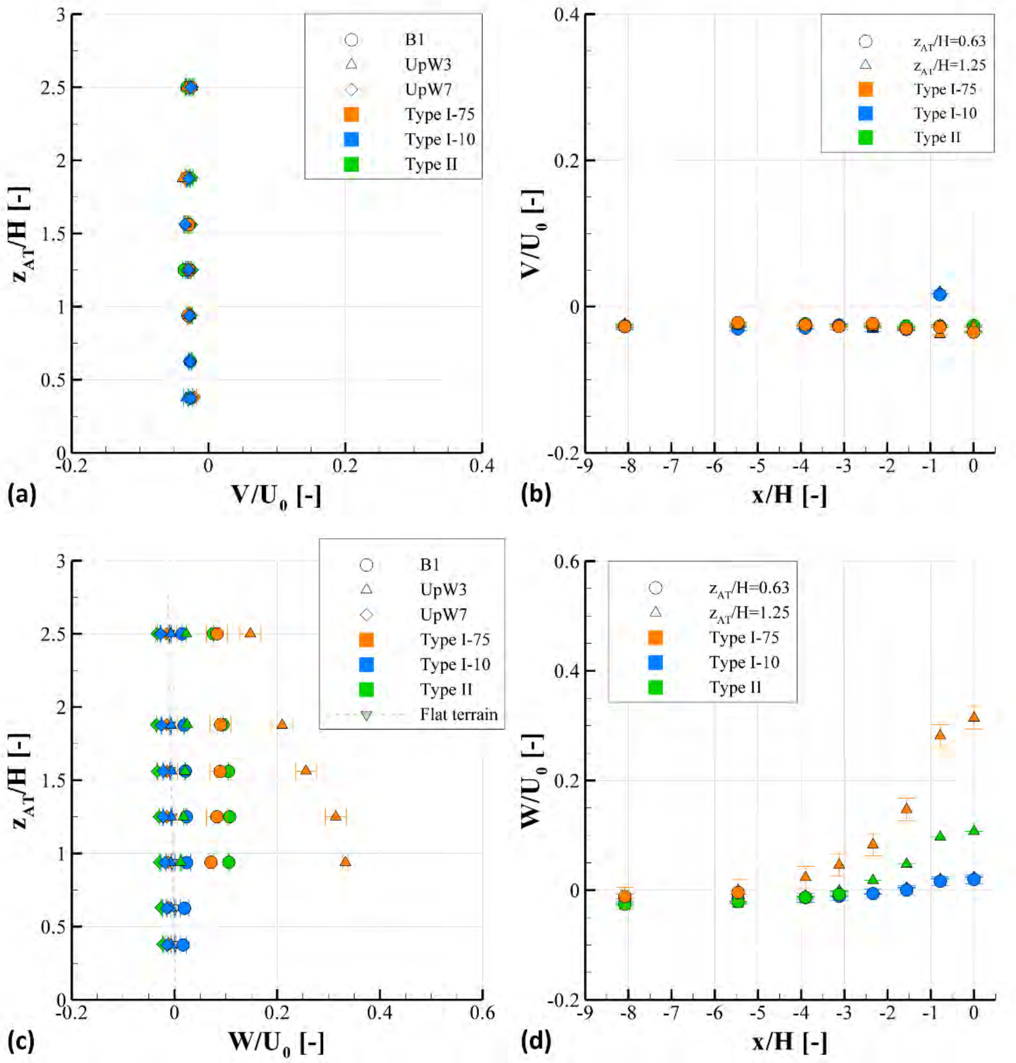

Figure D2. Vertical (a, c) and longitudinal (b, d) profiles of the mean dimensionless lateral (a, b) and vertical (c, d) components of the velocity above the Upwind subdomain (UpW) of the ridges.

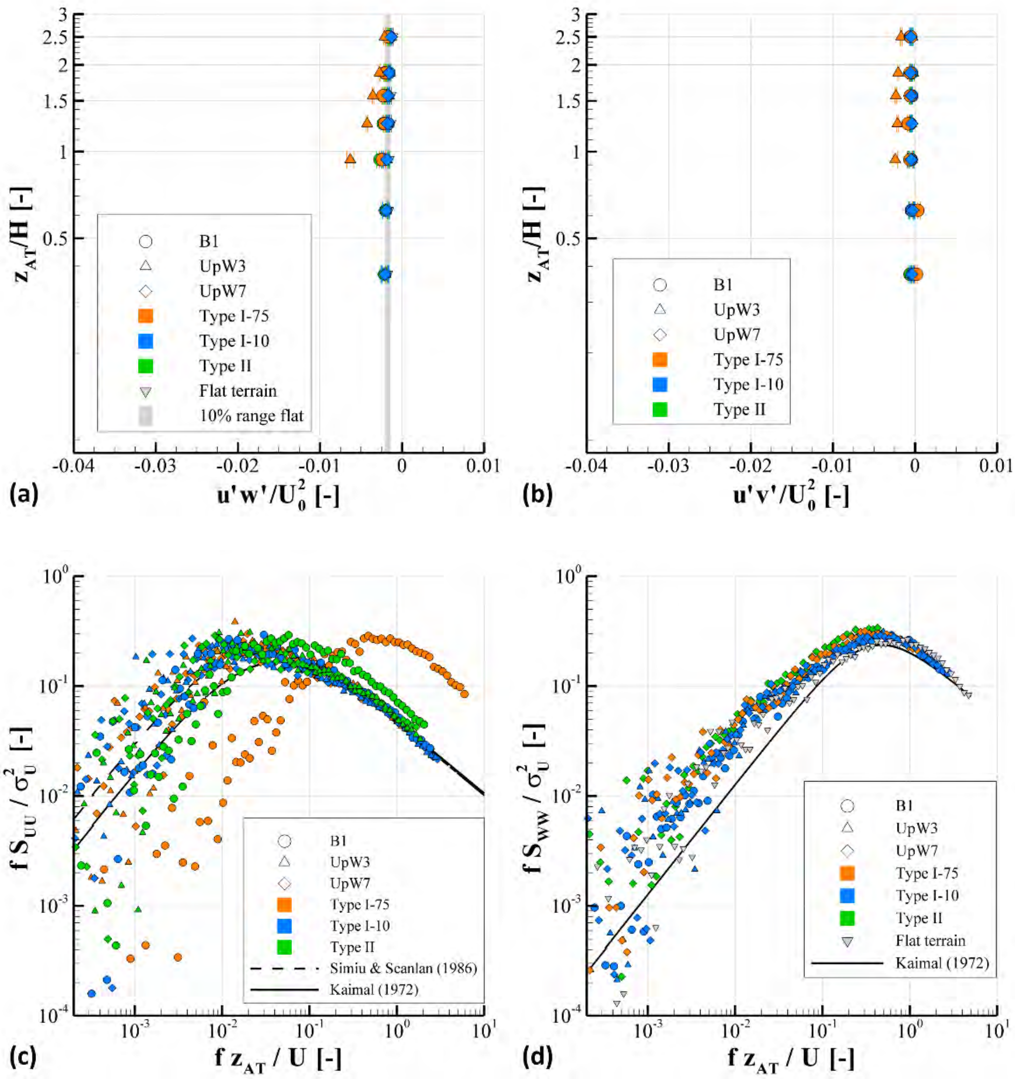

Figure D3. Semi-logarithmic vertical profiles of the mean dimensionless vertical (a) and horizontal (b) turbulent velocity fluxes, and spectral distributions of longitudinal (c) and vertical (d) turbulent energy at $z/H = 0.38$ above the Upwind subdomain.

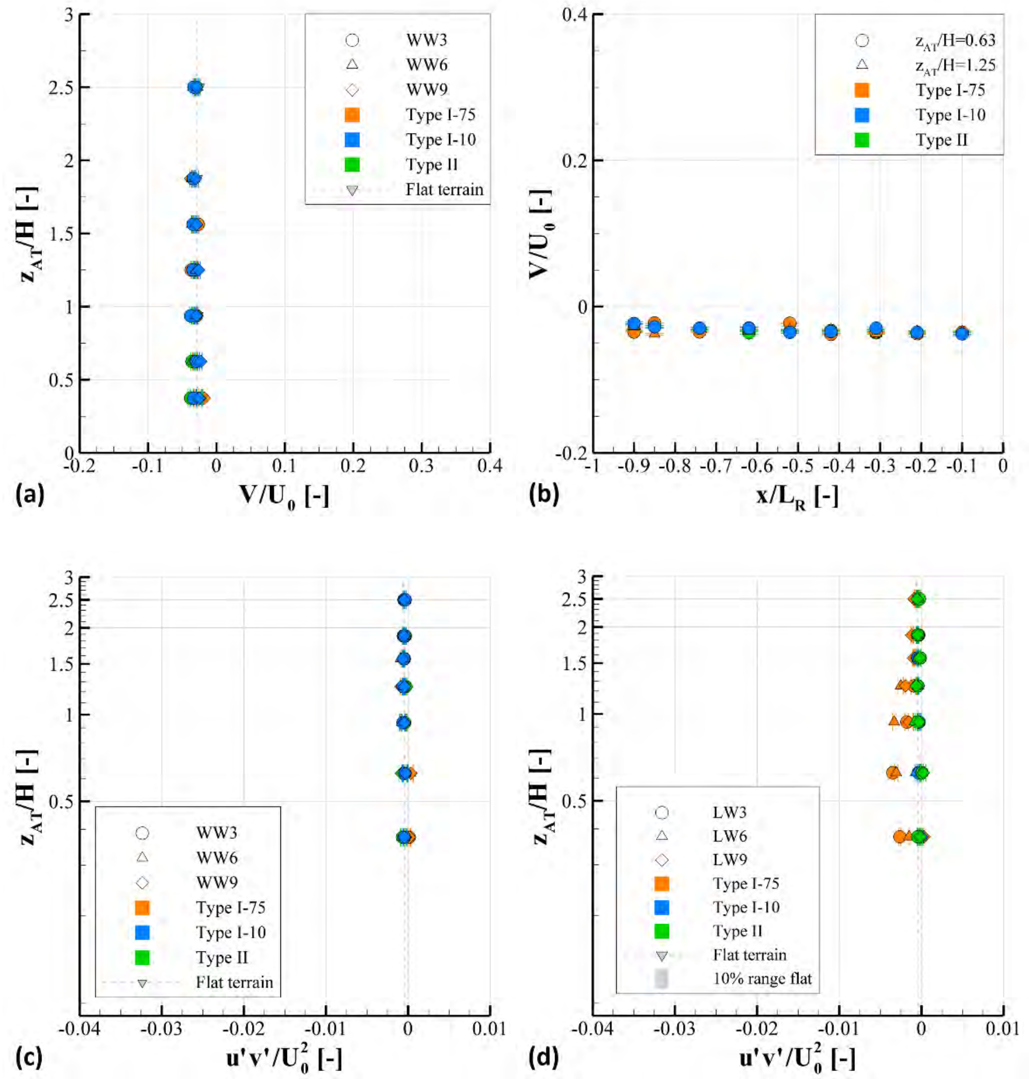

Figure D4. Vertical (a, c) and longitudinal (b) profiles of the mean dimensionless lateral velocity (a, b) and horizontal turbulent fluxes above the Windward slope subdomain (c) and above the Leeside slope subdomain (d) of the ridges.

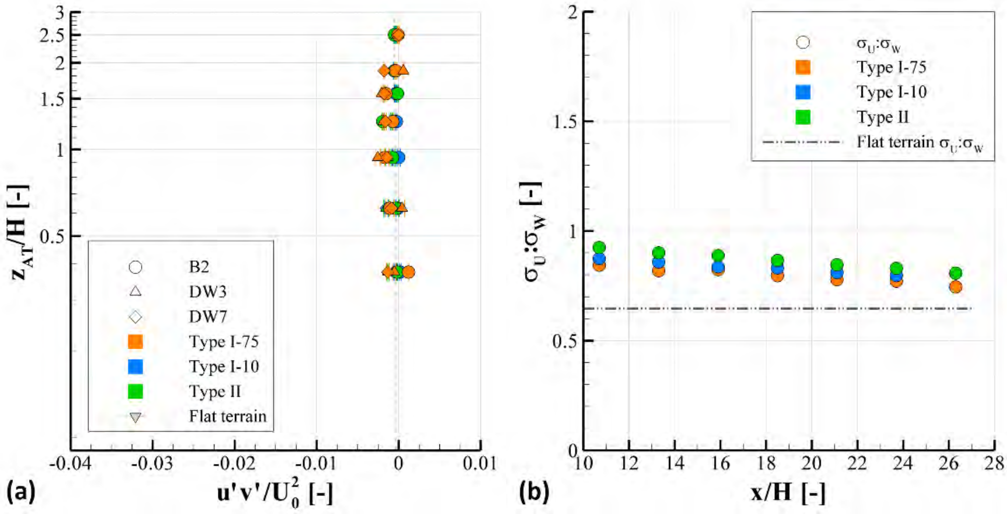

Figure D5. Vertical profiles of the mean dimensionless horizontal turbulent fluxes above the Downwind subdomain (DW) of the ridges (a) and longitudinal profiles of the average ratio of longitudinal to vertical velocity fluctuations from the lowest $Z = 100\,m$ above the Extended downwind subdomain (DDW) with reference values represented by dark grey lines (b).

APPENDIX E – FLOWS OVER VALLEYS

Table E1. Data uncertainties of mean dimensionless flow parameters of the modelled ABL flow above flat terrain of the valley campaign as function of height ranges.

height ranges (Δz_i)	Δz_1	Δz_2	Δz_3
U/U_0	± 0.0440	± 0.0432	± 0.0404
V/U_0	± 0.0033	± 0.0028	± 0.0028
W/U_0	± 0.0029	± 0.0032	± 0.0043
σ_U/U_0	± 0.0045	± 0.0055	± 0.0051
σ_V/U_0	± 0.0022	± 0.0016	± 0.0014
σ_W/U_0	± 0.0029	± 0.0016	± 0.0021
I_U	± 0.0082	± 0.0078	± 0.0051
I_V	± 0.0041	± 0.0030	± 0.0028
I_W	± 0.0090	± 0.0046	± 0.0046
$u'v'/U_0^2$	± 0.0001	± 0.0002	± 0.0002
$u'w'/U_0^2$	± 0.0001	± 0.0001	± 0.0002
L_U^X/H	± 0.7638	± 0.7422	± 0.9029

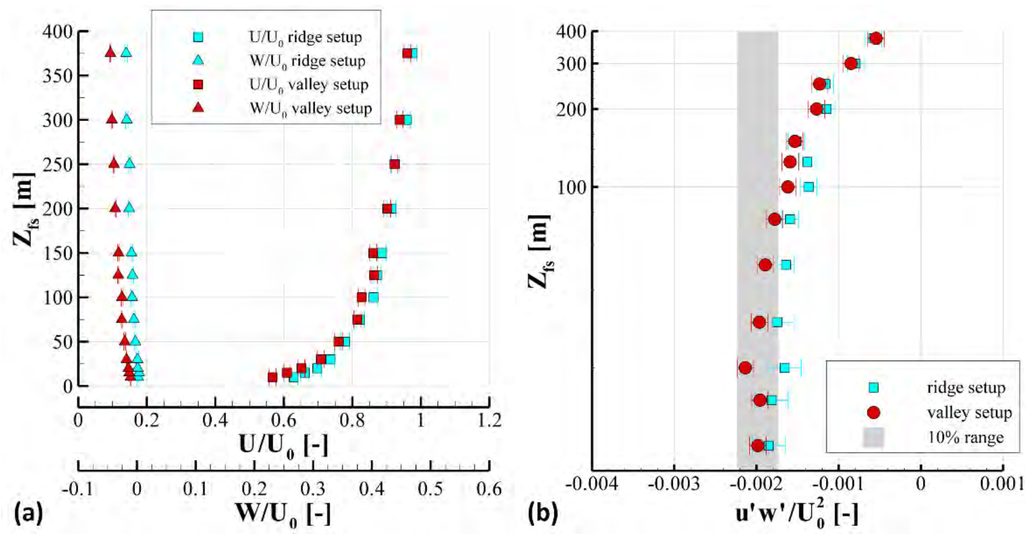

Figure E1. Vertical profiles of the mean dimensionless longitudinal (U/U_0) and vertical (W/U_0) velocities of the modelled ABL flow between valley (at $X = 2\ m$) and ridge ($X = 3\ m$) setups, where separate abscissa axes correspond to each velocity component (a), and semi-logarithmic vertical profiles of the mean dimensionless vertical fluxes of the modelled ABL flow above the same positions (b). The shaded region delimits a $\pm 10\%$ range around the mean of the lowest $Z = 50\ m$ above the surface of the valley setup.

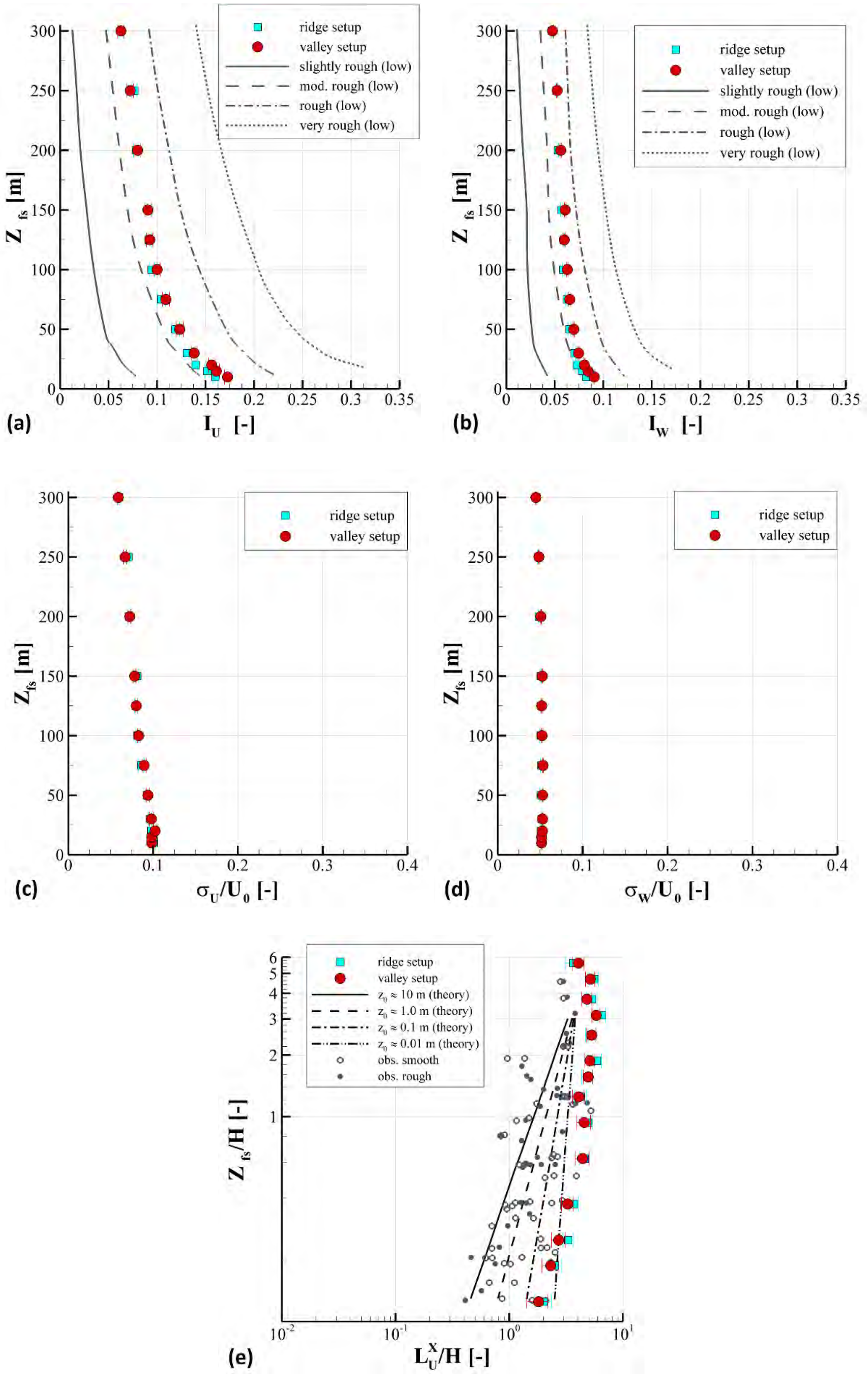

Figure E2. Vertical profiles of the mean dimensionless longitudinal (a, c) and vertical (b, d) turbulence intensities (a, b) velocity fluctuations (c, d), and logarithmic vertical profiles of the mean dimensionless longitudinal integral length scales (e) of the modelled ABL flow above $X = 2\ m$ for the valley setup and at $X = 3\ m$ from the ridge setup. Reference curves of in (a) and (b) represent the lower bounds of roughness classes (VDI, 2000). Reference data in (e) from the investigation of Counihan (1975) is represented in black.

Characteristics of flows over valleys

Table E2. Data uncertainties of mean dimensionless flow parameters of the flow above the crest of the first ridge (Cr1) of each valley geometry as function of height ranges. Uncertainties shaded in orange originate from the flat terrain repetition measurements and those in blue from the ridge repetitions of the previous setup.

height ranges (Δz_i)	Δz_1			Δz_2			Δz_3		
	Type I	Type II	Type III	Type I	Type II	Type III	Type I	Type II	Type III
U/U_0	± 0.0440	± 0.0440	± 0.0440	± 0.0432	± 0.0432	± 0.0432	± 0.0404	± 0.0404	± 0.0404
V/U_0	± 0.0040	± 0.0040	± 0.0040	± 0.0028	± 0.0028	± 0.0028	± 0.0028	± 0.0028	± 0.0028
W/U_0	± 0.0062	± 0.0055	± 0.0029	± 0.0082	± 0.0036	± 0.0032	± 0.0043	± 0.0204	± 0.0043
σ_U/U_0	± 0.0045	± 0.0045	± 0.0045	± 0.0055	± 0.0055	± 0.0055	± 0.0051	± 0.0051	± 0.0051
σ_V/U_0	± 0.0022	± 0.0022	± 0.0022	± 0.0016	± 0.0016	± 0.0016	± 0.0014	± 0.0014	± 0.0014
σ_W/U_0	± 0.0029	± 0.0071	± 0.0029	± 0.0016	± 0.0326	± 0.0016	± 0.0021	± 0.0042	± 0.0021
$u'v'/U_0^2$	± 0.0001	± 0.0001	± 0.0001	± 0.0002	± 0.0002	± 0.0002	± 0.0002	± 0.0002	± 0.0002
$u'w'/U_0^2$	± 0.0001	± 0.0007	± 0.0001	± 0.0001	± 0.0002	± 0.0001	± 0.0002	± 0.0004	± 0.0002
L_U^X/H	± 0.7638	± 0.7638	± 0.7638	± 0.7422	± 0.7422	± 0.7422	± 0.9029	± 0.9029	± 0.9029

Table E3. Data uncertainties of mean dimensionless flow parameters of the flow at all longitudinal analyses positions downwind from the first ridge (MV, Cr2, and DW7) of each valley geometry as function of height ranges. Uncertainties shaded in orange originate from the flat terrain repetition measurements and those in blue from the ridge repetitions of the previous setup.

height ranges (Δz_i)	Δz_1			Δz_2			Δz_3		
	Type I	Type II	Type III	Type I	Type II	Type III	Type I	Type II	Type III
U/U_0	± 0.0440	± 0.0440	± 0.0440	± 0.0432	± 0.0432	± 0.0432	± 0.0404	± 0.0404	± 0.0404
V/U_0	± 0.0033	± 0.0041	± 0.0033	± 0.0046	± 0.0028	± 0.0034	± 0.0028	± 0.0042	± 0.0039
W/U_0	± 0.0029	± 0.0083	± 0.0029	± 0.0032	± 0.0055	± 0.0032	± 0.0043	± 0.0043	± 0.0060
σ_U/U_0	± 0.0045	± 0.0075	± 0.0045	± 0.0055	± 0.0104	± 0.0055	± 0.0051	± 0.0051	± 0.0051
σ_V/U_0	± 0.0022	± 0.0022	± 0.0022	± 0.0017	± 0.0016	± 0.0021	± 0.0014	± 0.0016	± 0.0039
σ_W/U_0	± 0.0029	± 0.0069	± 0.0029	± 0.0016	± 0.0050	± 0.0018	± 0.0021	± 0.0021	± 0.0021
$u'v'/U_0^2$	± 0.0001	± 0.0001	± 0.0001	± 0.0002	± 0.0005	± 0.0003	± 0.0002	± 0.0002	± 0.0002
$u'w'/U_0^2$	± 0.0002	± 0.0007	± 0.0001	± 0.0001	± 0.0011	± 0.0001	± 0.0002	± 0.0002	± 0.0002
L_U^X/H	± 0.7638	± 0.7638	± 0.7638	± 0.7422	± 0.7422	± 0.7422	± 0.9029	± 0.9029	± 0.9029

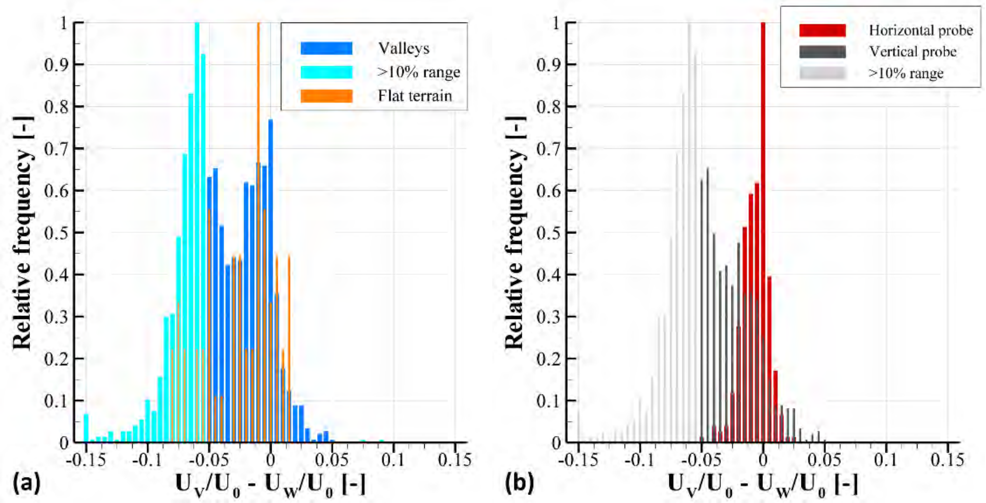

Figure E3. Relative frequency distribution of the differences between longitudinal velocities measured with UV and UW settings (a), and horizontal and vertical alignments for UW measurements (b) above the valley positions

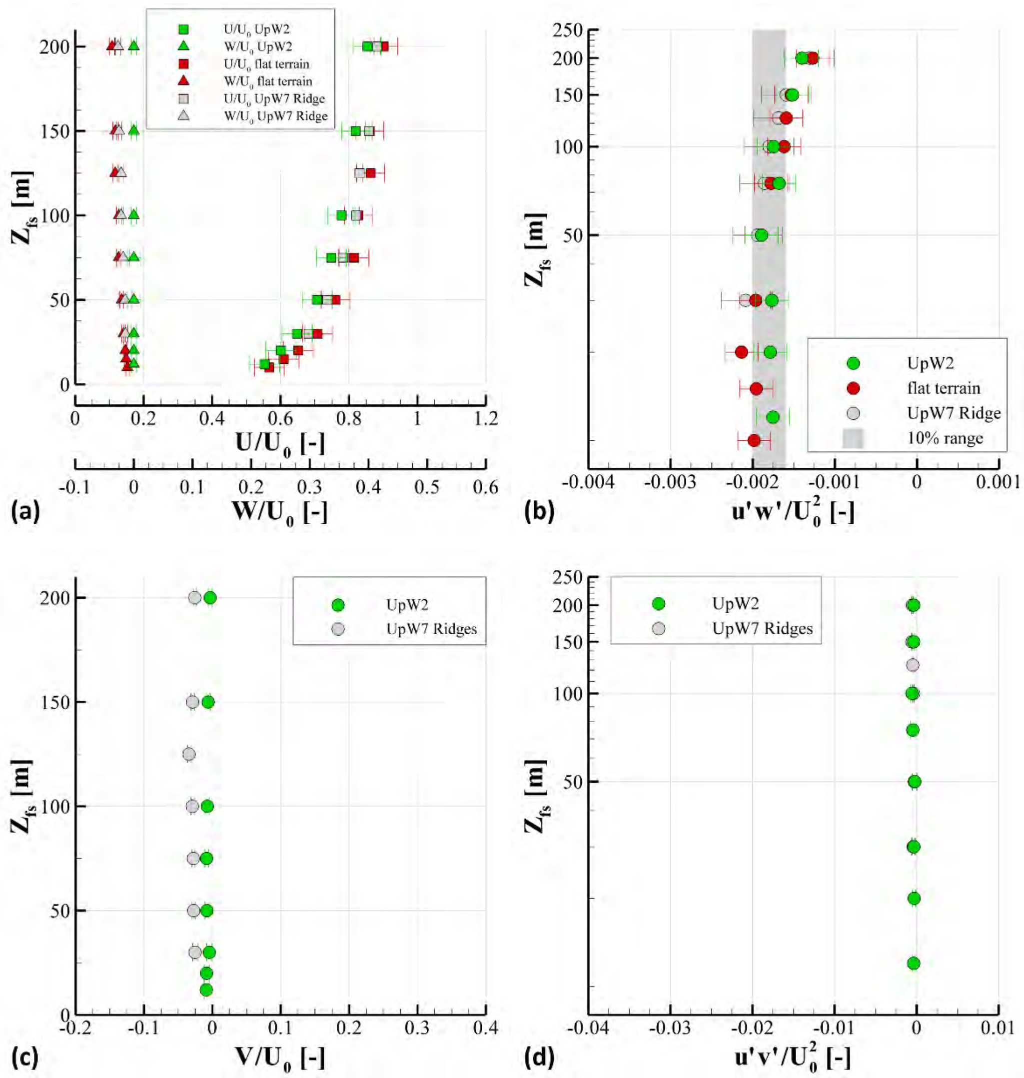

Figure E4. Vertical profiles of the mean dimensionless longitudinal and vertical velocities (a), lateral velocities (c) and semi-logarithmic vertical profiles of the mean dimensionless vertical (b) and horizontal (d) fluxes of the flow above UpW2 of the Type I valley, the flat terrain data, UpW7 of the Type I-10 single ridge. The shaded region in (b) delimits a $\pm 10\%$ range around the mean fluxes from the lowest $Z = 50\ m$ above UpW2.

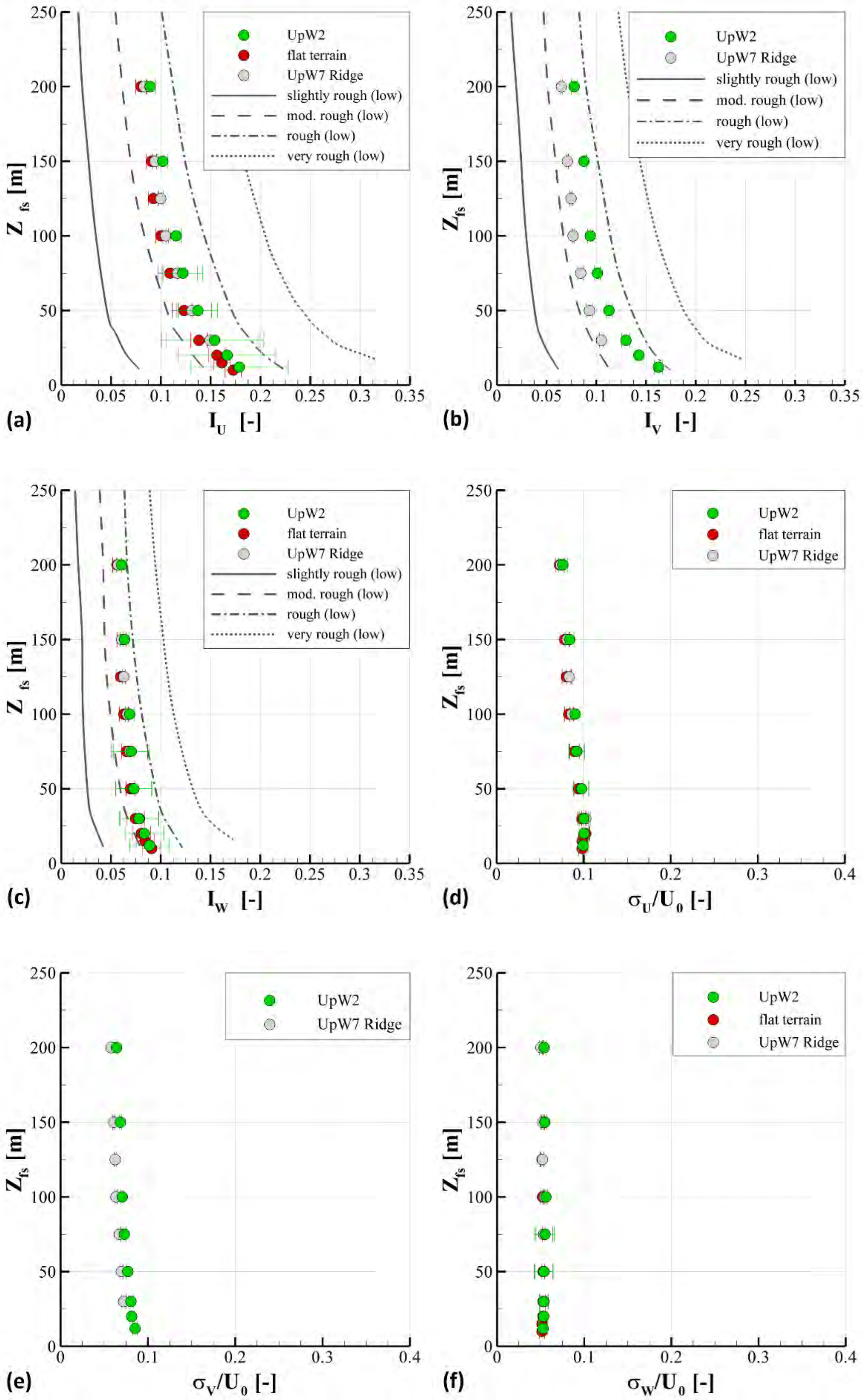

Figure E5. Vertical profiles of the mean longitudinal (a, d), lateral (b, e), and vertical (b, f) turbulence intensities (a, b, c) and velocity fluctuations (d, e, f) of the flow above UpW2 of the Type I valley, the flat terrain data, UpW7 of the Type I-10 single ridge. Reference curves in (a), (b), and (c) represent the lower bounds of roughness classes (VDI, 2000).

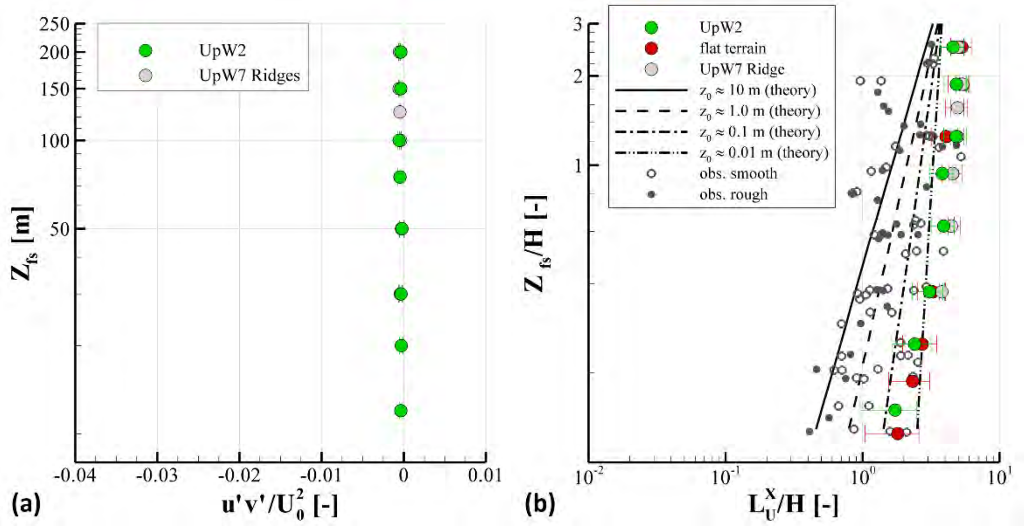

Figure E6. Semi-logarithmic and logarithmic vertical profiles of the mean dimensionless horizontal fluxes (a) and longitudinal integral length scales (b) of the flow above UpW2 of the Type I valley, the flat terrain data, UpW7 of the Type I-10 single ridge. Reference data in (b) from the investigation of Counihan (1975) is represented in black.

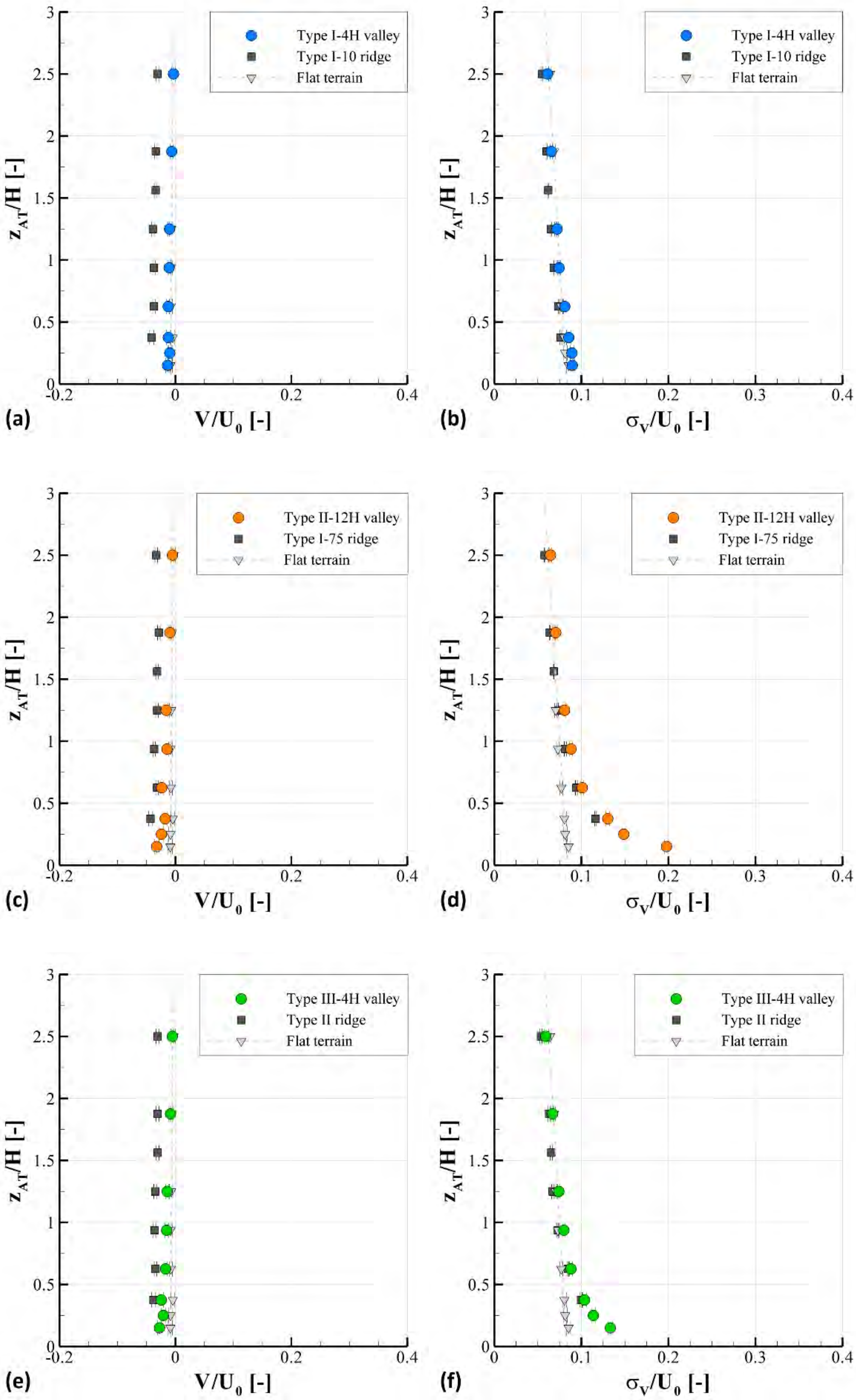

Figure E7. Vertical profiles of the mean dimensionless lateral velocities (a, c, e) and velocity fluctuations (b, d, f) above the crest of the first ridge of Type I (a, b), Type II (c, d), and Type III (e, f) valleys.

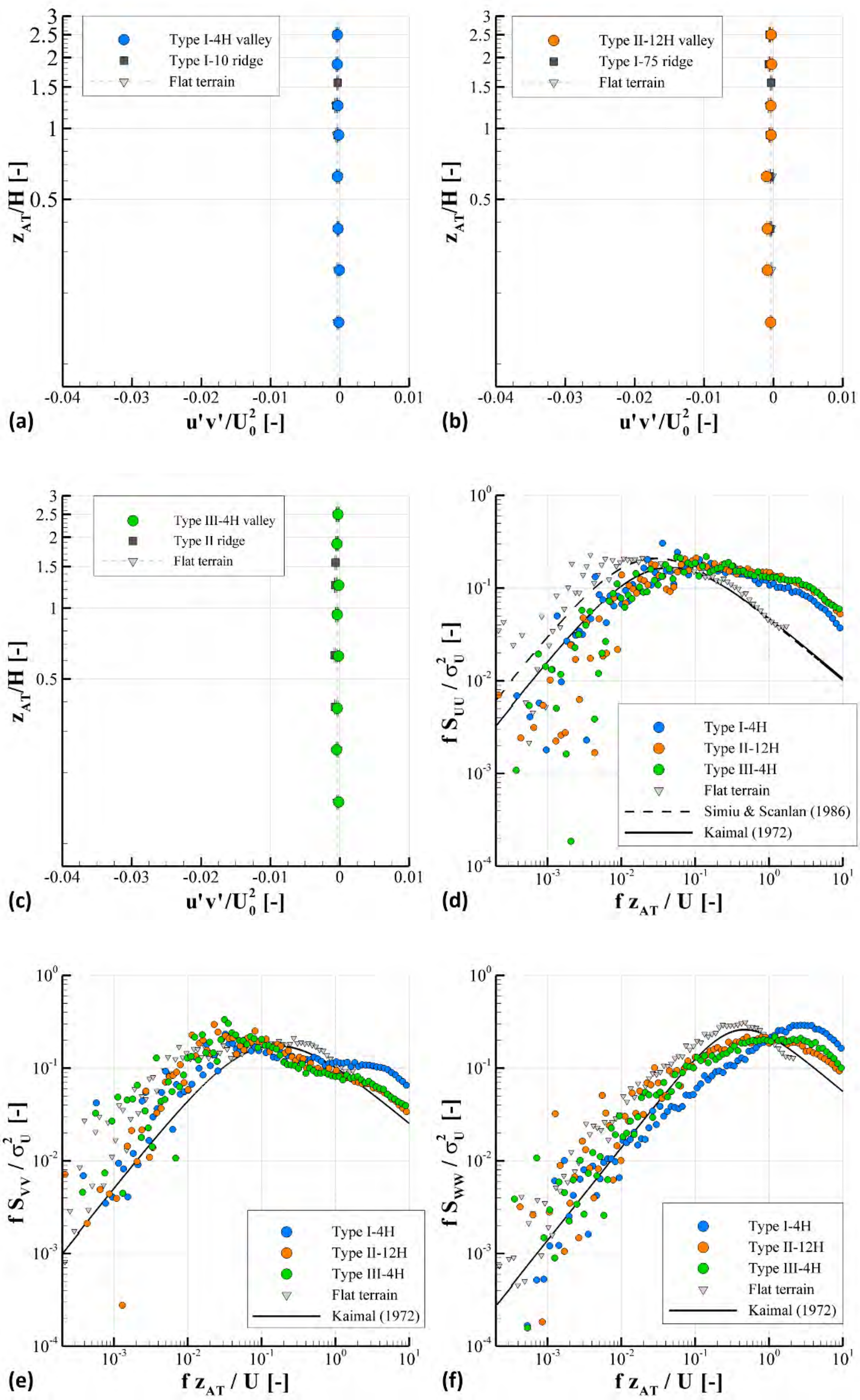

Figure E8. Vertical profiles of the mean dimensionless horizontal turbulent velocity fluxes (a, b, c), and spectral distributions of longitudinal (d), lateral (e), and vertical (f) turbulent energy at $z/H = 0.15$ above the crest of the first ridge of all valley geometries.

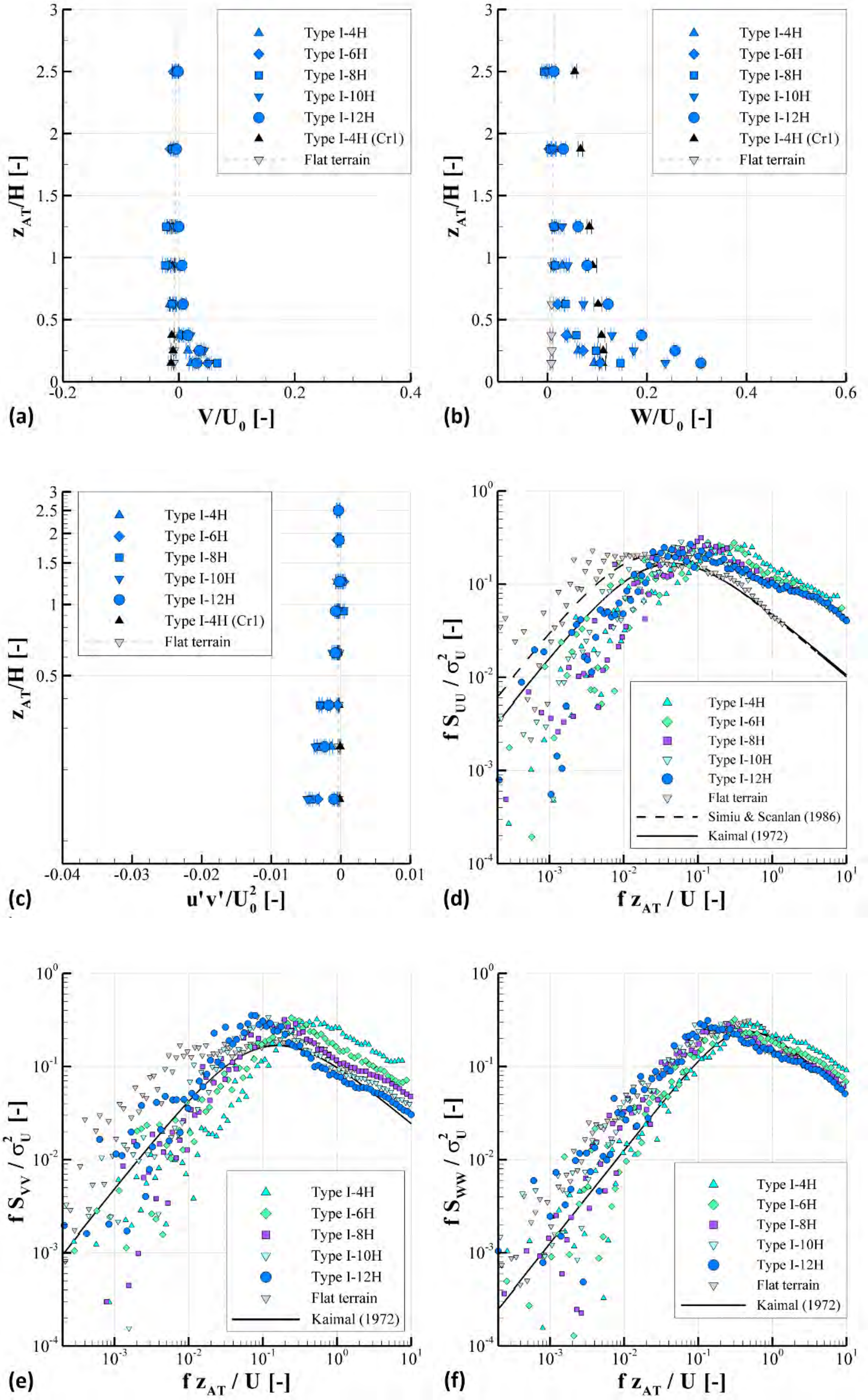

Figure E9. Vertical profiles of the mean dimensionless lateral (a) and vertical (b) velocities, horizontal turbulent velocity fluxes (c), and spectral distributions of longitudinal (d), lateral (e), and vertical (f) turbulent energy at $z/H = 0.15$ above the crest of the second ridge of all widths of Type I valleys. Vertical profiles of the flow above the crest of the first ridge is represented in black.

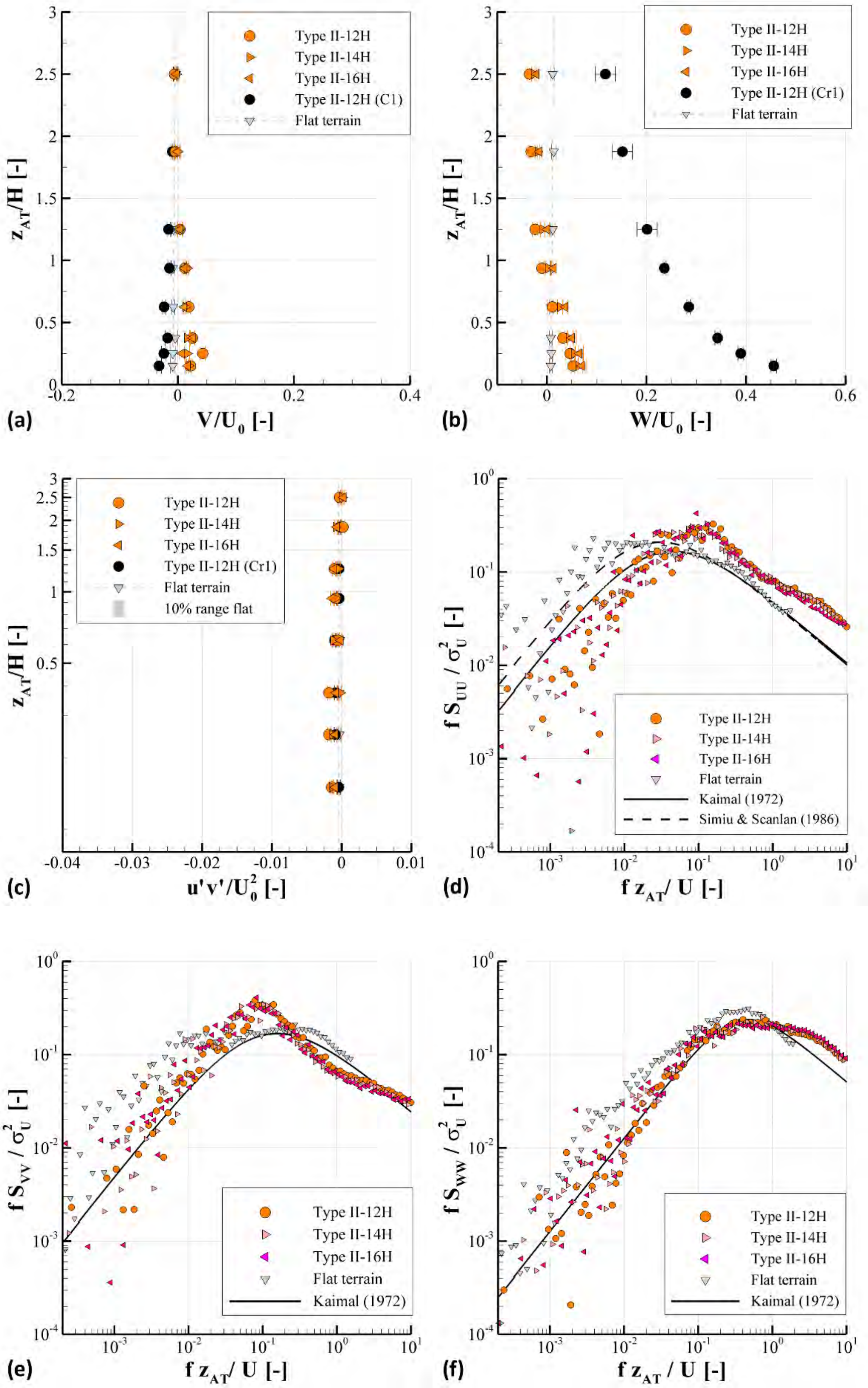

Figure E10. Vertical profiles of the mean dimensionless lateral (a) and vertical (b) velocities, horizontal turbulent velocity fluxes (c), and spectral distributions of longitudinal (d), lateral (e), and vertical (f) turbulent energy at $z/H = 0.15$ above the crest of the second ridge of all widths of Type II valleys. Vertical profiles of the flow above the crest of the first ridge is represented in black.

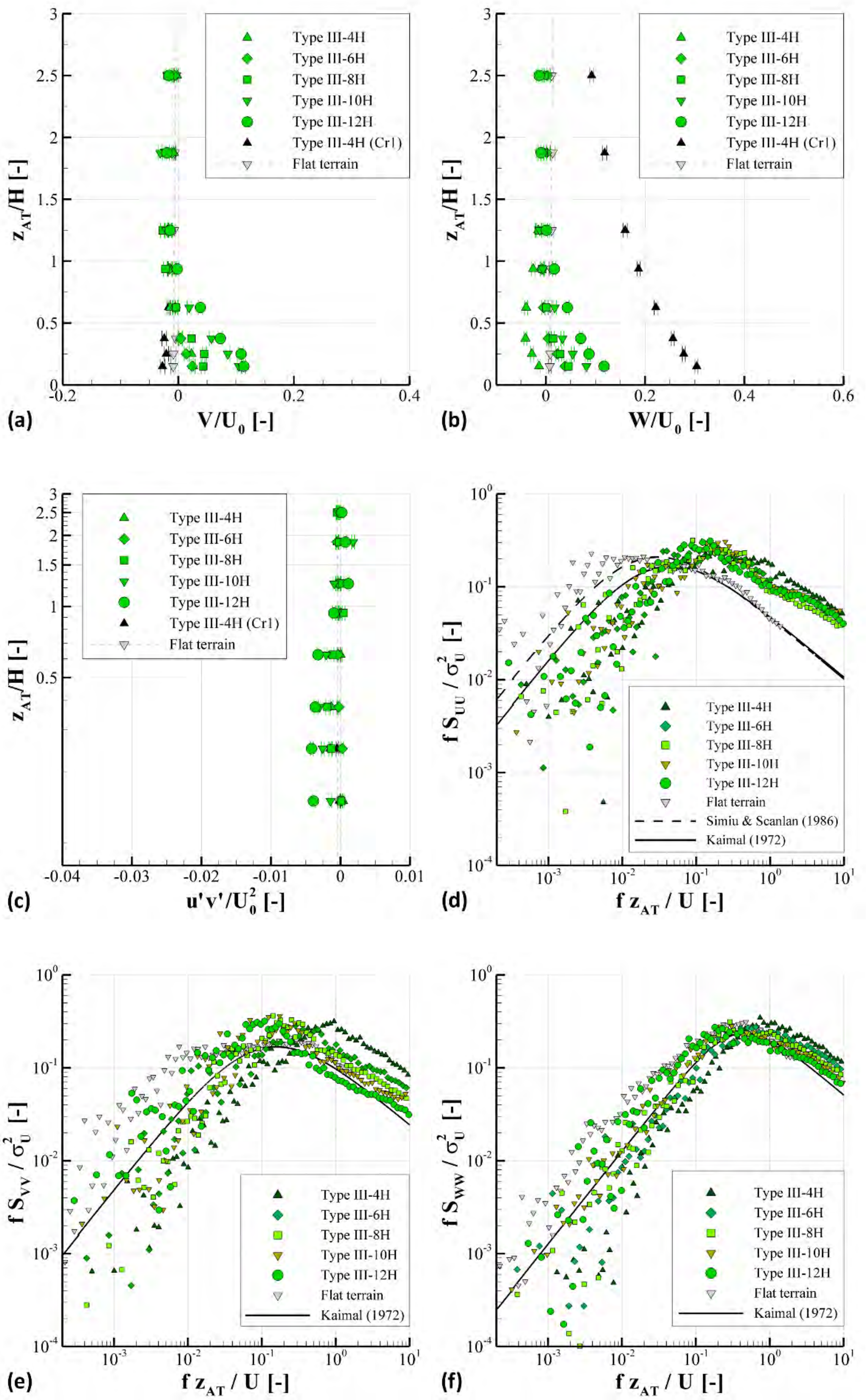

Figure E11. Vertical profiles of the mean dimensionless lateral (a) and vertical (b) velocities, horizontal turbulent velocity fluxes (c), and spectral distributions of longitudinal (d), lateral (e), and vertical (f) turbulent energy at $z/H = 0.15$ above the crest of the second ridge of all widths of Type III valleys. Vertical profiles of the flow above the crest of the first ridge is represented in black.

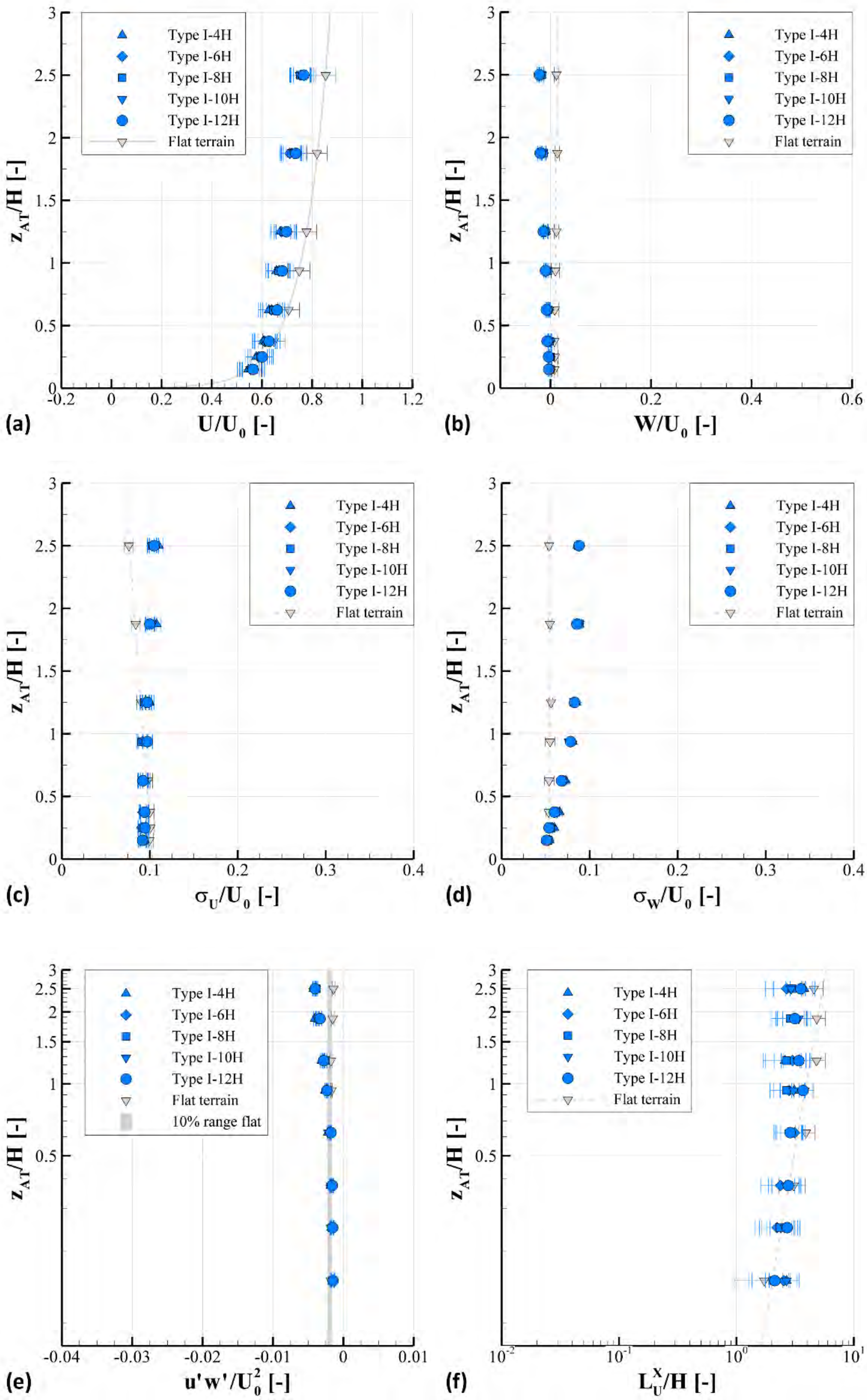

Figure E12. Vertical profiles of the mean dimensionless longitudinal (a, c) and vertical (b, d) velocities (a, b) and velocity fluctuations (c, d), vertical turbulent velocity fluxes (e), and integral length scales (f) above the furthermost downwind location from all of the Type I valleys.

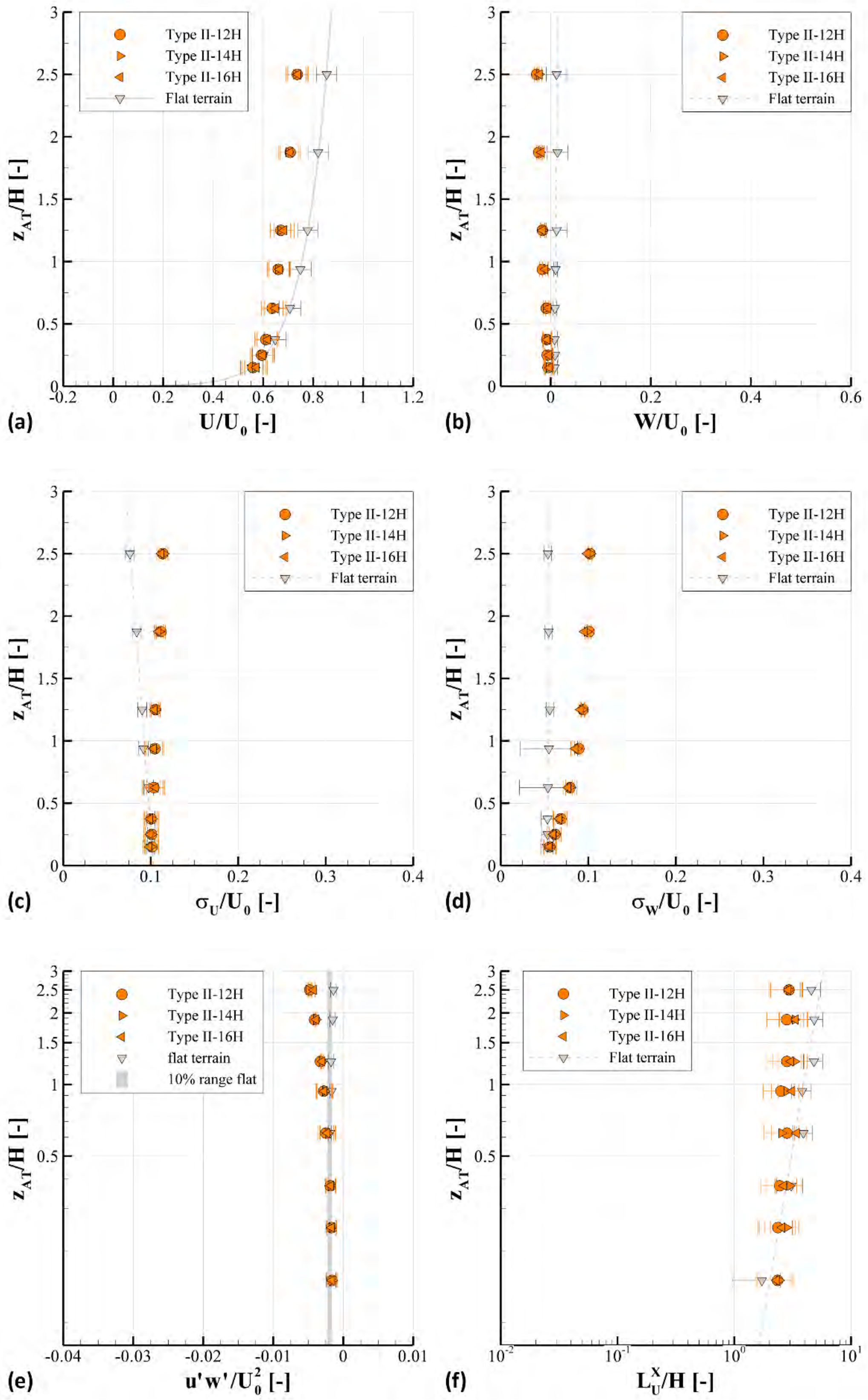

Figure E13. Vertical profiles of the mean dimensionless longitudinal (a, c) and vertical (b, d) velocities (a, b) and velocity fluctuations (c, d), vertical turbulent velocity fluxes (e), and integral length scales (f) above the furthermost downwind location from all of the Type II valleys.

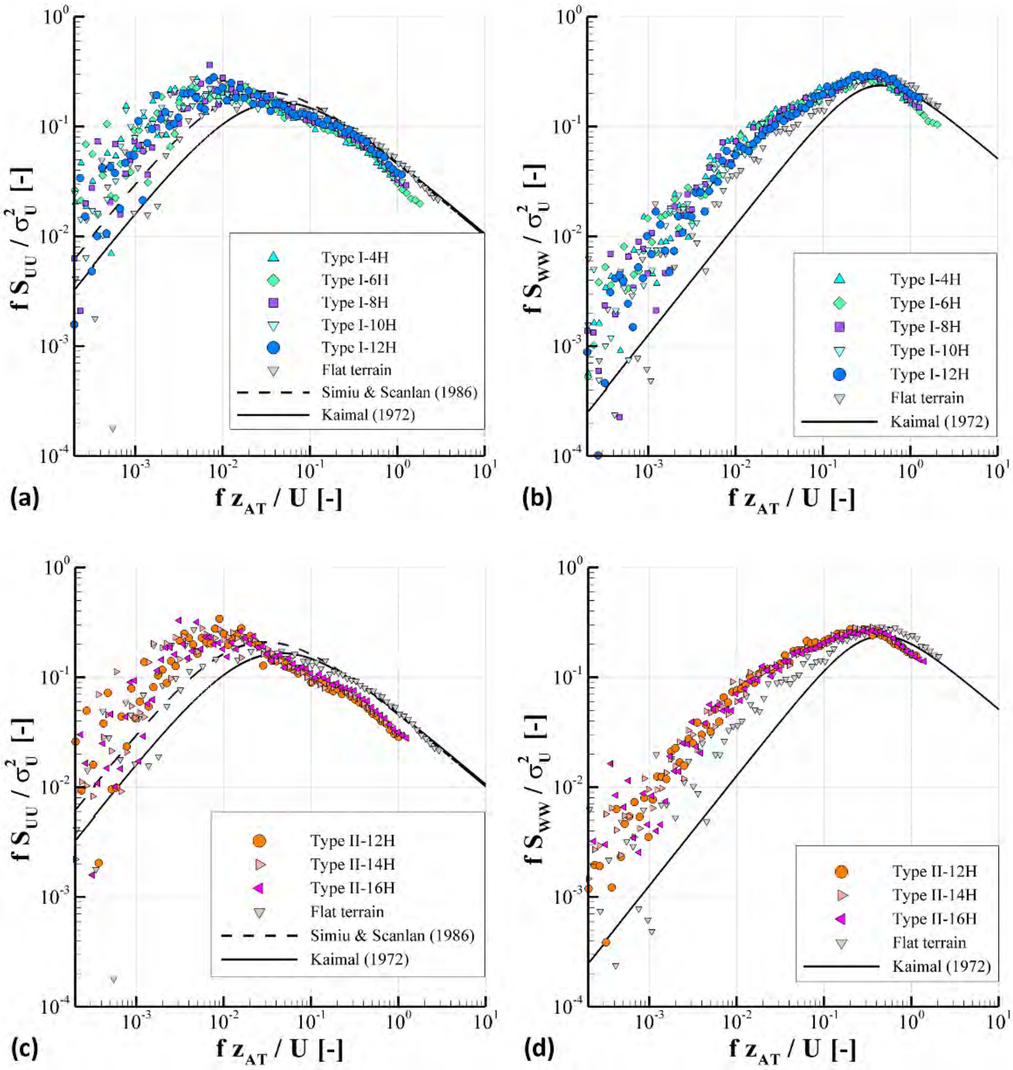

Figure E14. Spectral distributions of longitudinal (a, c) and vertical (b, d) turbulent energy at $z/H = 0.15$ above the furthermost downwind location from Type I (a, b) and Type II (c, d) valleys.

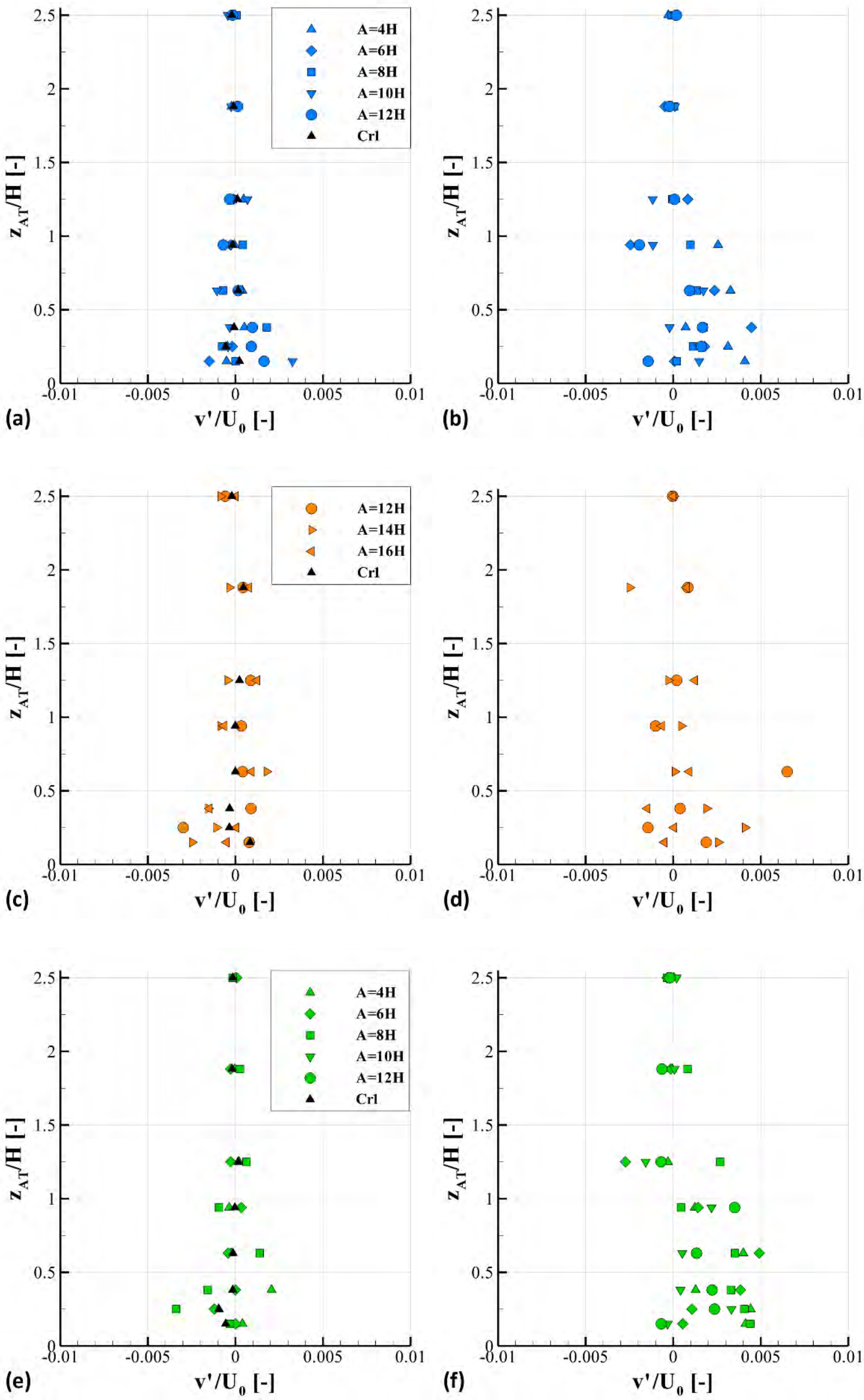

Figure E15. Vertical profiles of the dimensionless transient lateral fluctuations above the crests (a, c, e) and mid-valley (b, d, f) of Type I (a, b), Type II (c, d), and Type III (e, f) valleys. For all valley types, data from the crest of the first ridge is presented in black colour.

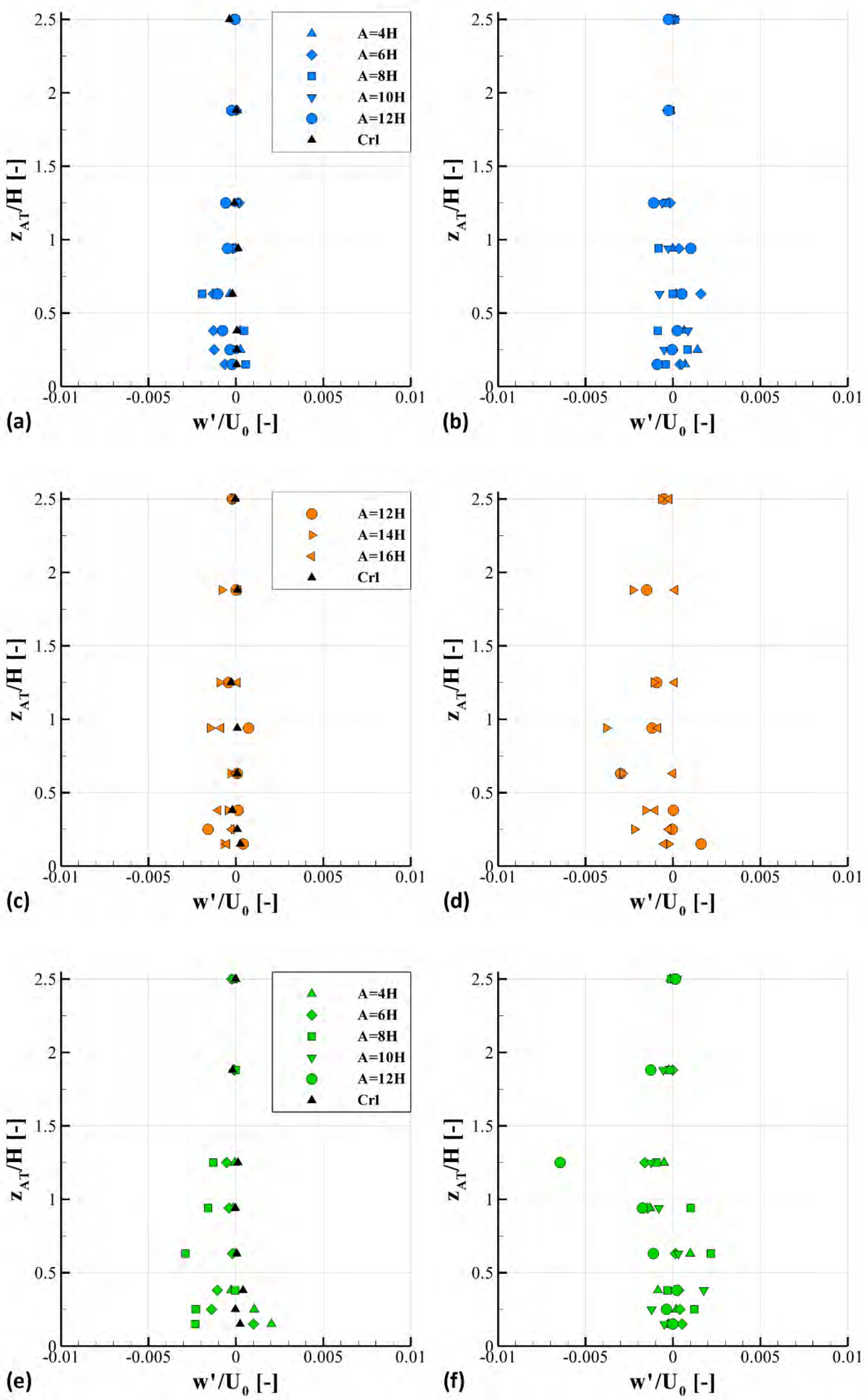

Figure E16. Vertical profiles of the dimensionless transient lateral fluctuations above the crests (a, c, e) and mid-valley (b, d, f) of Type I (a, b), Type II (c, d), and Type III (e, f) valleys. For all valley types, data from the crest of the first ridge is presented in black colour.

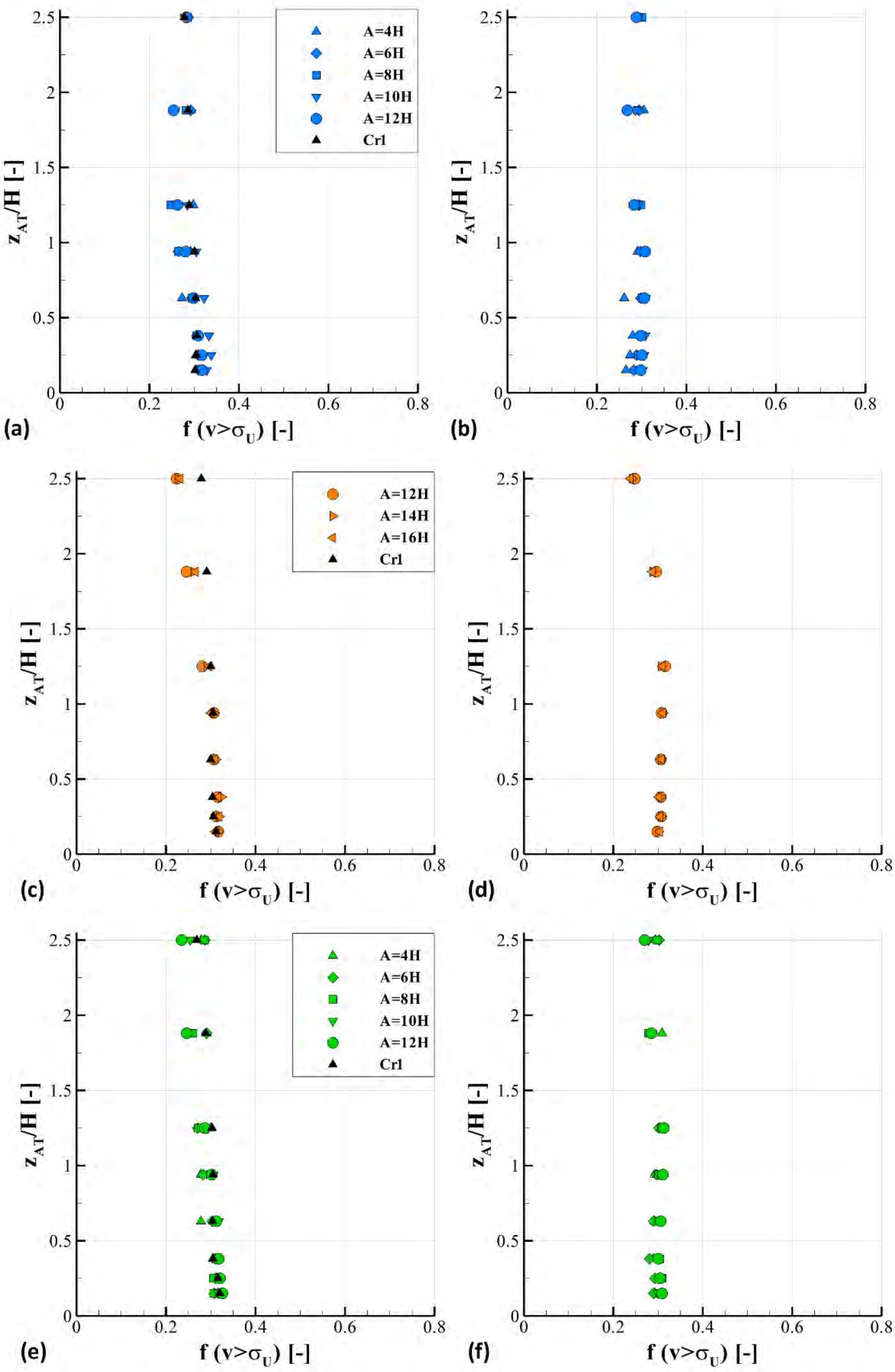

Figure E17. Vertical profiles of the frequencies at which the lateral velocities are larger than the averaged transient longitudinal velocity fluctuations above the crests (a, c, e) and mid-valley (b, d, f) of Type I (a, b), Type II (c, d), and Type III (e, f) valleys. For all valley types, data from the crest of the first ridge is presented in black colour.

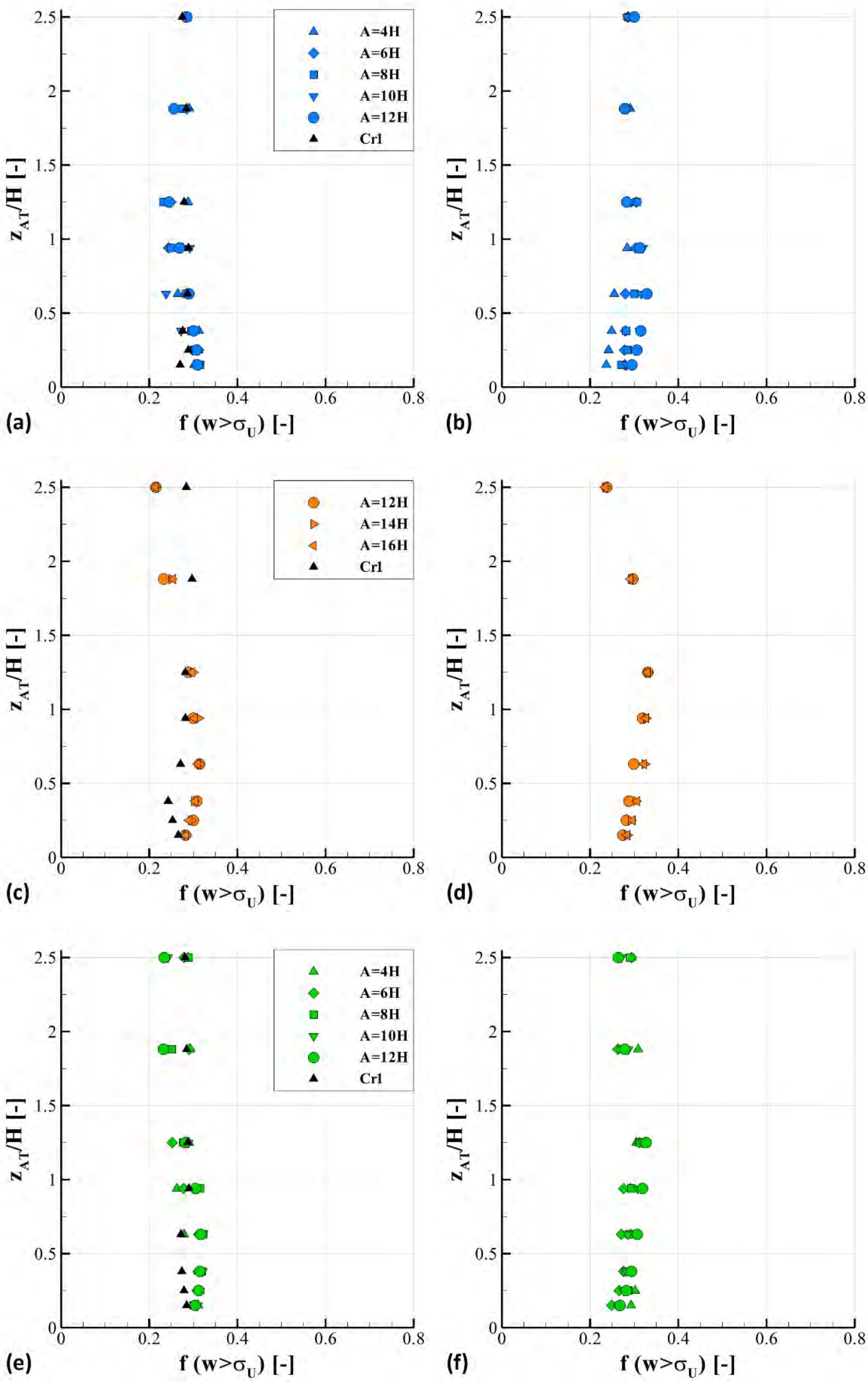

Figure E18. Vertical profiles of the frequencies at which the vertical velocities are larger than the averaged transient longitudinal velocity fluctuations above the crests (a, c, e) and mid-valley (b, d, f) of Type I (a, b), Type II (c, d), and Type III (e, f) valleys. For all valley types, data from the crest of the first ridge is presented in black colour.

Table E4. Average ratios of longitudinal to lateral and to vertical turbulent velocity fluctuations from the lowest $Z = 100\ m$ above the mid-valley (MV) position of all valleys.

width (A)	Type I		Type II		Type III	
	$\sigma_U : \sigma_V$ [−]	$\sigma_U : \sigma_W$ [−]	$\sigma_U : \sigma_V$ [−]	$\sigma_U : \sigma_W$ [−]	$\sigma_U : \sigma_V$ [−]	$\sigma_U : \sigma_W$ [−]
$4H$	1.19	0.79	−	−	1.22	0.79
$6H$	1.21	0.78	−	−	1.09	0.71
$8H$	1.00	0.79	−	−	1.22	0.80
$10H$	1.03	0.82	−	−	1.13	0.79
$12H$	1.04	0.82	1.16	0.83	1.07	0.80
$14H$	−	−	1.13	0.80	−	−
$16H$	−	−	1.09	0.79	−	−
Flat terrain	0.82	0.55				

Table E5. Average ratios of longitudinal to lateral and to vertical turbulent velocity fluctuations from the lowest $Z = 100\ m$ above the crest of the second ridge (Cr2) of all valleys. Differences to the corresponding ratios obtained above the crest of the first ridges (Cr1) are displayed in parentheses.

width (A)	Type I		Type II		Type III	
	$\sigma_U : \sigma_V$ [−]	$\sigma_U : \sigma_W$ [−]	$\sigma_U : \sigma_V$ [−]	$\sigma_U : \sigma_V$ [−]	$\sigma_U : \sigma_W$ [−]	$\sigma_U : \sigma_V$ [−]
$4H$	0.93 (−0.03)	0.76 (+0.12)	−	−	0.91 (−0.21)	0.72 (+0.02)
$6H$	0.99 (+0.03)	0.81 (+0.17)	−	−	0.93 (−0.19)	0.73 (+0.03)
$8H$	1.08 (+0.12)	0.89 (+0.25)	−	−	0.99 (−0.13)	0.77 (+0.07)
$10H$	1.15 (+0.19)	0.95 (+0.31)	−	−	1.12 (±0)	0.87 (+0.17)
$12H$	1.23 (+0.27)	0.98 (+0.34)	1.12 (−0.07)	0.80 (+0.06)	1.23 (+0.11)	0.95 (+0.25)
$14H$	−	−	1.15 (−0.04)	0.80 (+0.06)	−	−
$16H$	−	−	1.19 (±0)	0.81 (+0.07)	−	−
Flat terrain	0.82	0.55				

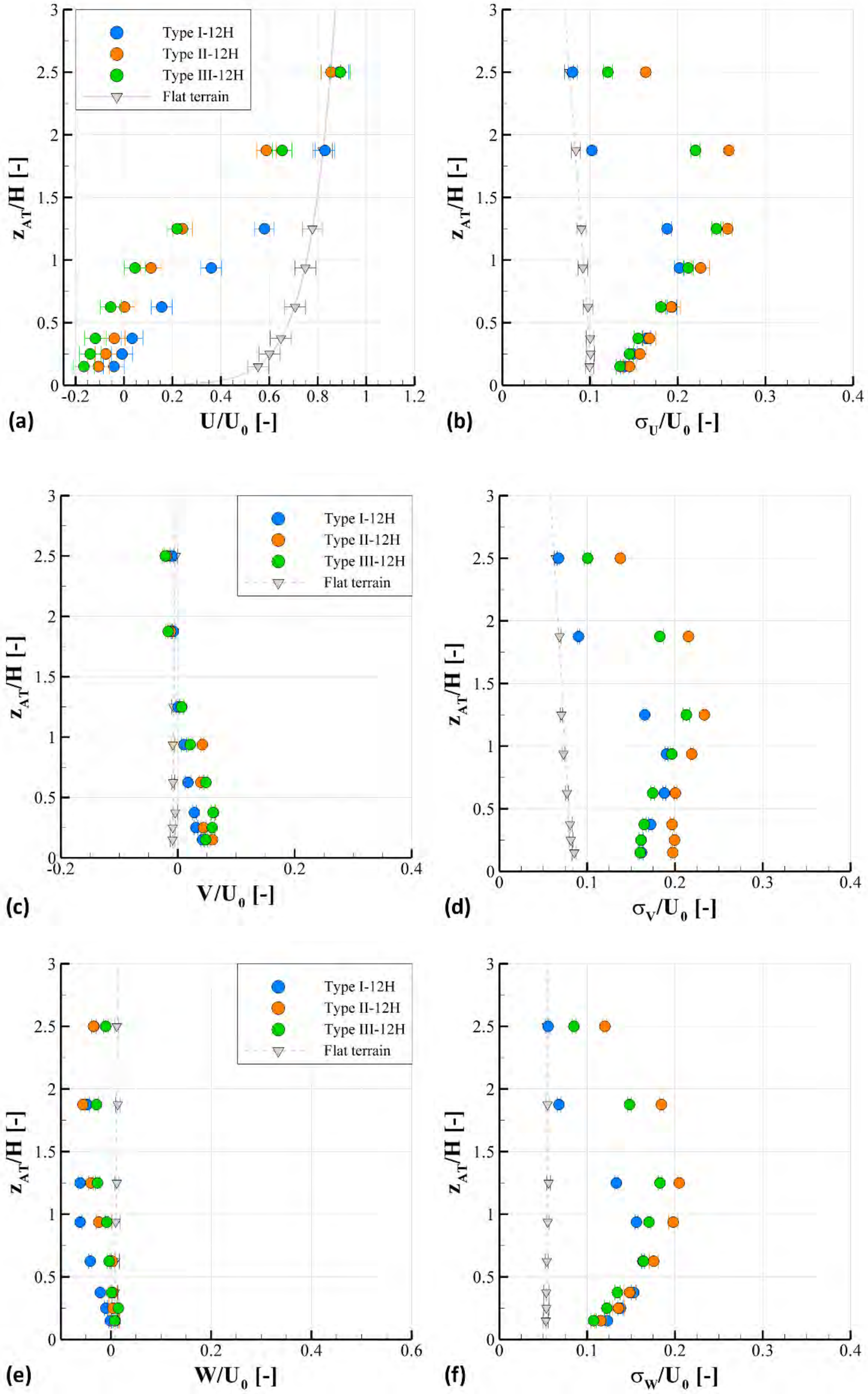

Figure E19. Vertical profiles of the mean dimensionless longitudinal (a, b), lateral (c, d), and vertical (e, f) velocities (a, c, e) and velocity fluctuations (b, d, f) above the mid-valley position (MV) of all valleys of width $A = 12H$.

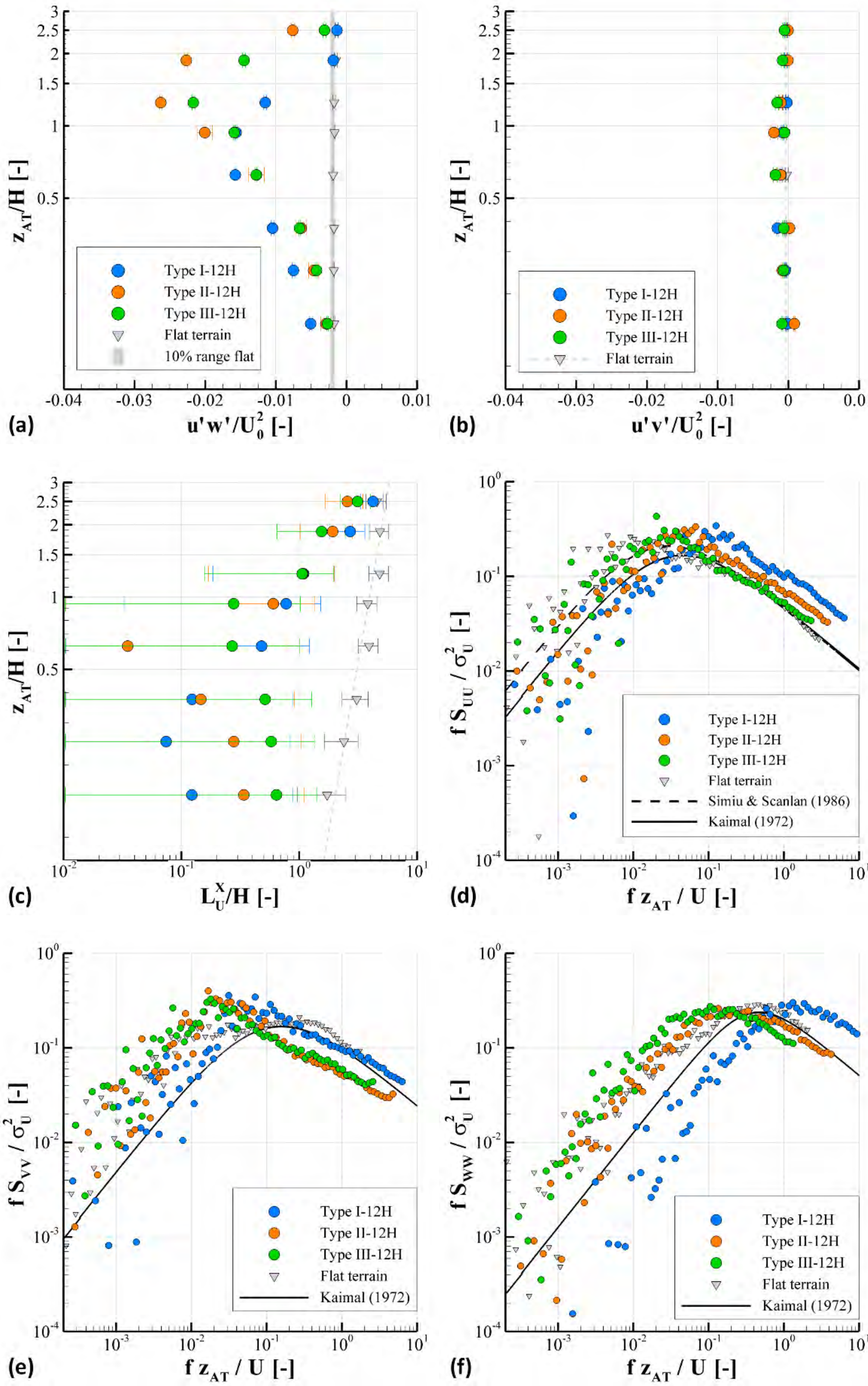

Figure E20. Vertical profiles of the mean dimensionless vertical (a) and horizontal (b) turbulent velocity fluxes, and integral length scales (c), and spectral distributions of longitudinal (d), lateral (e), and vertical (f) turbulent energy at $z/H = 0.15$ above the mid-valley position (MV) of all valleys of width $A = 12H$.

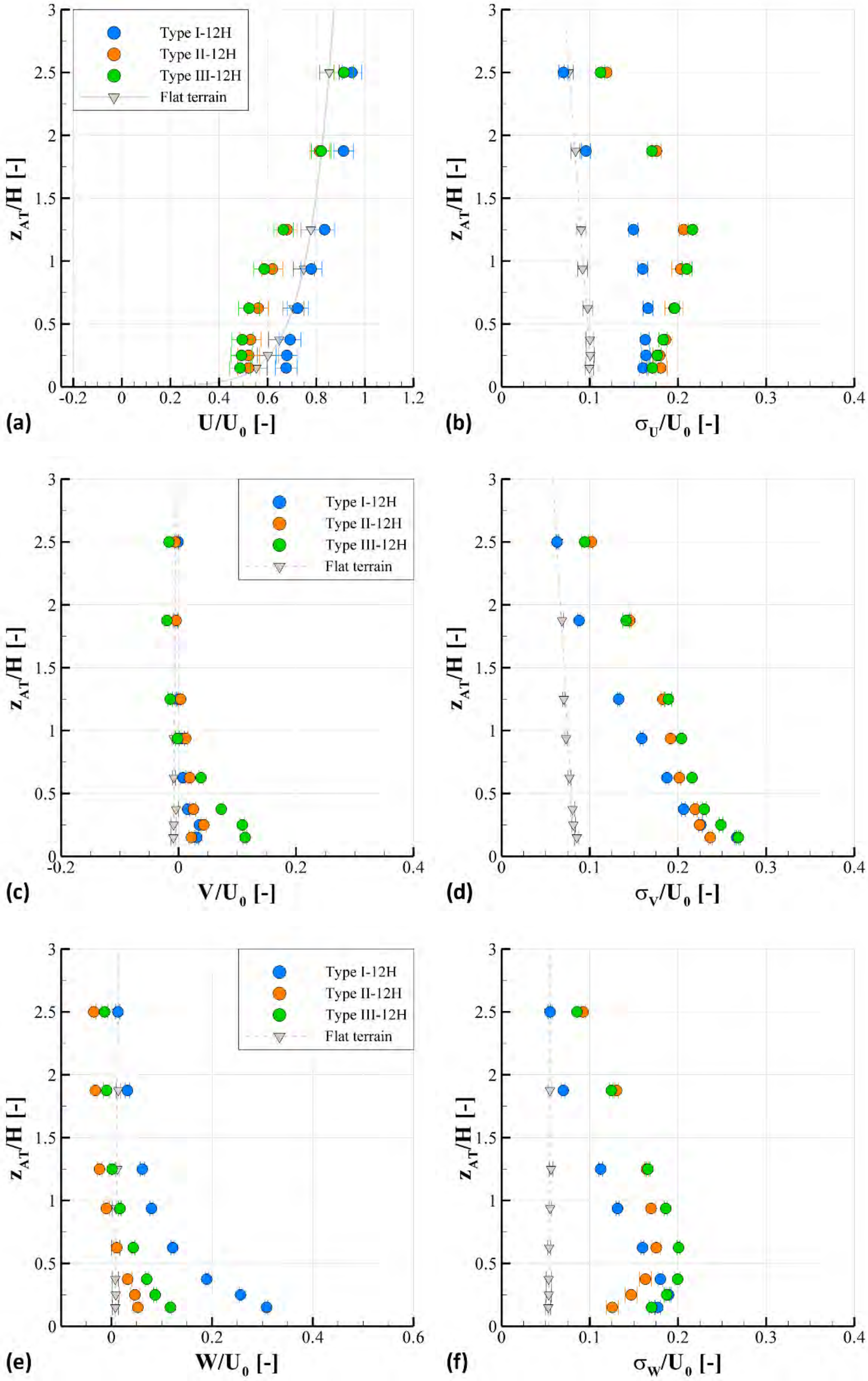

Figure E21. Vertical profiles of the mean dimensionless longitudinal (a, b), lateral (c, d), and vertical (e, f) velocities (a, c, e) and velocity fluctuations (b, d, f) above the crest of the second ridge (Cr2) of all valleys of width $A = 12H$.

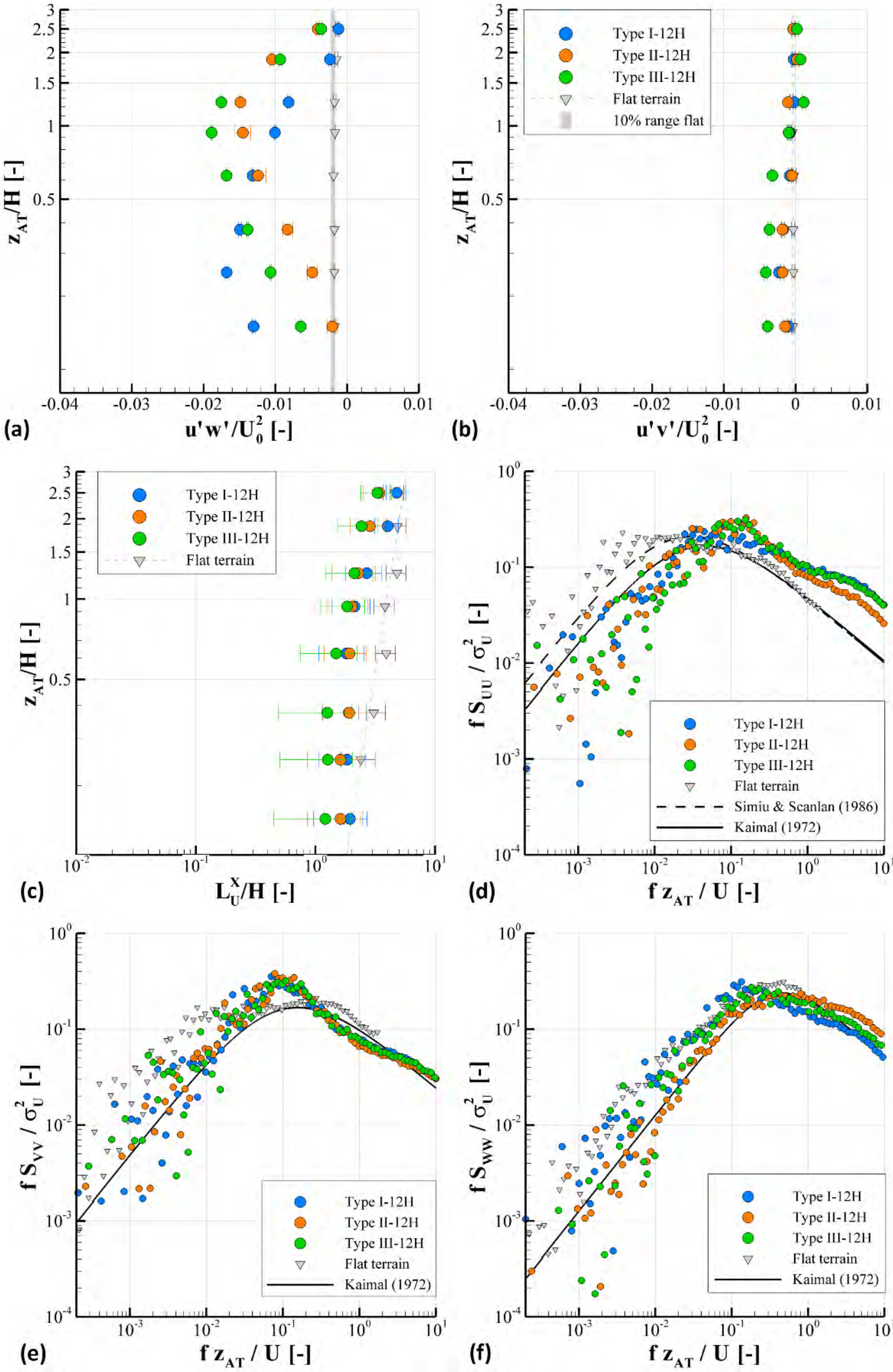

Figure E22. Vertical profiles of the mean dimensionless vertical (a) and horizontal (b) turbulent velocity fluxes, and integral length scales (c), and spectral distributions of longitudinal (d), lateral (e), and vertical (f) turbulent energy at $z/H = 0.15$ above the crest of the second ridge (Cr2) of all valleys of width $A = 12H$.

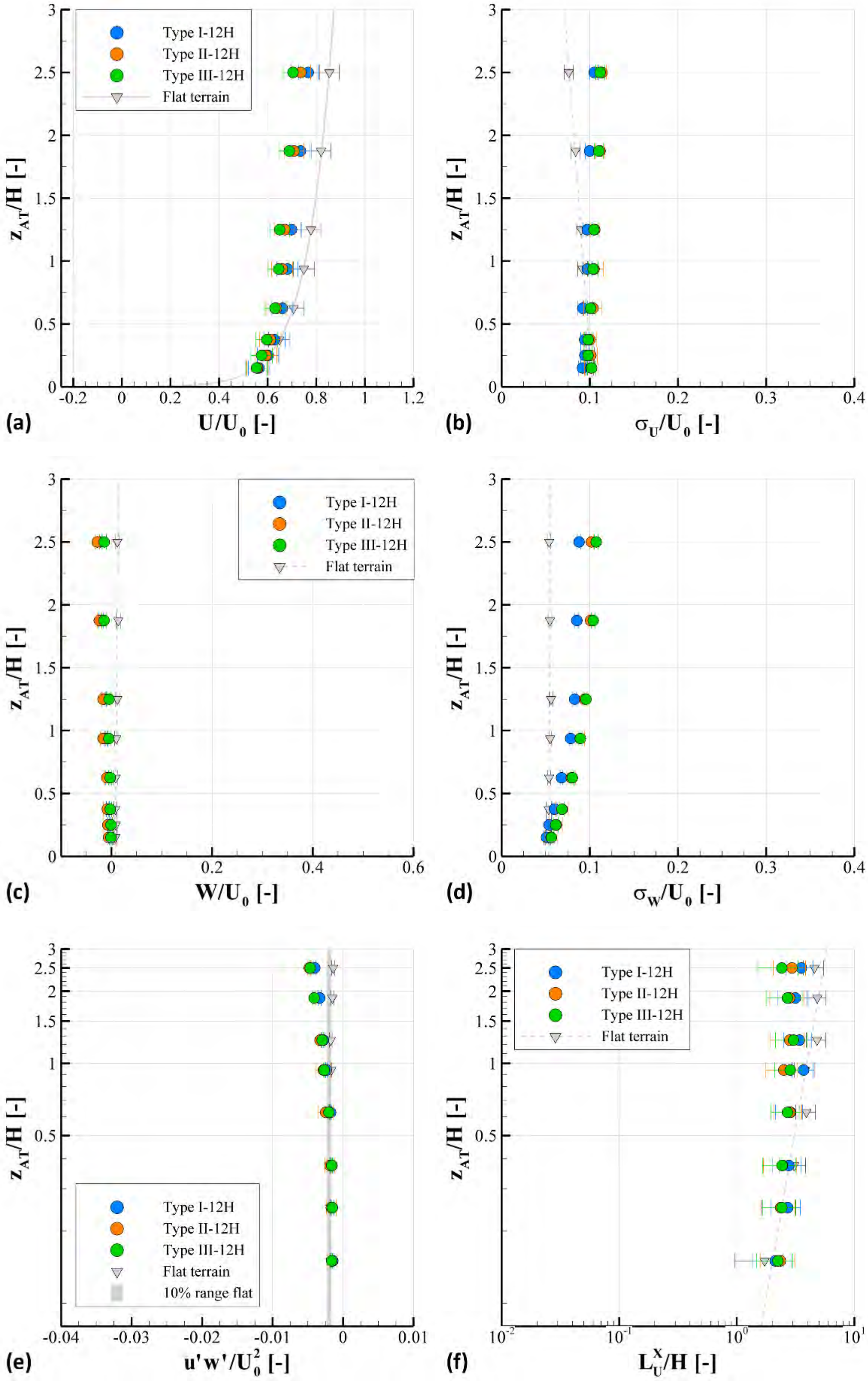

Figure E23. Vertical profiles of the mean dimensionless longitudinal (a, b), and vertical (c, d) velocities (a, c) and velocity fluctuations (b, d), vertical turbulent velocity fluxes (e), and integral length scales (f) above the furthermost downwind position (DW7) from all valleys of width $A = 12H$.

APPENDIX F – COORDINATE SYSTEMS ANALYSIS

Flow-referenced data is obtained via a rotation matrix applied to the present single ridge data using the script created by Diezel (2019). Longitudinal components originate from UW measurements and data uncertainties from the Earth coordinate system are adopted for the rotated datasets. Added uncertainties that may arise from the transformation of the data are neglected under this approach. Figure E1 displays the vertical profiles of the mean longitudinal velocity and all components of the mean velocity fluctuations above two streamwise locations of the steep windward slope (*Type I-75* ridge), together with the approach flow data (predominantly horizontal flow).

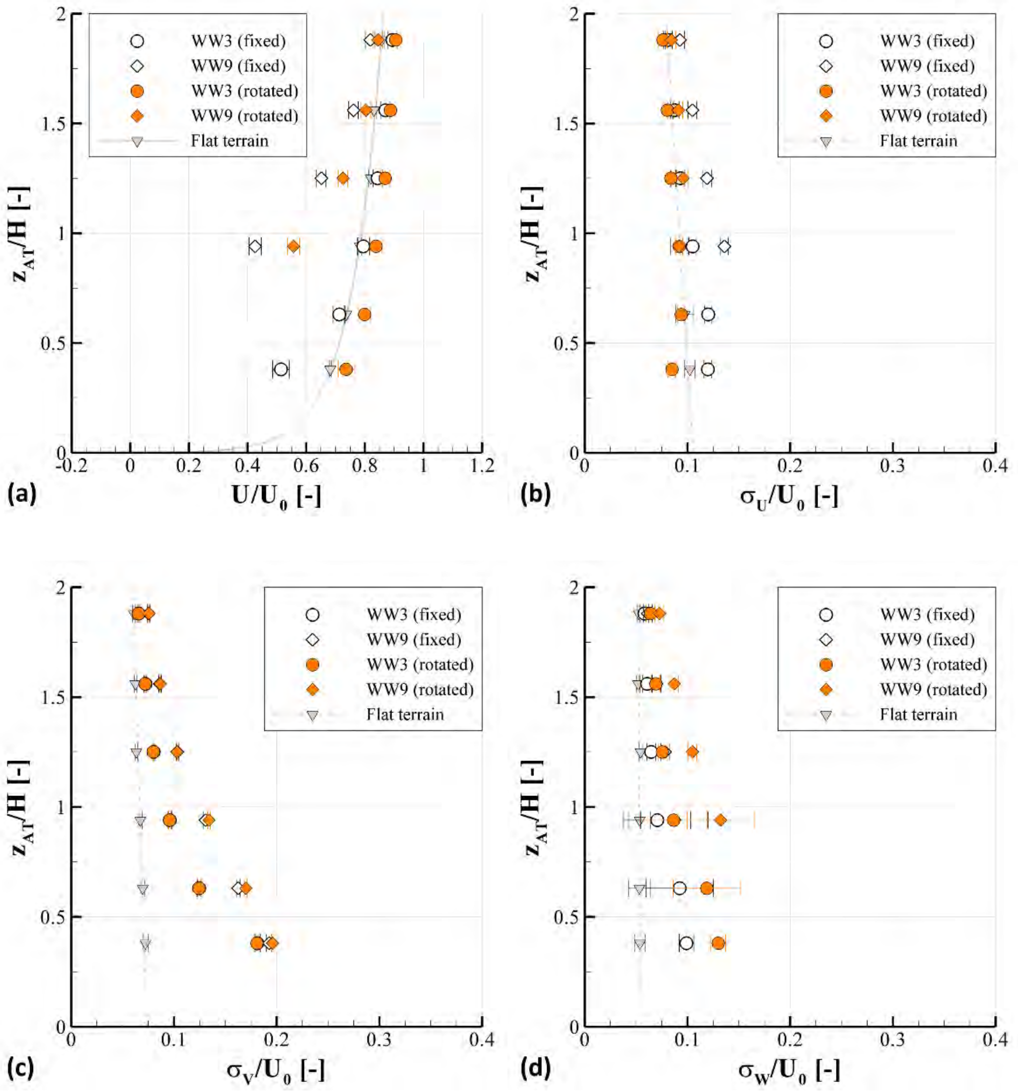

Figure F1. Vertical profiles of the mean dimensionless longitudinal velocity (a), and longitudinal (b), lateral (c), and vertical (d) velocity fluctuations above the windward slope of the Type I-75 ridge using Earth (fixed) and flow-referenced (rotated) coordinate systems.

The largest differences between coordinate systems are expectedly found at the near-surface and at the furthermost distances from the crest. Mean velocities are most sensitive to the transformation between coordinate systems, as highlighted by the $\approx 45\%$ increase of the rotated data relative to the fixed system at $z_{AT}/H = 0.38$. This exemplifies the advantages of the flow-referenced coordinate system in capturing the strongest magnitudes of streamwise velocity. Velocity fluctuations exhibit distinct trends: fixed data presents the largest longitudinal magnitudes and the rotated data the maxima of the vertical components. The maximum difference between longitudinal fluctuations is found above *WW9* (at $z_{AT}/H = 0.94$), where fixed data is $\approx 50\%$ larger than the flow-referenced counterpart. At the lowest height ($z_{AT}/H = 0.38$) above the near-crest (*WW3*), the rotated data is $\approx 20\%$ smaller than the approach flow value. This indicates that dampening of longitudinal turbulence takes place, but has no correspondence with the fixed data. Vertical components display inverse trends, the rotated data exhibiting the largest magnitudes of turbulence. Lateral fluctuations are less affected.

From the profiles of the velocity fluctuations above the leeside slopes, presented in Figure F2, ridge-specific trends are noticeable on the coordinate systems. Differences between data increase with increasing inclinations of the windward slopes of the ridges. Fluctuations are less dependent on the coordinate system above the steep leeside slope (*Type I-10* ridge), as evidenced by the convergence between data at all heights. Inversely, the largest differences are observed above the leeside slope of the *Type I-75* ridge. Clear dependence on the coordinate systems is observed above the furthermost downwind position from the crest (*LW9*), symmetric to the trend of the windward slope. Above the leeside slope, the rotated longitudinal components are larger than those of the fixed coordinate system and the inverse is observed for the vertical components. This occurs at all measurement heights except for the lowest ($z_{AT}/H = 0.38$), where the longitudinal component of the fixed data overpowers the rotated counterpart by $\approx 40\%$ and the rotated vertical component is $\approx 30\%$ larger than the fixed data.

Different orientations of horizontal (UV) and vertical (UW) plane velocity vectors above the landforms renders data transformation impractical for 3D flow characterisations made from independent 2D measurements. This is exemplified by the vertical profiles of the longitudinal fluctuations, measured with UV and UW settings, above *WW9* and *LW9* of the *Type I-75* ridge in Figure F3. Significant differences between rotated UV and UW datasets of the mean longitudinal fluctuations (σ_U/U_0) can be observed. The evaluation of longitudinal turbulence characteristics above orography using rotated data from UV measurements fails to capture the strongest slope effects on flow turbulence above orography.

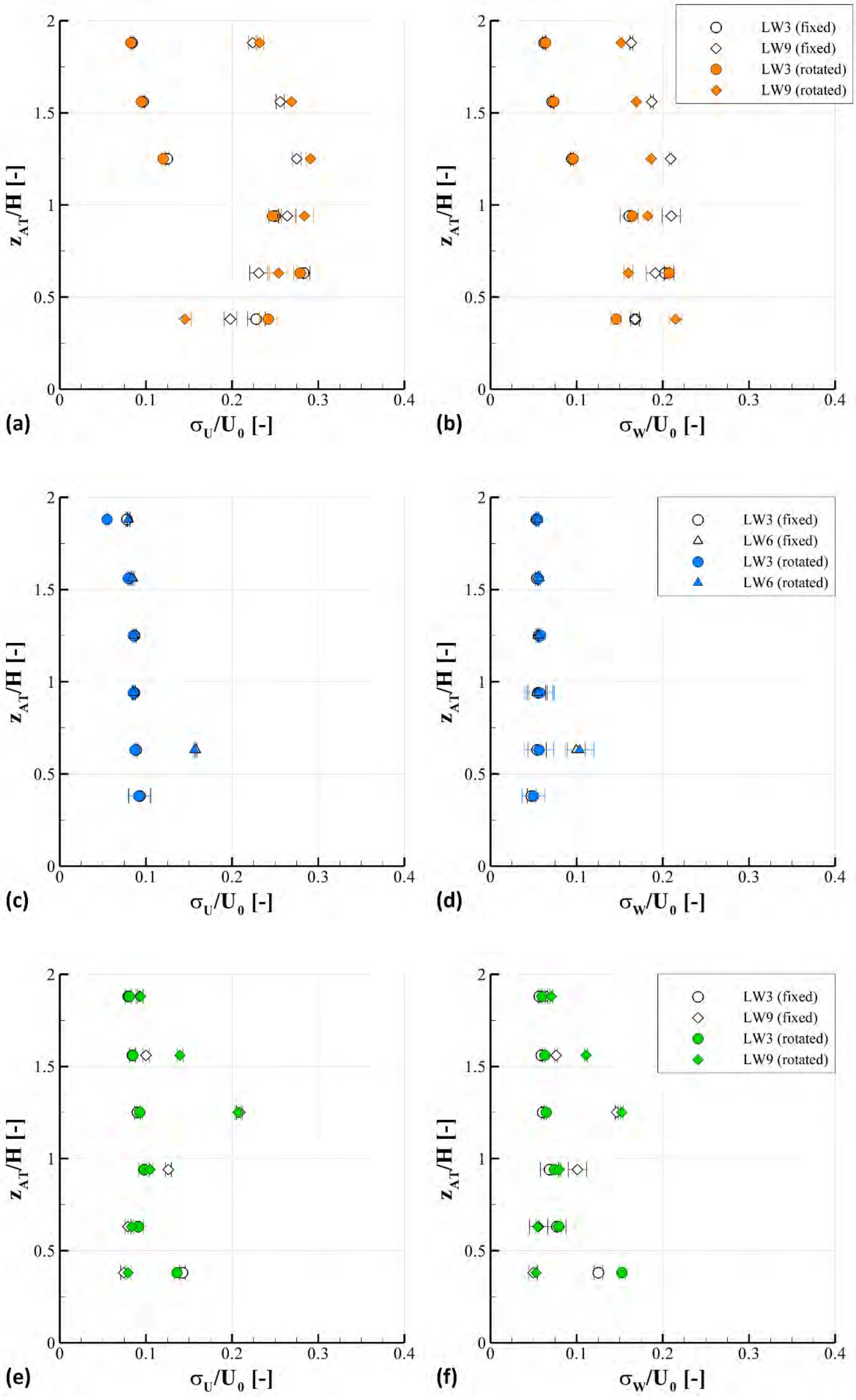

Figure F2. Vertical profiles of the mean dimensionless longitudinal (a, c, e), and vertical (b, d, e) velocity fluctuations above the leeside slope of Type I-75 (a, b), Type I-10 (c, d), and Type II (e, f) ridges using Earth (fixed) and flow-referenced (rotated) coordinate systems.

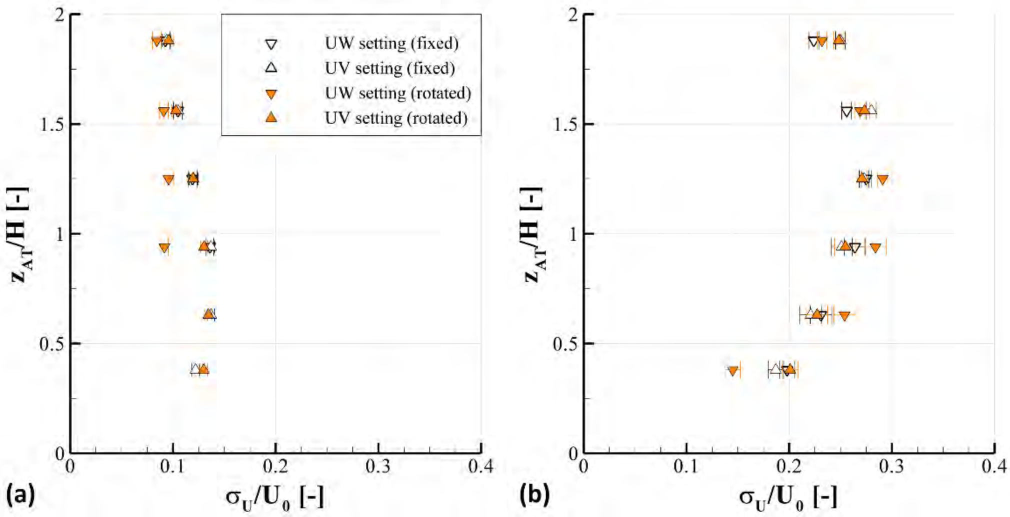

Figure F3. Vertical profiles of the mean dimensionless longitudinal velocity fluctuations, measured with UV and UW LDV orientations, above the furthermost positions of the windward (a) and leeside (b) slopes from the crest of the Type I-75 ridge using Earth (fixed) and flow-referenced (rotated) coordinate systems.

Rotation of the spectra to flow-referenced coordinates can provide insight into the shifts of the frequencies of peak energy, observed in Chapters 7 and 8. Figure F4 displays longitudinal and lateral spectra of fixed and rotated data at $z_{AT}/H = 0.38$ above *LW3* of the *Type I-10* ridge. At this location, the difference between the underlying slope inclination and the vertical plane mean velocity vector is $\approx 80°$. Rotation of the data results in minimal changes to the frequencies of peak energy when compared to the shifts of orders of magnitude observed between orography and approach flows. Frequencies of the rotated data shift to higher frequencies relative to the Earth coordinate data. Intensities of peak energy are relatively unaffected.

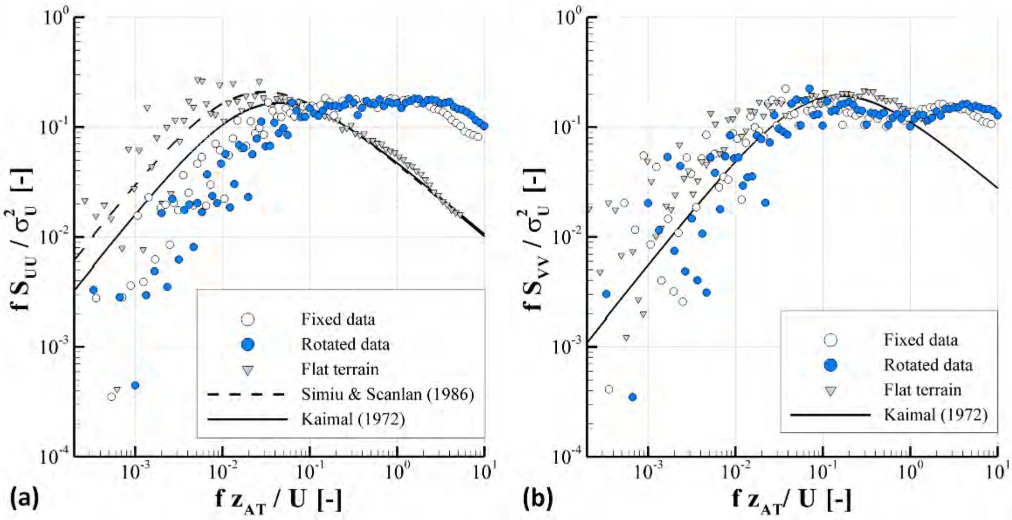

Figure F4. Spectral distributions of longitudinal (a) and lateral (b) turbulent energy at $z/H = 0.38$ above the near-crest position of the leeside slope (LW3) of the Type I-10 ridge using Earth (fixed) and flow-referenced (rotated) coordinate systems.

BIBLIOGRAPHY

Abdi, D.S., & Bitsuamlak, G.T. (2014). Wind flow simulations on idealized and real complex terrain using various turbulence models. *Advances in Engineering Software 75*, pp. 30-41.

Antonia, R.A., & Luxton, R.E. (1971). The response of a turbulent boundary later to a step change in surface roughness-Part 1 Smooth to rough. *J. Fluid Mech. 48 (4)*, pp. 721-761.

Arya, S.P.S., & Gadiayaram, P.S. (1986). An experimental study of flow and dispersion in the wakes of three-dimensional low hills. *Atmospheric Environment 20 (4)*, pp. 729-740.

AWEO (2018). Industrial wind turbine models and specifications. Available at following web link: http://www.aweo.org/windmodels.html (consulted in March 2018).

Ayotte, K.W., & Hughes, D.E. (2004). Observations of boundary-layer wind-tunnel flow over isolated ridges of varying steepness and roughness. *Boundary-Layer Meteorology 112*, pp. 525-556.

Bardal, L.M., & Soetran, L.R. (2016). Wind gust factors in a coastal wind climate. 13th Deep Sea Offshore Wind R&D Conference, EERA DeepWind'2016, Trondheim, Norway. *Energy Procedia 94*, pp. 417-424.

Bechmann, A., Berg, J., Courtney, M., Ejsing Jorgensen, H., Mann, J., & Sorensen, N.N. (2009). The Bolund experiment: Overview and background. Roskilde: Danmarks Tekniske Universitet, Riso Nationallaboratoriet for Baeredygtig Energi. (Denmark. Forskningscenter Risoe. Risoe-R; No. 1658 (EN)).

Bechmann, A., Sorensen, N.N., Berg, J., Mann, J., & Réthoré, P.E. (2011). The Bolund experiment, part II: Blind comparison of microscale flow models. *Boundary-Layer Meteorology 141*, pp. 245-271.

Berg, J., Mann, J., Bechmann, A., Courtney, M.S., & Jorgensen, H.E. (2011). The Bolund experiment, part I: Flow over a steep, three-dimensional hill. *Boundary-Layer Meteorology 141*, pp. 219-243.

Berselli, L.C., Iliescu, T., & Layton, W.J. (2005). Mathematics of large-eddy simulation of turbulent flows, first edition. Springer.

Blackmore, P.A. (1987). A static pressure probe for use in turbulent three-dimensional flows. *Journal of Wind Engineering and Industrial Aerodynamics 25*, pp. 207-218.

Blocken, B., Stathopoulos, T., & Carmeliet, J. (2007). CFD simulation of the atmospheric boundary layer: wall function problems. *Atmospheric Environment 41 (2)*, pp. 238-252.

Bowen, A.J. (2003). Modelling of strong wind flows over complex terrain at small geometric scales. *Journal of Wind Engineering and Industrial Aerodynamics 91*, pp. 1859-1871.

Britter, R.E., Hunt, J.C.R., & Richards, K.J. (1981). Air flow over a two-dimensional hill: Studies of velocity speed-up, roughness effects and turbulence. *Quarterly Journal of the Royal Meteorological Society 107*, pp. 91-110.

Brown, A.R., Hobson, J.M., & Wood, N. (2001). Large-eddy simulation of neutral turbulent flow over rough sinusoidal ridges. *Boundary Layer Meteorology 98*, pp. 411-441.

Brown, G.O. (2003). Henry Darcy's perfection of the Pitot tube. In: Brown, G.O., Garbrecht, J.D. & Hager, W.H. (eds) Henry P. G. Darcy and Other Pioneers in Hydraulics: Contributions in Celebration of the 200th Birthday of Henry Philibert Gaspard Darcy. ASCE, Reston, VA, pp. 14-23.

Buchhave, P., George Jr, W.K., & Lumley, J.L. (1979). The measurement of turbulence with the Laser-Doppler Anemometer. *Ann. Rev. Fluid Mech. 11*, pp. 443-503.

Cao, S., & Tamura, T. (2006). Experimental study on roughness effects on turbulent boundary layer flow over a two-dimensional steep hill. *Journal of Wind Engineering and Industrial Aerodynamics 94*, pp. 1-19.

Cao, S., & Tamura, T. (2007). Effects of roughness blocks on atmospheric boundary layer flow over a two-dimensional low hill with/without sudden roughness change. *Journal of Wind Engineering and Industrial Aerodynamics 95*, pp. 679-695.

Castro F.A., Palma, J.M.L.M., & Silva Lopes, A. (2003). Simulation of Askervein flow. Part I: Reynolds averaged Navier-Stokes equations (k-ε turbulence model). *Boundary-layer Meteorology 107*, pp. 501-530.

Chappell, A., & Heritage, G. (2007). Using illumination and shadow to model aerodynamic resistance and flow separation: An isotropic study. *Atmospheric Environment 41 (28)*, pp. 5817-5860.

Chaudhari, A., Hellsten, A., & Hamalainen, J. (2016). Full-scale experimental validation of large-eddy simulation of wind flows over complex terrain: The Bolund hill. *Advances in Meteorology 2016*.

Cheng, G. (2019). Urban ventilation for heatwave events and typical summer in Hong Kong. Master thesis in Meteorology. University of Hamburg.

Cheng, H., & Castro, I.P. (2002). Near-wall flow development after a step change in surface roughness. *Boundary-layer Meteorology 105*, pp. 411-432.

Cobelli, C., Carson, E.R., Finkelstein, L., & Leaning, M.S. (1984). Validation of simple and complex models in physiology and medicine. *American Journal of Physiology 246 (Regulatory Integrative Comp. Physiol. 15)*, pp. R259-R266.

Conan, B., Chaudhari, A., Aubrun, S., van Beeck, J., Hamalainen, J., & Hellsten, A. (2016). Experimental and numerical modelling of flow over complex terrain: The Bolund hill. *Boundary-layer Meteorology 158*, pp. 183-208.

COST732 (2007). Best practice guideline for the CFD simulation of flows in the urban environment. In: Franke, J., Hellsten, A., Schlünzen, H. & Carissimo, B. (eds) COST Action 732 – Quality Assurance and Improvements of Microscale Meteorological Models.

Counihan, J. (1975). Adiabatic atmospheric boundary layers: A review and analysis of data from the period 1880-1972. *Atmospheric Environment 9*, pp. 871-905.

Dantec Dynamics (2012). BSA Flow Software v5.03. Dantec Dynamics A/S, Skovlunde, Denmark.

Deardorff, J.W. (1970). A numerical study of three-dimensional turbulent channel flow at large Reynolds numbers. *J. Fluid Mech., 41 (2)*, pp. 453-480.

Deaves, D.M. (1980). Computations of wind flow over two-dimensional hills and embankments. *Journal of Wind Engineering and Industrial Aerodynamics 6*, pp. 89-111.

Del Alamo, J.C., & Jimenez, J. (2009). Estimation of turbulent convection velocities and corrections to Taylor's approximation. *J. Fluid Mech. 640*, pp. 5-26.

Diebold, M., Higgins, C., Fang, J., Bechmann, A., & Parlange, M.B. (2013). Flow over hills: A large-eddy simulation of the Bolund case. *Boundary-layer Meteorology 148 (1)*, pp. 177-194.

Diezel, J. (2019). The influence of v-shaped valleys on near-surface winds. Master thesis in Meteorology. University of Hamburg.

Erdmann, F. (2017). Wind tunnel study of terrain induced flow modification and spatial resolution effects. Master thesis in Meteorology. University of Hamburg.

Ferreira, A.D., Lopes, A.M.G., Viegas, D.X., & Sousa, A.C.M. (1995). Experimental and numerical simulation of flow around two-dimensional hills. *Journal of Wind Engineering and Industrial Aerodynamics 54/55*, pp. 173-181.

Fischer, R. (2011). Entwicklung eines problemorientierten Software-Pakets zur automatisierten Aufbereitung, Analyse und Dokumentation von im Windkanal produzierten Daten zur LES-Validierung. Doctoral dissertation in Natural Sciences. University of Hamburg.

Foken, T. (2008). Micrometeorology. Springer.

Frandsen, S., Jorgensen, H.E., & Sorensen, J.D. (2007). Relevant criteria for testing the quality of turbulence models. In: The European Wind Energy Conference and Exhibition, EWEC 2007, Milan.

George, W.K. (1988). Quantitative measurement with the burst-mode Laser Doppler Anemometer. *Experimental Thermal and Fluid Science 1*, pp. 29-40.

Germano, M. (1992). Turbulence: the filtering approach. *J. Fluid Mech. 238*, pp. 325-336.

Gillmeier, S. (2014). Boundary layer wind tunnel modelling of large-scale wind flow over complex terrain-a feasibility study. Master thesis in Meteorology. University of Hamburg.

Gong, W., & Ibbetson, A. (1989). A wind tunnel study of turbulent flows over model hills. *Boundary Layer Meteorology 49*, pp. 113-148.

Gosseau, P., Blocken, B., & van Heijst, G.J.F. (2013). Quality assessment of large-eddy simulation of wind flow around a high-rise building: Validation and solution verification. *Computers & Fluids 79*, pp. 120-133.

Griffiths, A.D., & Middleton, J.H. (2010). Simulations of separated flow over two-dimensional hills. *Journal of Wind Engineering and Industrial Aerodynamics 98*, pp. 155-160.

Gualtieri, G., & Zappitelli, G. (2015). Investigating wind resource, turbulence intensity and gust factor on mountain locations in Southern Italy. *Int. J. Green Energy 12*, pp. 309-327.

Hamilton, M.A. (1991). Model validation: An annotated bibliography. *Commun. Statist. Theory Meth. 20 (7)*, pp. 2207-2266.

Hanjalic, K., & Kenjeres, S. (2008). Some developments in turbulence modelling for wind and environmental engineering. *Journal of Wind Engineering and Industrial Aerodynamics 96*, pp. 1537-1570.

Hansen, A.C., & Cermak, J.E. (1975). Vortex-containing wakes of surface obstacles. Fluid Dynamics and Diffusion Laboratory Report CER75-76ACH-JEC16. Colorado State University, Fort Collins.

Harms, F. (2010). Systematische Windkanaluntersuchungen zur Charakterisierung instationarer Ausbreitungsprozesse einzelner Gaswolken in urbanen Rauigkeitsstrukturen. Doctoral dissertation in Natural Sciences. University of Hamburg.

Hasselman, T.K., Wathugala, G.W., & Crawford, J. (2002). A hierarchical approach for model validation and uncertainty quantification. Fifth World Congress on Computational Mechanics, Vienna, Austria. Mang, H.A., Rammerstorfer, F.G. & Eberhardsteiner, J. (eds).

Hunt, J.C.R., Leibovich, S., & Richards, K.J. (1988). Turbulent shear flow over low hills. *Quarterly Journal of the Royal Meteorological Society 114*, pp. 1435-1471.

Hussain, A.K.M.F. (1983). Coherent structures-reality and myth. *Physics of Fluids 26 (10)*, pp. 2816-2850.

Hussain, A.K.M.F. (1986). Coherent structures and turbulence. *J. Fluid Mech. 173*, pp. 303-356.

Iizuka, S., & Kondo, H. (2004). Performance of various sub-grid scale models in large-eddy simulations of turbulent flow over complex terrain. *Atmospheric Environment 38*, pp. 7083-7091.

Ishihara, T., Hibi, K., & Oikawa, S. (1999). A wind tunnel study of turbulent flow over a three-dimensional step hill. *Journal of Wind Engineering and Industrial Aerodynamics 83*, pp. 95-107.

Jackson, P.S., & Hunt, J.C.R. (1975). Turbulent flow over a low hill. *Quarterly Journal of the Royal Meteorological Society 101*, pp. 929-955.

JCGM 100:2008 – Joint Committee for Guides in Metrology. (2010). Evaluation of measurement data – Guide to the expression of uncertainty in measurement, rev. 1st Ed. 2008.

Jimenez, J. (2003). Computing high-Reynolds-number turbulence: Will simulations ever replace experiments? *Journal of Turbulence 4 (22)*, pp. 2-14.

Johnson, P.L., & Meneveau, C. (2017). Turbulence intermittency in a multiple-time-scale Navier-Stokes-based reduced model. *Physical Review Fluids 2*, 072601(R).

Kaimal, J.C., & Finnigan, J.J. (1994). Atmospheric boundary layer flows: Their structure and measurement. Oxford University Press

Kaimal, J.C., Wyngaard, J.C., Izumi, Y., & Coté, O.R. (1972). Spectral characteristics of surface-layer turbulence. *Quarterly Journal of the Royal Meteorological Society 98*, pp. 563-589.

Kim, H.G., Lee, C.M., Lim, H.C., & Kyong, N.H. (1997). An experimental and numerical study on the flow over two-dimensional hills. *Journal of Wind Engineering and Industrial Aerodynamics 66*, pp. 17-33.

Kim, H.G., & Patel, V.C. (2000). Test of turbulence models for wind flow over terrain with separation and recirculation. *Boundary-layer Meteorology 94*, pp. 5-21.

Kempf, A.M. (2008). LES validation from experiments. *Flow Turbulence Combust. 80*, pp. 351-373.

Letson, F., Barthelmie, R.J., Hu, W., & Pryor, S.C. (2019). Characterizing wind gusts in complex terrain. *Atmos. Chem. Phys. 19*, pp. 3797-3819.

Liu, L., Sun, Z., Wang, Q., Zhuang, B., Han, Y., & Li, S. (2012). Eddy covariance tilt corrections over a coastal mountain area in South-east China: Significance for near-surface turbulence characteristics. *Advances in Atmospheric Sciences 29 (6)*, pp. 1264-1278.

Liu, Z., Ishihara, T., Tanaka, T., & He, X. (2016). LES study of turbulent flows over a smooth 3-D hill and a smooth 2-D ridge. *Journal of Wind Engineering and Industrial Aerodynamics 153*, pp. 1-12.

Liu, Z., Hu, Y., Fan, Y., Wang, W., & Zhou, Q. (2019). Turbulent flow fields over a 3D hill covered by vegetation canopy through large eddy simulations. *Energies 12*, *3624*.

Lopes, A.S., Palma, J.M.L.M., & Castro, F.A. (2007). Simulations of the Askervein flow. Part 2: Large-eddy simulations. *Boundary-layer Meteorology 125*, pp. 85-108.

Lorenz, E.N. (1963). Deterministic nonperiodic flow. *Journal of the Atmospheric Sciences 20*, pp. 130-141.

Loureiro, J.B.R., Pinho, F.T., & Silva Freire, A.P. (2007). Near-wall characterization of the flow over a two-dimensional steep smooth hill. *Experiments in Fluids 42*, pp. 441-457.

Loureiro, J.B.R., Monteiro, A.S., Pinho, F.T., & Silva Freire, A.P. (2008). The effect of roughness on separating flow over two-dimensional hills. *Experiments in Fluids 46 (4)*, pp. 577-596.

Lubitz, W.D., & White, B.R. (2007). Wind-tunnel and field investigation of the effect of local wind direction on speed-up over hills. *Journal of Wind Engineering and Industrial Aerodynamics 95*, pp. 639-661.

Lumley, J.L. (1965). Interpretation of time spectra measured in high intensity shear flows. *Physics of Fluids 8 (6)*, pp. 1056-1062.

Mahrt, L. (1989). Intermittency of atmospheric turbulence. *Journal of the Atmospheric Sciences 46 (1)*, pp. 79-95.

Mann, J., Angelou, N., Arnqvist, J., Callies, D., Cantero, E., Chávez-Arroyo, R., Courtney, M., Cuxart, J., Dellwik, E., Gottschall, J., Ivanell, S., Kühn, P. Lea, G., Matos, J.C., Veiga Rodrigues, C.M., Palma, J.M.L.M., Pauscher, L., Peña, A., Sanz Rodrigo, J., Soderberg, S., & Vasiljevic, N. (2017). Complex terrain experiments in the New European Wind Atlas. *Philosophical Transactions of the Royal Society of London. A 375*, 20160101.

Mason, P.J., & Sykes, R.I. (1979). Flow over an isolated hill of moderate slope. *Quarterly Journal of the Royal Meteorological Society 105*, pp. 383-395.

Menke, R., Vasiljevic, N., Hansen, K.H., Hahmann, A.N., & Mann, J. (2018). Does the wind turbine wake follow the topography? A multi-lidar study in complex terrain. *Wind. Energ. Sci. 3*, pp. 681-691.

Menke, R., Vasiljevic, N., Mann, J., & Lundquist, J.K. (2019). Characterization of flow recirculation zones at the Perdigão site using multi-lidar measurements. *Atmos. Chem. Phys. 19*, pp. 2713-2723.

Meroney, R.N., Bowen, A.J., Lindley, D., & Pearse, J. (1978). Wind characteristics over complex terrain: Laboratory simulation and filed measurements at Rakaia Gorge, New Zealand. Dep. Of Energy Report RLO/2438-77/2.

Meroney R.N. (1990). Fluid dynamics of flow over hills/mountains—Insights obtained through physical modelling. In: Blumen W. (eds) Atmospheric Processes over Complex Terrain. Meteorological Monographs, Vol 23. American Meteorological Society, Boston, MA, pp. 145-171.

Mizuno, T., & Panofsky, H.A. (1975). The validity of Taylor's hypothesis in the atmospheric surface layer. *Boundary-layer Meteorology 9*, pp. 375-380.

Moin, P., & Mahesh, K. (1998). Direct numerical simulation: A tool in turbulence research. *Annu Rev Fluid Mech 30*, pp. 539-578.

Moin, P. (2009). Revisiting Taylor's hypothesis. *J. Fluid Mech. 640*, pp. 1-4.

Molki, A., Khezzar, L., & Goharzedeh, A. (2013). Measurement of fluid velocity development in a laminar pipe flow using laser Doppler velocimetry. *Eur. J. Phys. 34*, pp. 1127-1134.

Monin, A.S. (1970). The atmospheric boundary layer. *Ann. Rev. Fluid Mech. 2 (1)*, pp. 225-250.

Morales, A., Wachter, M., & Peinke, J. (2012). Characterization of wind turbulence by higher-order statistics. *Wind Energy 15*, pp. 391-406.

Nobach, H. (1999). Processing of stochastic sampled data in Laser Doppler Anemometry. Proc. of the 3rd International Workshop on Sampling Theory and Applications, 11-14 August 1999, Loen, Norway.

Oberkampf, W.L., & Trucano, T.G. (2002). Verification and validation in computational fluid dynamics. *Progress in Aerospace Sciences 38*, pp. 209-272.

Patankar, S.V. (1980). Numerical heat transfer and fluid flow. Hemisphere Publishing Corporation. McGraw-Hill, USA.

Peña, A., Dellwik, E., & Mann, J. (2019). A method to assess the accuracy of sonic anemometer measurements. *Atmos. Meas. Tech. 12*, pp. 237-252.

Peralta, C., Parente, A., Balogh, M., & Benocci, C. (2014). RANS simulation of the atmospheric boundary layer over complex terrain with a consistent k-epsilon model. Proceedings of the 6th International Symposium on Computational Wind Engineering, Hamburg, Germany.

Petersen, E.L., Mortensen, N.G., Landberg, L., Hojstrup, J., & Frank, H.P. (1998). Wind power meteorology. Part I: Climate and turbulence. *Wind Energy 1*, pp. 2-22.

Petersen, G. (2013). Wind tunnel modelling of atmospheric boundary layer flow over hills. Doctoral dissertation in Natural Sciences. University of Hamburg.

Pope, S.B. (2000). Turbulent flows. Cambridge University Press.

Pope, S.B. (2004). Ten questions concerning the large-eddy simulation of turbulent flows. *New J. Phys. 6 (35)*, pp. 1-24.

Prospathopoulos, J.M., Politis, E.S., & Chaviaropoulos, P.K. (2012). Application of a 3D RANS solver on the complex Hill of Bolund and assessment of the wind flow predictions. *Journal of Wind Engineering and Industrial Aerodynamics 107-108*, pp. 149-159.

Raupach, M.R., Antonia, R.A., & Rajagopalan, S. (1991). Rough-wall turbulent boundary layers. *Applied Mech. Rev. 44 (1)*, pp. 1-25.

Reynolds, O. (1895). On the dynamical theory of incompressible viscous fluids and the determination of the criterion. *Philosophical Transactions of the Royal Society of London. A 186*, pp. 123-164.

Ristic, S. (2007). Laser Doppler Anemometry and its application in wind tunnel tests. *Scientific Technical Review 57 (3-4)*, pp. 64-75.

Ruck, B. (1991). Distortion of LDA fringe pattern by tracer particles. *Experiments in Fluids 10*, pp. 349-354.

Salim, S.M., Cheah, S.C., & Chan, A. (2011). Numerical simulation of dispersion in urban street canyons with avenue-like tree plantings: Comparison between RANS and LES. *Building and Environment 46*, pp. 1735-1746.

Schliffke, B., & Wiedemeier, J. (2018). Windtunnel Documentation, Release 0.0.1. EWTL, University Hamburg.

SCOPUS (2017). Statistics of publications related to flows over complex terrain and flow modelling. From the following web link: http://www.scopus.com (consulted in January 2017).

Simiu, E., & Scanlan, R.H. (1986). Wind effects on structures: An introduction to wind engineering. John Wiley & Sons, Hoboken.

Snyder, W.H. (1981). Guideline for modeling of atmospheric dispersion. Environmental Sciences Research Laboratory, Environmental Protection Agency Report EPA-600/8-81-009.

Snyder, W.H. (1985). Fluid modelling of pollutant transport and diffusion in stably stratified flows over complex terrain. *Annual Rev. Fluid Mech. 17*, pp. 239-266.

Snyder, W.H., & Britter, R.E. (1987). A wind tunnel study of the flow structure and dispersion from sources upwind of three-dimensional hills. *Atmospheric Environment 21 (4)*, pp. 735-751.

Snyder, W.H., & Castro, I.P. (2002). The critical Reynolds number for rough-wall boundary layers. *Journal of Wind Engineering and Industrial Aerodynamics 90 (1)*, pp. 41-54.

Sorbjan, Z. (2004). Large-Eddy simulations of the Atmospheric Boundary Layer. In: Zanetti, P. (ed) Air Quality Modeling-Theories, Methodologies, Computational Techniques, and Available Databases and Software. Vol II-Advanced Topics. EnviroComp Institute and Air & Waste Management Association.

Stull, R.B. (1988). An introduction to boundary layer meteorology. Kluwer Academic Publishers.

Sun, J. (2007). Tilt corrections over complex terrain and their implication for CO_2 transport. *Boundary-Layer Meteorology 124 (2)*, pp. 143-159.

Sykes, R.I. (1980). An asymptotic theory of incompressible turbulent boundary-layer flow over a small hump. *J. Fluid Mech. 101*, pp. 647-670.

Takahashi, T., Ohtsu, T., Yassin, M.F., Kato, S., & Murakami, S. (2002). Turbulence characteristics of wind over a hill with a rough surface. *Journal of Wind Engineering and Industrial Aerodynamics 90*, pp. 1697-1706.

Tamura, T., Okuno, A., & Sugio, Y. (2007). LES analysis of turbulent boundary layer over 3D steep hill covered with vegetation. *Journal of Wind Engineering and Industrial Aerodynamics 95*, pp. 1463-1475.

Taylor, G.I. (1938). The spectrum of turbulence. *Proceedings of the Royal Society of London. Series A, Mathematical and Physical Sciences*.

Taylor, P.A., & Teunissen, H.W. (1983). Askervein '82: Report on the September/October 1982 experiment to study boundary-layer flow over Askervein, South Uist. Atmospheric Environment Service, Canada.

Taylor, P.A., & Teunissen, H.W. (1987). The Askervein hill project: Overview and background data. *Boundary-Layer Meteorology 39*, pp. 15-39.

Teunissen, H.W., Shokr, M.E., Bowen, A.J., Wood, C.J., & Green, D.W.R. (1987). The Askervein hill project: Wind-tunnel simulations at three length scales. *Boundary-Layer Meteorology 40*, pp. 1-29.

Townsend, A.A. (1956). The structure of turbulent shear flow. Cambridge University Press.

Townsend, A.A. (1976). The structure of turbulent shear flow, 2nd Edition. Cambridge University Press.

Triton, D.J. (1988). Physical fluid dynamics. Oxford University Press Inc., New York.

Troen, I., & Lundtang Petersen, E. (1989). European Wind Atlas. Roskilde: Riso National Laboratory.

Vasiljevic, N., Palma, J.M.L.M., Angelou, N., Mtos, J.C., Menke, R., Lea, G., Mann, J., Courtney, M., Ribeiro, L.F., & Gomes, V.M.M.G.C. (2017). Perdigão 2015: methodology for atmospheric multi-Doppler lidar experiments. *Atmos. Meas. Tech. 10*, pp. 3463-3483.

VDI (2000). Physical modelling of flow and dispersion processes in the atmospheric boundary layer – Application of wind tunnels. Guideline VDI-3783-12, Verein Deutscher Ingenieure.

Versteeg, H.K., & Malalasekera, W. (1995). An introduction to computational fluid dynamics – The finite volume method. Longman Scientific and Technical.

Vetrano, M.R., & Riethmuller, M. (2010). Laser Doppler velocimetry and phase Doppler interferometry. Introduction to Measurement Techniques – Von Karman Institute for Fluid Dynamics.

Volter, H. (2015). The movement of clouds around Mount Fuji – Photographed and filmed by Masanao Abe. Spector Books.

Walmsley, J.L., & Taylor, P.A. (1996). Boundary-layer flow over topography: Impacts of the Askervein study. *Boundary-Layer Meteorology 78*, pp. 291-320.

Wilczak, J.M., Oncley, S.P., & Stage, S.A. (2001). Sonic anemometer tilt correction algorithms. *Boundary-Layer Meteorology 99*, pp. 127-150.

Wood, D.H. (1982). Internal boundary layer growth following a step change in surface roughness. *Boundary Layer Meteorology 22*, pp. 241-244.

Wood, N. (2000). Wind flow over complex terrain: A historical perspective and the prospect for large-eddy modelling. *Boundary Layer Meteorology 96*, pp. 11-32.

World Meteorological Organization (2008). Guidelines for converting between various wind averaging periods in tropical cyclone conditions.

Wyngaard, J.C. (2004). Toward numerical modeling in the "Terra Incognita". *Journal of the Atmospheric Sciences 61*, pp. 1816-1826.

Yeh, Y., & Cummins, Z.H. (1964). Localized fluid flow measurements with an He-Ne laser spectrometer. *Applied Physics Letters 4 (10)*, pp. 176-178.

Yeow, T.S., Cuerva-Tejero, A., & Perez-Alvarez, J. (2015). Reproducing the Bolund experiment in wind tunnel. *Wind Energy 18*, pp. 153-169.

Zhiyin, Y. (2015). Large-eddy simulation: Past, present and the future. *Chinese Journal of Aeronautics 28*, pp. 11-24.

LIST OF FIGURES

LIST OF TABLES

Versicherung an Eides statt – Affirmation on oath (§59 Abs. 3 HmbHG)

Hiermit versichere ich an Eides statt, dass ich die vorliegende Dissertation mit dem Titel:

“Investigation of terrain effects on wind dynamics within the lower atmospheric boundary layer”

selbständig verfasst und keine anderen als die angegebenen Hilfsmittel – insbesondere keine im Quellenverzeichnis nicht benannten Internet-Quellen – benutzt habe. Alle Stellen, die wörtlich oder singemäß aus Veröffentlichungen entnommen wurden, sind als solche kenntlich gemacht. Ich versichere weiterhin, dass ich die Dissertation oder Teile davon vorher weder im In- noch im Ausland in einem anderen Prüfungsverfahren eingereicht habe und die eingereichte schriftliche Fassung der auf dem elektronischen Speichermedium entspricht.

I hereby declare on oath that I have written the present dissertation, with the title:

“Investigation of terrain effects on wind dynamics within the lower atmospheric boundary layer”,

on my own and have not used other than the acknowledged resources and aids. All passages taken literally or analogously from other publications are identified as such. I further declare that this thesis has not been submitted to any other German or foreign examination board and that the submitted written version corresponds to that on the electronic repository.

Hamburg, 18/12/2019 ________________________________

(Signature)